

Cyclotron Irradiation on Tungsten & Co-relation of Thermo-Mechanical Properties to Displacement and Transmutation Damage

Rahul Rayaprolu

Energie & Umwelt / Energy & Environment

Band / Volume 540

ISBN 978-3-95806-552-9

Forschungszentrum Jülich GmbH
Institut für Energie- und Klimaforschung
Plasmaphysik (IEK-4)

Cyclotron Irradiation on Tungsten & Co-relation of Thermo-Mechanical Properties to Displacement and Transmutation Damage

Rahul Rayaprolu

Schriften des Forschungszentrums Jülich
Reihe Energie & Umwelt / Energy & Environment

Band / Volume 540

ISSN 1866-1793

ISBN 978-3-95806-552-9

Bibliografische Information der Deutschen Nationalbibliothek.
Die Deutsche Nationalbibliothek verzeichnet diese Publikation in der
Deutschen Nationalbibliografie; detaillierte Bibliografische Daten
sind im Internet über <http://dnb.d-nb.de> abrufbar.

Herausgeber
und Vertrieb: Forschungszentrum Jülich GmbH
 Zentralbibliothek, Verlag
 52425 Jülich
 Tel.: +49 2461 61-5368
 Fax: +49 2461 61-6103
 zb-publikation@fz-juelich.de
 www.fz-juelich.de/zb

Umschlaggestaltung: Grafische Medien, Forschungszentrum Jülich GmbH

Druck: Grafische Medien, Forschungszentrum Jülich GmbH

Copyright: Forschungszentrum Jülich 2021

Schriften des Forschungszentrums Jülich
Reihe Energie & Umwelt / Energy & Environment, Band / Volume 540

D 82 (Diss. RWTH Aachen University, 2021)

ISSN 1866-1793
ISBN 978-3-95806-552-9

Vollständig frei verfügbar über das Publikationsportal des Forschungszentrums Jülich (JuSER)
unter www.fz-juelich.de/zb/openaccess.



This is an Open Access publication distributed under the terms of the [Creative Commons Attribution License 4.0](https://creativecommons.org/licenses/by/4.0/),
which permits unrestricted use, distribution, and reproduction in any medium, provided the original work is properly cited.

500000

Fakultät für Georessourcen und Materialtechnik

S. Frenzel-Gumlich

Intzestr. 1

52056 Aachen

Fax: 0241-80-92370

E-Mail: doctoral-studies-fb5@rwth-aachen.de

Statutory Declarations

I certify that I composed the thesis autonomously. Any help I made use of,
I stated precisely.




Signature

Jülich, 08.07.2020

place, date

In case the doctoral thesis was not written at the RWTH:

I certify that the publication of the thesis does not breach any existing trade secrets



Signature

Jülich, 08.07.2020

place, date

Executive summary

Re is the largest transmutation product under neutron irradiation of W. It is known to precipitate under fission neutron irradiations. Recent work has shown that Re affects dislocation behaviour in W, and this cannot be reproduced by self ion irradiations. Therefore, only a combined damage study can completely uncover the fusion neutron damage environment of W.

30 MeV protons induce a combined; displacement and transmutation damage, with a fusion relevant Re transmutation in W. This thesis has set up and trial tested the use of 30 MeV proton irradiation on W. Further experiments will detail the irradiation behaviour of W. While, a fusion neutron source is still required for detailed investigations and true quantification of the post irradiation material property data, 30 MeV protons can serve as an accelerated test bed for fusion neutron irradiations and this study has laid the foundation for long term irradiation work of W.

Abstract

Neutron damage is a major deciding factor in the commercialisation of a fusion power plant. Neutron damage inflicted on the walls of the reactor during operation, leads to changes in the behaviour of materials and ultimately decides the life time of the component. Consequently, it is essential that fusion relevant materials are tested under fusion irradiation conditions in order to qualify them, prior to use. Tungsten is a key material for the plasma facing component in a fusion reactor, and is located directly in the path of high energy fusion neutrons. Currently, it is not possible to test the change in material behaviour under high energy neutrons as there exists no high flux fusion neutron source. Moreover, high flux fission reactors are unable to reproduce the high energy neutron damage. However, this work demonstrates the use of 30 MeV protons to induce fusion relevant neutron damage on tungsten.

This work involves the first irradiation of tungsten using high energy protons (30 MeV). A complete irradiation cycle, including irradiation planning, sample design and manufacturing, polishing, irradiation, the setting up of post irradiation devices and post irradiation investigation was carried out within the scope of this work. Optimal sample geometry for accelerator irradiations, which is also directly comparable and compatible with fission reactor irradiations, was manufactured. The sample holder was designed such that in-situ temperature measurements were possible for the first time. Additionally, hot cell and remote handling conforming, punch and indentation testing have been developed and demonstrated through the use of irradiated active samples.

In order to understand proton damage, pure tungsten was irradiated using three different proton energies 3, 16 & 30 MeV. The 3 MeV proton irradiation produces pure displacement damage, while the 16 & 30 MeV induce a combination of displacement and transmutation damage. Moreover, instrumented indentation was performed on the irradiated samples in a radiation environment (controlled areas). For all proton energies, an irradiation hardening of 0.6 GPa was observed at low doses of 0.003 dpa for 30 MeV protons and 0.005 dpa for 3 MeV protons. Further experiments with 3 MeV protons displayed an initial further increase followed by saturation at 0.4 dpa. A similar behaviour has been reported with self ion irradiations on pure tungsten. The TEM observations of 3 MeV proton irradiated tungsten shows the development of dislocation loops, which grow in size but also achieve a saturation in loop density. This correlates well with the saturation in irradiation hardening.

Irradiation modelling was performed using MCNP6.1 and FISPACT-II on both the sample and the sample holder to estimate the damage capability of 30 MeV protons. Post irradiation, gamma analysis showed good agreement with the modelling. Additionally, dose rate measurements were in-line to estimates from the simulations. This, by extension validates the transmutation capability of 30 MeV protons and their ability to simulate fusion neutron damage in W.

Keywords

Fusion, tungsten, neutron damage, ion irradiation, proton damage, transmutation

Kurzfassung

Neutronenschäden sind ein entscheidender Faktor für die Kommerzialisierung eines Fusionskraftwerks. Neutronenschäden, die während des Betriebs an den Wänden des Reaktors entstehen, führen zu Veränderungen im Verhalten der Werkstoffe und entscheiden letztlich über die Lebensdauer der Komponente. Folglich ist es unerlässlich, dass fusionsrelevante Werkstoffe vor ihrem Einsatz unter Fusionsbestrahlungsbedingungen getestet werden, um sie zu qualifizieren. Wolfram ist ein Schlüsselwerkstoff für die dem Plasma zugewandten Komponenten in einem Fusionsreaktor und befindet sich direkt im Feld der hochenergetischen Fusionsneutronen. Gegenwärtig ist es nicht möglich, die Veränderung des Materialverhaltens unter Hochenergie-Neutronenbestrahlung zu testen, da keine Hochenergie-Fusionsneutronenquelle mit den erforderlichen Neutronenflüssen existiert. Darüber hinaus sind Hochfluss-Fissionsreaktoren nicht in der Lage, die Schädigung durch hochenergetische Neutronen zu reproduzieren. Deshalb demonstriert diese Arbeit die Verwendung von 30 MeV-Protonen zur Induktion von fusionsrelevanten Neutronenschäden an Wolfram.

Diese Arbeit umfasst die erste Bestrahlung von Wolfram mit hochenergetischen Protonen (30 MeV). Im Rahmen dieser Arbeit wurde ein kompletter Bestrahlungszyklus einschließlich Bestrahlungsplanung, Probenentwurf und -herstellung, Polieren, Bestrahlung, Einrichtung von Nachanalyseeinrichtungen und die Nachanalyse selbst durchgeführt. Es wurde eine optimale Probengeometrie für Beschleunigerbestrahlungen hergestellt, die auch direkt mit Fissionsreaktorbestrahlungen vergleichbar und kompatibel ist. Der Probenhalter wurde so konstruiert, dass erstmals in-situ-Temperaturmessungen möglich waren. Zusätzlich wurden Heißzellen- und Fernhandhabungs-aufbauten und-, Stanz- und Eindringversuche entwickelt und durch die Verwendung bestrahlter aktiver Proben erprobt.

Um Protonenschäden zu verstehen, wurde reines Wolfram mit drei verschiedenen Protonenenergien 3, 16 & 30 MeV bestrahlt. Die Protonenbestrahlung mit 3 MeV erzeugt reine Versetzungsschäden, während die 16 & 30 MeV eine Kombination von Versetzungs- und Transmutationsschäden induzieren. Darüber hinaus wurde an den bestrahlten Proben in einer Strahlenschutzumgebung (Kontrollierte Bereiche) instrumentierte Eindringprüfung durchgeführt. Für alle Protonenenergien wurde eine Strahlungshärtung von 0,6 GPa bei niedrigen Dosen von 0,003 dpa für 30 MeV-Protonen und 0,005 dpa für 3 MeV-Protonen beobachtet. Weitere Experimente mit 3 MeV-Protonen zeigten einen anfänglichen weiteren Anstieg, gefolgt von einer Sättigung bei 0,4 dpa. Über ein ähnliches Verhalten wurde bei der W-Ionen Bestrahlung mit reinem Wolfram berichtet. Die TEM-Beobachtungen von mit 3 MeV-Protonen bestrahltem Wolfram zeigen die Entwicklung von Versetzungsschleifen, die an Größe zunehmen, aber auch eine Sättigung in der Schleifendichte erreichen. Diese korreliert gut mit der beobachteten Sättigung der Strahlungshärtung.

Die Bestrahlungsmodellierung wurde mit MCNP6.1 und FISPACT-II sowohl an der Probe als auch am Probenhalter durchgeführt, um die Schädigungseigenschaften von 30 MeV-Protonen abzuschätzen. Nach der Bestrahlung zeigte die Gamma-Analyse der Probenaktivität eine gute Übereinstimmung mit der Modellierung. Zusätzlich passten die Dosisleistungsmessungen zu den Schätzungen aus den Simulationen. Dies validiert die Transmutationseigenschaften von 30 MeV-Protonen und ihre Fähigkeit, Fusionsneutronenschäden in W zu simulieren.

Keywords

Fusion, Wolfram, Neutronenschäden, Ionen Bestrahlung, Protonenschäden, transmutation

Preface

The work described in this thesis is carried out by the author at the Forschungszentrum Jülich GmbH, Institut für Energie- und Klimaforschung – Plasmaphysik, Partner of the Trilateral Euregio Cluster (TEC), 52425 Jülich, Germany. It is carried out under the supervision of Prof. Christian Linsmeier and Dr. Sören Möller. No part of this thesis has been attempted to be submitted for a degree at this or any other university. All of the work is original and if reproduced, it has been clearly cited and referenced in the text. A list of references is given at the end of the thesis.

Partial funding has been received and is acknowledged from the EUROfusion consortium and the Euratom research and training programme 2014-2018 and 2019-2020 under grant agreements No. 633053. The views and opinions expressed in this work herein, do not necessarily reflect those of the European Commission.

Part of this work has been detailed and reported at the following conferences and in the listed publications:

Conferences

- 28th IEEE Symposium on Fusion Engineering, Ponte Vedra, June 2019
- 30th Symposium on fusion technology, Sicily, September 2018
- 16th International conference on plasma-facing materials and components, Neuss, May 2017
- Deutsche Physikalische Gesellschaft e.V. spring meeting, Bremen, March 2017

Publications

- R.Rayaprolu et al., Simulation of neutron irradiation damage in tungsten using higher energy protons, Nuclear Materials and Energy, 2016
- S.Möller et al., HiperFer, a reduced activation ferritic steel tested for nuclear fusion applications, Nuclear Materials and Energy, 2018
- S.Möller et al., Deuterium retention in tungsten and reduced activation steels after 3 MeV proton irradiation, Nuclear Materials and Energy 2020
- R.Rayaprolu et al., Indentation testing on 3 MeV proton irradiated tungsten, Nuclear Materials and Energy 2020

List of abbreviations

JET	Joint European Torus
DEMO	DEMOstration fusion power plant
E_d	Displacement threshold energy
DBTT	Ductile to Brittle Transition Temperature
PKA	Primary Knock on Atom
NRT	Norbert, Robinson and Torrens damage model
DFT	Density Functional Theory
MD	Molecular Dynamics
dpa	displacements per atom
ALARA	As Low As Reasonably Achievable
EDM	Electro-Discharge Machining
SEM	Scanning Electron Microscopy
FIB	Focussed Ion Beam
TEM	Transmission Electron Microscopy
EDX	Energy Dispersive X-ray spectroscopy
SSTM	Small Scale Testing Methods
ISO	International Standards Organisation
HML	Hot Materials Laboratory
FEM	Finite Element Methods
LVDT	Linearly Varying Differential Transducer
IIT	Instrumented Indentation Testing
apm	atomic parts per million
ICP-MS	Inductively Coupled Plasma - Mass Spectroscopy
ICP-OES	Inductively Coupled Plasma - Optical Emission Spectroscopy

TOF-SIMS	Time Of Flight - Secondary Ion Mass Spectrometry
EP	Electro-polishing
APT	Atom Probe Tomography
HPGe	High Purity Germanium detector
ENDF	Evaluated Nuclear Data File
HFR	High Flux Reactor (fission) in Petten
HFIR	High Flux Irradiation Reactor (fission) in Oak Ridge

Contents

Executive summary	v
Abstract	vii
Preface	ix
List of abbreviations	xi
1 Introduction	1
1.1 Fusion	2
1.2 Magnetically confined fusion	4
1.3 Fusion first wall and materials	6
1.4 Neutron damage	8
1.5 Proton irradiation	9
2 Neutron damage	11
2.1 Displacement damage	12
2.2 Transmutation damage	18
2.3 Combined damage	22
3 Accelerator irradiation	27
3.1 Accelerator technology	27
3.2 Accelerator irradiation review	30
3.3 Ion- displacement damage	31
3.4 Feasibility study-proton damage	36
4 Tungsten	47
4.1 Manufacturing	47
4.2 Neutron damage	48
4.3 Modelling radiation damage	52
4.4 Ion irradiation of W	55
5 Small scale testing methods	59
5.1 Motivation for small scale methods	59
5.2 Sample design & preparation	60
5.3 Instrumented indentation	67
5.4 Shear punch testing	72
5.5 Hot cells & radiation safety	77

6	3 MeV proton irradiation	83
6.1	3 MeV damage	83
6.2	Bragg peak effects & heat loads	87
6.3	Post mortem analysis - TEM	91
6.4	Post mortem analysis - IIT	94
7	16 MeV proton irradiation	99
7.1	Baby cyclotron	99
7.2	Sample holder	101
7.3	Sample activity simulations	102
7.4	Irradiations & power loading	106
7.5	Post irradiation sample analysis	111
8	30 MeV proton irradiation	117
8.1	Cyclotron	117
8.2	Irradiation & heat loading	119
8.3	Post irradiation analysis	121
9	Cold neutrons	133
9.1	Sample preparation	134
9.2	Irradiation stations	138
9.3	Sample assembly	140
9.4	Proposal and discussion	142
10	Concluding discussion	145
	Summary	151
	Outlook	155
	Bibliography	157
	List of Figures	177
	List of Tables	185
	Appendix Elemental composition	189
	Appendix Cold neutrons	193
	Appendix Accelerator target	199
	Appendix Shear punch	205
	Acknowledgement	211

Chapter 1

Introduction

Electricity is a key component of today's lifestyle and the further upcoming technology such as wide spread use of electric mobility, artificial intelligence and communication are heavily electricity dependent. In fact electricity has been positioned as fundamental to human development [1],[2], equaling to a human right. On a macroscopic level, there is evidence of country's economic growth depending on the reliability of its electricity supply [3],[4]. This is reflected in the world energy outlook 2018 report's [5] 'electricity section', where there is an estimated increase of 62% in global electricity generation between 2017 and 2040, of which the highest would be in developing countries. The international energy agency forecasts a tremendous increase in the energy demand in Asia with a three fold increase projected for India alone [6]. However a major dilemma facing the global policy makers is the intertwined problem of achieving the energy requirement projections without further escalating the human driven climate change [7]. The 2015 climate change agreement, "Paris agreement", enforces a policy obligation on countries to limit their emissions so as to contain the average global temperatures to 1.5-2°C above the pre-industrial levels [8],[9]. Furthermore, world wide protests on government inaction on curtailing climate change has led to debates and increasing assurances for changes in energy systems [10].

Electricity production is one of the sectors with largest decarbonisation capacity [11],[12]. Presently a mix of renewables and fossil fuels are used to power countries of which the share of renewables has been steadily increasing. For instance in the year 2013, renewables made up for more than 50% of the global power capacity addition [13]. However, high-penetration of renewables comes with its own set of problems like power oscillations [14] and fluctuating electricity generation due to inherent nature of renewable [15],[16]. Presently in most countries coal based power plants are required in the energy generation mix to optimise inherent supply-demand fluctuations. On the other hand coal being a major air polluter and green house gas emitter is sought to be replaced by a cleaner and sustainable source of base load energy. At a time where climate research and protection has taken a top priority, nuclear energy as a carbon free energy source is included in almost all climate stability alternatives [17],[18],[19].

Chernobyl and Fukushima fission reactor accidents left large dents within the nuclear industry and public sentiment. Major efforts in increasing safety has been a top priority for the nuclear fission industry with nuclear energy projected to increase upwards of 17% of the total energy mix by the 2050's [20]. Modern generation III & IV reactors with inherent shutdown modules and proliferation [21] techniques led the design changes and safety concepts. Fusion on the other hand while also a form of nuclear energy is yet to enter commercial electricity production. Fusion as against fission combines two light nuclei into a heavier nucleus and

in turn release energy. Nuclear fusion as an electricity source has been conceptualised since the 1930's [22] and it has been seen as a source of limitless clean energy [23],[24],[25]. It is inherently safe as against fission's explosive nature and major advances in safe fusion conditions on earth are reached. The advancement of technologies for fusion reactors is slowly reaching maturity and it might be possible to demonstrate commercial viability of fusion energy sooner than later.

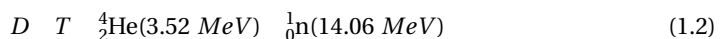
1.1 Fusion

Sun is the best example of nuclear fusion in our everyday life. In the history of the universe, thermo-nuclear fusion reactions existed since a few moments after the big bang. The initial condition post big bang were such that quarks existed as free particles in a quark-gluon mix [26],[27]. Shortly after, with expansion and decreasing temperature to about 10^{11} K, neutrons and protons were formed. These sub atomic particles started the first nuclear fusion reactions, leading to the formation of helium. Further expansion, decrease in temperature and stability of formed helium stopped the reaction chain, leading to the cosmic dark ages.

Fusion is the merging or coalescence of two particles leading to a heavier particle. In order to achieve nuclear fusion, the two fusing ions must overcome the coulomb repulsion between them. For protons, this is in the range of 200 keV (2.3×10^9 K). However, due to the wave nature of particles, they are able to overcome this energy barrier and there exists a finite cross-section for fusion [28]. Despite the temperature of the universe being below 10^9 K, as the dense clumps of gas slowly contracted to form stars, subsequent gravitational potential energy increased temperatures back to about 10^7 K. This led to gradual restart of fusion reactions. Fusion reactions in stars of sun size are based primarily on the proton proton fusion reactions [28] as shown in Equation 1.1.



The proton-proton fusion reaction proceeds through the weak force, beta decay channel and thereby is an extremely slow reaction which can't be put into use and achieve viable fusion power on earth. The reaction rates for alternate viable fusion reactions are compared in Figure 1.1. The reaction rate for a (p,p) reaction is orders of magnitude lower and isn't seen on the graph. The deuterium tritium (DT) reactions has one of the highest cross-sections at the lowest energies/ temperatures (20 keV or 2.3×10^8 K). This is due to the highly stable product ^4He , alpha particle (helium nucleus), produced from the reaction. The reaction has a high Q value of 17.6 MeV and is shown in Equation 1.2. This is a neutronic reaction wherein the neutron carries 80% of the energy. The inputs for this reaction are deuterium which is naturally available and can be extracted from sea water and tritium which is radioactive with a half life of 12.3 years. Very small amounts of tritium are found in the upper layers of ionosphere, however these minute quantities aren't of much use towards power generation. Tritium is also generated in the CANDU fission reactors but the quantity per year is limited and small [29]. Hence, tritium has to be bred using a neutron capture reaction within a fusion reactor. Beyond the energy for highest cross-section, the reaction rate decreases due to shorter interaction times between the charged ions.



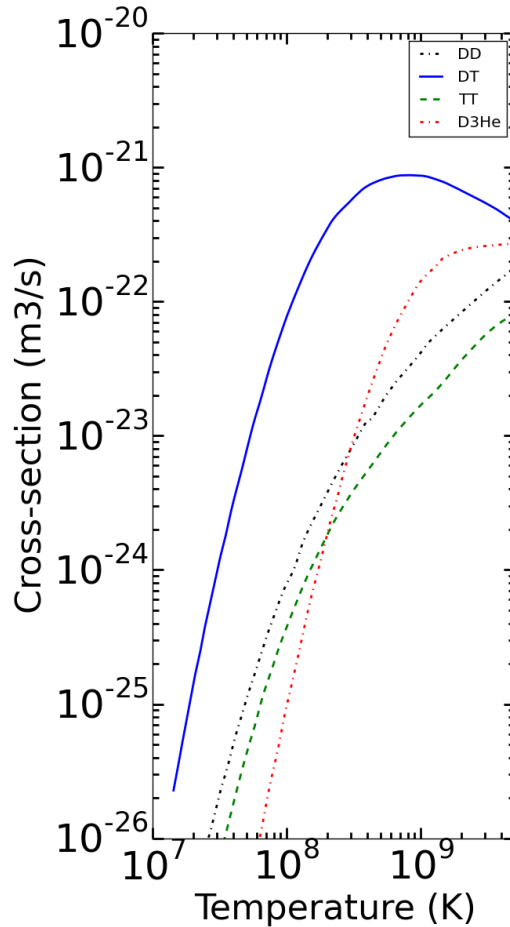


Figure 1.1: Comparison of fusion reaction rates for light ions [30]. Deuterium tritium reactions have the highest cross-section for lower ion temperatures. This is due to the release of a stable alpha particle (helium nucleus) as a reaction product.

DT fusion reactions need temperatures above 10^8 K (refer Figure 1.1). Also in order to induce the necessary fusion reaction rate (fusion reactions per second), a certain ion density is needed. Consequently, the entire hot plasma of pre-estimated density should be confined to induce collisions and avoid losses. Machines called tokamaks are used to contain the hot ion plasma and reach fusion conditions. These have advanced significantly in terms of design and technology over the years and are considered the vessel for fusion power production on earth.

1.2 Magnetically confined fusion

The charged particles in a plasma are susceptible to magnetic fields and can be directed into pre-determined paths. Using magnetic fields the hot ions can be forced into confinement and is one of the favoured (agreed upon) methods. A reactor would thus use magnetic fields to contain and insulate a hot plasma within a vacuum vessel and keep it away from the walls. This was known to be the crucial aspect from the very beginning [31]. Different magnetic confinement techniques such as dynamic pinch, inverse pinch, magnetic mirrors have over the years culminated in the design of a toroidal shaped confinement device called the Tokamak. Designed in the late 1960's by then Soviet scientists, it uses the combination of toroidal magnetic fields to create twisted magnetic field lines. These magnetic field lines are closed and thus the charged particles move along these closed field lines and avoid interacting with the wall, thereby being contained. As shown in Figure 1.2, a tokamak is a toroidal vessel into which gas is injected. This gas is then ionized and forms the plasma held in shape with the toroidal magnetic fields. To induce collisions within the plasma in a tokamak, a current is induced into the plasma using large transformers called the central solenoid. Ramping the current up or down in the plasma, through the central solenoid produces the poloidal magnetic field. Together the toroidal and poloidal magnetic fields shape and contain the plasma. A combination of increase in tokamak dimensions with parallel increase

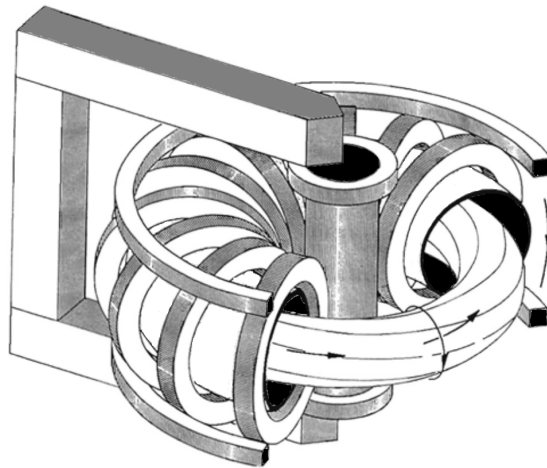


Figure 1.2: A general sketch of Tokamak facility highlighting the toroidal coils and the central solenoid adapted from [32]. The magnetic flux representation are also shown for particle motion.

in input heating power and total magnetic power has been crucial in the development of fusion bringing us to present day machines [33] as shown in Figure 1.3 adapted from [34]. The combination of the three conditions (temperature, density and confinement time) is termed as the fusion triple product and is seen as a measure of the development of fusion capabilities. Initial machines built and operated in the 1960's such as the T3 were able to achieve modest temperatures of 0.2 keV (2.3×10^6 K) with good confinement. A significant jump in plasma heating and confinement were achieved on the tokamak TFR in 1970's, driving temperatures to 2 keV (2.3×10^7 K). A combined European machine; the Joint European Torus (JET), which started construction in the 1970's led the deuterium plasma experiments. In

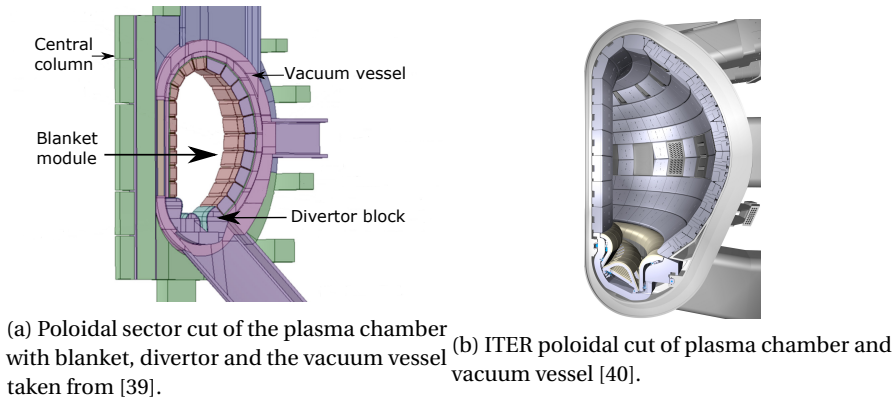


Figure 1.4: Poloidal cuts of the plasma chamber.

power plant however, would require larger fusion triple product (larger energy multiplication), longer pulse lengths and higher availability or, for a successful power plant the energy released from fusion should be larger than the energy required to heat the plasma. The power plant would also need to sustain the fusion reaction for continuous net power output. This places a considerable strain on the technology required to operate safely and economically for long time frames. Materials in particular would be required to show high usability with low damage impact for sustained operations under heavy environmental loading conditions. A large proportion of research is committed to ensure material behaviour for fusion operations and is a key technology challenge in the roadmap to fusion power.

1.3 Fusion first wall and materials

Fusion reactors place heavy requirements on materials during operation. There is an influx of heat loads, high energy ions and neutron fluxes which are constantly present during the reactor cycle. The core of the reactor is the plasma chamber which encloses the hot high energy ions within its walls. The walls themselves are a combination of armour material and a blanket module. A radiation shield and the vacuum vessel [38] follow outwards from the wall. A poloidal cut out sector of 11.25° adapted from [39] is shown in Figure 1.4. The blanket module is a complex adaptation of the armour and the tritium breeding blanket. It has two major functions; tritium breeding for further operation and power extraction for electricity generation, and thus must be protected in order to function with high efficiency. It is protected from the direct line of sight of incident plasma by the armour. The armour is essentially a few mm thick metal shield and faces the hot plasma. Steady state heat fluxes of 1 MWm^{-2} are incident on the armour. Additionally, localised effects leading to bursts of plasma or ELMs' are also projected on the armour which could lead to localised melting and damage.

Under normal circumstances, the plasma is exhausted using the divertor module, which is shown in detail in Figure 1.5 taken from [41]. It exhausts power and helium (He) ash created from the fusion reaction at high rates. Originally proposed by Spitzer in early 1950's, it has additional poloidal coils to create the null profile. The assembly is actively cooled to accommodate steady heat fluxes between $10 - 20 \text{ MWm}^{-2}$, and continually pumped to remove impurities and He particles from the plasma. The entire assembly of the blanket and divertor systems is vacuum sealed by the vacuum vessel. This assists in the nuclear shielding of the

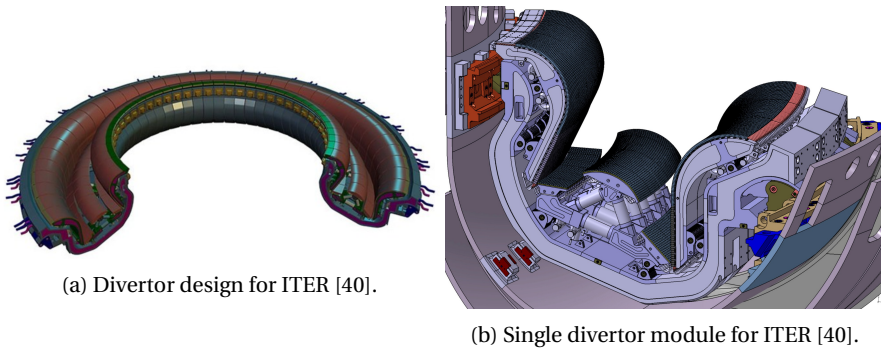


Figure 1.5: Divertor design and cassette.

magnetic coils and forms the first confinement body of the nuclear machine.

The interaction of plasma with material could result in various disturbances such as overheating and melting of material. Furthermore, the release of material and incorporation as impurity within the plasma, leading to rapid cooling and extinguishing the core plasma is possible. Chemical and physical sputtering from energetic ions on the material and subsequent re-deposition in other areas is another prime concern. Such interactions degrade the material over time and pose a serious threat to components. Thereby, materials considered for plasma facing components such as the divertor, armour and wall have extremely high requirements. The blanket module and the divertor experience a steady heat flux and are expected to withstand high operating temperatures and large temperature gradients of the order of 10^6 K m^{-1} [42]. In a tokamak, plasma facing materials face the brunt of the damage with plasma loads of upto $10^{23} \text{ m}^{-2} \text{ s}^{-1}$ and 50 MW m^{-2} in absence of plasma detachment [43]. Accordingly, one of the foremost options to choose a qualifying material is its high melting point and large thermal conductivity. This restricts the options significantly to carbon, a few rare earth elements and the refractory metals such as tungsten(W). Another important criteria for the selection of materials with direct contact to the plasma is its low tritium retention capability. Tritium requires breeding for use as a primary fuel within the fusion reactor. It is also radioactive and has inventory limits placed on this. Thus any tritium trapped within the wall is lost and cant be used to induce fusion reactions. The above combined with low erosion properties and good mechanical stability make the ideal material.

Initially the material SS316L or Inconel was used for the vacuum vessel walls and for plasma facing components [44]. With increasing plasma temperatures, refractory materials such as tungsten and molybdenum were used for their high melting points and good thermal behaviour and crack resistance upon plasma contact [45]. However, at relatively low plasma densities and high power, very high edge plasma temperatures were observed and large core radiation was recorded due to W impurities incorporated by the plasma [46]. To avoid core radiation, low Z materials were considered and nuclear grade graphite was used. Graphite or carbon however, traps tritium and leads to the formation of hydrocarbons. The DT experiments at JET observed operational issues with graphite. This was compounded by its poor mechanical properties, especially under neutron irradiation [46]. Recent progress on machines such as EAST, ASDEX-Upgrade have shown good plasma performance with W, while in the mean time beryllium has filled the void for low Z graphite replacement. Its oxygen gathering properties, good thermal conductivity and low affinity for hydrogen isotopes has made it a viable starting option for ITER.

The present material choices for future tokamaks revolve around a selection of low activation steels, W and tritium breeding materials. SS316L(N)-IG is considered as the primary choice for the vacuum vessel. Its considered composition taken from [39]. Multiple blanket designs are being tested which are in turn based on the selection of coolants, water or He [47]. Eurofer, a reduced activation ferritic martensitic steel [48] is considered as the primary in-vessel steel for fabrication of the blanket casings amongst other components. These materials are specially designed for low residual activity post irradiation by substituting Mo, Nb and Ni by Ta, W and V elements. For the areas of high heat loads, W is the prime candidate. W is considered for the armour and the first wall which is estimated to be 2 mm thick. It is also considered for the divertor which is actively cooled (water cooled) with a 5 mm thick W layer.

W with its high melting point of 3422°C, high thermal conductivity, low sputtering and retention has gained wide acceptance as the first wall armour and plasma facing material. Systematic approaches to understand and develop low activation, creep resistant and high temperature performance materials have led to advanced materials such as W fibre-W and Eurofer-97 steels [49],[50]. The new materials are subjected to a wide range of thermo-mechanical tests along with plasma exposures and thermal shocks [51],[52]. However, the limitations of the presently used irradiation methods severely limits our knowledge of the irradiation behaviour from advanced materials.

1.4 Neutron damage

Nuclear fusion is deemed safe for its low environmental impact. This comprises of no CO₂ emissions, intrinsic safety and shut down, and no potential long term nuclear waste problems [53]. From the very beginning a huge emphasis on safety is associated to fusion technology development. The in-vessel components are subjected to high steady state temperatures, large thermal gradients during transient events and irradiation effects [54]. However, the most significant damage would arise from the flux of high energy neutrons. Neutrons are released as a result of the fusion reaction and carry away 80% of the reaction energy. This energy must be harnessed from the neutron and channelled into power generation. Simultaneously, neutrons are required to breed ³H for the DT reaction to continue and thus play a major role in fusion. However, materials under fusion neutron loads is an uncharted territory and needs urgent attention [55], [56].

Our knowledge of neutron effects on materials is based on the impact of fission neutrons on materials and their subsequent testing. The interaction of neutrons with materials activates the materials by producing unstable isotopes which results in radioactivity. These isotopes can be long lived and create potential safety hazards. The safety aspects range from potential radiation release, occupational radiation exposure and potential long term radioactive waste inventories [21]. Additionally, neutrons are known to displace and transmute elements induce property changes in materials. The displacement and transmutation damages then cause engineering changes, leading to an early failure of the component.

The damage created by neutrons is often collapsed to a number called displacements per atom (dpa) and can be estimated using the neutron spectrum (further details in chapter neutron damage). 1 dpa is a large quantity and represents a lattice environment where each atom has been displaced once from its original position due to neutron induced damage. Many micro-structural changes are seen in materials post neutron irradiation to 1 dpa dose. For instance, voids are known to form in the range between 0.05 - 0.5 dpa and is associated with swelling of materials. In W, large precipitation of Re is seen to formed as a result of neutron irradiation between 0.5 - 1 dpa damage and is linked to the rapid rise in hardness of

materials.

Fusion reactor, plasma facing materials are expected to undergo damages between 6 - 7 dpa/year [57]. This creates harsh operating conditions for materials which are expected to operate for extended lifetimes. Such strong damage is yet to be tested in fission reactors. Moreover, the fusion neutron energy spectrum is peaked at a much higher energy of 14 MeV as compared to the fission neutron spectrum and as a result fusion neutrons produce larger and denser displacement cascades with higher surviving defects in the material [58]. These cascades and the subsequent atomic processes can induce swelling, brittleness and hardening of the material. Furthermore, with higher neutron energies, threshold nuclear reactions such as (n, α) , (n,p) and $(n,2n)$ are feasible, leading to a composition change within the material. In the case of pure W, fusion neutrons are expected to induce a displacement damage of upto 6 dpa/year along with compositional change to W - 1Re0.2Ta within two years of operation [59]. Thereby, the correct damage composition can't be reproduced by fission neutrons.

While fission reactors are the closest approximation to having neutron irradiation testing, long cycle times, highly active samples, differences in neutron energy spectrum (neutron damage), the inability to achieve high damage rates has led the need for other irradiation options such as ion damage.

1.5 Proton irradiation

Since the 1970's, ions have been used to replicate neutron damage. Ion irradiation parameters can be easier adapted to replicating fusion neutron damage as compared to fission reactors and with the advancement in accelerator technology, faster rates of damage creation are feasible. Moreover, access to ion irradiations is easier than fission irradiations. Over the years low energy protons, self ions and heavy ions have been used to induce displacement cascades and study their effects in materials [60]. In the past, ion irradiations have purely focussed on displacement damage or have used alloys to induce compositional changes (transmutation damage) within the material. This has the benefit of handling and testing of samples in a non radioactive environment as the samples remain inactive post irradiation. Binary collision approximation and first principle studies have resulted in large progress towards understanding of radiation mixing and damage evolution. However to completely mimic fusion neutrons a combined displacement and transmutation damage evolution needs to be studied. Also, in view of qualification of advanced material concepts, a combined damage post irradiation testing is quintessential.

The mass of a proton is similar to that of a neutron (938.2 & 939.5 MeVc⁻²). High energy protons are capable of producing pure coulomb scattering which replicates a high energy neutron scattering. Simultaneously, high energy (>12 MeV for W) protons produce significant transmutation reactions which alter the material composition and thereby can be used to simulate combined, displacement and transmutation damage from neutrons. They also produce significant quantities of He and H similar to fusion reactors. Previous findings reported in [61] suggest proton energies between 16 - 30 MeV could reasonably simulate combined damage arising from fusion neutrons. The range of ions unlike that of neutrons is limited by electronic and nuclear stopping in materials. This places a limitation on the sample thickness (size) which can be irradiated. With increasing energies, the range of ions increases and 30 MeV protons are seen to have ranges above 1 mm total and upto 500 μ m of constant damage in W. Such ranges allow for macroscopic testing which can be compared along side neutron irradiation.

Small scale testing techniques have evolved along with ion irradiation. Advantages of small scale testing are lower sample activity (or dose), advanced materials are often produced in small quantities and often a better understanding of the microscopic behaviour. Fusion material development and research has contributed to the development of small scale testing techniques such as shear punch, nano indentation and small scale tensile sample testing [62]. Methods to extract engineering properties such as toughness, DBTT, hardness and tensile strength from the small scale testing techniques are also established. While small scale, the techniques register macroscopic material properties. These design parameters would be used to engineer materials for upcoming and future fusion devices and understand irradiation induced changes.

The aim of this work is to demonstrate and investigate the applicability of cyclotron produced *30 MeV proton irradiation of W* for fusion neutron damage studies. This novel technique facilitates the development of a close replication the fusion neutron irradiation environment. This study covers the design, set up, improvement and establishment of high energy proton irradiation along with the post irradiation testing in a nuclear environment. In order to integrate post irradiation radioactivity of the samples, the entire process is treated and approached with a nuclear engineering work concept.

The thesis is structured in the following way: Chapter 2 provides an introduction to fusion neutron damage with an emphasis on combined (displacement and transmutation) damage. Listing the drawbacks of currently available fission neutron sources and the necessity for a correct damage scenario, Chapter 3 covers the way in which ions can be used to emulate neutron damage. The use of protons as a method to induce combined damage is further discussed in this chapter and is augmented through simulations using established codes. Simulations using state-of-the-art nuclear codes - MCNP6.1 and FISPACT-II to simulate the closeness of fusion neutron damage using 30 MeV protons are described with their results. These results presented alongside comparison to other irradiation sources.

Chapter 4 focusses on W and highlights the findings from previous irradiation works. The current gap in knowledge is emphasised, which reinforces the use of 30 MeV protons to describe neutron induced combined damage in W. Chapter 5 outlines the *nuclear engineering design* for pre- and post irradiation work. It introduces the sample design for pure W samples of 300 μm and 500 μm . The method for manufacturing and production of the samples are described in detail. In addition, Chapter 5 includes the modernisation and commissioning of instrumented indentation testing, shear punch testing and tensile testing devices for use in a hot cell towards obtaining properties of irradiated samples. Specific examples of reconstruction for this work are described. Chapter 6, 7 and 8 describe the test irradiations with three different proton energies; 3, 16 and 30 MeV protons respectively. In these chapters, the set up of the irradiation is discussed. Further, it is described how the active irradiated samples are tested using instrumented indentation, which is combined with TEM studies for 3 MeV proton irradiated inactive samples. Finally, a comparison to fission irradiated samples and self ion damaged samples is discussed in the concluding discussion. A summary with an outlook towards further developments in optimising the technique concludes the thesis.

Chapter 2

Neutron damage

Fusion reactors are required to demonstrate a high degree of availability and environmental friendliness. Post Chernobly and Fukushima (fission reactors), safety concerns have been raised worldwide and the focus has been on intrinsic safety measures. Fusion has been driven with the idea of low potential impact of environment and very good safety performance [63]. Unlike fission where the reaction products are radioactive and long lived, products of DT fusion reaction (the helium nucleus and a neutron) are stable. However, the high energy, 14.1 MeV neutron is reactive and in turn capable of significant damage and activation. Neutrons are not charged and consequently not confined by the magnetic fields inside the tokamak. They interact extensively with the plasma facing materials in particular, and with components upto the vacuum vessel. This interaction is often the source of extensive damage and results in degradation of material properties over time.

The neutron is however fundamental to the fusion cycle. Its high interaction probability with ${}^6\text{Li}$ is exploited towards breeding tritium in order to continue the fusion cycle. It also carries 80% of the DT reaction energy which when converted into thermal energy would drive the primary cycle of the reactor. Accordingly, the neutron and its kinetic energy should be exploited for generating tritium and power respectively and thus should be channelled appropriately into the wall and the blanket [56]. The implication being that the high energy neutrons have to be considerably slowed down through collisions within the wall and blanket (elastic recoils and scattering), each time creating a large atomic damage spike in the material and finally tunneled into a neutron capture reaction with ${}^6\text{Li}$ to produce tritium. An urgent need to understand and develop materials which can operate at high temperatures and withstand significant high energy neutron damage is considered as one of the foremost requirements of fusion technology [21].

A natural choice for material characterisation post neutron irradiation are fission reactors. Macroscopic effects of neutron damage on graphite moderator and uranium fuel was forecasted and observed first in the 1940s [64]. From the first fission power reactors generation I (1950-1960s) to the latest generation IV, extensive corrosion studies and radiation damage studies with experimental campaigns have been carried out [65],[66],[67],[68],[69],[70],[71],[72]. Post irradiation characterisation using thermo-mechanical testing, microscopy, tomography, spectroscopy have added to the understanding of damage creation and propagation upto the extent of failure of component. These studies have established that neutrons produce structural damage within the component and can additionally change its material composition, i.e. the fundamental damage creation by neutrons is based on its reaction channel with the material. The two major reaction channels; neutron scattering and neutron absorption can be quantified using reaction rates R , as represented in Equation 2.1, where

is the incoming neutron flux, σ is the reaction channel cross-section and N is the number of nuclei in the path of the neutron (atomic density).

$$R = \phi N \sigma \quad (2.1)$$

Cross-sections represent the probability of the reaction channel to occur and as shown in Figure 2.1 for an (n,p) reaction, are material and neutron energy dependent. The reaction rate is cross-section dependent, which implied that the damage rates (reaction rates) are material specific and a function of the neutron energy. Based on the reaction channels classified into scattering and absorption reactions, the associated neutron damage can be categorised into displacement damage and transmutation damage.

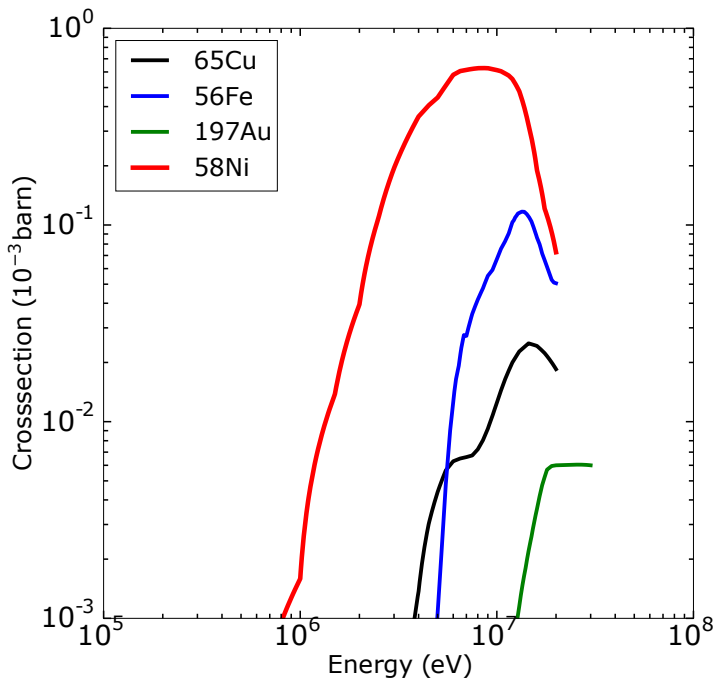


Figure 2.1: Cross-section comparison for (n,p) reaction on Cu65, Au197, Fe56 and Ni58. The cross-sections are material and neutron energy dependent which in turn determines the reaction rates for the material. Cross-sections taken from ENDF/B-VII.1 [73] and JANIS [74].

2.1 Displacement damage

The most straightforward way a neutron interacts with the material atom or nucleus is via scattering. As in billiards, the neutron, a particle scatters upon impact with the incident atom on its path. In a crystalline material, the atoms are bound and arranged together in an orderly fashion called lattice. This arrangement lends a binding energy towards stable lattice configuration and a minimum energy is needed to disturb the atom from its original position. The displacement threshold energy (E_d) is understood to be the minimum energy required in order to remove the atom from its lattice and create a stable defect. For metals this is between

20 – 90 eV. A neutron unhindered by the coulomb force can elastically scatter from the tightly bound lattice atom in its path thus transferring a portion of its energy to it. If the transfer of energy to the atom is greater than (E_d), then the recoiling atom is kicked out of its position. This initial recoiling atom is termed as a primary recoil atom (PKA) and could further induce a sequence of recoils with other lattice atoms called secondary recoils till it is depleted of its kinetic energy. The secondary recoils create tertiary recoils and so on till the initial transfer energy is spent. A representation of this is shown in Figure 2.2, where the neutron shown in black collides with a lattice atom (PKA-red) and imparts energy higher than E_d to it, which in-turn further creates secondary and tertiary recoils (orange).

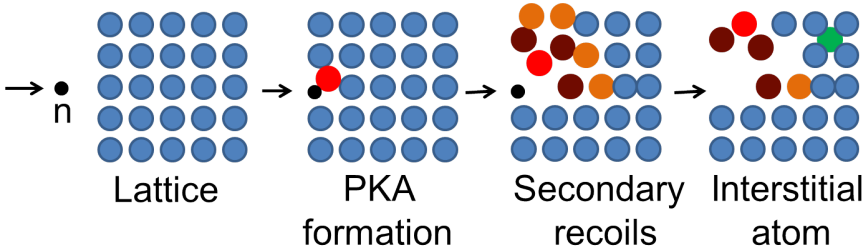


Figure 2.2: Neutron displacement damage flowchart.

Post recoil the PKA might come to rest within the interstices of the lattice and this constitutes a point defect in the lattice [75]. The vacant original spot of the PKA in the lattice is termed as a vacancy while the present intermediary location between defined lattice sites is called an interstitial as shown in Figure 2.3 adapted from [76]. The number of defects created

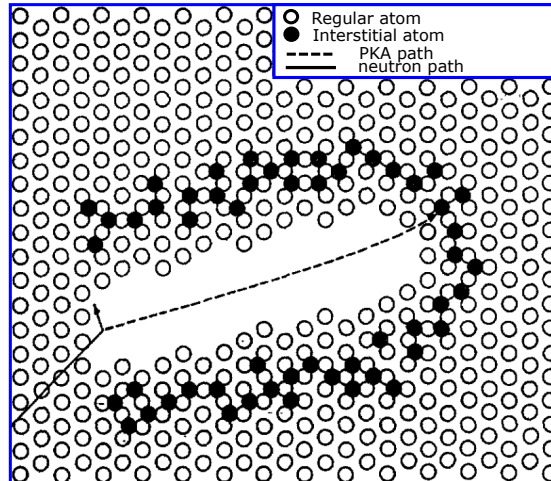


Figure 2.3: Depiction of the interstitials created along the path followed by a PKA post neutron scattering interaction. Adapted from [76].

is proportional to the PKA energy which in itself is a function of the incoming neutron energy. In an elastic collision, the neutron would transfer an energy 'T' as described in Equation 2.2.

For a 14 MeV DT neutron, energy transfers upto 300 keV ($3000 \times E_d$) are possible onto a W lattice atom (PKA) in a single scattering collision. The PKA can further using Equation 2.2 for $M_1 = M_{PKA}$ transfer energies upto its entire 300 keV in a single collision to another W atom in the lattice. These subsequent recoils produced by a PKA can be quantified through the widely used Kinchin and Pease model [77].

$$T = \frac{4EM_1M_{PKA}}{(M_1 + M_{PKA})^2} \quad (2.2)$$

Initially, the number of recoils per PKA can be assumed as a simple step function, where when the PKA transfers energy greater than E_d there exists a recoil otherwise not, as depicted in Equation 2.3.

$$\text{displacement} = \begin{cases} 0 & \text{if } T < E_d \\ 1 & \text{if } T \geq E_d \end{cases} \quad (2.3)$$

Considering the energy of the PKA as T and $\nu(T)$ as the number of further secondary displaced atoms, the Equation can be written as shown in 2.4. When 'T' lies between E_d and $2E_d$ and transfers energy greater than E_d to the lattice atom, the recoil lattice atom is displaced from the lattice site which is taken up by the PKA. This results in a single displacement from the interaction.

$$\nu(T) = \begin{cases} 0 & \text{if } T < E_d \\ 1 & \text{if } E_d \leq T < 2E_d \end{cases} \quad (2.4)$$

This was further advanced by Kinchin and Pease who proposed that for energies above $2E_d$ and upto an upper limit, with increasing PKA energies 'T', there is a linear increase in the number of defects produced (recoils) as shown in Equation 2.5 [75]. The upper limit was defined by a cut off energy E_c , which relates to the electron stopping energy loss. While the PKA had an energy greater than E_c , no displacements would take place till, the electronic energy losses brought the PKA below E_c [78]. This is represented by a step function as shown in Figure 2.4.

$$\nu(T) = \begin{cases} 0 & \text{if } T < E_d \\ 1 & \text{if } E_d \leq T < 2E_d \\ \frac{T}{2E_d} & \text{if } 2E_d \leq T < E_c \\ \frac{E_c}{2E_d} & \text{if } E_c \leq T \end{cases} \quad (2.5)$$

Snyder and Neufeld attempted to improve the Kinchin Pease model by the introduction of an energy loss term and the notion that both atoms leave the lattice site after the interaction, thus increasing the number of recoils generated [78]. Further on, Sanders [79] substituted the hard sphere model for a better fitting inverse square potential interaction between the PKA and the recoil which results in a much better expression as shown in Equation 2.6 taken from [78].

$$\nu(T) = \begin{cases} 0 & \text{if } T < E_d \\ 1 & \text{if } E_d \leq T < 2E_d \\ 0.52 \frac{T}{2E_d} & \text{if } 2E_d \leq T < E_c \end{cases} \quad (2.6)$$

Lindhard and co-workers submitted that the PKA loses energy in a combination of electronic excitation losses and nuclear losses as shown in Equation 2.7.

$$\frac{dE}{dx} \text{TOTAL} = \frac{dE}{dx} \text{Electronic} + \frac{dE}{dx} \text{Nuclear} \quad (2.7)$$

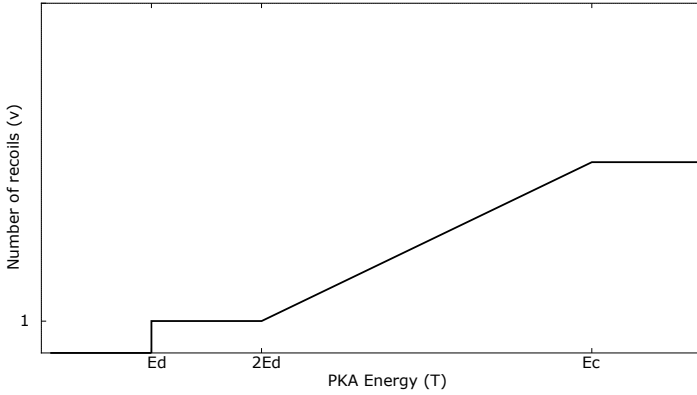


Figure 2.4: Kinchin Pease model for secondary displacements resulting from a PKA of energy T in a lattice with displacement threshold energy E_d and an upper cut off energy E_c .

The electronic excitation losses are energy losses to the electrons in the path of the PKA, while the nuclear losses are towards the lattice atoms. Lindhard et al. [80] accorded energy losses to both electronic excitation and nuclear collisions and using Sanders work proposed that the PKA collisions are competing for energy with the electronic excitation losses. Thereby only the nuclear stopping loss portion of the PKA energy should be used for the collision energy transfer calculation. Consequently, this was used as the basis for the widely accepted and present standard Nobert, Robinson and Torrens (NRT) model. The NRT model building on Lindhard's work considers only the net core nuclear collision energy against the total PKA energy as shown in Equation 2.8. Here, the net nuclear core energy E_D also called the damage energy is calculated by removal of the electronic excitation losses from the total PKA energy.

$$E_D = T \quad (2.8)$$

The NRT model provides the total number of secondary displacements with a displacement efficiency of 0.8 and is independent of mass and temperature [78]. The displacement efficiency of 0.8 accounts for the relativistic effects on damage and was determined using extensive binary collision approximation codes [64].

$$N_{NRT} = 0.8 \frac{E_D}{2E_d} \quad (2.9)$$

The NRT model is based on damage energy which is a function of the PKA energy. With high energy PKAs ($>1\text{keV}$), electronic losses increase rapidly and the displacements do not increase proportional to the initial PKA energy. Similar to the table in [75], Table 2.1 shows the number of displacements for neutron of a given energy. The average PKA energy is considered to be half of the maximum PKA energy, produced in an elastic reaction with the neutron. The secondary displacements are rounded to the next whole number. The partitioning of energy towards electronic losses also is seen to increase with higher PKA energies which reduces the net energy available to carry out displacements.

Neutron energy (MeV)	Average PKA energy (keV)	Damage energy (keV)	Secondary displacements	T_d/E_{PKA}
0.00335	0.036	0.034	0	0.96
0.00682	0.074	0.070	0	0.95
0.0175	0.189	0.179	1	0.95
0.0358	0.387	0.364	2	0.94
0.0734	0.793	0.741	4	0.93
0.191	2.06	1.90	9	0.92
0.397	4.29	3.92	18	0.91
0.832	8.99	8.13	37	0.90
2.28	24.65	21.90	98	0.89
5.09	55.02	48.12	214	0.87
12.3	132.97	114	507	0.86
14.1	152.43	130.25	579	0.85

Table 2.1: W recoil and displacement cascade size as predicted by the NRT model using Lindhard's screened electronic loss partitioning. Adapted from similar calculations described for iron (Fe) in [75].

Using the NRT model, the displacement cross-section as shown in Equation 2.10 is defined as an integral of the product of the number of secondary displacements (ν_{NRT}) and the reaction channel cross-section (σ) between the minimum and maximum transfer energies for an incoming neutron of energy E_i .

$$\sigma_D(E_i) = \int_{E_d}^{T_m} \nu(T) \sigma(E_i) dT \quad (2.10)$$

Starting with a neutron, as seen from Table 2.1, a chain of events leading to large number of displacements called a displacement cascade is feasible. The cascade event creates multiple interstitial and vacancy defects (Frenkel pairs). The damage in itself is an initial primary act and is in the order of 0.1 - 1 ps time scale. It leads to a thermal spike and subsequent cooling at the atomic scale, the secondary act which is between 1 - 10 ps [81]. During the thermal spike and subsequent cooling, many interstitial-hole pairs can recombine which reduces the total number of defects. It is known that the NRT model over estimates the number of secondary recoils by a factor of two [82]. However the highlight of the NRT model is the extracted parameter, "displacements per atoms" or "dpa". Dpa is used to co-relate the radiation damage created through displacement damage and its associated thermal spike contribution with the change in material properties. The NRT-dpa condenses a particular radiation environment into a quantitative number which describes the total energy deposited into the material and estimates the possible displacements realised on the atomic scale [83]. 1 dpa is a high damage quantity, as it implies that on average the entire set of atoms have been displaced once from their position. The dpa is given as a product of the flux and the

displacement cross-section as shown in Equation 2.11.

$$\text{dpa} = \phi \sigma_D = \int_{E_d}^{T_m} \phi(E) v(T) \sigma(E_i) dT \quad (2.11)$$

Thereby, for the same material, the neutron energy-flux spectra can greatly influence the dpa. The reactor design generates a reactor type specific neutron flux profile within the reactor volume. Based on the placement of various components within the reactor, a specific neutron flux is projected onto the components. This in turn can influence the damage inflicted on the component. Each reactor generates a specific damage proportion on its components leading to lattice material changes.

Lattice defects are created within the material as a direct consequence of the displacements. Interstitials and vacancies are the fundamental defects arising out of displacement knockons. Interstitials could further lead to clustering or combine with impurity atoms during irradiation. The mixing of interstitials with Re atom as a W-Re dumbbell is well established. Similar examples of Fe-Cr interstitial-impurity bonding have been noticed in Fe-Cr alloys [78]. On the other hand vacancies have high migration energies which usually bind them to their place. Vacancies are known to also bond with oversized lattice impurity atoms. Over time (or neutron fluence) these defects build up and result in changes within the microstructure. This evolution of changes can be primarily seen in the form of dislocation loops from interstitials and vacancy clusters under a transmission electron microscope. The vacancy clusters can further develop into voids. The displacement spike also leads to enhanced diffusion of the impurities, vacancies and interstitials which can effectively create recombination of defects and precipitation of impurities. At high operating temperatures as foreseen for fusion materials, the balance between defect generation, diffusion and annihilation balance and describe the defect development. Such developments lead to major changes in the material's property. In order to understand the evolution of neutron damage associated property changes, the extensive study and development of defects under neutron damage is required. While neutron fluences are a record of the irradiation, the unit dpa has an advantage of being able to specifically correlate with mechanical property changes for comparison with other irradiation sources. An example of the same is shown in fig 2.5, adapted from [78]. Here, the macroscopic property of swelling, radiation hardening and conductivity are shown to relate with increasing damage, which is dpa. Such correlations make for better judgement of failure and replacement for components operating under neutron irradiation conditions.

The damage unit dpa, reduces the entire neutron energy flux over time to a number. This effectively leads to a suitable comparison unit for different reactor irradiations or different irradiation environments over a similar irradiation damage range. One can attempt to justify the build up of displacement damage over time using the dpa damage dose from a particular irradiation scheme and compare it with other complementary techniques of irradiation. However, dpa doesn't provide any comparison between damages in different materials or help understand the evolution of damage. Moreover, the aspect of irradiation temperature which is crucial to the micro-structure development is not covered by the dpa unit. While many consider it a unit of damage measurement, it should be used only for comparison of the damage between various irradiation sources and not as a measure of damage itself.

To understand the evolution of damage as highlighted in the section above, primary damage along with its evolution must be detailed. Modern approaches include MD simulations, kinetic monte carlo methods and use of software such as SPECTRA-PKA which is a processing code utilising the ENDF based nuclear recoil cross-section matrices and condensing it with the flux to obtain the instantaneous PKA energy distributions [83]. The code is capable of

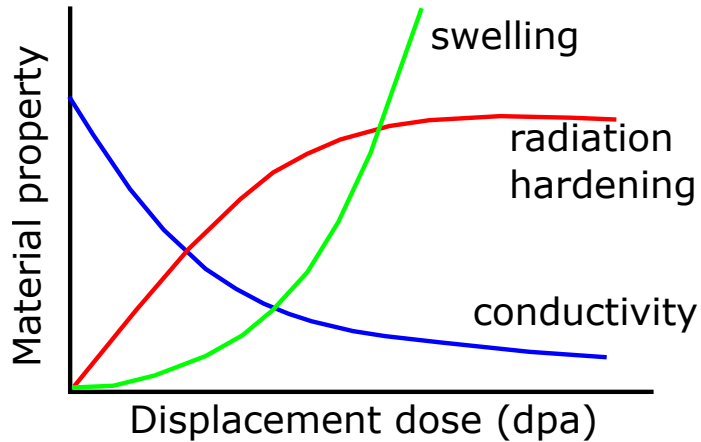


Figure 2.5: Dependence of material properties as a function of increasing displacement damage (dpa) in the lattice due created by neutron irradiation. Adapted from [78].

incorporating scattering and nuclear reactions and provides output is PKAs/s for any given flux. This can be combined with other codes such as molecular dynamics to obtain the development of the cascade for the desired neutron flux spectrum. SPECTRA-PKA has been used in this work to compare the various irradiation possibilities. However, alongside displacement damage, neutrons also have the potential to activate materials leading to transmutational changes or transmutation damage.

2.2 Transmutation damage

Neutron capture, charge particle reaction and neutron producing reactions are the second category of neutron material interaction. In this channel of interaction, the neutron tunnels into the nucleus and is absorbed. The nuclear reactions usually follow a compound nucleus reaction model, where an equilibrium is reached post neutron absorption and the available energy is shared between the various nucleons. Shortly after, the excess energy is lost by emitting radiation and/or particles [28] and the nucleus attempts towards its ground state. In case of a high energy excited state emission, charged particles might be emitted. As the sum of the rest mass from the products of the reaction is greater than the sum of the rest mass of the reactants, the emission of charged particles is usually a threshold reaction and requires a minimum neutron energy. Similarly, in high energy interactions more than one nucleon may be emitted [28]. A neutron reaction cross-section for (n, γ), (n,p), (n, α) and (n,2n) on ^{186}W is shown in Figure 2.6, where it is seen that particle emissions occur only at incoming neutron energies higher than 7 MeV. This aspect has a high relevance for fusion irradiations and differs with respect to fission neutron spectra as discussed shortly after in Section 2.3.

A common aspect of the three reaction types is that the neutron is absorbed by the nucleus and the compound nucleus is formed. However it is a possibility for these reactions to form an unstable product which after decay results in a completely different element than the reactant. An example of neutron reactions on ^{186}W is shown in Figure 2.7, where the reactions in blue depict reactions leading to different elements. The yellow dotted lines indicate the decay onto

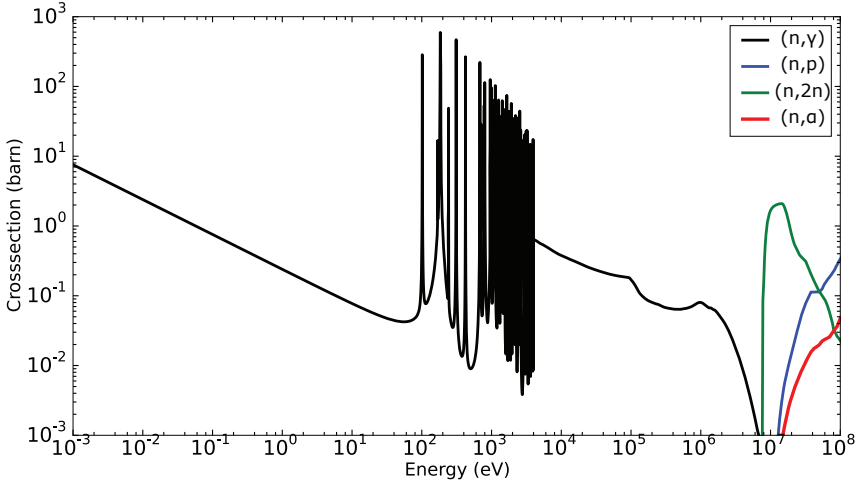


Figure 2.6: (n,γ) , (n,p) , $(n,2n)$ and (n,α) reaction cross-section for ^{186}W from ENDFVII.1 [73] and JANIS4.0 [74]. The particle emissions are threshold reactions requiring energies greater than 7 MeV.

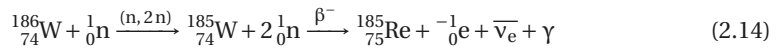
stable elemental isotopes. For instance, the $(n,2n)$ reaction on ^{186}W leads to production of ^{185}W which is unstable and has a half life of 75.1 days. This decays by a β^- reaction to ^{185}Re , which is stable but a completely different element. As seen from Figure 2.6, the production of elements depends on the neutron energy. This is quantified by using reaction cross-sections as described in Equation 2.12, where N is the number of reactant nuclei, $\sigma(E)$ is the reaction cross-section and $\phi(E)$ is the neutron flux at energy E . A integral of the reaction cross-section over the entire neutron energy spectrum would lead to the transmutation rate R for the product.

$$R = N \int \sigma(E)\phi(E)dE \quad (2.12)$$

$$N_A(t) = \frac{R}{\lambda} (1 - \exp^{-\lambda t})$$

$$N_B(t) = \frac{\lambda_A}{\lambda_B - \lambda_A} N_A(0) (e^{-\lambda_A t} - e^{-\lambda_B t}) \quad (2.13)$$

As the reaction product could further undergo decay, the net resultant nuclide produced at time t is given by Equation 2.13 where A stands for the mother nuclide and B for the daughter nuclide post decay. In the example of a $(n,2n)$ reaction on ^{186}W as shown in Equation 2.14, ^{186}W is the reactant which forms ^{185}W via a $(n,2n)$ reaction. The product ^{186}W has N_A atoms formed which decays into ^{185}Re forming atoms N_B .



λ is defined as the decay constant and is a measure of the decay rate calculated by Equation 2.15, where $T_{1/2}$ is the half life of the unstable isotope.

$$\lambda = \frac{\ln 2}{T_{1/2}} \quad (2.15)$$

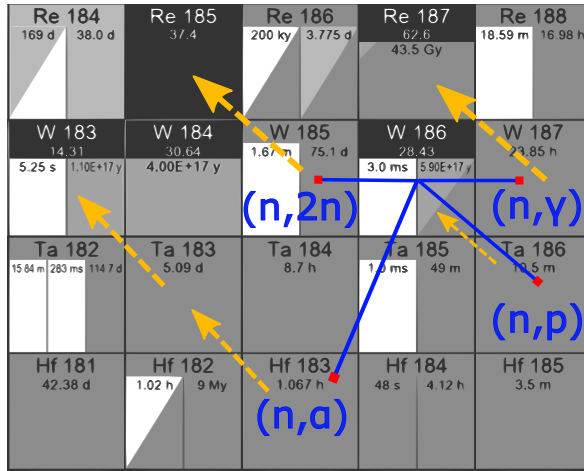
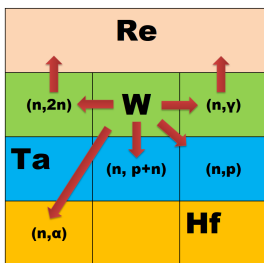
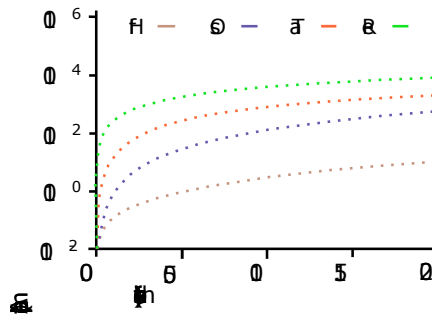


Figure 2.7: Neutron reaction and decay routes for ^{186}W . The blue lines depict the end products from the various neutron transmutation reactions and the yellow dotted lines indicate further decay routes onto stable products.

Over time (fluence), depending on the reaction rates (cross-section) and the half lives, there is a gradual build-up of the transmuted elements. The transmuted elements accumulate and large elemental changes might occur within the material under neutron irradiation leading to compositional change of the material. An example of the estimation of such an elemental buildup in W under DEMO neutron irradiation taken from [59] is shown in Figure 2.8. Starting out with a pure W component, sub-figure(a) shows the change in elements through the possible reaction channels and sub-figure(b) estimates the buildup of the elements. A change of W into W-1%Re is seen within 18 months of DEMO neutron irradiation. Similar calculations show a change into W-18Re-3Os within a damage dose of 50 dpa [84]. These changes result in degradation of thermo-mechanical properties which potentially might lead to the failure of the component.



(a) An neutron reaction block diagram.



(b) Elemental composition change over time in W.

Figure 2.8: Elemental composition change in W under neutron irradiation for DEMO reactor from [59]. Pure W changes into a an alloy of 1 atomic % (10^4 ppm) Re in under two years.

Pure unirradiated materials usually have high thermal conductivities and mechanical properties. Through the buildup of transmutation over time, these properties are known to change. In spite of being below the solubility limit, due to neutron irradiation, the precipitation of transmuted elements (solute) can occur. This well known phenomenon is called radiation induced precipitation. W has excellent thermal properties with very high thermal conductivity which drops by 50% on the addition of 5% Re [84]. Reports of radiation induced precipitation of Re in W resulting in the rapid rise of irradiation hardening have been well documented [85], [84]. Re precipitates have been shown to appear as ϵ phases, which are brittle by nature and substantially decrease the ductility of W [86].

Another major product formed within the material via (n,p) and (n, α) reactions are the light charged particles, hydrogen (H) and helium (He). These light particles form voids and bubbles within the micro-structure. He bubbles are known to have detrimental effects on the micro-structure and lead to rapid rise in the hardness of the material [87]. Closer to the surface, He bubbles create blisters and have shown nano fuzz like formation which could result in higher sputtering of W and consequently lower plasma performance. The He clustering is seen to occur with self trapping and gathering forming bubbles with high binding potentials [88], thus stabilising the bubble. This might lead to embrittlement of the material. Voids are mobile at high operating temperatures and link together to grow, resulting in swelling being observed under neutron irradiation.

Significant transmutation is a concern and while it has detrimental effects on the cycle time of a component, the half lives and decay radiation of induced transmutations could additionally create a radioactive hazard and require a nuclear waste disposal scenario. Fusion products intrinsically aren't radioactive but the fast neutrons as seen above transmute and activate materials in its path. The activated material can emit α , β and γ radiation, and depending on the lifetimes of the active element could have a large environmental effect. Long life times and high radiation can impair maintenance operations, recycling prospects and end of life costs [39]. Also, in case of an accidental scenario, the release of radioactivity would have major economic, political and geographical consequences and thus would have to be avoided at all costs.

The amount of radioactivity induced and the half life of the induced isotopes is a critical factor in the selection of materials. Shown in Figure 2.9 is the decaying dose rate over time for a list of candidate elements present in a reactor. The quantities taken from [59] represent contact dose from γ rays emitted by radioactive isotopes of 1 kg of the respective element post two full power years (fpy) of irradiation as the first wall material in a 1.6 GW DEMO power plant. The elapsed time represents the cooling period post irradiation upto 10^4 years cooling time. Two additional dashed lines at 10^{-2} Sv.hr⁻¹ and 8×10^{-8} Sv.hr⁻¹ mark the doses for remote handling limit and natural background respectively. 10 mSv.hr⁻¹ marks a safety limit for electronics in remote handling devices while 80 nSv.hr⁻¹ is the natural background radiation on earth. Elements which display high dose rates for a long period of time should be particularly avoided. In Figure 2.9, Co displays a high dose rate of 1Sv/hr for over 100 years and should be avoided. Similarly, Ni, Nb, Mo and Al show high dose rates for 100s of years and should be avoided. A list of elements C, Si, Ti, Fe, Cr and V are considered as low activation materials and are advisable for use in a fusion neutron irradiation environment [89]. Considerable research in this direction has yielded alternatives such as low activation steels Eurofer, F82H which substitute the trace elements in steel with elements having faster decay times and lower reaction rates, along with reduced impurity concentrations.

2.3. Combined damage

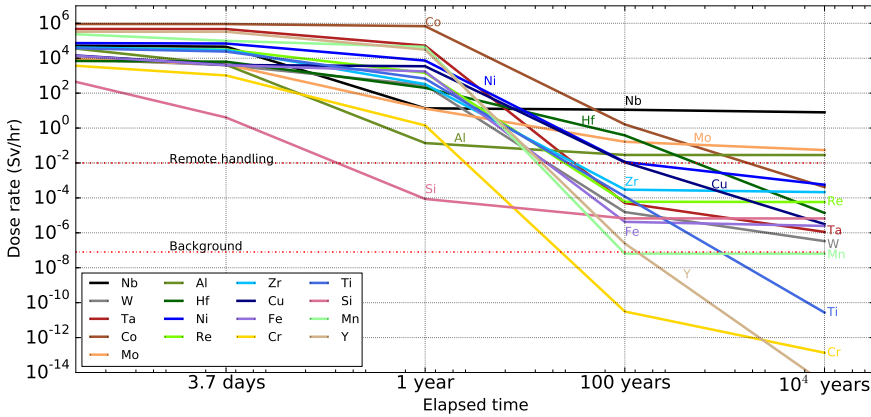


Figure 2.9: Contact doses post two years of irradiation in a 1.6 GW DEMO reactor for candidate elements. Data taken from [59].

To obtain transmutation data, inventory codes are often used. FISPACT-II is an inventory calculation software which reads ENDF style libraries such as TENDL-2015 and using its solver is capable of solving activation, transmutation, dose rate and heating for the given input particle flux [90]. Using monte carlo programs to obtain the neutron flux, transmutation scenarios for various irradiation and cooling time schedules and on different elements are feasible.

While transmutation is an unavoidable consequence of neutron irradiation, attempts to understand and lower the impact of its adverse effects are being studied by substituting elements which display higher stability or using V or Si based alloys which display higher resistance. However, in a fusion reactor transmutation damage is often stabilised by displacement damage and should be analysed in union with displacement damage effects.

2.3 Combined damage

Neutron damage is a combination of the two sub damages; displacement damage, which is based on neutron scattering and transmutation damage, where the neutron is absorbed and the nucleus stabilises itself through the release of particles and radiation. While it is beneficial to understand the damage created by each of the two modes separately, within a reactor they occur concurrently and stabilise each other. For instance the radiation induced precipitation under neutron irradiation is known to be associated with void suppression [91]. In return, the formation of precipitates is linked to the vacancy motion. Also, experimental campaigns have seen a link between dislocation loops and precipitates in W [84]. Meanwhile in Fe systems, displacements and solutes in combination are known to induce phase changes during irradiation, which generate corrosion and mechanical property changes [92]. It was observed that point defects can accelerate the phase separation in Fe-Cr systems by many orders of magnitude [93]. Thus in order to simulate or recreate fusion neutron damage, a combination of the two damage types in concurrence is necessary as shown in Figure 2.10.

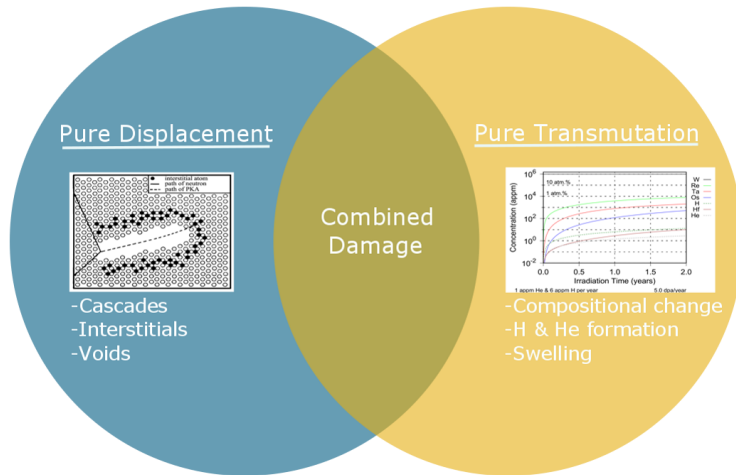


Figure 2.10: Neutron damage is the combination of the two types of neutron interactions; scattering induced displacement damage and neutron absorption induced transmutation damage.

In fusion research, as early as 1980s, the international energy agency adopted a program of research and development on fusion materials. A significant effort has been put in to minimise the replacement of blanket and wall components and include recycling of materials. This has steered the research focus towards high neutron load resilient materials with low activation [94]. Similar to road undertaken by fission reactor material development, the basic understanding of the impact of fusion neutrons on materials and further safety issues has largely been based on experimental fission reactor campaigns. There are two compelling reasons for this; firstly the possibility of combined damage in a fission neutron environment and secondly as of date, fission reactors are the lone possibility to achieve and irradiate materials with high neutron fluxes ($10^{14} \text{ cm}^{-2} \text{ s}^{-1}$). However, there are known spectral differences between fission and fusion as shown in Figure 2.11. It is well known that the neutron flux spectrum has a major impact on the damage created within the material and as such each of the reactors are produce a varied damage within the material [95]. A fission (HFR) and fusion (DEMO) neutron flux spectrum based on the neutron energy with the effective displacement cut-off superimposed is observed in Figure 2.11.

The DEMO neutron spectrum is distinctly different from high flux reactors due to its characteristic 14 MeV peak. It shows a hard fast (high energy) neutron flux which culminates into the 14 MeV peak. While, the fast neutron flux is considerably softer in fission reactors which display a Maxwellian drop at 2 MeV. The high energy recoils are seldom produced in the fission reactors due to lack of high energy neutrons. These high energy fusion neutrons are capable of producing large displacement cascades. For low energy PKA's a binary collision reaction follows. However, this changes for high energy PKAs, which can be frequent in fusion reactors. An example taken from [75] is shown in Figure 2.12, where the peak damage snapshots from MD calculations at 100 K are superimposed to appreciate the role of PKA energy in cascade development in Fe. Scattering from high energy neutrons would produce high energy cascades in fusion devices. The cascade breaks off into smaller sub cascades as seen with the 100 keV PKA and in turn appreciates the number of surviving defects. These cascades are harder to mimic using the high flux reactors and as such the displacement defects

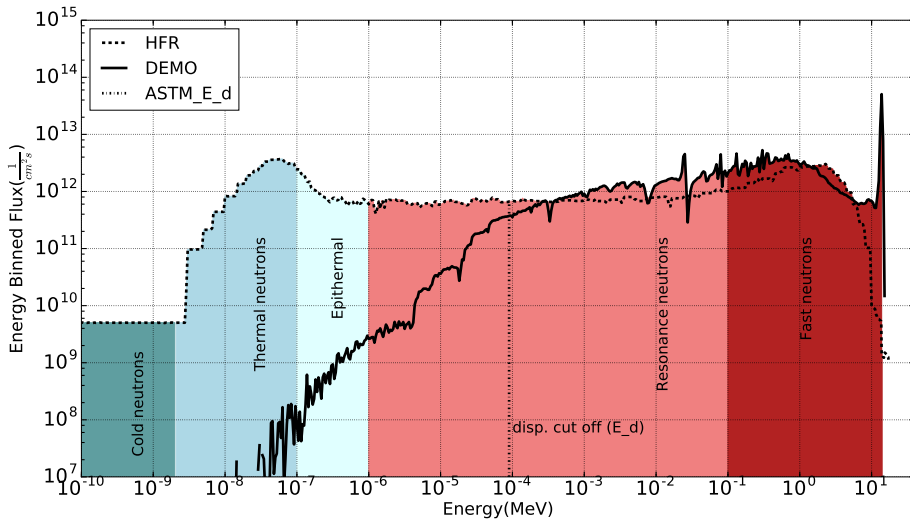


Figure 2.11: Sub-division of fission and fusion neutron spectrum based on neutron energy with the effective displacement cutoff superimposed. Binned neutron-energy flux spectrum for fission (HFR) and fusion (DEMO) and cold neutron (FRM-II) reactors taken from [83]. A clear distinction in the neutron energies between the spectra, especially with the 14 MeV peak for a fusion reactor is observed.

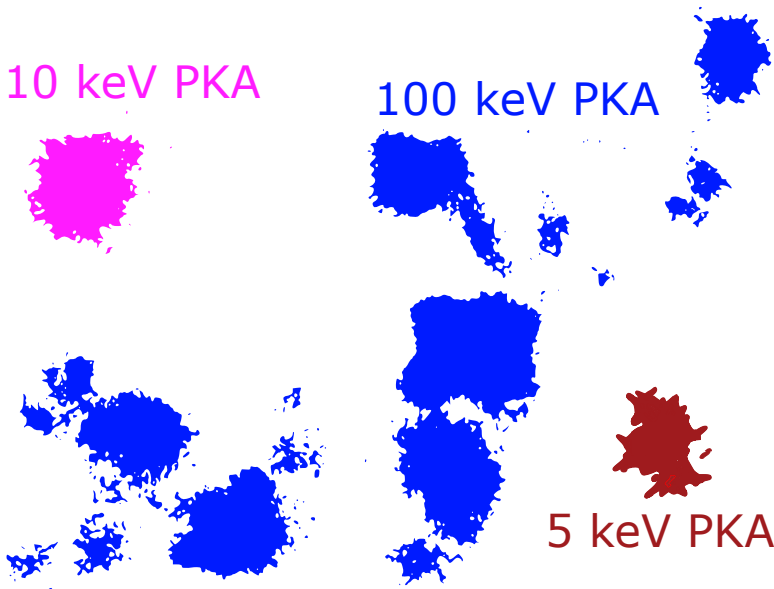


Figure 2.12: Superimposed captures of the extent of peak damage from a 5 keV PKA (maroon), 10 keV PKA (pink) and 100 keV PKA (blue) MD simulations in iron at 100 K adapted from [75]. The high energy 100 keV cascade splits itself into mini sub cascades, resulting in greater number of surviving defects.

could be under-shadowed by the transmutation effects. Consequently, the dpa damage dose for fusion first wall materials is substantially higher than fission reactors [96], [97] and [68]. Moreover, the damage evolution under the right proportion is altered. Transmutation elements such as Re are known to suppress voids and thereby swelling. This microstructure evolution must be considered while analysing and simulating damage. Damage calculations estimate 9.2 & 6 dpa/year in a fusion power plant [59] as against 4 & 2 dpa/year in a fission power plant for an Fe and W component respectively.

The fast neutrons above the threshold barrier for charged particle and neutron producing reactions trigger (n,p) , $(n,2n)$ and (n, γ) reactions. The fast DEMO neutrons would thereby also produce significant hydrogen and helium within the materials which can't be replicated by the fission reactors due to the lack of high energy neutron fluxes. Damage calculations estimate 90 and 503 appm/year of He and H in a fusion power plant [59] as against 1 & 20 appm/year of He and H in a fission power plant for an Fe component. The same for W is estimated to be 1 & 6 appm of He and H in a fusion power plant [59] as against 0 appm of He and H in a fission power plant. Moreover, hydrogen and helium from the plasma can penetrate deep into the first wall, much beyond the implantation depth and create large stable blisters. This has been observed and recreated in proton experiments [98]. Such changes occurring over time under neutron irradiation accelerates the material degradation and reduces the lifetime of the component. The light charged particles carry away large energies and can also induce significant cascades of their own [83], which would induce further stress into the materials.

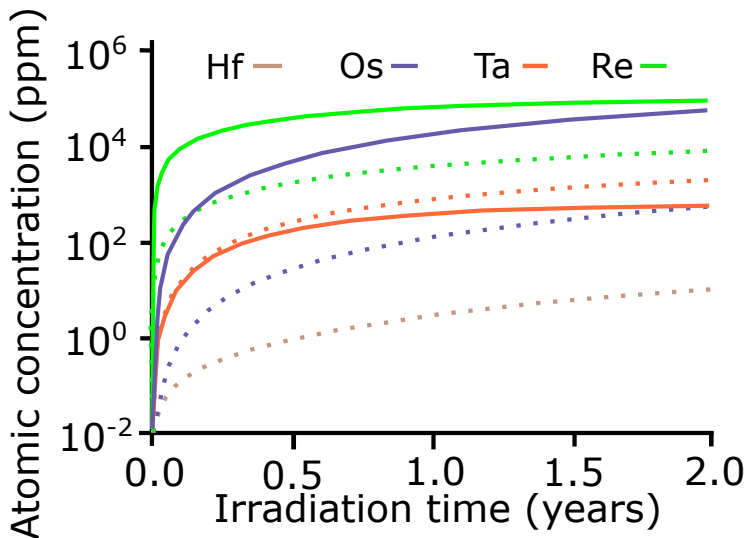


Figure 2.13: Elemental build up from transmutation reactions in W within a fission (bold) and fusion (dotted) reactors. Thermal neutrons are responsible for the rapid rise of Re and Os in W for fission reactors while this is much slower in fusion reactors.

The fission reactor spectrum additionally has a large thermal neutron (low energy) spectrum tail which lies far behind the displacement cut off for most metals ($\approx 20 - 90$ eV). The thermal neutrons cannot induce any displacement but rather undergo thermal capture which is a (n, γ) reaction. This again biases the transmutation damage to the displacement damage for fission compared to fusion reactors. The rapid rise in Re and Os in W as a result of this for fission reactors is shown in Figure 2.13 in bold as against the delayed build up in fusion

reactors shown in dotted lines.

Considering a damage dose of 6 dpa/year and 2 dpa/year for W in a fusion and fission power plant respectively and combining it with the Re transmutation from Figure 2.13, the Re transmutation rate can be estimated as 500 appm/dpa for fusion vs 50000 appm/dpa for fission. This shows that the transmutation to displacement damage ratio in a fusion reactor is upto 0.01x smaller than a fission reactor. Thus, the microstructure evolution will be certainly different. Test reactors such as HFR, Petten [67], HFIR, Oakridge [99], BRII, Mol [100], JMTR, JAERI Japan [101] have dedicated material test irradiation stations often located within or near the core of the fuel elements in order to maximise high energy neutron fluxes. Test reactor fusion material irradiation campaigns have been instrumental in exposing materials to combined displacement and transmutational damage. Post irradiation thermo-mechanical testing with microscopy has essentially created a database of irradiated material properties which can be suitably used to design components under neutron fluxes. However, as seen high flux test fission reactors are not able to replicate the the correct proportion of damage as fusion reactors would impart. Additionally, fission reactors also have other drawbacks such as the low irradiation volumes up close to the fuel elements, difficulty in temperature control and measurement and long cycle times to achieve the damage doses needed for material investigations. Thus complementary sources and techniques of simulating the damage are seen as a necessity to obtain an understanding and quantification of the material property change.

Chapter 3

Accelerator irradiation

Accelerators have seen a rapid development and modernisation in the last four decades. The first nuclear reaction using accelerated particles was performed on the Cockcroft and Walton design in 1932. From there there has been a steady development through Van de Graph generators, linear accelerators, tandem machines and high current cyclotrons. They have moved from being a tool for physics experiments and leading the formation of new elements to playing an important role in society through radiation therapy and numerous industrial and scientific applications. Accelerators have the ability to trace minute elements using ion beam analysis, generate radio-isotopes such as ^{18}F for cancer therapy and are slowly getting into the mainstream industry. The X ray devices used in airports and industries are a direct result of the accelerator technology. The nature of being able to shut down the device as an intrinsic safety makes it feasible to be located within a university campus, industry or hospitals.

3.1 Accelerator technology

An accelerator is a device which pushes charged particles (ions or electrons) to high energies (velocities) using electromagnetic force. Accelerators consist of a charged particle source and an electric field to accelerate the particles. The idea originated from the need for artificial particles in 1923, shortly following Rutherford's experiments with natural emitters. The first device consisted of a series of linear drift tubes in an evacuated vessel which was found to be more suitable for ions than electrons [102]. Nowadays, based on the electric field, the accelerators can be categorised as direct current (DC) machines or alternating current (AC) machines. DC accelerators generally use a transformer-rectifier unit to accelerate particles. There is a physical maximum limit which is imposed on these machines and thereby they are applied for low energy continuous particle acceleration, with an energy gain of $q \cdot V$. Here q is the ion charge and V is the induced high voltage [28]. One of the widely used DC accelerators is the tandem accelerator where two stages of acceleration are conducted in tandem. Here, the source is normally kept at ground potential and negative ions are extracted from the source into the evacuated vessel with a positive terminal. Upon reaching the positive terminal, the negative ions are sourced through a stripper, where a gas or foil strips the negative ions of its electrons. The stripped, now positive ions, accelerate through the next stage towards the target which is kept at ground potential. This is illustrated in Figure 3.1. A combined acceleration of $(1+q) \cdot V$ is obtained on tandem machines. While tandem accelerators can multiply the acceleration, there exists a voltage breakdown limit beyond 1 MVm^{-1} [103].

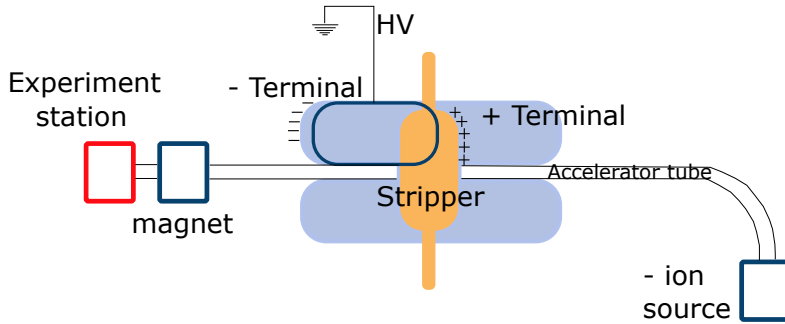


Figure 3.1: Construction of a tandem accelerator where two stages of acceleration exist in tandem within a single machine. The source is a negative ion and a stripper converts it halfway into a positive ion which adds further to the acceleration.

Higher acceleration uses radio-frequency (AC) electric fields in repetitive steps to overcome the voltage breakdown. In a linear set-up, a series of hollow drift tubes connected to the precise radio frequency pushes the ions through the tubes as shown in Figure 3.2. As the ions cross the drift tubes, they are accelerated by the correct polarity and during the passage through the tubes, they are shielded from the negative field. The central principle for the application of linear accelerators is the correct timing and phase synchronisation of the radio frequency cycle with the accelerating ions. This is achieved by increasing the length of the drift tubes with increasing particle energy. After n gaps, the net acceleration is nqV [28]. Long lengths are required for large acceleration and the ideal step would be to bend the beam. Varying ion energy is also difficult in linear accelerators (linac).

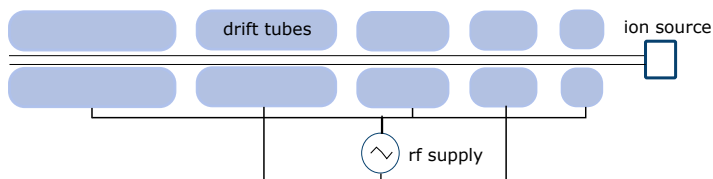


Figure 3.2: Schematic representation of a Sloan-Lawrance, drift tube linear accelerator. Here a series of drift tubes connected to an alternating rf supply conducts the ions through it.

Bending the beam in a spiral would encapsulate and accelerate the ions in a compact configuration. In a cyclotron, the ions orbit in circles and the drift tubes are replaced by two semi-circular chambers called 'dees' as shown in Figure 3.3 [28]. The ions are accelerated while crossing the gap between the dees and are guided in a spiral motion within the dees via a vertical magnetic field. The frequency of the polarity is synchronised to the velocity of the ion, which ensures the acceleration each time. For the acceleration to be in phase, for an ion of mass m , charge q and velocity v directed perpendicular to the magnetic field B , the ion would take a path with the radius as shown in Equation 3.1. Thus the cyclotron frequency would be as shown in Equation 3.2.

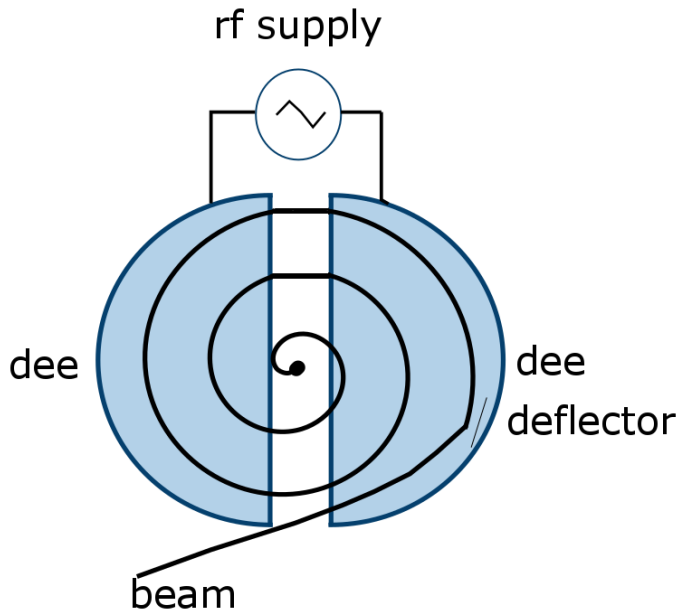


Figure 3.3: Sketch of a cyclotron with the two semi-circular dees, adapted from [28].

$$r = \frac{mv}{qB} \quad (3.1)$$

$$f = \frac{v}{2r} = \frac{qB}{2m} \quad (3.2)$$

The classical cyclotrons have been successfully developed to accelerate particles upto 20 MeV. Using a frequency modulation or the radial magnetic B field increase for compensation, the relativistic limit was eliminated and cyclotrons upto 730 MeV are built and operated [104]. For larger energies, the ions from a cyclotron are injected and slowly accelerated in large storage rings (synchrotron rings). A major characteristic of AC machines is the pulsed nature of the beam as against the continuous nature of DC machines. The bunches of ions arrive in phase and often lead to a small off time of the machine where there is no beam output. Latest machines have superconducting magnets which have significantly increased the quality of the beam while shrinking the machine size simultaneously.

Accelerators used in scientific research are often having energies larger than the binding energy of nucleons (MeV) and range between 1 - 1000 MeV. In the range of 1 - 100 MeV, the accelerated ion sees the nucleus as a whole or as a collection of many nucleons. With increasing energy, the ion is in the wavelength of individual nuclei and has interactions with individual nucleons [104]. Some measures of accelerator performance are the energy spread of the beam, beam luminosity or convergence of the beam (which determines the bunching and the intensity of the beam and its pulse frequency) [104].

3.2 Accelerator irradiation review

Since 1960, ions have been used as surrogate to investigate neutron damage. With the advancement of fast breeders, the use of ion to simulate neutron damage increased. The major advantage of ions over reactors is the ability to hasten damage through higher ion fluxes and larger interaction rates as compared to neutrons. The ability to obtain better control on the experimental conditions in an accelerator based ion environment as against the reactor is additionally favourable to understand and simulate damage [105]. Logan et al. proposed the use of protons to mimic fusion neutron damage in 1973 [106]. Their technique was to mimic the displacement damage rate while retaining the metallurgy of the sample. In parallel, another technique using heavy ions was investigated to simulate high fluence, fast neutron damage. Initial experiments on SS316 steel had shown extensive volume swelling under fast breeder neutron fluxes [107] and were simulated using 20 MeV C⁺ ions, 1.2 MeV protons, 5 MeV Cu⁺ ions and 8 MeV Se⁺ ions [108].

The notion that PKAs produce most of the damage has led to heavy ion irradiation. The ideal situation was considered irradiating the metal with identical ions (self ions), such as W on W. Self ions have traditionally been preferred to avoid any chemical influence on the metallurgy and induce phase transformations. Also, He ions were avoided as they could generate voids at high temperature and influence the micro-structure development [108]. During the "Radiation Effects and Tritium Technology for Fusion Reactors" conference in 1975, a large number of studies using ion bombardment were presented and discussed. These ranged from identification of void swelling using ⁶⁹Ni⁺ ions to proton simulation of 14 MeV neutron damage. Most of the work in this period was limited to iron systems with a few studies on refractory metals for fast breeder reactor concepts.

A large number of studies establishing ion irradiation as a useful method to study neutron damage led way to deeper co-relation between micro-structures. In fact the workshop "Correlation of neutron and charged particle damage" early in 1976, focussed on inter-correlation programs for fast breeders and fusion technology. Further irradiation effects such as radiation induced precipitation [109] were explored and probed using ion irradiation [110],[111] which led the dependence on ion irradiation to simulate damage. Similar studies using protons were conducted to understand changes in micro-structure and resistance with increasing radiation dose [112]. Simulations of radiation damage have additionally helped fill the gaps of know-how [113]. Simulations on many real materials were attempted and in turn specific experiments were proposed to be conducted using ion beams. The dose dependencies and results from proton, electron and ion irradiations formed the basis for simulations in radiation damage [114]. With increasing understanding of radiation damage, better and fusion specific experiments are being set-up. Experiments with dual and multi beams have been performed [115] which allow for experiments closer to neutron irradiation effects to be realised [116].

Many studies are performed on candidate fusion materials using accelerator based ion irradiation methods. Today, accelerators have enabled the experiments to be conducted in combination with in-situ TEM [117],[118] or in-situ mechanical testing [119],[120] where the increase in damage is directly measured. While the advancement of accelerator technologies has pushed radiation damage studies towards maturity, its use for damage studies has arisen from need for faster damage creation, easier experimental access and possibility of individual damage-factor study. New set-ups specifically designed for fusion neutron damage in combination with plasma exposures are planned which can simulate all aspects (radiation, thermal and plasma) of damage onto select candidate materials [121].

3.3 Ion- displacement damage

The absence of a high flux fusion neutron source for irradiation studies has led to its simulation using accelerator based ion damage studies. Based on the ion energy, the elastic scattering (cross-section) by the ion can be up to 10^4 x higher than neutrons [105]. This leads to higher damage rates. Also, modern high current accelerators can achieve high ion fluxes which further adds to faster damage accumulation. Accelerator damage using ions can be versatile and experimentally flexible thus allowing to mimic specific features of radiation damage studies such as void formation, radiation induced precipitation and radiation induced diffusion. Accompanied with specific post irradiation characterisation techniques such as APT, TEM etc., the individual mechanisms of damage evolution can be identified and suitably studied.

Advancement in accelerator technologies especially with respect to beam energies and currents has led to the availability of a wide variety of ions for simulating radiation damage. The list includes protons, He^+ , heavy/ self ions (Au^+ , W^+ , Fe^+) and electrons of varied energies. Each projectile type, i.e. electrons, medium energy light ions, high energy light ions, medium energy heavy ions have their own particular damage profile, range and evolution. A comparison of the interaction of various particles having 1 MeV energy in Nickel adapted from [122] is shown in Figure 3.4. Despite all the particles having the same amount of energy, the interac-

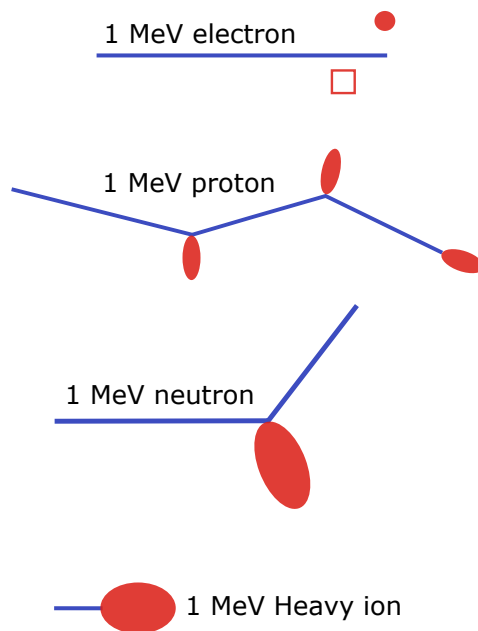


Figure 3.4: Representation of the path and damage by various ions having 1 MeV energy on a sample of pure Ni adapted from [122]. Neutrons and protons have widely spaced interactions while heavy ions induce cascades of similar intensities to that of neutrons.

tion type and extent vary largely. High energy protons undergo widely spaced interactions where the mean free path increases with energy. This is similar to neutrons which have a large mean free path in materials. However, on average these interactions produce lower PKA/SKA

density as compared to neutrons. Alternately, heavy ions have large energy transfers similar to neutrons but loose their energy rapidly in a single or few interactions within a short range. Neutrons and heavy ions can produce dense cascades which are localised by recombination of point defects. Electrons normally can produce only a few Frenkel pairs. As seen in Figure 2.12, the cascades are representative of the extent of damage and their evolution. Thus, the selection of an ion with its desired energy determines the damage impact or interaction with the target.

Neutrons carry no charge, have low cross-sections and, thereby large ranges in materials. Ions however, carry charge and encounter electronic losses (electron interactions) and ion material interactions. From these interactions, ions start to rapidly loose energy. Ions while passing through the sample, in the vicinity of many nuclei, feel the effects of a potential field. The interaction between an ion and a nuclei can be described by using these potential fields. If the distance between the two atoms is r , r_e is the spacing between the nearest neighbours in a crystal (≈ 0.25 nm) and a_0 is the Bohr radius of the hydrogen atom (≈ 0.053 nm), then the interaction potential can be described as shown in Equation 3.3 [78].

$$V(r) \begin{matrix} \frac{Z_1 Z_2}{r} & \text{Coulomb potential} & r & a_0 \\ \frac{Z_1 Z_2}{r} \exp\left(-\frac{r}{a}\right) & \text{Screened Coulomb potential} & r & a_0 \\ A \exp\left(-\frac{r}{B}\right) & \text{Born Mayer potential} & a_0 & r & r_e \end{matrix} \quad (3.3)$$

Where $A = 2.58 \cdot 10^{-5} (Z_1 Z_2)^{\frac{11}{4}}$ and $B = 1.5 \frac{a_0}{(Z_1 Z_2)^{\frac{6}{5}}}$ derived empirically [76]. Combination of these were considered by Brinkman, Firsov and Thomas-Fermi who suggested potentials which dominate at particular separations for specific materials. Upon consideration, it was shown that for heavy ions having energies between 1 keV to 100 keV, which represent PKAs in the material, the screened Coulomb potential with an inverse square function is best suited and the average recoil energy from a high energy heavy ion is given by Equation 3.4.

$$\bar{T} = \frac{E_i}{E_d} \quad (3.4)$$

In the case of high energy-light ions, on occasion, they come head on with a nucleus and due to their high energies the distance of nearest approach is closer than the innermost electron shells. Thus, the ions have a simple Coulomb interaction which when substituted is analogous to Rutherford's inverse fourth power scattering law and can be approximated as shown in Equation 3.5 taken from [78].

$$T = E_i \text{ and } \check{T} = E_d \ln\left(\frac{E_i}{E_d}\right) \quad (3.5)$$

From the Equations we can derive the maximum T , minimum \check{T} and average \bar{T} recoil energies for high energy protons. This is listed in Table 3.1 and compared against self ion irradiation and DEMO neutron average taken from [83]. There is a mismatch which can be seen for both high energy protons (0.35 keV) and self ions (16 keV) as compared to DEMO neutrons (3.2 keV). While the average recoils from protons have low energies, on occasion, the protons can produce a high energy recoil which induces a displacement similar to neutron interactions. This max recoil energy can extend upto 645 keV recoil PKA for 30 MeV protons.

As the ion traverses through the target material, it looses energy and undergoes stopping losses. This determines its range within the material. In the case of MeV protons and heavy ions two distinct zones of stopping are seen; electronic stopping (electron interaction) and

Energy (MeV)	Protons			Self Ion	DEMO neutron
	max T (keV)	min \check{T} (keV)	avg. \bar{T} (keV)	avg. \bar{T} (keV)	avg. \bar{T} (keV)
3	65	0.09	0.24	16	3.2
16	344	0.09	0.32	38	
30	645	0.09	0.35	52	

Table 3.1: Upper, lower and average recoil energies in Tungsten using $E_d = 90$ eV [123] for high energy protons and self ions calculated using the Coulomb potential and Rutherford scattering against the DEMO average PKA recoil energy of 3.2 keV [83].

nuclear stopping (nuclide interaction). Initially as the ion enters with high energy (or velocity), it encounters electronic stopping. For the ion with charge state ze , where z is the atomic number of ion and e the electric charge, passing through the sample with velocity v , it starts to interact with the electrons in its vicinity. This Coulomb interaction transfers energy to the electrons at the cost of the ions energy. The electrons mass is (e^- $9.1 \cdot 10^{-31}$ kg vs H^+ $1.6 \cdot 10^{-27}$ kg) small in comparison to the ion and the ion tends to follow a straight path without major deflections. However, with every subsequent electron interaction, it loses energy and this loss called the electronic stopping is given by stopping power S_e as shown in Equation 3.6.

$$S_e = \frac{dE}{dx} \quad (3.6)$$

For N and Z being the number density and atomic number of the sample material and m_0 the electron rest mass, the stopping power can be integrated for all energy transfers and described by the Bethe formula [124] as shown in Equation 3.7 which is valid for non-relativistic particles.

$$S_e = \frac{dE}{dx} = \frac{4}{m_0 v^2} N B \quad (3.7)$$

$$B = Z \left[\ln \frac{2m_0 v^2}{I} - \ln \left(1 - \frac{v^2}{c^2} \right) - \frac{v^2}{c^2} \right]$$

As the ion travels further, energy loss or decrease in velocity from electronic stopping, S (stopping power) increases and ion tends to lose more energy, thus slowing down. At low velocities, the interactions between the nucleus and the ion become relevant and the Bethe formula tends to fail, nuclear collision stopping dominates the energy loss. For light ions this is around 1 MeV/atomic mass unit [125] and the ion tends to pick up electrons to achieve charge neutrality. This range of nuclear stopping is called the Bragg peak. The ion rapidly loses energy by scattering between the nuclei and comes to a rest. Together the electronic and nuclear stopping determine the range of the ion within a specific material. Heavier the ion (higher Z), larger is the stopping power energy loss. This implies, shorter range for heavier ions. Thereby, heavy ions in high density materials will encounter the largest stopping and are often limited to a depth of a few μ m. This is potentially a large drawback of heavy ion irradiation; the narrow width of damage creation (range). In comparison, light ions have a much larger range in materials as shown in a comparison in Figure 3.5 for tungsten. As seen, heavy ions such as 20 MeV W^+ penetrate a maximum of 2 μ m in tungsten as against 400 μ m and 1 mm by 5 MeV and 30 MeV H^+ ions respectively. SRIM/ TRIM (stopping/ transport and range of ions in matter) [126] is a program which uses a monte-carlo approach and infers the

interaction which the ion has while travelling through the sample material and can be used to judge ranges of ion within a variety of materials.

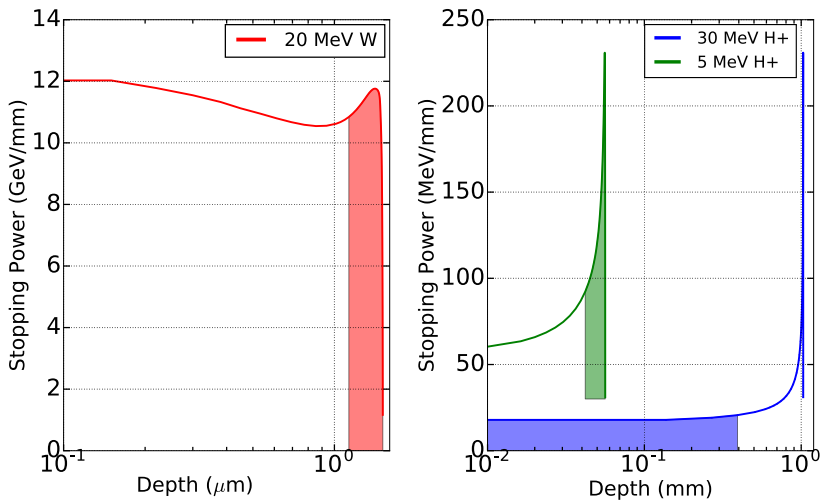


Figure 3.5: Range comparison for 20 MeV self ion (W^+) on the left and 5 MeV & 30 MeV protons in tungsten on the right. The self ion deposits its energy in the first 2 μm while, 5 MeV & 30 MeV have a range of 60 μm & 1 mm respectively. The highlighted areas indicate the area of interest for damage investigation.

The range also determines and establishes the region of interest within the sample, which in turn establishes the analysis methods and material parameters which can be assessed. The rise at the end of the ions range seen in Figure 3.5 is the Bragg peak where interactions between the ion and the nucleus dominate and sudden intense energy transfers between the ion and the nucleus through scattering is observed. This region of high energy transfers has traditionally been the region of interest for damage investigations. The Bragg peak for 20 MeV W^+ ions in red and 5 MeV protons in green is highlighted in the Figure 3.5 and as seen represents a very narrow width of damage. Considering the Kinchin- Pease model of displacement damage, dense cascades with large number of recoils are produced within the Bragg peak. Thus a situation with a high energy PKA density and its cascade evolution is simulated in the Bragg peak area. The accompanying damage would amount to $\frac{T}{2E_d}$. This creates a highly dense damage area of investigation.

Another approach with medium to high energy protons is to consider the plateau of damage prior to the Bragg peak. With high energy protons highlighted in purple in Figure 3.5, the range of constant damage preceding the Bragg peak can be considered as the range of interest. Here the interactions are purely coulombic in nature and produce widely spaced high energy recoils similar to neutrons. This also presents us with a larger range of investigation with constant damage creation from ion irradiations. A larger range of investigation ensures macroscopic damage which can be quantified using macroscopic measurements and additionally, the influence of surface effects is minimised.

To sum up, the selection of a particular energetic ion in order to replicate neutron damage establishes not only the type of damage, but also the range of the ion, the region of investigation and consequently the post irradiation analysis method applicable for damage

quantification. An example of various ion damages in $\text{dpa}\cdot\text{ion}^{-1}\text{cm}^{-2}$ in a nickel sample is contrasted against their range and compared with neutrons in Figure 3.6 from [127] and adapted based on [78]. Self ions or heavy ions induce rapid damage creation in the range of 10^{-17} - 10^{-14} $\text{dpa}\cdot\text{ion}^{-1}\text{cm}^{-2}$ due to their large energy transfers but at the cost of lower range of < 2 μm , as seen from 7.5 MeV Ta^+ or 5 MeV Ni^+ ion irradiation. While protons produce damage at rates of 10^{-19} - 10^{-17} $\text{dpa}\cdot\text{ion}^{-1}\text{cm}^{-2}$, which lies between heavy ions and neutron damage rates, however with a much larger range of > 5 μm and have a region of constant damage creation avoiding the Bragg peak. The differences in damage rates also translate into damage evolution, where extensive damage can be seen in self ion irradiation, however at the cost of no voids being found due to the large number of self interstitials. Protons can sway the micro-structure as large voids can be developed.

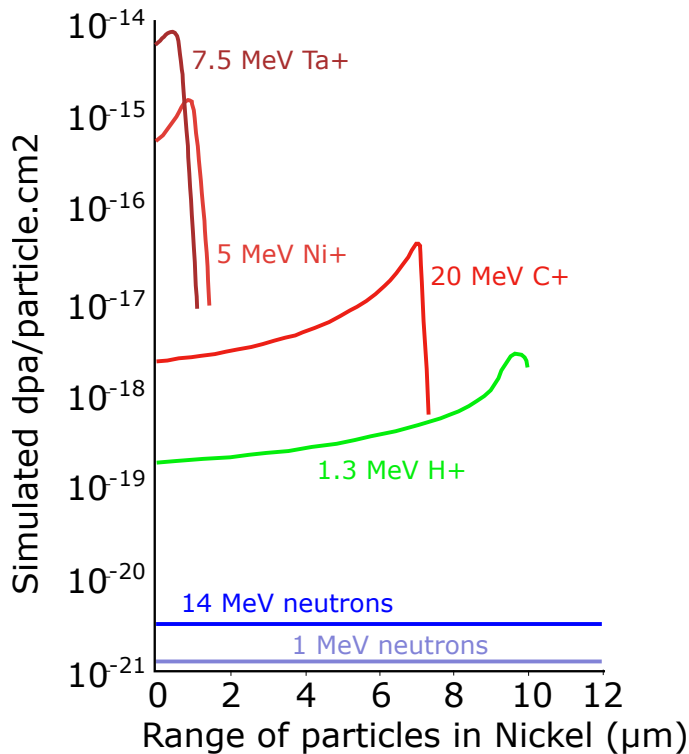


Figure 3.6: Damage vs range for different ions and neutrons in Nickel sample taken from [127] and adapted from [127]. The range of ions in materials depends on the interaction between ion and the sample material which also determines the damage registered in the material.

3.4 Feasibility study-proton damage

Currently, *proton damage* is not considered as main-stream, fusion neutron damage simulation technique. However energetic protons have the ability to induce combined damage within the sample. Therefore, prior to the commencement of the main body of research for this thesis, an initial feasibility study is undertaken to assess the impact of proton damage to recreate fusion neutron damage. It involves modelling the damage using state-of-the-art nuclear codes and latest nuclear cross-sections. In this section, the results from the nuclear codes used to model proton irradiation are discussed. The early development stage of proton damage shows promising results and proof-of-concept for the current work.

Under neutron irradiation, displacement damage creates many lattice defects which change the macroscopic property of the material whilst operation. In parallel neutrons also induce transmutational damage within the sample. The transmutation reactions of elements introduces chemical and metallurgical changes which slowly buildup with time into the micro-structure of the material. Fission reactor studies have shown transmutation induced precipitates to be the leading cause of irradiation hardening in tungsten [70]. This is known to occur in conjugation with displacement damage induced mixing. Thereby, a combined damage scenario is required to predict fusion neutron irradiation behaviour on materials.

Protons have many advantages as compared to heavy ions and have been successfully used to mimic neutron damage [128],[129],[130]. The highlights of protons as compared to other forms of damage emulation are listed below:

- Protons have nearly a similar mass as neutrons; $938.27 \text{ MeV}\cdot\text{c}^{-2}$ vs $939.56 \text{ MeV}\cdot\text{c}^{-2}$ and with high energies on occasion create similar recoils as neutrons from Coulomb interactions, but differences remain.
- With high energies, protons also have a larger range of investigation. 30 MeV protons induce a constant damage upto 550 μm as against a Bragg peak damage of 1 μm for 20 MeV self ion irradiations. This introduces the possibility to have macroscopic tests on the irradiated region of the sample.
- Protons upon exceeding the threshold energy can tunnel through the Coulomb barrier and introduce nuclear reactions similar to neutrons. Thus, transmutation reactions are possible in a proton environment.

The produced chemical changes in a material under neutron irradiation are the result of transmutation over time. While protons can mimic the results, it is important to note that the products of proton induced transmutation reactions tend to be neutron deficient isotopes and neutrons tend to create neutron rich isotopes. This is due to the difference in the reaction paths which are undertaken. An example of proton and neutron reaction paths are illustrated in Figure 3.7 for reactions on ^{186}W . The black arrows represent neutron induced reactions, while the reactions from protons are displayed in red. From the Figure it is seen that rhenium (Re) is introduced directly via a (p,xn) proton reaction in W, while neutrons lead to the formation of unstable W isotopes which decay onto stable Re via a β^- reaction. The production of tantalum via protons is similarly produced via a (p,2p) reaction as against a (n,p) reaction for neutrons. From the above it can be noted that protons are able to successfully produce the same elements as neutrons but the isotope would be different due to the different reaction pathway. However, from a metallurgical perspective, isotopes of the same element are known to induce similar chemical changes in the material which would ultimately induce the same chemical changes as neutrons. Moreover as the Re isotopes

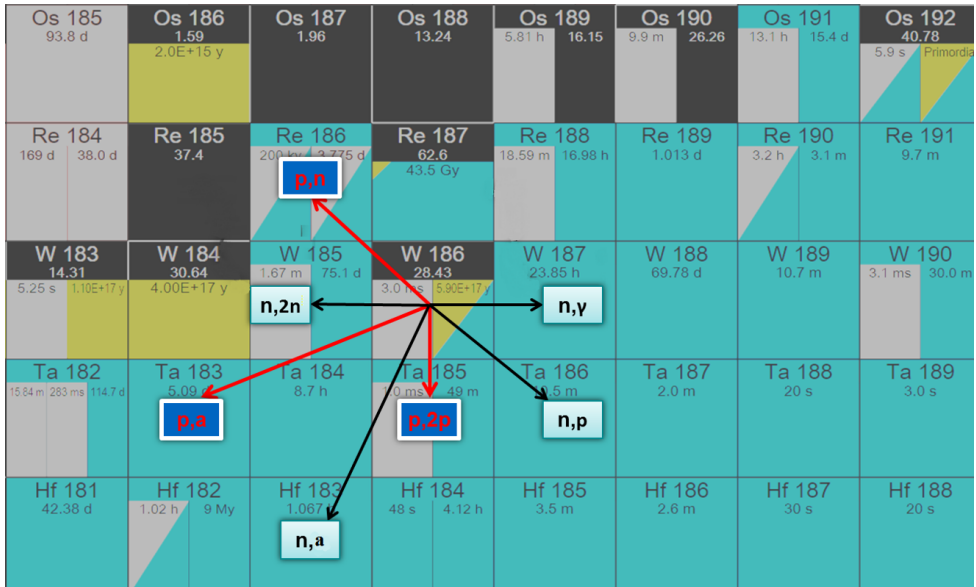


Figure 3.7: Reaction pathways undertaken by protons and neutrons which lead to similar chemical changes within the material over time.

are different, the half lives are different and there is a time dependent Re concentration from proton irradiations.

In order to introduce transmutation reactions, a threshold proton energy is required. Another important criterion is to induce appropriate proportions of all transmutational reactions to derive the correct balance of heavy and light reaction products similar to neutrons. In Figure 3.8, the threshold reaction energy to induce the reactions (p,xn), (p,2p), (p,n+p), and (p,a) are seen. A minimum cross-section of 1 mbarn was considered for obtaining any noticeable reaction rate. The reactions are seen to have a minimum and a maximum energy where they are significant. The shaded area represents energies where all reactions are induced and will induce damage. The (p,xn) reactions have the highest cross-section and indicate that Re will have the largest production rate. He (or α) production is seen to vary the most and has a peak between 20 - 25 MeV proton energy. This would be the ideal range to induce He within the target. For the same energy range, (p,2p) reaction which produces H seems negligible, however this is offset by another H producing reaction (p,n+p).

The above graph suggests that for proton energies between 15 - 25 or 30 MeV, the transmutation reactions induced would produce similar observable changes as neutron irradiations. However, to simulate fusion neutron damage, both aspects of damage; displacement and combined damage should be simulated and such an estimate can be generated using established codes. 30 MeV protons have a range of 1.03 mm in W. As seen earlier in Figure 3.5, the initial 550 μm displays a constant damage level. This range is macroscopic and yet far away from the Bragg peak or the surface to avoid any influence from either. Considering an investigation depth of 550 μm from the total range of 1.03 mm for 30 MeV protons in W, the energy loss can be estimated as 15 MeV. Using this as input for established codes, the ability to create and simulate combined damage by 30 MeV protons as against fission neutrons is estimated and compared against DEMO neutron irradiation.

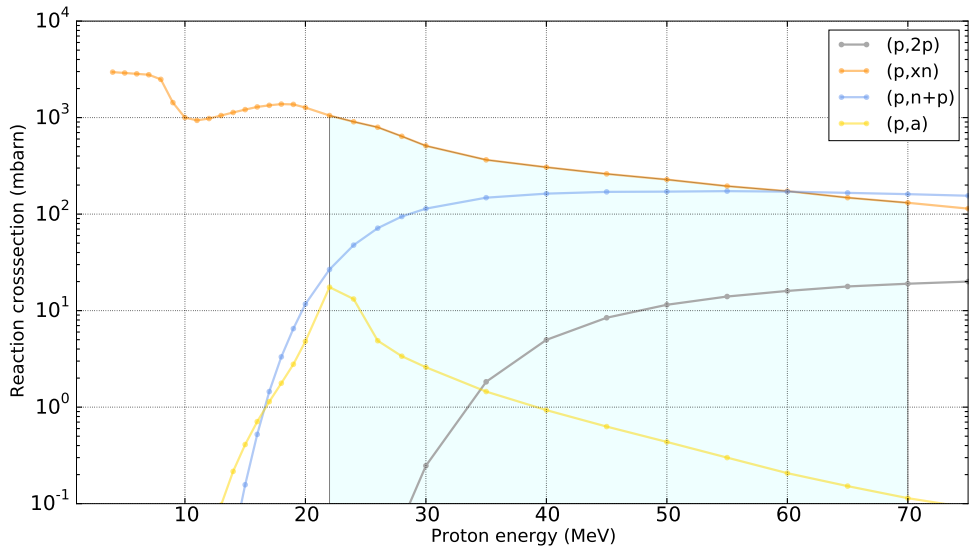


Figure 3.8: Cross-sections vs energy for common proton induced reactions on 186W. Data taken from [74]. A minimum cross-section of 1 mbarn was considered for noticeable reaction rates. As seen a threshold energy is required to activate reactions. The shaded area represents a region where all major reactions occur simultaneously.

The modelling is commenced through the use of a Monte-Carlo based code (MCNP6.1). The proton energy flux distribution is computed for the above parameters and grouped into a CCFE 162 group scheme. The set-up in MCNP6.1 consisted of a 10 mm diameter disk sample with a 10 A current projected on it. A total number of 10^6 particle histories were run to ensure that the relative flux bin errors were below 5%. The simulated proton energy binned flux is plotted against DEMO [59] and HFR [131] neutron spectrum in Figure 3.9. As the beam passes through the sample, protons undergo stopping and loose energy. However, inspite of traversing over 0.5 mm, the energy spread of the proton beam is extremely narrow and degrades from 30 MeV at entry to 15 MeV at the exit. The advantage of using CCFE 162 bin structure is that it can be directly collapsed with TENDL-2015 cross-sections in FISPACT-II. The inventory software uses Bateman Equations and acts as a solver to establish mother-daughter nuclide and production Equations to estimate the nuclide inventory for a given set of irradiation and cooling times. FISPACT-II requires the energy binned flux as input and thereby is considered a 0-d approach to inventory calculations.

The flux was further sorted into bins of 25 m travel range to observe if any major fluctuations in transmuted element production. MCNP 6.1 provided the correct energy flux distribution now for every 25 m range. FISPACT-II calculations performed using fluxes of $2.78 \cdot 10^{14} \text{ p.cm}^{-2}\text{s}^{-1}$ incident on a sample of 10 mm diameter for 14 hours resulted in 1 dpa damage. The output quantifies the transmuted element quantities immediately post irradiation at 0 time step, which is plotted in Figure 3.10. The Re generation stays constant while the other elements do show signs of variation. A few appm of He would be produced in the sample which isn't seen in the fission neutron irradiations. H is seen to taper of considerably over the range of investigation in the sample. This is beneficial as an excess of H is seen to be produced. Two different reactions ($p,n+p$) and ($p,2p$) are responsible for the H production

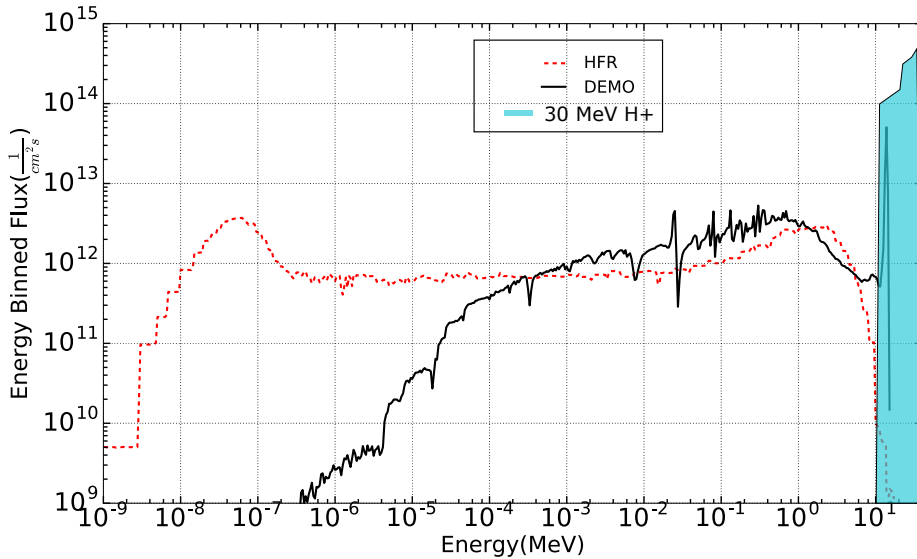


Figure 3.9: Modelling of 30 MeV proton flux spectra in a 550 μm sample of W compared with the DEMO neutron spectrum, computed using MCNP6.1. The protons have a narrow energy width and degrade from 30 MeV at entry to 15 MeV at exit of the sample. This is the first step in the feasibility study of proton irradiation for fusion neutron damage simulation.

which results in and the net production is the combination of both. Also, given the high mobility of H in W at irradiating temperatures, there might be certain diffusion towards the surfaces of the sample and a decrease in H could be possible. All other elements stay within a factor of 5x throughout the sample range.

Often the formed isotopes from transmutation reactions are unstable and decay onto stable nuclides (radioactive decay). This is accompanied by emission of particles and radiation which makes the sample radioactive by nature. FISPACT-II can additionally also estimate the decay activity and the decay dose rate, which for the 1 dpa damage dose from 30 MeV protons is shown in Figure 3.11. Here, the dots represent the dose rate from a point source measured at a distance of 30 cm away, while the bars represent the proportions of radioactivity in the sample. The decay of the activity is shown over a cooling time of 1.5 years and it is seen that at each step, the dose and the activity decreases. It can be also observed that unlike the fission waste, activity is negligible at 10^{-4} Bq. Additionally, the main source of radiation is seen to be from the activity, as most elements decay via decay or internal transition accompanied with the release of energetic electrons. The first 3 main nuclides responsible for the radioactivity over a cooling time of 12 year are shown in Table 3.2. The main nuclides are Re isotopes. This level of radioactivity places a handling and laboratory constraint on the post irradiation treatment of the samples. The dose rate is seen to drop to mSv/hr level after 1.5 years. From the Table 3.2, it is seen that the Re isotopes formed start to decay back to W. Major Re isotopes after the initial cooling period are ^{183}Re and ^{184}Re having a half life of 70 and 35 days respectively. This decay places a constraint on the post irradiation measurement period. If the cooling period is extended, then the influence of Re is seen to decrease. However, the same sample can be tested over a period of time to note the influence of Re formed through transmutation of W.

3.4. Feasibility study-proton damage

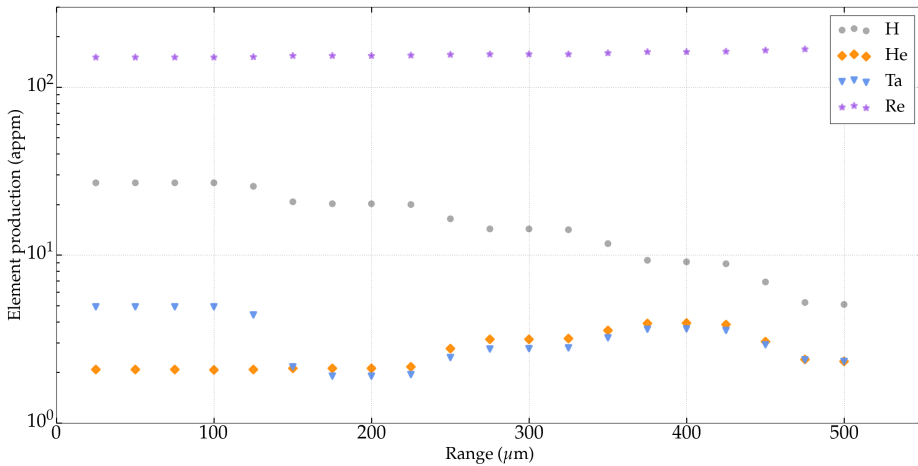


Figure 3.10: Modelling the change in transmutation elements in appm post 1 dpa of 30 MeV proton irradiation over a sample depth of 550 μm . The production of Re is stable and within 2x over the entire range of 550 μm . This reinforces the validity of macroscopic sample testing using protons.

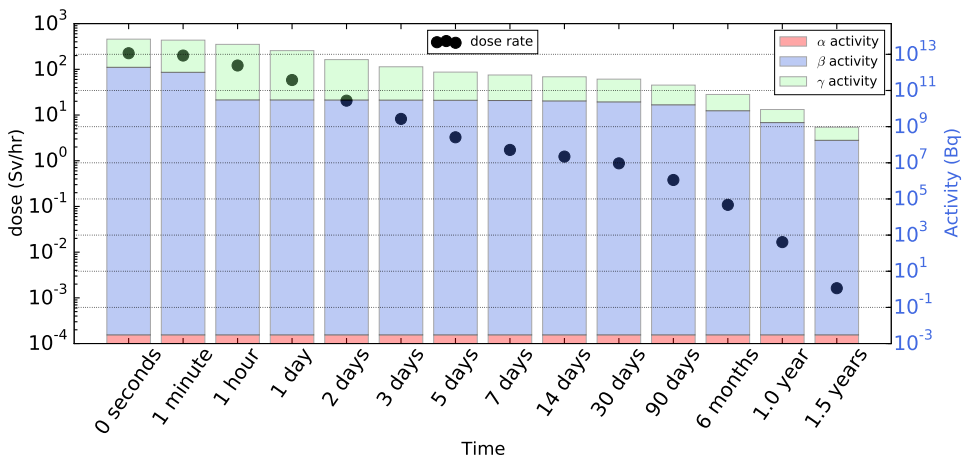


Figure 3.11: Activity calculations for 30 MeV protons on W calculated using FISPACT-II for a total dose of 1 dpa. The dots represent the dose rate which the bars represent the induced activity in Bq. The blue representing β activity is seen to be the largest source of activity.

Another aspect of fusion neutron damage; the displacement damage was estimated using potentials in Section 3.3 and the PKA energies compared in Table 3.1. Using the established code SPECTRA-PKA, an instantaneous picture of the PKA recoil spectrum can be afforded and directly compared with the fusion neutron induced PKA spectrum. This allows for a complete energy picture to be compared instead of a simple average. TENDL-2015 [132] contains recoil cross-sections for protons along with the a database for the nuclear reactions. However, the recoil cross-sections are available for energies above 5 keV, which places a lower cutoff on the plot. A comparison of PKAs produced by 30 MeV protons against DEMO neutron recoil

Cooling step	Dominant -1		Dominant -2		Dominant -3	
0 second	180Re	2.46 m	181 Re	19.9 h	182 mRe	14.4 h
1 minute	180Re	2.46 m	181 Re	19.9 h	182 mRe	14.4 h
1 hour	181 Re	19.9 h	182 mRe	14.4 h	182 Re	64.2 h
1 day	181 Re	19.9 h	182 Re	64.2 h	182 Re	64.2 h
2 days	182 Re	64.2 h	181 Re	19.9 h	183 Re	70 d
3 days	182 Re	64.2 h	183 Re	70 d	181 W	121.2 d
5 days	182 Re	64.2 h	183 Re	70 d	181 W	121.2 d
7 days	183 Re	70 d	181 W	121.2 d	184 Re	35.4 d
14 days	183 Re	70 d	181 W	121.2 d	184 Re	35.4 d
1 month	183 Re	70 d	181 W	121.2 d	184 Re	35.4 d
3 months	181 W	121.2 d	183 Re	70 d	184 Re	35.4 d
6 months	181 W	121.2 d	183 Re	70 d	184 mRe	169 d
1 year	181 W	121.2 d	184 mRe	169 d	184 Re	35.4 d

Table 3.2: The 3 main radionuclides along with their half lives resulting from the 30 MeV proton irradiation on W over a cooling time of 1 year. The produced amount and half life result in the corresponding change of nuclides over time. Such an estimate is provided for nuclear safety and dose rate calculations.

spectra cut off at 5 keV is shown in Figure 3.12, while the complete range is shown in Figure 3.13. The recoils are calculated for normalised fluxes of fusion and fission neutron spectrum. The protons (550 m range) is plotted in blue. The fission and fusion neutron spectrum is considered stable within this range. The 30 MeV PKAs (blue) plotted on log scale is seen to start at 5 keV and extends beyond the fusion PKA spectrum (green) to 650 keV similar to the maximum mentioned in Table 3.1. It should be noted that this represents the PKA at time 0 and no evolution is covered.

A facet seen in the Figure 3.13 is the ability of protons to produce high energy recoils. A drop is seen between the energies of 15 - 60 keV, where fission neutrons (red) show close approximation to the fusion neutron damage. The fission reactor neutron PKA production drops largely beyond 30 keV. The 30 MeV protons are seen to match the DEMO neutron PKA production beyond 60 keV and largely captures the high energy recoils upto 200 keV. As seen in the Figure, above 20 keV, the PKA rate drops rapidly for fission reactors (HFR) as compared to fusion neutron spectrum (DEMO). Recoils from high energy protons are largely energy dependent as seen from the Figure. While there is a dip for PKA generation at 20 keV, at higher energies the PKA generation rises and could result in similar recoils as fusion DEMO recoils. The average recoil energy is additionally calculated by SPECTRA-PKA and weighted for isotopic abundance is shown in Table 3.3. A difference to Table 3.1 can be immediately noticed. This Table lists the recoils calculated using recoil cross-sections and not using empirical relations. Also, as the recoil cross-sections have a lower limit of 5 keV in the case of protons, the results are skewed to higher energies. The naturally occurring

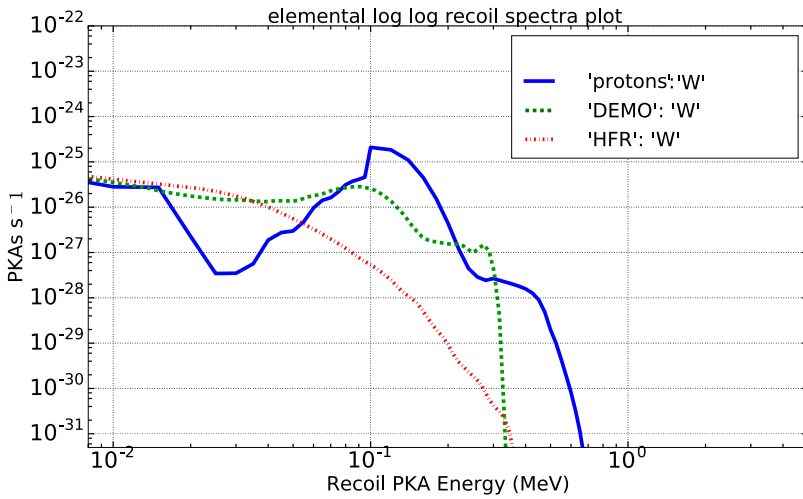


Figure 3.12: High energy PKA recoil spectra for proton entry at 30 MeV(blue) per second per W atom per proton compared with the DEMO and HFR recoil spectrum.

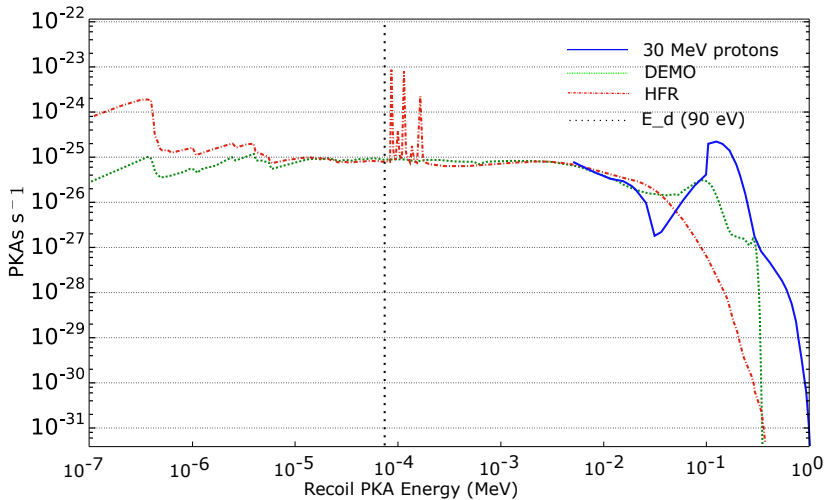


Figure 3.13: Modelling of the complete PKA recoil spectra obtained from SPECTRA-PKA [59] in comparison with recoil spectra from 30 MeV protons. Using recoil cross-sections, this novel approach allows a correct displacement damage scenario is estimated.

isotopes of ¹⁸⁴W and ¹⁸⁶W are seen to have a lower PKA recoil energy as against the isotopes formed through transmutation. Such a behaviour isn't limited to protons but is noticed also in neutrons. The Q value from the transmutation reactions aids in higher recoil energies for protons and neutrons for unstable isotopes. The average W energy is biased towards high energies for proton irradiations due to unavailability of low energy recoil cross-sections under

Isotope	Proton Avg PKA (keV)	Neutron Avg. PKA (keV)
181W	111.5	85.2
182W	111.5	3.2
183W	99	5.7
184W	20	2.2
185W	144.9	65.9
186W	11.7	1.9
Total W	106	3.8

Table 3.3: The average PKA energy for W isotopes and net W element, calculated by SPECTRA-PKA for 30 MeV protons, compared against DEMO neutron irradiation. The PKA energy for 30 MeV protons on W has a lower limit of 5 keV due to the recoil cross-section availability in TENDL-2015. The average differs from 3.1 due to the lower limit of 5 keV placed, additionally, these calculations are based on recoil cross-sections as against approximations.

5 keV for protons in TENDL-2015. A cumulative PKA spectra for the various isotopes is shown in Figure 3.14. The Figure 3.14 similar to Table 3.3 displays comparatively low energy recoils

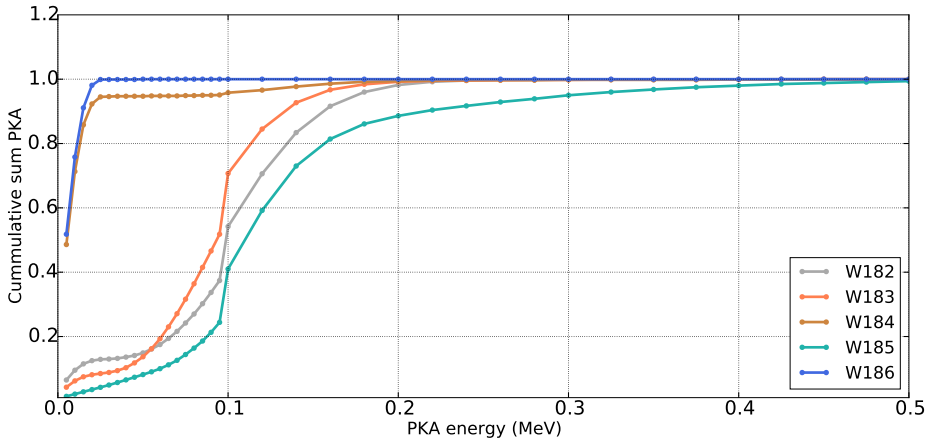


Figure 3.14: The cumulative PKA-energy distribution for W isotopes shows the difference in recoil energies from 30 MeV protons on W. The naturally occurring W isotopes consist of low energy recoils while the transmutation produced show higher recoil energies from the Q value.

from 184W and 186W. While the transmutation channels induce high energy recoils for the other W isotopes.

The results of SPECTRA-PKA endorse the high energy recoil PKA production capability estimated from 30 MeV protons. Higher energy protons are also known to have widely spaced interactions similar to neutrons. Additionally, the results of transmutation calculations of 30 MeV proton irradiation from FISPACT-II shows low and heavy nuclide production, similar

3.4. Feasibility study-proton damage

Production (for 1 dpa in W)	30 MeV Protons	Heavy Ion Accelerators	Fission Reactor (HFR) ^[7]	DEMO First Wall ^[8]
Time taken	14 hours	hours	6 months	3 months
Thickness Range	550 μ m	1 -10 μ m	200 μ m - 4mm	-
Hydrogen Production	15 appm	0	0.01 appm	1 appm
Helium Production	2.5 appm	0	0.001 appm	0.5 appm
Rhenium Production	195 appm	0	50000 appm	700 appm

Table 3.4: Comparison of ion damage with neutron damage on W. The initial modelling of protons performed in this work and listed within this section as the early development stage of proton damage shows promising results and proof-of-concept for the current work.

to neutron damage. The transmutation products are seen to have a steady production rate throughout the considered range of 550 μ m in W. Thus, 30 MeV protons can induce an ideal mix of displacement and transmutation damage similar to fusion neutron damage at damage rates higher than fission reactors. This makes it complementary to fission irradiations. Also, as the range of investigation for 30 MeV protons in W is between 550 μ m, the influence of surface effects can be ignored. The Bragg peak for 30 MeV protons is at 1 mm and restricting the range to 550 μ m also drastically reduces the influence of Bragg peak on damage investigations. If we consider W to have an average grain size of 10 μ m, the range of investigation is over 50 grains. This is essentially macroscopic in nature and can be combined with small scale testing for macroscopic property investigations. Thus, engineering parameters can be extracted from the accelerated proton irradiations for fusion neutron damage simulation.

However, the nuclear reactions associated with high energy protons induce high levels of radioactivity. The decay times as seen earlier are long and it takes above an year to approach 1 mSv/hr after 1 dpa irradiation dose. Thus, the interest to protect man and equipment from harmful irradiation is paramount and necessitates the use of hot cells and special radioactive laboratories for testing. This involves dedicated set-up and configurations which are detailed in Chapter 5.1. While this reduces the advantage of ions, which are considered as inactive methods of simulating neutron damage, it improves the relevance of the obtained results.

Ion damage is versatile and can be suitably adjusted to mimic neutron damage. It has an advantage of experimental ease as compared to fission reactors which use actual neutrons for experimental campaigns. A comparison of heavy ions, 30 MeV protons, fission neutrons against DEMO neutron damage is shown in the Table 3.4. Heavy ions can accelerate the damage significantly and create large damage cascades. The entire damage produced in 6

months to a year in a high flux reactor can be replicated in a couple of hours. High energy protons can closely introduce combined displacement and transmutation damage within the sample. 30 MeV protons under irradiation to a damage level of 1 dpa introduce transmutation changes amounting upto 195 appm of Re and 2.5 appm of He, directly after irradiation(no cooling). Upto 15 appm of H is induced through nuclear reactions (p,2p) in W for 1 dpa dose using 30 MeV protons which in comparison is hardly produced in fission reactors. Protons can also speed up the damage significantly while their large range creates damage on a macroscopic level. However, this increase in damage rates is beam current, beam size and power loading capability of the sample dependent. Post irradiation these samples can be tested and the material properties which are extracted can be used successfully for obtaining engineering parameters. Overall high energy protons allow a speedy technique, complementary to fission irradiation for simulating fusion neutron irradiation effects.

Chapter 4

Tungsten

As the feasibility study performed at the start of this work shows promising results, this Section details the current understanding of the selected plasma-wall material Tungsten (W). It highlights the gap in knowledge and highlights the need for 30 MeV proton irradiation work.

W is a refractory metal and a part of the transition elements of the periodic table. It has one of the highest densities amongst metals measuring 19.25 g.cm^{-3} at room temperature and has a body-centered cubic lattice structure. Its large thermal conductivity ($\kappa = 175 \text{ W.m}^{-1}\text{K}^{-1}$ at room temperature), high melting point of 3695 K [133], good sputtering resistance and low retention properties make it an ideal candidate as a plasma facing material.

It is a brittle metal under tensile loads which is attributed to weak grain boundary strength. It has an average hardness of 450 HV₂ [134] at 273 K and a high ductile to brittle transition temperature (DBTT) ranging between 473 - 673 K [135]. The high DBTT of W makes it a difficult metal to mould, shape and form. W is expected to operate at temperatures above 973 K within a fusion reactor [136]. At high temperatures, W readily forms oxides and humidity accelerates the entire process. It is also susceptible to radiation damage from neutrons impinging on it from the fusion reactions within the plasmas.

4.1 Manufacturing

W has a high melting point, thereby is produced via the powder metallurgy route. Metallic powder having grain sizes between 0.1 and 10 μm is produced from reduction of high purity W oxides at temperatures between 973 - 1373 K [137]. The powders are produced with high chemical purity often to limits of 99.999 g.g^{-1} for most elements. It is followed by a compaction process for obtaining the shape in moulds. The high hardness of W makes it difficult to compact and often cold isostatic pressing using hydraulic pressure is used to obtain compaction. Compaction pressures range from 200 - 400 MPa and post compaction a theoretical green density between 55 - 65 % is obtained [137].

Post compaction, the green parts are sintered at high temperatures between 2273 - 3273 K under hydrogen atmosphere. The sintering process reduces the surface area of the powders and induces growth of particles leading to an increase in density. Post sintering, average theoretical densities between 80 - 92 % are reached. Powder particle size, purity, temperature, time and green density are a few parameters which are controlled during the manufacture [137]. Finally to achieve near full density, mechanical forming techniques such as rolling and forging of the parts are carried out at temperatures upto 1873 K. This particularly removes porosity and refines grain size [137]. While other methods such as plasma spraying, chemical vapour deposition are growing, large scale manufacturing still retains the powder metallurgy

route.

Annealing is usually performed at 1200 K for one hour in order to provide stress relieving post cold work. No visible change in grain size has been shown to occur at this temperature [138]. The recrystallisation temperature of W is near 1500 K [139] and beyond this temperature, W is known to recrystallise with changes in grain structure. Initially stress recovery would occur over a period of several hours post which the recrystallisation takes over. This places an upper operating limit on W.

W is often doped with potassium to decrease its brittleness in its use as filaments. The addition of potassium also leads to an increase in strength relative to pure W as seen at high temperatures [140]. Similar ideas have been pursued for fusion application through the addition of Re, Ta in W which form alloys and solid solutions. These are added at the manufacturing stage prior to the sintering process. However, the success of these alloys has been limited due to neutron irradiation damage [141].

The samples used in this work are cut from a 99.97% chemically pure W bar of dimensions 36 × 36 × 480 mm, obtained from Plansee GmbH Austria. The bar was forged and annealed post sintering and has elongated grains in the longitudinal direction. Aside from the annealing performed by the manufacturer, no further heat treatment was performed on the W samples. The chemical purity was confirmed using inductively coupled plasma-mass spectrometry (ICP-MS) and inductively coupled plasma-optical emission spectroscopy (ICP-OES). The impurities in ppm or ($\frac{g}{g}$) is compared against the manufacturers specification and listed in Table 4.1. Alongside the chemical purity, the isotopic composition of the sample was also confirmed using ICP-MS and time of flight mass spectrometry. This is compared against its natural composition in Table 4.2. The sample's chemical purity was found to be higher than that stated in the manufacturer's specification of 99.8%.

4.2 Neutron damage

W is the first line of defence for the wall and its components against neutrons and energetic particles. The neutrons produced in the plasma bombard the W and create material defects which leads to changes in material property during operation. In DEMO and fusion reactors, the average neutron flux on the outboard equatorial side is estimated to be 5×10^{14} n.cm⁻²s⁻¹ [59]. The neutrons create displacement damage and transmutation damage in W and this is compounded by the addition of gaseous elements injected from the plasma. Atomic scale modelling, microscopy and post irradiation small scale testing techniques have led to a general understanding of the problems which can arise from radiation damage in W. These tools however are unable to precisely quantify and predict mechanical behaviour for fusion conditions and as such new methods and techniques are being sought.

Unavailability of a fusion neutron source to test material properties post irradiation has led to the development of proxy testing tuned to optimal conditions. The obvious proxy for damage are the fission test reactors. Test reactors use highly enriched uranium to produce high neutron fluxes. The incident neutron energy spectrum on the material is dependent on the material's location within the reactor. This in turn determines the type and extent of the damage within the sample. W has been a material of consideration since the 1970's with its inception as a high temperature measurement thermocouple. W-Re thermocouples were introduced for temperature ranges upto 2473 K for which resistivity measurements and recovery rates were established [142],[143]. However, under neutron irradiation, W-10 at.% Re showed disruptions in the measurements, which upon analysis, proved to be agglomeration of Re precipitates [144]. The precipitation of Re was found to induce a calibration change of

Element	Manufacturer spec.	Measured $\frac{g}{g}$
Al	15	< 20
Fe	30	< 3
Si	20	
H	5	
Cd	5	0.027
Cr	20	0.19
K	10	< 8
Mo	100	25
N	5	
Hg	1	< 2
Cu	10	0.022
Ni	20	0.145
C	30	
O	20	
Pb	5	0.006
Re	0	< 0.5
Ta	0	0.08
S	0	< 0.001

Table 4.1: A comparison of the impurities measured using ICP-MS and ICP-OES with the manufacturer's specification leading to a chemical purity of 99.98%. The impurities are listed in $\frac{g}{g}$ or ppm of W. Most impurities are below the manufacturers limits except Al.

Isotope	nat. composition(%)	ICP-MS(%)	TOF-SIMS(%)
^{180}W	0.12	0.12	0.12
^{182}W	26.50	26.3	26.31
^{183}W	14.31	14.5	14.43
^{184}W	30.64	30.7	30.74
^{186}W	28.43	28.4	28.4

Table 4.2: The isotopic composition of W measured using ICP-MS and TOF-SIMS against its natural isotopic composition.

upto 35% under neutron fluence of $2 \cdot 10^{21}$ n.cm⁻² [145]. Additionally void suppression was seen in W-Re alloys irradiated at EBR-II reactor [146] as compared to pure W. Some initial

defect characterisation using transmission electron microscopy(TEM) was attempted [147] and an increase in the DBTT of W was observed [148] but not until the end of 1990's when W was proposed as a divertor material [149],[150] was it systematically investigated.

In the 2000's, a series of fission reactor irradiations in USA, Japan and Europe were conducted. A mixture of W and W-xRe alloys were irradiated and investigated during this period where initial results focussed on TEM and hardness measurements. Nemoto et al. irradiated W-26Re samples at FFTF reactor and upon TEM investigation both α and β phases were identified [151]. Tanno et al. reported void formation even for damage doses of 1.54 dpa under fast reactor JOYO irradiation [152] and confirmed void suppression for W-10Re alloys [84]. Irradiation hardening measurements were also performed within the study which predicted large influence from the Re precipitates. However, no transmutation calculations were noted in the study which undermine the effects of Re growth during irradiation. Similar observations were recorded from irradiations in JOYO, JMTR and HFIR reactors [153] where void lattices were the major defects at low doses (< 0.5 dpa) and with increasing damage dose, precipitates were seen to form leading to higher irradiation hardness [154]. Hasegawa et al. also observed that pure W under irradiation also displayed the formation of an ordered void lattice which aligned itself to coincide with the axis of the host metal [154]. With increasing temperature, the size of the precipitates was seen to increase with pure W irradiated at 773 K and 1073 K at HFIR, leading the formation of sparsely distributed large precipitates [155]. HFIR has a large flux of thermal neutrons leading to substantial transmutation and Fukuda et al. estimated post irradiation transmutation for pure W to be W-9% Re-5% Os. The development of defects under neutron irradiation on W summarised by Hasegawa et al. and adapted from [156] is shown in Figure 4.1. It shows the development of precipitates with increasing neutron dose and a void suppression in the case of W-xRe alloys. A high temperature irradiation carried out at HFR by Klimenkov et al. upto 1.6 dpa damage dose under 1173 K with conditions enhancing fast neutron environment showed agreement with the results from [157] shown in Figure 4.2. The study [158] observed a decrease in the number density of cavities with increasing temperature and void denuded zone accompanied by a void concentrated zone near the grain boundaries.

The irradiation defects form a barrier to the movement of dislocations. Vickers hardness testing was performed in most post irradiation measurements as it is a non destructive method. Using data from post irradiation testing of materials as shown in Figure 4.3, Hu et al. appropriated strength factors to voids, precipitates and dislocation loops to account for the increase in hardening [159]. This approach considers voids and precipitates to be strong obstacles while dislocation loops as weak obstacles to the dislocation glide plane. Under stress, the dislocation loops glide along a plane and avoid stress build-up in the material. Any hinderence to this movement results in material hardness increase. The initial increase in hardness arises from the dislocation loops and as the void lattice develops, a further hardening can be noticed. Then a jump in irradiation hardening can be observed from precipitates formation. Thus, W will eventually show large irradiation hardening due to the production and agglomeration of Re and Os under neutron irradiation. Additionally, as the precipitates play a major role in hardening, annealing of W would have limited benefit [160]. Garrison et al. reported a decrease in the ultimate tensile strength of irradiated W samples with increasing dose [160]. Additionally, the authors recognised a loss in ductility for the samples irradiated at elevated temperatures of 573 - 773 K to be between 0.1 and 0.5 dpa after testing at elevated temperatures, which they suspect corresponds to the ingrowth of precipitates from irradiation.

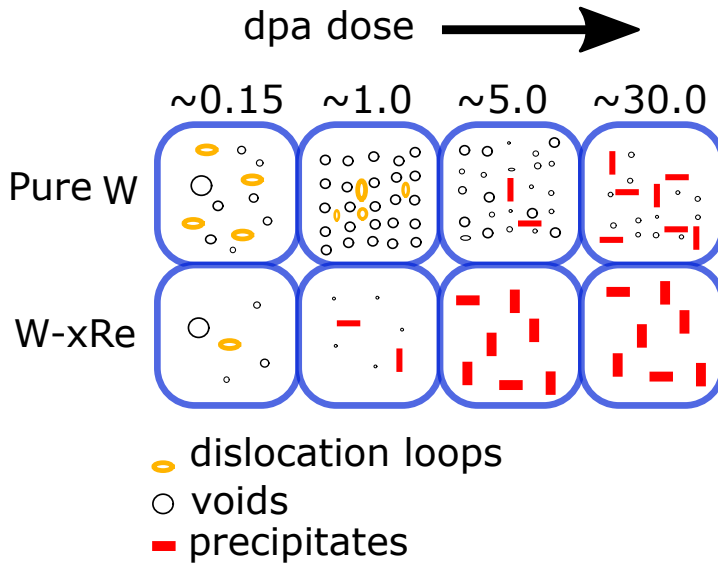


Figure 4.1: The development of irradiation defects from fission neutron irradiation on W, adapted from [156].

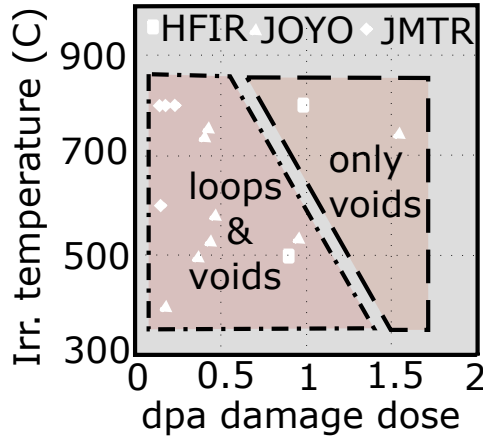


Figure 4.2: Compilation of defects observed from neutron damage on pure W adapted from [157]. At high temperatures and high dpa, only voids can be observed.

A larger database for neutron irradiated W is widely considered as an urgent requirement. Fission neutron irradiation has a biased displacement to transmutation damage ratio. In spite of optimising the neutron spectrum, it produces far more transmutation as compared to a fusion reactor and will induce a different post irradiation composition to fusion neutron irradiation. Material properties such as irradiation hardening are directly linked to transmutation as described above. Additionally, the higher peaked neutron energy spectrum found in fusion

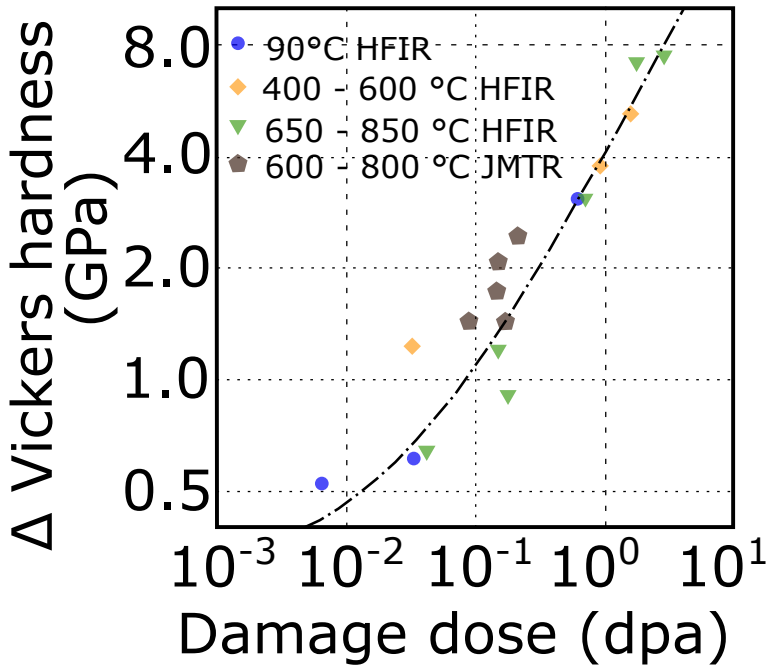


Figure 4.3: Increase in hardness with dose, based on post irradiation measurements at HFIR and JMTR adapted from [159].

produces larger displacement cascades as seen in Figure 2.12 which is not reproduced using fission irradiations. Much larger void density has been noticed under fast neutron irradiation [95] and leads to material embrittlement. The fission irradiations also cannot reproduce H and He introducing reactions in W. He in particular has been associated with void formation and swelling. In W, the He produced is much lower compared to steels and is another reason for W as the choice for divertor and armour material [161]. Ions alongside modelling and simulation activities have helped further the understanding of irradiation damage on W.

4.3 Modelling radiation damage

Modelling of radiation damage has focussed on irradiation hardening and He, H formation in steels and W. First modelling attempts were conducted to comprehend swelling in W [146]. Similar to other refractory metals, the properties of W are governed by its internal structure [162]. The H, He, Re and Os buildup in W has a huge influence on the material properties. This has to be correctly estimated and input into the materials for a proper inventory. Gilbert et al. introduced the necessity of neutron transport calculations and inventory calculations [163]. Today inventory software such as FISPACT-II [90] are routinely combined with neutron transport codes such as MCNP6 [164] to obtain the build-up as shown in Figure 2.13 adapted from [59] and [131]. Marian et al. have recently reviewed the modelling of radiation damage on W [162]. They illustrated the use of density functional theory (DFT) which uses electronic potentials to understand and study defect clusters and point defects within a set of cells. DFT results show stability of clusters containing three or more vacancies and the most stable

interstitial configuration of $\langle 111 \rangle$ self interstitial dumbbell type for W [165],[166]. The binding of vacancies with a He atom is also high [167] and can lead to the formation of He clusters or bubbles. Such a scenario can prevent the recombination of vacancies and self interstitial atoms. Additionally using DFT calculations, the binding energies of most impurities in W show a affinity to trap He atoms except Re atoms [162]. Re atoms are known to exist as W-Re dumbbell and DFT simulations have provided an easy rotatable solution for effective 3 dimensional diffusion of Re in W [168] which leads to solute precipitation [169].

Displacement damage on the other hand relates to the formation and propagation of knock on atoms within the structure of the crystal. It can also sum over the recoil elements which are produced and such a snapshot of the PKA can be used as an input for molecular dynamic (MD) simulations codes. MD simulations can handle $10^5 - 10^7$ atoms and describe the evolution of the cascade from the PKA spectrum. Semi-empirical potentials are used to describe the impact of PKA on the lattice for a given lattice direction [162]. While MD simulations have been around since the 1960s', more recent simulation of high energy PKA cascade development has revealed that a large recombination occurs post cascade which can be seen in Figure 4.4, adapted from [162] in 2 dimensional view. It can be seen that the

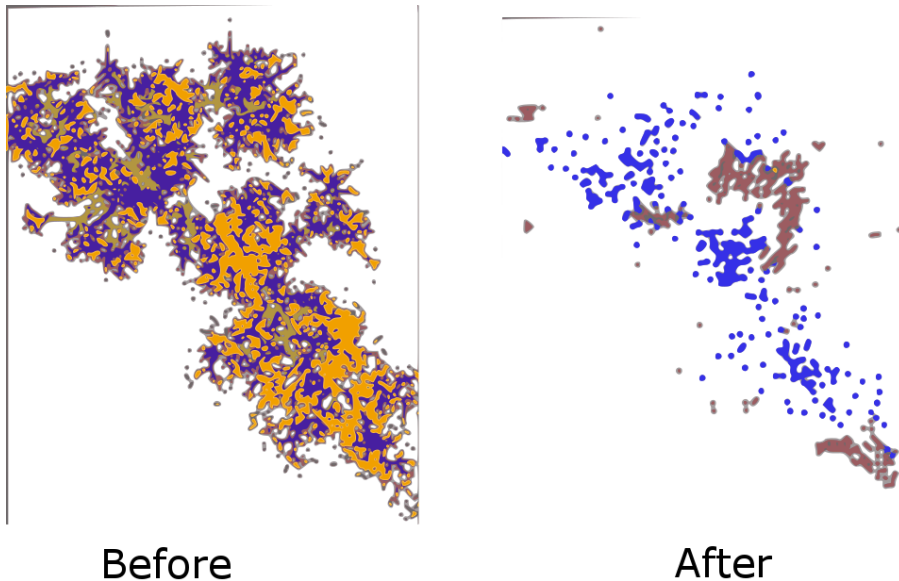


Figure 4.4: The 2 dimensional interpretation of a MD simulation result for a collision cascade in W from a 200 keV PKA adapted from [162]. Recoils having energy > 10 eV are shown in the Figure. The Figure on the left shows the starting impact of the PKA while the grab on the right shows the same cascade post 40 ps simulation time.

cascade branches out and results in the formation of large clusters of defects [170]. Similar MD simulations on high energy PKA also led to the understanding that the cascade development depends on the PKA energy but weakly on the temperature [58]. Only recently have the high energy PKA cascades damage been analysed and points to two different zones of PKA energy-damage relationship [171]. This is shown in Figure 4.5 adapted from [171]. At high PKA energies > 100 keV, the surviving defects are seen to increase rapidly and can be described as $N_{FP} = a(E_{PKA})^b$, where N_{FP} describes the number of surviving defects and a and b are fit parameters.

The NRT damage model (described in Equation 2.9), assumes a displacement efficiency of 0.8 with the PKA energy. However, a large recombination and the distribution of the cascade as shown above, highlights the importance of PKA energy and its correct simulation. Beyond the time scale of MD simulation, the cascade might evolve further and kinetic Monte-Carlo simulations are being attempted. A recent advancement in this field was conducted by Huang et al., where kinetic Monte-Carlo methods were combined with stochastic cluster dynamics to predict reactor scenarios based on the neutron and PKA spectra [172]. Scenarios for JOYO, HFIR and DEMO reactors were simulated towards loop, voids and precipitate cluster sizes and densities which was further correlated to irradiation hardening. However, as per the authors much work remains to be done to approach realistic experimental conditions [172].

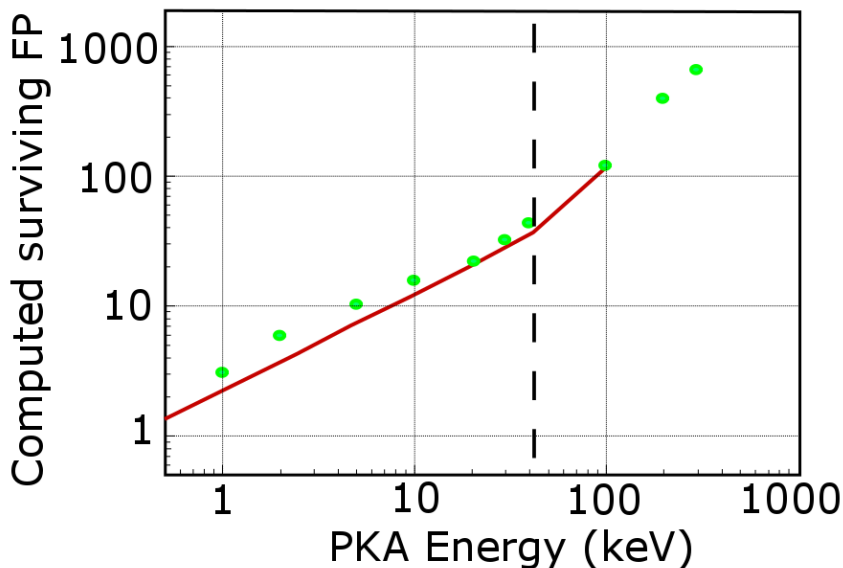


Figure 4.5: Simulated PKA energy dependent, number of surviving Frenkel pairs post a displacement cascade. The red line indicates recent results from [58]. The Figure adapted from [171] shows two different zones of PKA energy dependence at 40 keV. The Frenkel pairs are seen to scale upwards with increasing PKA energy for high energy cascades.

DFT simulation can be performed at 0 K and are limited to 10 - 100 atom clusters. MD simulations can adapt to the potentials calculated from DFT models and simulate a larger scale of atoms. It can describe a non equilibrium scenario and has been matched with TEM observations post irradiation [173]. They have predicted defect cluster densities, the extent of PKA energy impact on defect development. However, the scale of damage effects which can be simulated still remains low. Also, a single damage entity is added at each step while a combination occurs within the fusion reactor. This plays an important role during the evolution of damage in the material. While simulation still lack the ability to predict the fusion reactor damage scenario, they are an essential tool to aid experiments and understand processes which are essentially too fast in time to be experimentally observed.

4.4 Ion irradiation of W

Fission irradiation experiments are presently the only neutron damage experiments possible. However, in order to understand the changes occurring within the material, a closer examination with flexible experimental construction is required which often isn't the case with fission experiments. Additionally, the long cycle time spanning from planning to experiment, cooling and post irradiation coupled with expenses are a large hurdle in the path of material development. Furthermore, in order to approach high doses, the time required is often impractical in test reactors. Thus, ion irradiations were constructed as a swift alternate method to mimic fusion neutron irradiation conditions. Ion sources are largely accessible and can induce high damage dose rates in order to expedite and reach high dpa doses.

Ion irradiation as a surrogate for neutron damage was originally motivated by the fast breeder material development program. Due to their larger scattering probability and the possibility to have high fluxes (beam currents), ions have a higher damage rate between 10^{-5} to 10^{03} dpa.s⁻¹ as compared to neutron damage rates of 10^{07} dpa.s⁻¹. While this results in a faster damage creation, the overall evolution of damage can be different and experiments require suitable compensation. A change in dose rate is often compensated by a trade off in temperature and such temperature shifts of upto 400 K are used to correlate the dose rate differences between ions and neutrons [78]. These shifts are result specific and are used to compare a particular area of radiation damage such as swelling or radiation induced segregation or void growth and can vary accordingly [174]. A recent review by Harrison R.W. covers the ion irradiation of W in detail [60]. Ion irradiations can be broadly classified on the basis of the irradiating species as heavy ions and light ions. Each has its characteristic damage profile and while heavy ions create dense cascades within the first few μm of the target, light ions have a deeper penetration range and can create isolated defects.

Self ions (W^+ ions) of 150 keV were used as the irradiating species on a W and W-5Re target at 773 K by Yi et al. for studying irradiation damage. Both vacancy and interstitial type loops of $\langle 100 \rangle$ and $1/2\langle 111 \rangle$ were formed during the irradiation, with the vacancy loops being formed early on from cascade collapse [117]. Additionally, from the comparison of pure W and W-5Re samples, Re was seen to counter loop growth. Further experiments to higher temperatures of 1073 K displayed a dominance of $b = 1/2\langle 111 \rangle$ loops with rise in temperature [175]. Yi et al. reported no occurrence of voids within the TEM observations. Voids of 1 - 2 nm sizes were reported post 2 MeV W^+ self ion irradiation and annealing by Ferroni et al. at temperatures above 1073 K and were observed to be stable. Ferroni et al. also registered a increase in loop sizes above 1073 K which were completely annealed at 1673 K [176]. Earlier experiments were carried out to a damage dose of 1.5 dpa, which was extended upto 5 dpa by Hwang et al. by self ion damage using 18 MeV W^{6+} ions at 773 and 1073 K. Voids were observed as early as 0.2 dpa in pure W and similar to dislocation loops, their sizes increased with dose to 1.6 nm, however were smaller in diameter to the neutron irradiation observations of 4.7 nm [177]. Irradiation hardening measurements made by Hwang et al. showed an increase to 1 dpa and subsequent saturation [177]. However as no void was reported for the same temperature by Yi et al. [117], the micrograph from irradiations by Hwang et al. at similar temperatures is under doubt.

High dose irradiations were performed by Armstrong et al., where W and W-5Re were irradiated with 2 MeV W^+ ions at 573 K upto 33 dpa damage dose. A jump to 0.4 dpa and subsequent saturation in irradiation hardening at 0.4 dpa damage dose was measured for pure W [178]. W-5Re samples were observed to show clustering at 13 dpa and upto 3 nm clusters of Re were noticed using atom probe tomography at 33 dpa damage level. This

clustering is thought to be the precursor to phase precipitate formation [178]. Xu et al. extended the application of self ion damage using 2 MeV W^+ ions upto 33 dpa to W-1Re-1Os at 573 K and 773 K. This was done to measure and compare the precipitation assist from Os atoms. Strong aggregation of Os atoms instead of Re atoms was found using atom probe tomography. Additionally, with increase in temperature, the composition of the aggregates increased in atom% of the solute [179]. Indentation hardness measurements showed a higher irradiation hardness for the W-1Re-1Os alloy in comparison with the W-Re alloy. However unlike neutron irradiation induced precipitates, the clusters formed from self ion irradiation are considered as weak deterrents to dislocation motion. The range of investigation in self ion damage while dependent on the ion energy is often limited to the first 1 - 5 μ m. This restricts the investigation to nano-indentation studies. Self ion irradiations can induce a large excess of self interstitials within the sample. This leads to recombination with the vacancies and void suppression from the irradiations. The extremely high damage rate from heavy ions and self ions also induces dynamic annealing as against the slow thermal stabilisation from neutron irradiations.

Proton irradiations on the other hand have a 10 - 100x larger range and can be used to study behaviour of a few grains to bulk samples. Ippatova et al. conducted irradiations on W and W-5Ta alloys using 40 keV (in-situ) and 3 MeV protons at 623 K upto 2 dpa damage levels. The TEM investigation revealed presence of interstitial loops of $a/2 \langle 111 \rangle$ type while no voids were noticed from the irradiation, however, ex-situ 3 MeV irradiation showed the presence of dislocation tangles which aren't seen in the 40 keV low energy irradiation [180]. The proton irradiation damage on W so far has focussed on the implantation and retention studies. Ippatova et al. recently have published findings on the void evolution of proton irradiation W at 1073 K, which isn't seen using self ion damage [181]. However, proton irradiation studies are rather few and are yet to reach fusion relevant damage conditions. Additionally, post irradiation mechanical testing is largely lacking. The motivation for this work is the ability to simulate and comprehend fusion neutron damage in W through proton irradiation of 3 MeV, 16 MeV and 30 MeV protons. This involves sample manufacturing, irradiation set-up, post irradiation testing set-up, sample irradiation, transport and post irradiation characterisation.

Neutron irradiation conducted at HFIR and JMTR have a large biased transmutational discrepancy in comparison to fusion reactor damage. They additionally are unable to generate H and He in sufficient quantities for experimental investigation of fusion reactor damage. JOYO being a fast reactor has a comparatively high neutron energy, shifted flux spectrum and thereby, a lower transmutation. However, in JOYO, studies only upto 1.6 dpa damage have been performed. Fission reactor irradiations are costly and often have large constraints of space and environmental conditions. In such cases ion damage studies can be suitably modified and most studies can be repeated. In order to accelerate damage self ion irradiation is often performed, however the rapid damage creation might lead to a difference in damage creation such as lack of precipitates. Self ions damage also creates an excess of interstitials which is thought to reduce the effects of vacancies during damage [182]. Additionally, the low area of damage restricts the possibilities of investigation methods and extraction of bulk material properties. In such conditions, the use of protons provides possibilities to overcome above mentioned drawbacks. Protons have a range from 25 μ m (3 MeV) to 1 mm (30 MeV) and irradiate over multiple grains of W. The choice of proton energy can additionally introduce transmutation alongside displacement damage. Protons create widely spaced damage but additionally create large number of low energy collisions. These collisions can be reduced using a higher proton energy. Proton beams are additionally widely used and easier to control, thus enabling a damage rate control during irradiation.

In summary, W is a leading choice for divertor and armour material in future fusion power plants. It is in the direct line of fire from neutrons and plasma. Fission reactor studies with post irradiation examinations have focused on hardness testing, TEM measurements and micro-structure evolution. They indicate an increasing radiation hardening, void lattice development and precipitate formation post neutron irradiation. However, the differences in neutron energy spectrum between the fission and fusion irradiation environment are significant and do not account for the extent of damage W would endure in a fusion reactor. Fission reactor studies are additionally expensive, are often inflexible and have long cycle times. It is also not easy to reproduce the results from fission reactors. Ion irradiations with conditionable irradiation environments along with simulation studies have helped understand the damage evolution in W. Although, the majority of the studies were performed with self ion irradiation or heavy ions which have short ranges and inaccessible to macroscopic property changes. Additionally, in order to recreate the fusion irradiation environment, the correct combination of displacement and transmutation damage is sought. To date, no study has attempted to use proton damage on W in order to study combined; displacement and transmutation damage. As seen in Section 3.4, the protons are capable of producing a close complementary irradiation environment to measure the effects of radiation damage on W. This can be followed up with post irradiation examination and has a low cycle time. They have macroscopic damage creation abilities and irradiation which can take upto 2 years in a fission reactor can be recreated within weeks. This work attempts to test the simulation capability of fusion neutron damage using high energy protons in W and, alongside set up the post irradiation examinations to qualify W in a fusion neutron environment.

Chapter 5

Small scale testing methods

The proposed method of using energetic protons to simulate fusion neutron damage offers potential solutions to bridge the knowledge gap of irradiated W. As the current work introduces a novel technique leading to radioactive samples, special experimental arrangements are set-up within the scope of this work. The manufacturing technique and experimental arrangements, based on the feasibility study carried out and listed in Section 3.4, are described in detail within this section.

The motivation for analysing hazardous materials and/or critical parts without affecting the overall integrity of the component has led to the rapid development of small scale testing methods (SSTM). The scope of research consists of small scale sample geometry, small scale testing methods and devices, and extraction of properties from the samples. Within the scope of fusion material research, high induced activity and consequently high dose rates, lack of irradiation volume, high heating rates and low amount of irradiated component material availability has necessitated construction of scaled geometry.

This chapter details the design and manufacturing of the small scale sample created for accelerator irradiations, while adhering to the SSTM recommendations for sizes. It then lists the design of a shear punch device and the working of the instrumented indentation method for small specimen testing. The chapter ends with a description of adaptation of the testing machines for operations inside a hot cell.

5.1 Motivation for small scale methods

The development of 2nd and 3rd generation nuclear fission power was largely supported by material development for high temperature and irradiation resistance. The samples which were often prototype of novel materials, were accelerated for testing in reactors with smaller than standard specimen sizes. The large constraint of irradiation volume at high flux regions of the reactor also necessitated reduction in sample size or geometry [183]. The high flux reactors also have limitations on gamma heating and flux gradients in the material which place radiological limits on the amount of material which can be irradiated [184]. This combined with the reduction of post irradiation activity for sample testing is seen as a major motivation for the small scale specimen or miniaturised sample development.

Ion irradiations further strengthened the need for small scale testing methods [183]. Ion irradiations are often focussed using quadrapole magnets and collimators to diameters between 5 - 20 mm, thus being unsuitable for full scale testing. While the sample size and geometry designs were traditionally based on scaled down versions of the original sizes, certain generic sizes like the TEM disk (3 mm diameter disks) were also introduced and

methods designed around them. A comprehensive summary of the methods and sample sizes can be found in reference [183].

Through the 1980s' and 1990s', a complete conference series on small specimen testing techniques by ASTM led to the increased adaptation of a quasi-standard and scaled sample sizes. In each series, methods were described and evolved to meet testing standards. Initially, the effort was to investigate irradiation based changes such as the jump in ductile to brittle transition temperature. However, moving forwards, they led way to extracting standard thermo-mechanically relevant engineering properties post irradiation [183]. The materials are usually selected on basis of their load bearing capacities, ductility, fatigue endurance and so on. For most materials, these properties are well defined and listed in an engineering material selection database. Irradiation however, introduces major damages in the micro-structure which often has detrimental effects on the material's behaviour. Thus, post irradiation, the material properties would need to be reassessed based on the damage introduced. Materials are usually subjected to tensile, fatigue, toughness, impact and creep tests as a standard. The bulk samples used for standard tests such as ASTM E8 tensile testing are carefully regulated by design and reporting. This isn't the same for small scale testing and a recommendation for sample sizes was introduced by Jung et al. [184]. The authors based their recommendations while considering grain size effects, surface effects, specimen preparation, specimen handling amongst other things. The small scale testing methods should also as far as possible be redundant. Lastly, a major condition for the use of small scale testing methods is the conformity of testing results with standard samples or an empirical solution of association. This association should be available for a variety of loading conditions and materials [184]. The straight-forward methods to account for irradiation damage are hardness testing and tensile testing. The engineering parameters of material hardness, yield stress, ultimate tensile strength and ductility for unirradiated samples are widely known and tabulated. Post irradiation the properties can be measured and the influence of radiation damage can be estimated. Thus, the extraction of these parameters from irradiated samples forms a major part of this work and has been detailed in this chapter. The samples have been designed in view of easy comparison to fission irradiation studies, spallation studies and macroscopic property estimation. Additionally, in view of redundancy of testing results, tensile testing, punch testing and instrumented indentation testing were adopted.

5.2 Sample design & preparation

In order to obtain macroscopic material properties, measurements should not be limited to a single or couple of grains. Macroscopic samples offer this possibility of material property measurements by definition. Our design sample geometry must crucially fulfil two major conditions; encapsulate the tensile specimen based on the recommended macroscopic dimensions and the sample can be a maximum of 13 mm in diameter.

Tensile testing is a universally accepted way of obtaining mechanical behaviour and benchmarking of materials. It is a fundamental testing method for obtaining the yield stress and ultimate tensile stress (UTS), creep and cyclic fatigue data of material under loading. ASTM E8 designates the gauge length of 50 mm or 25 mm to be standard [185]. Small scale testing has reduced the sample sizes much below the ASTM limits. Experiments have shown that if sufficient number of grains are present within the gauge thickness of the tensile sample, the yield stress data is within the limits of error for standard specimen scatter [183]. Small scale tensile sample often have a larger width to thickness ratio combined with a reduced gauge length which ensures compatibility between standard and small scale specimens [183].

Recent studies indicate the convergence of miniaturised samples for sample thickness larger than 3x grain size [184], however, these might be subject to surface effects and localised failure from manufacturing inconsistencies such as cracks. A conservative approach is to consider 20x grain size as the minimum thickness for extracting good tensile data. Some of the reactor standards for tensile specimens taken from [183] are listed in Table 5.1.

Type	Gauge length (mm)	Gauge width (mm)	Gauge thk. (mm)
SS-1	20.3	1.52	0.76
SS-3	9.0	1.52	0.76
RTNS-II (USA)	5.10	1.03	0.254
RTNS-II (Japan)	5.0	1.2	0.15

Table 5.1: Reactor based tensile test specimen geometry for miniaturised samples considered for irradiation campaigns taken from [183].

The recommended specimen size [184] as shown in Figure 5.1 has been widely used in reactor irradiations. The sample geometry used in this work is based on this recommendation. Aside from the sample thickness which for 30 MeV protons is 0.55 mm, the other dimensions

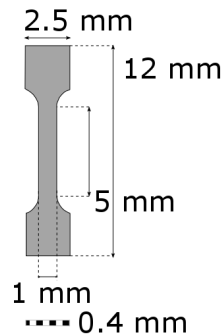


Figure 5.1: Recommended tensile sample dimensions from [184].

remain constant and the sample was built along these recommendations. The sample used was a flat dog bone sample with an intent to keep the grip section un-irradiated. This would help against the hardening of the grip sections and reduce the chances of failure during sample loading. A screw spindle driven electro-mechanical tensile testing machine from MTS, Synergie 400, was retrofitted for tensile testing. The machine can load to a maximum of 2000 N and has a maximum uncertainty of 0.87%, while the travel has a maximum uncertainty of 0.2% measured for at 100 mm of travel. The crosshead can travel with speeds between 0.001 mm/min and 1000 mm/min.

The second condition of being maximum 13 mm in diameter is a restriction based on the cyclotron beam size and solid target capacity. The sample should be macroscopic while attempting to reduce total sample activity. With increasing sample size, the post irradiation activity increases and a compromise between macroscopic size and radioactivity is sought. Unlike reactors, accelerators can handle one sample at a time. Thus, the intention to have multiple samples which can generate complementary results within the same irradiation was

also considered. The ability to extract mechanical properties from 3 mm TEM disk samples has been investigated widely. A growing technique amongst small scale testing laboratories is punch testing. Thus, punch samples are additionally placed alongside the tensile sample for additional redundant testing of samples with the same irradiation conditions. Another testing technique, instrumented indentation is also included in the testing techniques. However, this is non-destructive and can be carried out prior to the punch testing. Lastly, the sample geometry is kept similar to neutron irradiation campaigns. This forms a basis for direct comparison to fission and spallation irradiation results under different radiation environments.

A suitable sample geometry was selected from a set of different sample configurations based on the two constraints of sample thickness ($\approx 500 \mu\text{m}$) and sample diameter (13 mm). This geometry is shown in Figure 5.2. Each sample has one miniaturised tensile sample

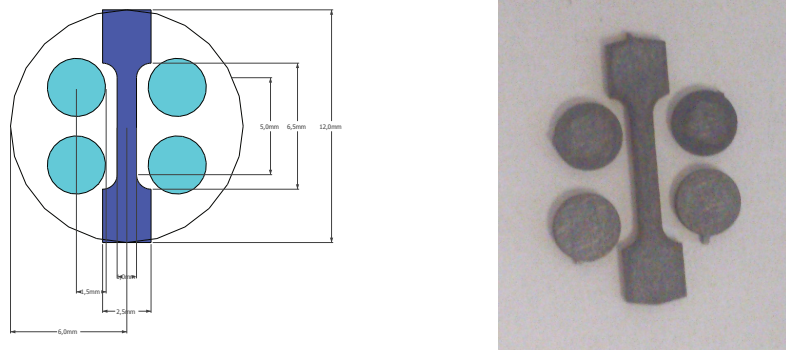


Figure 5.2: Sample geometry with dimensions. The sample itself consists of one miniaturised tensile sample and four shear punch samples. The cut sub samples are shown on the right.

in the middle with four 3 mm TEM disks surrounding it. The TEM disks would allow for complementary testing methods to be conducted and co-related with the tensile sample. This adds data points and redundancy in case of limited irradiations. Additionally, the 3 mm TEM disks are widely used in spallation and fission irradiations and the results could be directly compared without any size effects.

The samples were cut and investigated using two alternative methods; laser cutting and electro-discharge wire cutting. The laser cutting uses a 4 kW power continuous wave laser of 1030 nm with a high beam quality to make minute cuts. While the electro-discharge machining uses a thin brass wire to create sparks which erode the material while submerged within deionised water. A comparison of the cut tensile samples as seen under a scanning electron microscope (SEM) is seen in Figure 5.3. The freshly cut samples are finally cleaned using non contact ultrasonic bath cleansing method. The laser cut samples were finer and had a sharper cut around the edges. However, the laser cutting left a heat affected zone around the cut. While this wasn't the case with electro-discharge machining, there were impurities from the cut seen on the sample with thick oxide layers. This was investigated and proved to be the case using energy dispersive x-ray spectroscopy (EDX) as shown in Figure 5.4 and 5.5. Both Figures indicate a layer of WO_x on the sample surface with the impurities of Cu and Zn accounting for less than 5% of the atomic concentration. The cutting of W under deionised water is suspected to be the source of the layer of WO_x on the surface.

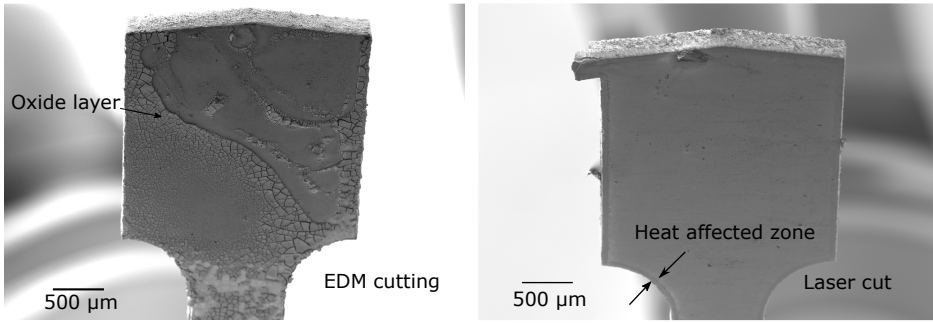


Figure 5.3: Scanning electron microscopy images of EDM cut tensile sample on the left and laser cut sample on the right under same magnification. Notice the heat affected band around the laser cut sample. While for EDM cut samples oxide layers are seen on the surface.

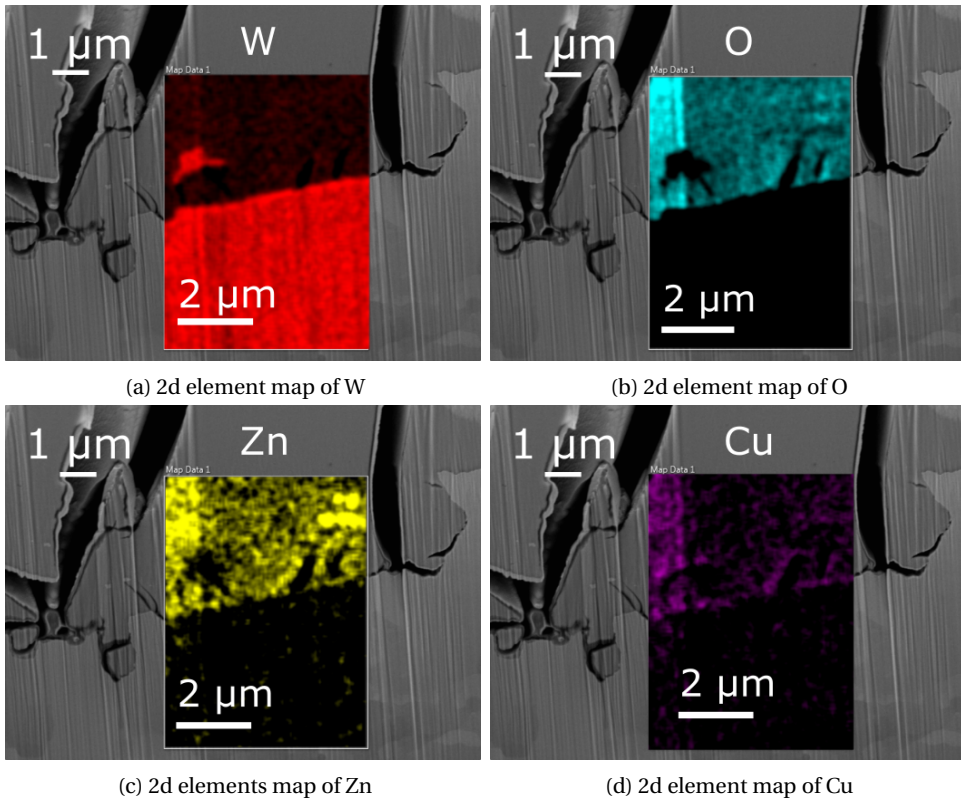


Figure 5.4: 2 dimensional mapping of the elements recognised from EDX measurements on the interface between the oxide layer and the buld sample for the EDM cut W.

The laser cut samples contain a heat affected zone often upto 50 μm thickness, thereby the EDM method was chosen for sample manufacturing. To remove the oxide layers, the EDM samples were mechanically ground using silicon carbide papers and then finally electro-polished. The initial mechanical grinding serves the dual purpose of removing of Cu/ Zn

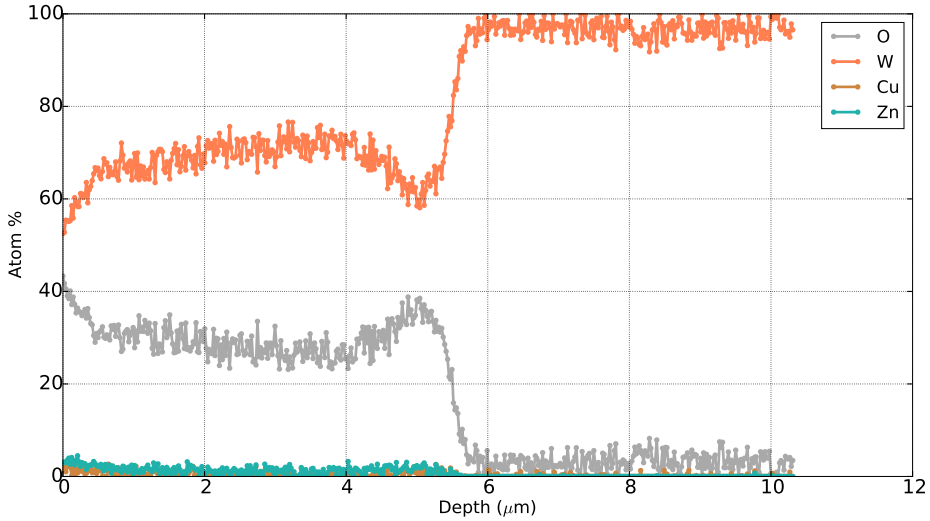


Figure 5.5: A line scan of the interface using EDX showing the atomic concentration in % for W, O, Cu and Zn in the EDM cut W sample.

deposition post EDM cutting and alongside the surface unevenness is corrected. Additionally, it is observed that the initial surface quality has a large influence on the electro-polishing (EP) result. The mechanical polishing uses SiC polishing papers, starting with P800 and gradually moving up to P4000. Care was taken not to insert any slope on the surface due to uneven pressure. An plan with polishing steps is developed and shown below in Table 5.2. As seen in Table 5.2, a fine polish using diamond paste of 3 μm grain size is the final step. Further to this polishing step and prior to EP, the sample is cleansed using an ultrasonic non contact cleanser to remove any remnants of mechanical polishing.

Polishing Paper	Time(min)
P800	1
P1200	1
P2500	1
P4000	2
Diamond 3 μm	15

Table 5.2: An approximation of the mechanical polishing steps used prior to electro-polishing.

An electro-polishing set-up was installed using a DC voltage supply source, a electrical stirrer with a heating option for the electrolyte and a wire mesh as the cathode. The set-up is shown in Figure 5.6. The sample (anode) is connected to the positive terminal of a constant voltage/ current power supply and negative terminal is connected to a steel mesh which acts as cathode. A voltmeter and ammeter are used to observe shifts in values. A glass beaker holding the EP solution is placed on a height adjustable tray. The EP solution is stirred continuously with a magnetic stirrer. A W crocodile clamp was fabricated to hold the sample

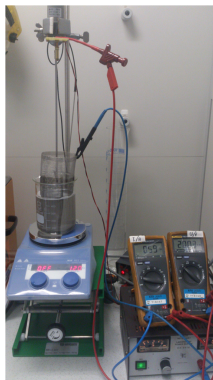


Figure 5.6: The electro-polishing set-up with a DC voltage power supply, an electric stirrer and the cathode wire mesh.

in position during EP with minimum force.

A good electro-polished sample relies on proper polishing conditions, i.e. the appropriate applied voltage, correct balance of EP solution and removal rate. This has to be established prior to the EP. However, these parameters are sample and material dependent. For instance, most commonly used operational settings for polishing of W samples are an applied voltage of 20 - 25 Volts and a 2.5 - 4% wt. electrolytic solution of NaOH [186],[187]. Though most EP processes are carried out using above mentioned parameters, our samples had fine mechanically polished conditions to start with and subsequently, a softer polishing technique close to described in [188] was chosen. The EP solution consisted of 6 g NaOH, 150 g distilled water and 225 g glycerol. As detailed in [188], the glycerol softens the erosion rate, resulting in lower unevenness of surface. From pilot experiments, a plateau is observed for 7 volts applied potential difference and is selected for EP. In order to avoid the dense glycerine from settling down at the bottom of the beaker, the EP solution is continuously stirred using the contactless magnetic stirrer at a speed of 300 rpm.

A comparison of the sample surface post P4000 rough grinding and post EP using scanning electron microscopy is seen in Figure 5.7. The scratches seen after grinding are no longer present on the surface post EP. Large grains can also be observed on the surface post EP. To observe the bulk of the sample below the surface, two cuts perpendicular to the surface using a focussed Ga^+ ion beam are made. The bands seen in Figure 5.7 are platinum deposits and mark the location of the cuts into the surface. The focussed ion beam (FIB) cuts are shown in Figure 5.8. A damage layer upto a depth of 1 μm is observed under the mechanically ground surface. This is due to the pressure exerted onto the sample during the mechanical polishing steps. However, the layer was not observed post EP. EP removes the damage layer of material from the surface induced by mechanical grinding as seen in Figure 5.8.

Thus, the combination of mechanical grinding and 7 V NaOH solution electro-polishing technique removes the oxide layer completely and the sub surface damage layer. However, some samples display cracks resulting from the EDM cut as shown in Figure 5.9. These cracks were observed on a few samples and persisted through all the grinding and polishing steps. The width of the crack is between 0.5 and 1 μm , while the depth of the crack extends upto 50 μm . As these cracks are visible to the eye, the particular samples can be avoided. After polishing, the samples can be loaded onto the sample holder for irradiation.

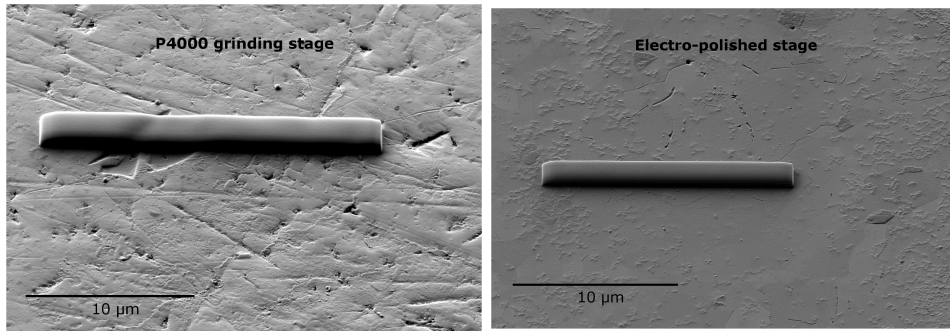


Figure 5.7: Comparison between mechanical grinding on the sample upto P4000 and electro-polishing. Clear scratches are seen on the mechanically ground sample while large grains can be recognised on the surface of the electro-polished sample.

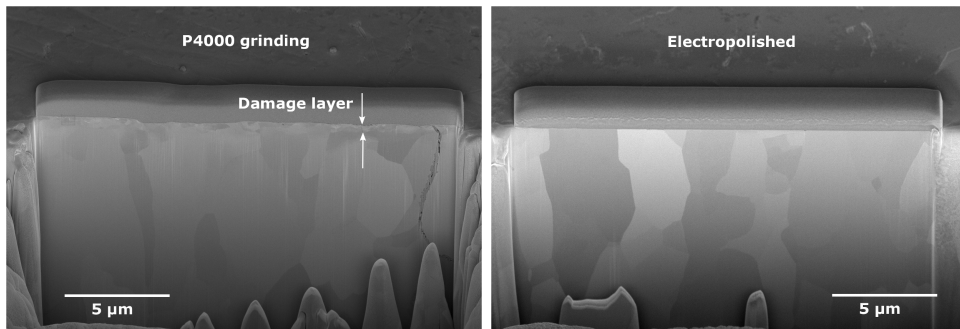


Figure 5.8: A comparison of the bulk sample below the surface post P 4000 grinding and EP. The perpendicular cross-section reveals a thin layer of damage just below the surface from mechanical grinding. This layer is removed by electro-polishing the sample.

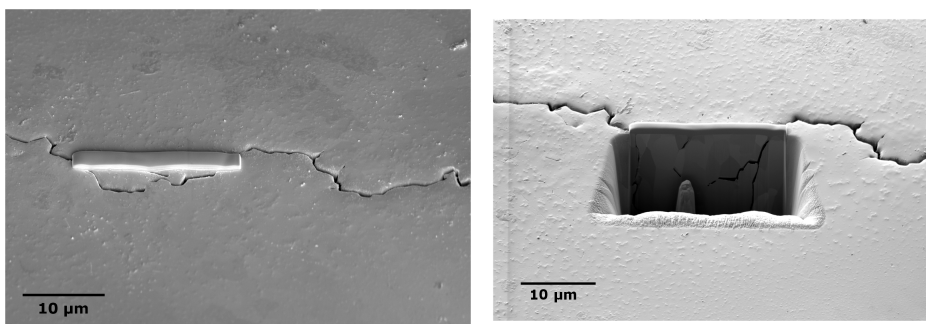


Figure 5.9: Cracks seen after polishing on an EDM cut sample. The cracks are of 1 μm thickness and penetrate more than 10 μm deep.

5.3 Instrumented indentation

A non-intrusive method for obtaining hardness data has been the micro hardness testing. In hardness testing a pyramidal diamond indenter imprints onto the sample from which the resistance to the impression is measured. The force is applied and after a prefixed dwell time the hardness is determined and assigned a single value. Instrumented indentation (IIT) is an advancement of this method where the force and displacement are recorded while the indenter is in contact with the material and can measure the Young's modulus (E) along with hardness (H) [189].

An example of the force displacement curve alongside the displacement of the indenter as taken from [190] is shown in Figure 5.10. Once the force is applied, the indenter comes

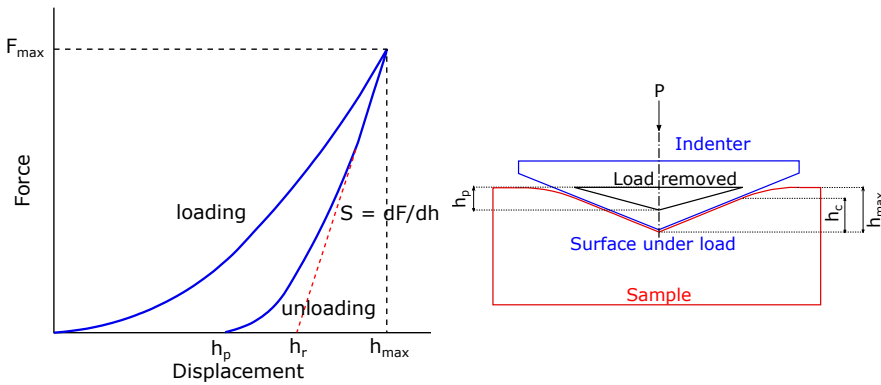


Figure 5.10: A basic force displacement curve for instrumented indentation showing the maximum indentation depth h_{max} at the maximum force, permanent indentation depth h_p post load removal and the point of intersection from the tangent to the curve at maximum force taken from [190].

in contact with the material and starts to deform the material by imprinting on it. As the force increases the depth increases to a maximum indentation depth (h_{max}) for a maximum force (F_{max}). As the indenter withdraws, the material relaxes and withdraws only to leave a permanent deformation of depth h_p in the material. Here, another variable h_c or contact depth can be described. It is defined as the depth which corresponds to the time the indenter has contact with the sample while unloading. This is seen in Figure 5.10 is described by Equation 5.1. Here, h_c is calculated using the fit parameters [191].

$$h_c = h_{max} \frac{F_{max}}{S} \quad (5.1)$$

Based on the recommendations of ISO14577-1:2015(E) [190], if the contact depth (h_c) is greater than 6 μm , then the projected contact area can be defined as in Equation 5.2.

$$\overline{A_p} = 4.950 h_c^2 \quad (5.2)$$

Another quantity h_r is derived from the intersection of the tangent to the unloading curve at F_{max} with the indentation depth axis. From this cycle of loading and unloading, engineering properties can be derived. The Oliver and Pharr method [191] states that while loading is both elastic and plastic deformation, during unloading, it is assumed that only elastic portion of

the sample recovers. Based on this assumption, the unloading curve can be fitted using the power law as shown in Equation 5.3.

$$F = B(h - h_f)^m \quad (5.3)$$

Here B and m are power law fitting constants which are material and experiment dependent. Another defined quantity in the method is the contact stiffness S, which is the stiffness to elastic unloading. The contact stiffness is defined as the slope of the upper portion of the unloading curve at the start of unloading itself (F_{max}) as described in Equation 5.4.

$$S = \frac{dF}{dh} \quad (5.4)$$

Using the above Equation, the estimate of elastic modulus can be found using Equation 5.5.

$$E_0 = \frac{1}{2C_s} \frac{1}{A_p(h_c)} \quad (5.5)$$

$$E_{IT} = \frac{1}{\frac{1}{E_n} - \frac{1}{E_i} - \nu_s^2}$$

Here, ν_s is the Poisson's ratio of the sample, ν_i is the Poisson's ratio of the indenter, E_i is the modulus of the indenter and E_r is the reduced modulus of contact. C_s is called the sample compliance which is the inverse of sample stiffness.

Compliance consists of two parts, one of the machine itself, self compliance and secondly the contact compliance. This is written in Equation 5.6, with the C_f term relating to machine compliance and the C_m term corresponding to the contact compliance.

$$\frac{1}{S} = C_t \quad (5.6)$$

$$C_t = C_s + C_m \quad (5.7)$$

From Equation 5.5, it is seen that the contact compliance is inversely proportional to the square root of the contact area. At lower applied forces, as is the case for nano indentation, the depths are shallow and correspondingly the contact areas are small. This leads to large contact compliance effects. However, for macroscopic indentation, i.e. with increasing loads, the effect of machine compliance or load frame compliance increases and is the dominant factor.

Recent interest in indentation has led to development and availability of commercial machines for the purpose. The measurement scales vary from nano indentation, where the depth of the indent is 2 μm to macro indentation of forces 2 N. A brief introduction to many is highlighted in [192]. However not many machines are capable of measuring over a wider applied force range. "Zwiki Z2.5" [193] from Zwick/Roell is capable of operating in the macro - micro range. This machine has a force range of 2 - 200 N with a force resolution of 0.01 N and a displacement resolution of 20 nm. It comes with a motorized table for easier hot cell application and co-axial light microscope. The head containing the displacement and force sensors adapted from [194] is shown in Figure 5.11. The ring surrounding the displacement transducer measures the contact to the surface and the displacement is directly measured between the sample surface and the indenter, thus being independent of the base. This enables us to measure miniaturised samples such as the 3 mm disks. Measured loading

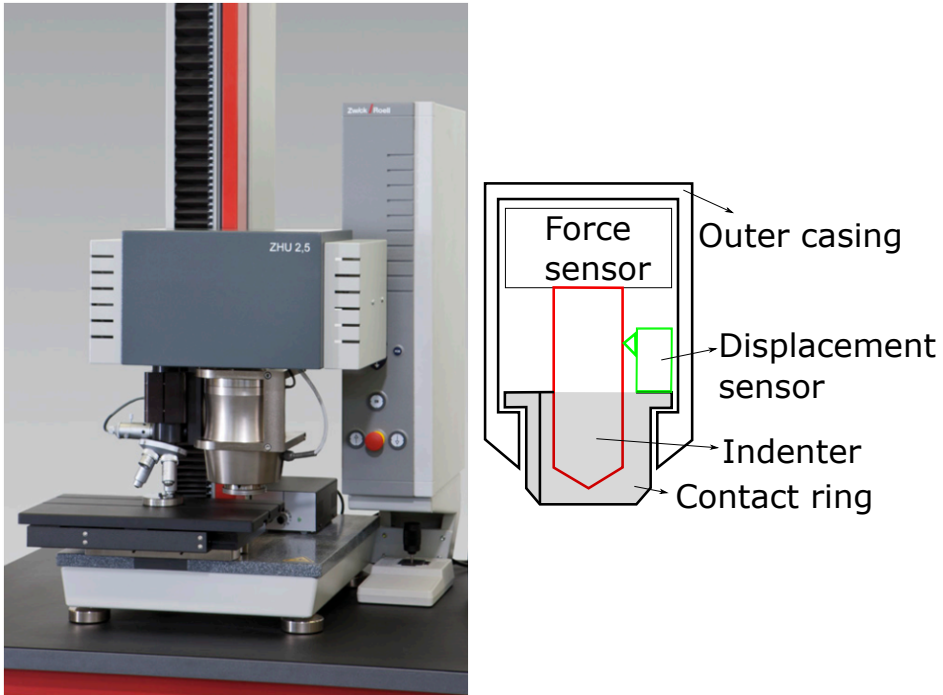


Figure 5.11: The head of Zwick Z2.5 consisting of the force and displacement transducers as adapted from [194]. The head consists of a ring which measures surface contact and enables the measurement for miniature samples like the 3 mm disks.

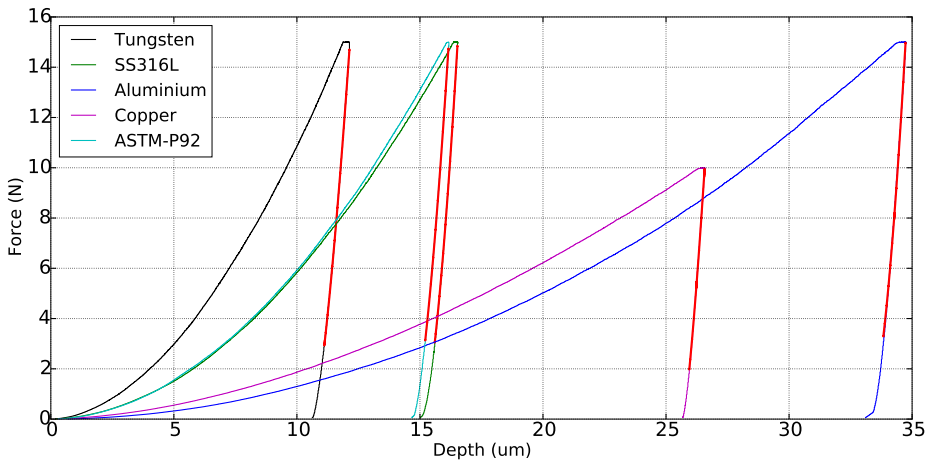


Figure 5.12: The loading and unloading curves for a W, SS316L, Aluminium(Al), Copper (Cu), and ASTM P-92. The maximum force for materials except Cu (10 N) is 15 N. As expected, a deeper indent is inscribed in Al while W shows a rather high resistance to indentation.

and unloading curves for 5 different metals using the Zwick are shown in Figure 5.12. Al being a ductile material has a much lower resistance to the indent as compared to W and thereby displays large penetration depth for the same force. SS316L and ASTM-P92 display similar loading and unloading behaviour. For each of the metals, the initial portion of the unloading curve is fitted with a power law and is marked in red. This portion of the curve is analysed to obtain material properties.

Prior to testing a machine compliance calculation is performed. This is to analyse the stiffness of the machine and correct for this deviation within the result. The machine compliance calibration was performed on SS316 and W samples to a loading (20 N) higher than the intended test load (15 N). The increasing force method as outlined by Ullner et al. [194] is used to correct for machine compliance. Increasing loads were applied on the spot to obtain a linear regression of the function C_t vs $F^{0.5}$ as given in 5.8.

$$\left[\frac{dh}{dF}\right]_{F_{max}} C_m = \frac{\overline{H_{IT}}}{2E_r \overline{F_{max}}} \tag{5.8}$$

The measurement results in a linear Equation of the form $y = mx + c$, c being the constant. This constant term is the machine compliance and can be derived from the graph directly. An

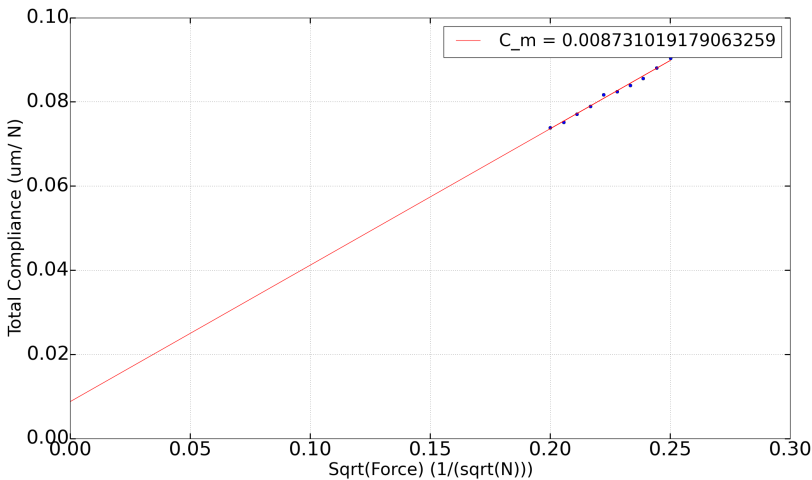


Figure 5.13: The compliance measured on a W sample using the linear regression between total compliance and $F^{0.5}$.

example of such a measurement on a W sample is shown in Figure 5.13. Here the machine compliance is the offset of the linear function on the Y axis and gives 0.009 ± 0.003 m/N force applied. Once the compliance has been determined, a Martens hardness measurement is performed on the preassigned spot to obtain a force displacement curve. 98% to 20% of the unloading curve is fit using a fitting program written in python script and the non linear least square minimisation method (Levenberg-Marquardt fit) [195]. The loading - unloading curve from a W sample along with the measured Vickers hardness is shown in Figure 5.14. Using m , B , h_r from Equation 5.3 and the machine compliance, Equation 5.8, the Young's modulus and hardness can be estimated. The machine is capable of directly measuring the diagonals post indentation and can also provide a Vickers hardness (HV) measurement. Measurements on a

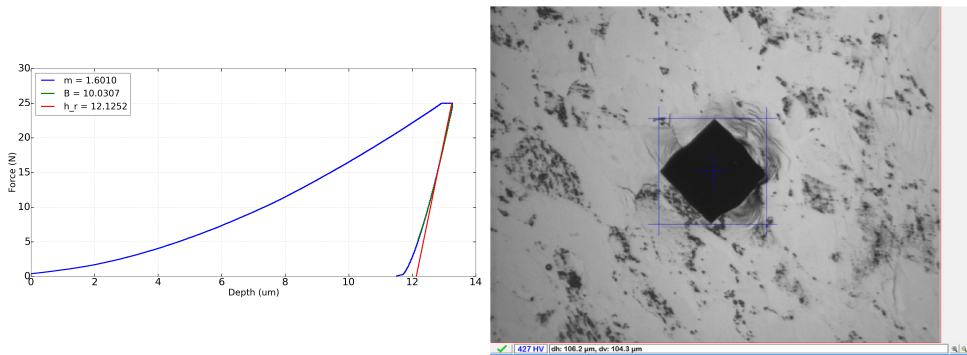


Figure 5.14: The loading-unloading curve from a Martens hardness test using a macroscopic instrumented indentation which measures the Vickers hardness at the end of the test. The unloading curve is fit using the least square method [195] according to [190].

blank sample resulted in a hardness measurement of 4.1 ± 0.02 GPa and indentation modulus of 362 ± 24.8 GPa. Tests are also conducted on 316L steel as a reference material. The results are shown in Figure 5.15, where the hardness and indentation modulus are measured using multiple indents on the same sample. The variation in the indentation modulus is measured as 209.6 ± 11 GPa as compared against the literature value of 193 GPa.

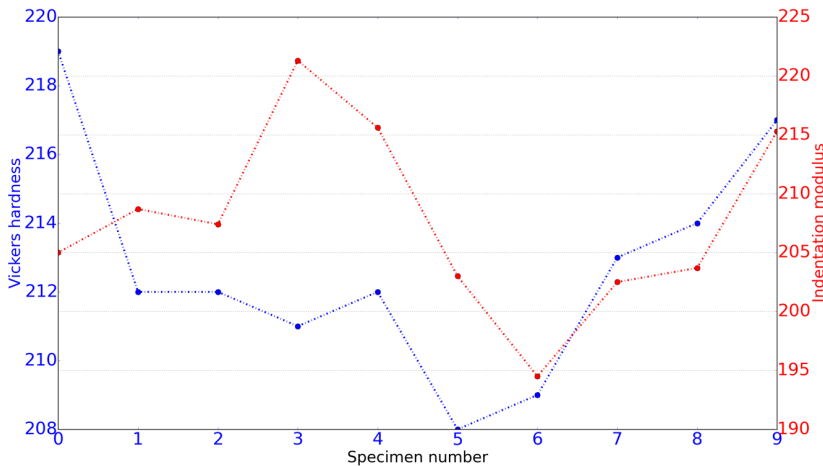


Figure 5.15: Instrumented indentation results on an unirradiated 316L sample showing 10 indents on the same sample. The variation between each indent can be observed in the Vickers hardness and indentation modulus.

The indents made by instrumented indentation device are under $20 \mu\text{m}$ for fusion relevant materials as seen from Figure 5.12. For a sample thickness of over $500 \mu\text{m}$ as in the case of W under 30 MeV proton irradiation, the indentation has penetrated less than 5% of the total depth. The diagonals are under $100 \mu\text{m}$ wide for a sample of $3000 \mu\text{m}$ diameter. Thereby, if the indent is performed slightly away from the centre, the indentation may be considered as non-destructive and potentially an additional test could be performed at the centre of the irradiated 3 mm disk. Post irradiation, the sample is expected to show hardening from the

change in micro-structure, This would further reduce the indentation depth and make the entire test non destructive.

5.4 Shear punch testing

A growing technique amongst small scale testing laboratories for extracting material data from 3 mm disks is punch testing. It can be adapted on various disk sizes and has been suitably tested on 3 mm disks. Similar to tensile testing, engineering properties such as ultimate strength and ductility can be estimated and correlated with tensile testing. It involves the application of load on disk samples which are 1 - 10 mm in diameter. In this method, the load and displacement are continuously recorded while disk samples are slowly punched through. Punch testing was initially developed to study radiation embrittlement and has subsequently been applied to other fields such as ceramics, dentistry, concrete testing etc. [196],[197],[198],[199],[200]. Different versions of punch testing are followed based on the application. But for small scale testing methods, a comprehensive method is described under the code of practice [201]. The document clearly states that a small punch test shall be carried out under a constant displacement rate.

A basic cross-sectional view of the set-up is shown in Figure 5.16. While shear punch is essentially a blanking operation, it consists of a loading system which is controlled to actuate at a certain constant displacement. The load and displacement of punch are to be recorded at all times. Screw-driven load systems are ideal for this operation. The sample itself is clamped in a testing rig and finally a linear variable differential transformer (LVDT) is used to measure deflection of the sample. Upon application of load, the sample is slowly deformed and punched out. An example of the sample and the punched out disk is seen in Figure 5.16.

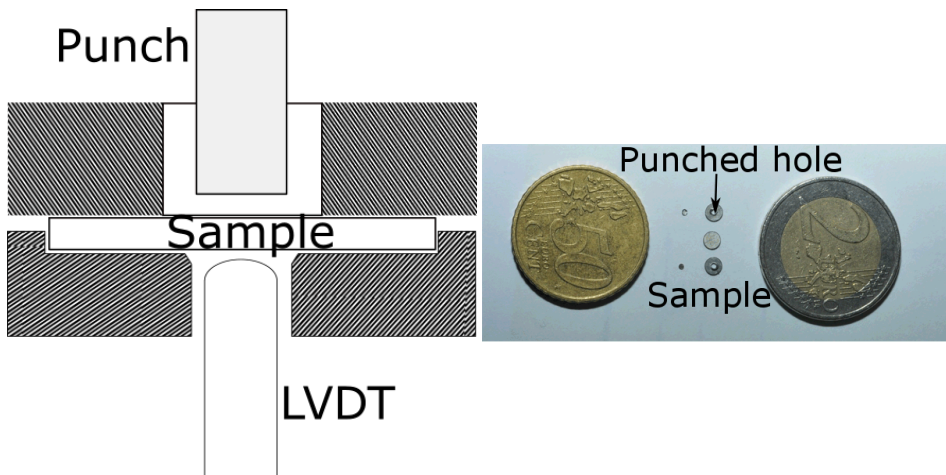


Figure 5.16: A cross-sectional view of the set-up and a size comparison of the sample with the punched out disks.

As the punch is driven through the sample, the load on the punch is monitored as a function of the punch displacement. The outcome of a shear punch test is in the form of a force versus displacement curve (Punch force versus displacement). This curve adapted from [202] is shown in Figure 5.17. As the sample is clamped, it can only deform within the small

clearance region between the die and the punch. Initially as the sample is loaded with the punch, it elastically deforms. With rise in load, the sample crosses the elastic limit and starts to undergo plastic deformation. The plasticity is accompanied with strain hardening which gives it a maximum loading force. Once the peak load is reached, the sample starts to crack, leading to decrease in load and ultimately failure. In an ideal case, failure of the sample occurs when the maximum shear strength of the material is crossed [202]. A pictorial representation of the punching process is shown in Figure 5.18, where the numbers correspond to 1- punch contact, 2- linear elastic regime, 3- shear yield limit, 4- ultimate shear limit, 5- plastic instability.

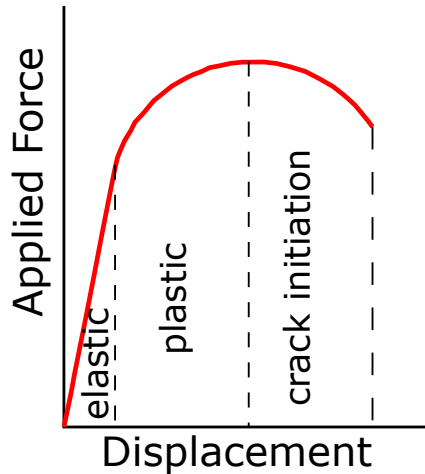


Figure 5.17: A typical force vs displacement curve for a shear punch test adapted from [202]. Similar to tensile testing, the punch curve has an elastic and plastic region.

Early on it was observed and derived that the stress state of the sample under deformation is not limited to pure shear [204] but rather a combination of bending, shear and compression. A correlation between the tensile studies and punch studies was attempted. The early studies [205],[206] performed disk bending studies using a rounded punch. Further studies [204],[207],[208],[209],[210],[211] have examined the factors such as specimen thickness and machine compliance towards punch testing results. Studies with experimental results [212],[202],[213],[214] and finite element simulations [215] have improved extraction of mechanical properties from punch testing. Empirical co-relations are used to associate the maximum stress with ultimate tensile loads and the deviation from linearity with axial yield stress [183]. The basic relation can be expressed as in Equation 5.9, where u is the ultimate punch stress, P is the peak load from the curve, F the friction load, r is the punch-die radius, t is the specimen thickness and C being a correlation coefficient.

$$u = \frac{P}{2} \frac{F}{rtC} \quad (5.9)$$

Unlike tensile tests, where the yield is considered at an offset, in punch test the yield is taken at the point of deviation from the linear portion of the load - displacement curve. However, studies have considered an offset of 0.2%, 0.5% and 1.0% to get a better fit with tensile studies. A similar Equation as can be written for the punch yield stress y using the load at yield. The

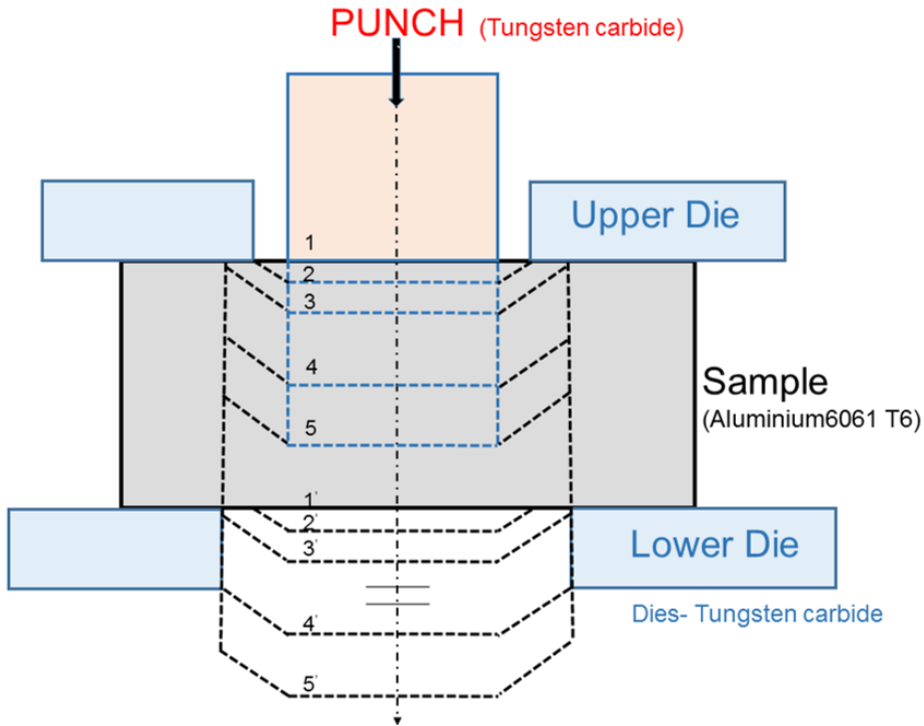


Figure 5.18: A sequential punching process with numbers corresponding to the various stages of the process taken from [203].

punch stress is correlated to the tensile tests using an experimental offset parameter for the punch stress data as seen in Equation 5.10.

$$\sigma_{punch} = m(\sigma_{tensile} - \sigma_0) \quad (5.10)$$

Each material is seen to have a characteristic slope and offset which is experimentally determined. The slopes are seen to be higher than the Von Mises criterion (i.e. $\sqrt{3}$ or 1.732), which is a result of a mix of stresses rather than pure shear during shear punch. Finite element methods have suggested that the compliance of measuring machines have a large impact on the correlation. Change in friction values had negligible effects on the shear punch results within FEM studies [216].

Toloczko et al. developed a new low compliance set-up which incorporated a displacement transducer and measured the bottom of the sample along with the crosshead movement [217]. They clamped the sample between two dies and held them together with corner bolts. Using FEM simulations they correlated 1% punch strain offset stress to the standard 0.2% offset corresponding tensile yield stress. Ductility correlations were also developed. However based on similar experience, the tightening of bolts results often in a misalignment which reduces the efficiency of the method. Thereby, a study was taken up and a new design for the shear punch system is developed in the frame of this work.

The punch set-up was developed to be installed on the tensile machine (MTS Synergie 400) described in section 5.2. The set-up would replace the gripping arms on the tensile test machine and sit aligned vertically along the spindle shaft. A lock pin is used to keep the set-up

in position. The single uni-axial set-up was considered ideal to avoid any cross loads on the sample during loading and alignment. The designed set-up for punch tests on 3 mm disks is shown in Figure 5.19. The prototype was constructed using SS316 steel but the final version would be designed using W with a tungsten carbide tip and tungsten carbide dies. A disk shaped adapter keeps the sample in place while the travel slide directs the punch vertically through it onto the centre of the 3 mm disk. The punch used was a 0.9 mm tungsten carbide bit with counter adapters having holes of 0.95, 1.0 and 1.05 mm diameters. Another aspect of the design is to have interchangeable parts which fit with ease to each other. This has the advantage of easy change in a radiation environment and for adaptability to larger diameters such as 8 mm diameter disks.

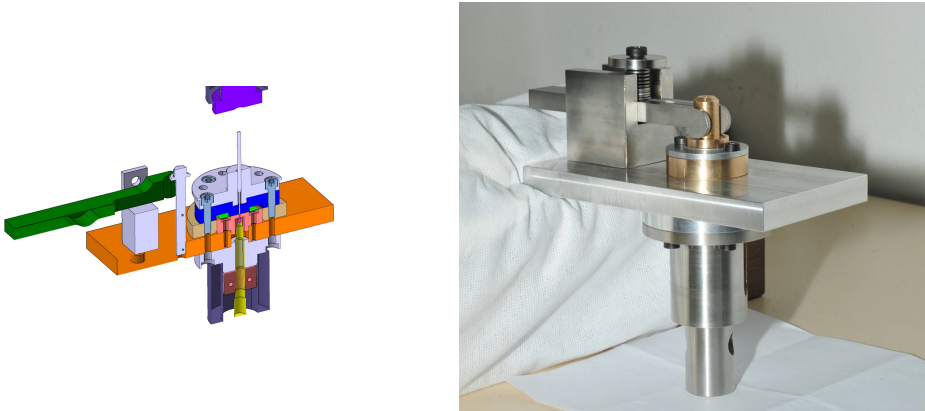


Figure 5.19: The concept and prototype of the Shear punch test design for 3 mm disks.

In line with Toloczko et al., a linear variable differential transducer was introduced below the adapter. The LVDT WETA is pneumatically operated with a sensitivity of $2.2 \frac{V/V}{m}$ and is pressed against the sample bottom side. It is spring loaded with a displacement travel of 1 mm and can be adapted to push the punched out centre back. A measurement frequency of 10 Hz was selected which results in a minimum measurement step of 167 nm. An independent measurement was set-up with a HDM Quantum MX440B data acquisition amplifier with a 10 Hz Bessel noise filter. The four configurable inputs are used to accommodate the LVDT, force voltage signal directly from the circuit board and a thermocouple. The force-voltage can registers a 30 mV signal which is 100x above the Bessel filter noise of 300 nN. This results in an independent measurement system alongside the tensile system force travel measurement.

Samples thinner than 0.5 mm display compression at the start of the loading curve and a change in the initial loading line is noticed [212]. 30 MeV proton samples have a thickness of 0.5 mm and above and can be correlated using shear punch tensile specimens. Finite element analysis simulations using pure W was performed on a 2d model of the punch test design in Ansys. A combination of three and four node plane elements, are used to create the mesh frame, with a denser mesh along the clearance and sample-die interaction areas. The corners have a minimum of five elements of 1 μm edge length with no adaptive re-meshing option active in order to simulate failure through stress. Also to facilitate an active contact between the punch and die at all times, the mesh deletion function was subsequently removed. The failure condition is set at the point of equivalent plastic strain. Results from the punch simulation on a W 3 mm disk is shown in Figure 5.21, where the adjoining values show increasing shear stress. The loading of force is applied vertically by the punch and the load

5.4. Shear punch testing

stages are ascending in the clockwise direction.

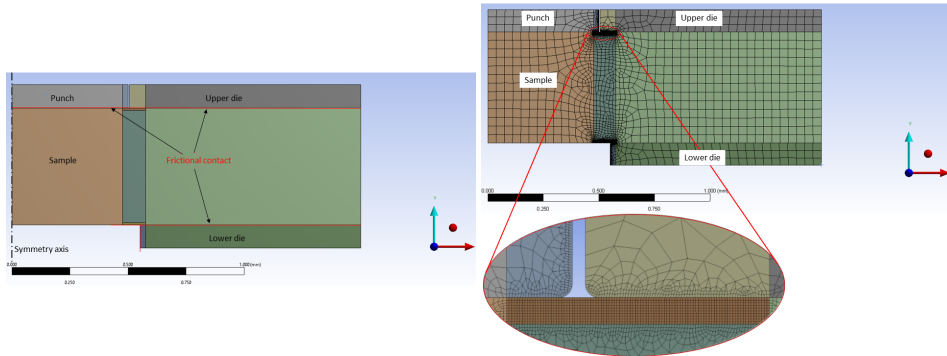


Figure 5.20: 2 dimensional finite element model of the shear punch prototype in Ansys. A wire mesh using 4 node and 3 node plane-182 elements are used with a finer allocation in the clearance region and the sample-die interaction areas. Adapted from [203].

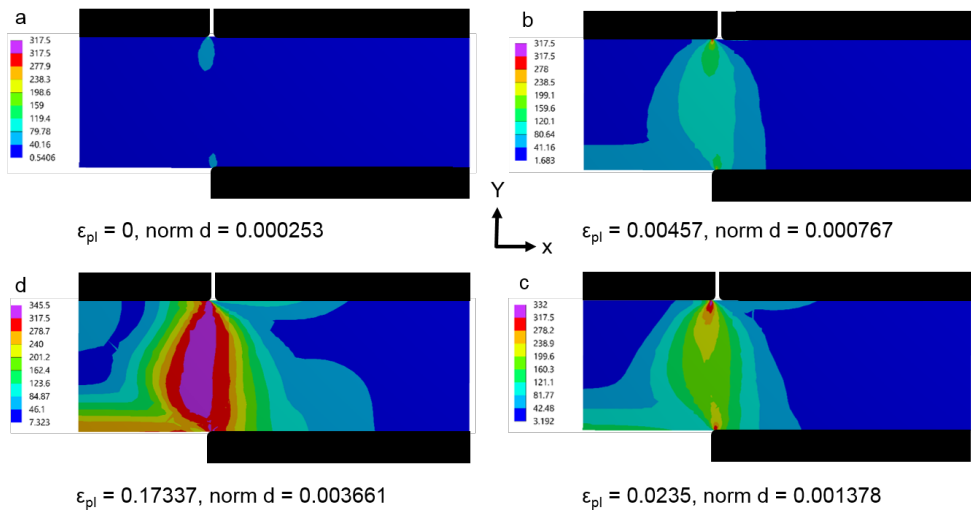


Figure 5.21: Results from the punch simulation performed in Ansys on a 3 mm W disk. The stages (a),(b),(c) and (d) represent elastic regime, yield point, sample yielding and plastic zone in the sample. The values listed show shear stress in the sample.

The point *a* represents a state within the elastic regime of the sample where the stress begins to penetrate through the clearance zone which can be recovered upon releasing the load. Point *b* marks the shear yield at the punch sample tip for the sample according to von-Mises criterion ($\frac{550}{3}$ MPa). As seen the entire sample is stressed along the clearance area between punch and die. Point *c* represents the state of the sample beyond yield point while point *d* is a stage where the equivalent stress which is greater than yield stress has spread through the sample thickness and this represents failure of the sample. Analysis of the directional stresses in the sample have shown a compressive stress on the punch sample

corner and the lower die - sample corner. In contrast the upper die sample corner encounters a strong tensile stress. This is shown in Figure 5.22 where the arrows mark the direction of stress in the sample.

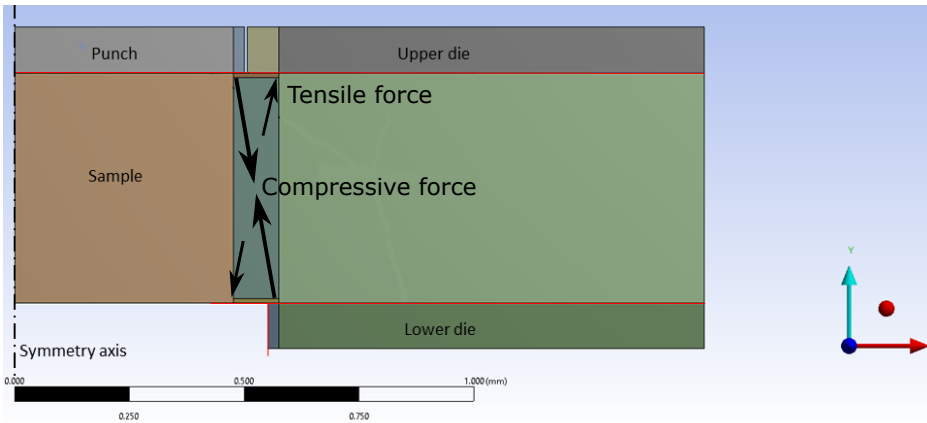


Figure 5.22: The sample has a compressive and tensile stress component which leads to a compound state of stress rather than pure shear adapted from [203].

The assumption of shear is considered within the clearance zone between the punch and die. The compound force behaviour within the clearance zone goes to prove that the stress states in a shear punch test are not pure shear but rather a combination of compressive, tensile and shear stress. The compound deformation nature of the shear punch arising from a mixture of shear, bending and tensile forces makes the process and failure difficult to predict. In turn the simulations have limited capability to predict strain at failure. The simulations also indicate to the possibility of bending at larger clearances ($>50 \mu\text{m}$) which would limit the clearance between punch and die to tight spaces for good experimental repeatability. Although the tight clearances would result in higher friction, increased wear and subsequently low punch/die lifetime.

5.5 Hot cells & radiation safety

The transport, storage, handling, investigation and disposal of radioactive substances is governed by special regulations which require monitoring and control. Strahlenschutzverordnung is a booklet published by the ministry, comprising of the free handling limits for most isotopes. This hard limit is set to quantify the maximum amount of radioactivity a material can accommodate for its release into the public sphere of life, while taking into account radiation hazard and public safety. An example is the naturally occurring ^{40}K having a limit of 10^6 Bq in total or a specific maximum activity of 10^2 Bq.g^{-1} as per the Strahlenschutzverordnung Table 1, appendix 4. If the activity of the sample is higher, special permits are required to store and handle the material. The hot material laboratory (HML) at Forschungszentrum Jülich has these special permits to handle radioactive materials within its enclosure. The license for handling radioactive samples is often limited by dose rates and/ or maximum activity limits which at the highest level is 10^{14} x of the free handling limit within areas of the HML, i.e. in the case of ^{40}K , the HML could handle upto 10^{20} Bq of total activity from ^{40}K . The radioactivity

limits for selected nuclides based on the different areas of the HML are shown in Table 5.3. Based on these limits, the total radioactive inventory is controlled inside the laboratory by radiation protection officers. As seen from the Table, ^3H has low limits as it can be released as

Nuclide	hot cells				active hall	
	solid dust) (Bq)	(no open source (Bq)	open source (Bq)	solid (dust) (Bq)	open source (Bq)	
^3H	2.5 10^{13}	2.5 10^{10}	2.5 10^{10}	2.5 10^{13}	2.5 10^{10}	
^{60}Co	1.0 10^{16}	1.0 10^{11}	1.0 10^{11}	1.0 10^{14}	1.0 10^{11}	
^{55}Fe	1.0 10^{17}	1.0 10^{12}	1.0 10^{12}	1.0 10^{15}	1.0 10^{12}	
^{65}Zn	1.0 10^{17}	1.0 10^{12}	1.0 10^{12}	1.0 10^{15}	1.0 10^{12}	
^{182}Ta	1.0 10^{15}	1.0 10^{10}	1.0 10^{10}	1.0 10^{13}	1.0 10^{10}	
^{184}Re	1.0 10^{17}	1.0 10^{12}	1.0 10^{12}	1.0 10^{15}	1.0 10^{12}	

Table 5.3: Maximum permitted licensed activity in HML for some expected nuclides based on the area and source type in Bq.

a gas and easily introduced into the environment. The closed solid sources such as irradiated W samples have higher inventory limits.

The hot cells within the HML are designed for highly active samples. They are large steel boxes or chambers, with 3 mm thick steel walls. Each cell has an internal volume of 2810 1680 1830 mm³ and is supported on a steel chassis which is placed on a set of rails as shown in Figure 5.23. The cells are further enclosed and sealed with lead bricks, thick concrete walls and maintained at a slight under pressure to avoid any chance of radiation or contamination release. The radioactive sample is handled, loaded and operated using a set of robotic manipulator arms which are operated from outside the cell. All activities can be coordinated through the window made up of borosilicate lead glass attached to front of the hot cells. The lead glass is used to protect the personnel from beta and gamma radiation while providing a view of the inside of the cells.

The testing of samples within the hot cells places additional constraints on the machines. Long cables, often greater than 5 m length are needed to overcome the circuitous route under and over the concrete shields. An example of the cable map for instrumented indentation machine designed in this work is shown in Figure 5.24. Cables are routed through the push fit end LEMO connectors which are vacuum sealed and recommended for use within the nuclear industry. The installation of long cables is usually accompanied with the degradation of signal quality over distance and connection terminals. This is checked post installation of the machines within the hot cells.

The robotic manipulator arms are designed to function similar to a human arm. They are mechanical in nature with 3-dimensional motion and a rotary screw operation function. The arm can handle a maximum weight of 60 kg using a centre hook and a maximum of 20 kg at full 5 m extension length. It has an active feedback function during operation which allows sensitivity of feel to operations performed. All tools which are needed during the operation of the machines within the hot cells were welded with two finger slot masks. The mask as shown in Figure 5.25 fits precisely onto the manipulator fingers and the tool or part can be accurately controlled.

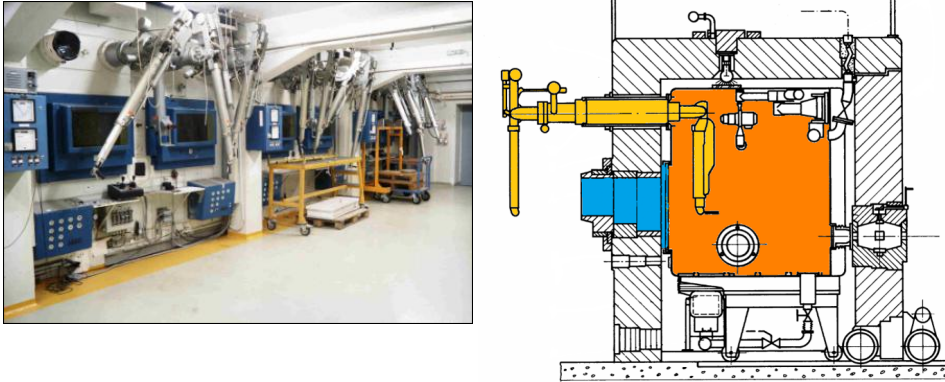


Figure 5.23: Hot cells in Forschungszentrum Jülich with the steel box in orange and enclosed with lead and concrete walls. The activities inside can be seen through a lead glass (blue) which is used to stop gamma rays and operations including handling of radioactive materials is performed using robotic arm manipulators (yellow).

An attempt has been made to remotely operate and control the machine, and the testing sequence as far as possible, however the loading and unloading of highly radioactive samples must take place inside the cells. The samples are introduced into the hot cells using lead shielded containers and the samples must be carefully lifted and placed into a sample holder for testing. Pneumatic suction tools are set-up for sample handling which can be suitably used with the manipulator arms. An example of this tool is shown in Figure 5.26, which can be suitably fitted with a variety of adapters for different sample geometries.

The handling of 3 mm disks is found to be difficult in spite of adapters and vacuum suction, which led to the development of special sample holders especially for shear punch testing. Post irradiation the samples are thereby handled as a whole and placed in the holder. The holders for shear punch is shown in Figure 5.27. The holder sits on the punch and acts as the lower die with an offset cavity for the sample placement. This offset is purposely calculated such that the 3 mm disk is located exactly at the centre for the punching to be performed. A hook shaped lock pin can be used to pick up the sample and rotate it for consequent punch tests on all four disks, while the die stays fixed. This ensures repeatability of the test without any die change inside the hot cells. Such adaptations are planned and are in the test phase for small scale testing of fusion radioactive materials.

The machines are to be loaded onto movable tables designed for the hot cells. An example of the table designed for the instrumented indentation machine is shown in Figure 5.28. A major advantage of the moveable tables is during loading and unloading of the samples. This being the precarious movement which needs most concentrated effort, the positioning of the table in direct convenient line of sight reduces the risk of error and need for rework. The table has four wheels and can be pushed into the line of sight using manipulators. Once the desired position has been reached a set of four screw driven foot stands can be deployed to hold the assembly in position. Damping material has been placed on the feet of the stands to soften the vibrations from the vacuum pumps in the cells.

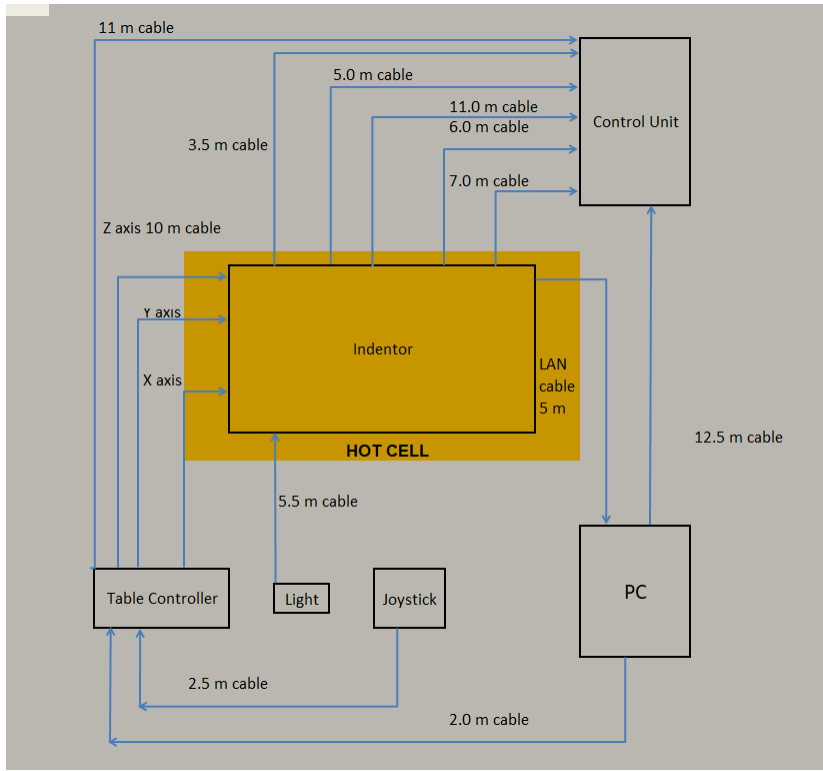


Figure 5.24: The cable diagram along with the placement inside the hot cells designed as part of this work. Cables lengths often longer than 5 m are needed for routing.

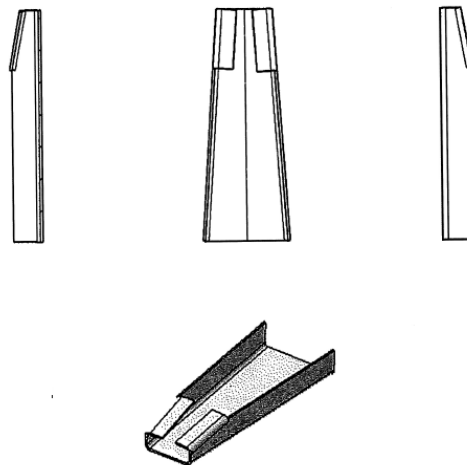


Figure 5.25: Manipulator finger masks which are welded on work tools and parts requiring movement for easier manipulator operation.



Figure 5.26: A vacuum operated pincer set for sample loading and unloading which can be suitably adapted onto the manipulator arms.

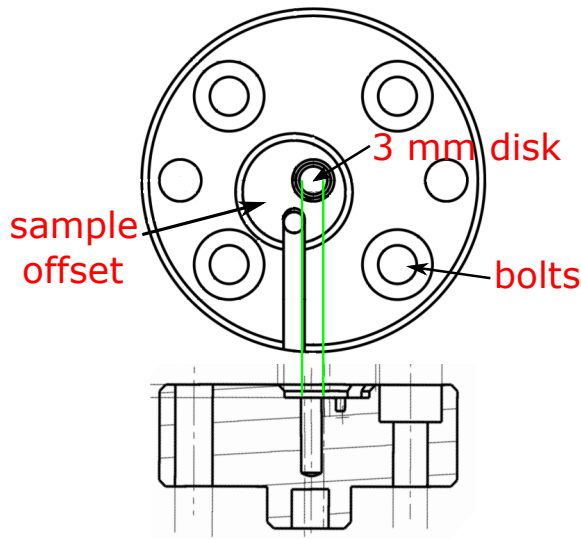


Figure 5.27: Sample holder with an offset cavity for the complete sample with 3 mm disks. The 3 mm disks are in the centre for the punch.

Another important adaptation to the hot cell functioning of testing devices is the inclusion of alternate calibration methods. Regular calibration is often demanded by testing methodology and poses a problem for machines out of reach such as inside hot cells. The machines are calibrated for design units such as the prescribed maximum incident force, force step and the travel of the head. These quantities are difficult to be precisely measured from outside the hot cell or through the lead window. While the fundamental quantities are difficult to measure, results can be used to compare against calibrated machines to check the accuracy and deviation of the machine. Thus standards corresponding to established high purity materials for various loads are installed alongside the machine inside the hot cells and tested based on the ISO methodology. Parameters are well established for the high purity materials and thus a direct comparison would indicate the deviation from the expected results. In the case of instrumented indentation Vickers hardness standard plates ranging from HV240 - HV720 are to be tested for a wide variety of forces. On the other hand the punch and tensile measurements would have standard high purity dog-bone samples which can be tested.

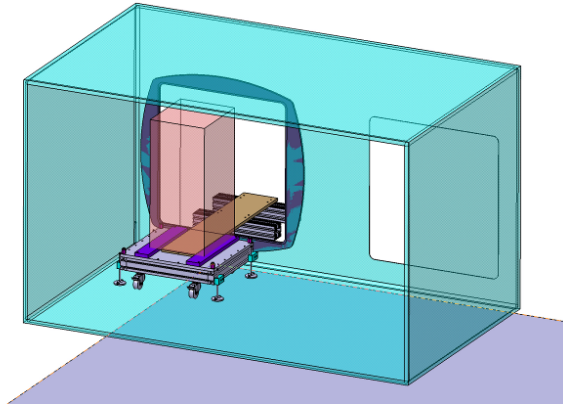


Figure 5.28: A moveable table designed for the instrumented indentation machine within the hot cell. Using the table, the machine can be conveniently moved into proper view for sample installation and suitable repair work if required.

Hot cells and hot material laboratories allow working and testing of radioactive materials to further research the properties of irradiation. However, these laboratories often need special tools and working strategies to prevent accidental radiation exposure to personnel or accidental release of activity into the environment. Small scale techniques are instrumental in lowering the radioactive inventory while obtaining engineering data from the materials. Within the scope of this work, shear punch, instrumented indentation and tensile testing methods are designed and adapted for hot cells application. High energy proton irradiated samples are active and would be tested on the installed machines within the hot cells. Each sample contains one tensile dog bone sample and four 3 mm disks. This provides a level of redundancy and repeatability to each irradiation.

Summary of experimental methods

In this work, potential techniques towards development of the methodology for cyclotron irradiation testing and post irradiation are developed. A nuclear approach is taken for the complete cycle of sample design, manufacture and post irradiation examination. The samples are designed to fit onto the solid target irradiation system at the cyclotron, while being adaptable to macroscopic testing and reducing overall radioactivity. Four shear punch samples along with one tensile test sample are combined in a sample casing per irradiation. Two post irradiation testing methods; shear punch and instrumented indentation are set-up for hot cell application. Modifications and adaptation are engineering for special radioactive environment.

Chapter 6

3 MeV proton irradiation¹

Prior to high energy proton irradiations, a low energy proton damage on W samples was considered. This has the advantage that if the energy of the protons is kept below 3 MeV, post irradiation the samples are under the free handling limit and not radioactive [218]. This allows for the testing of samples without any special radioactive requirements. Also, there is no cooling time or waiting time post irradiation for sample analysis. Additionally, the low energy proton damage would create a pure displacement damage scenario which can be directly compared with heavy ion damage.

Controlled experiments using proton beams to emulate neutron damage have shown close correlation in steels [78]. Benchmarking of damage produced on SS316 and SS304 steels was carried out to understand the extent of emulation in irradiated micro-structure, radiation hardening and radiation induced segregation [129]. The low energy (3 MeV) proton damage constructively replicates the neutron behaviour in steels. Attempts are only now being made on W [180] with similar irradiations. The study was concentrated on the radiation lattice defects observed in-situation during irradiation upto damage doses of 0.3 dpa and no post irradiation testing is reported. In our work, a range of damage doses were induced on the sample and post irradiation indentation testing was performed to conclude the effects of radiation hardening from 3 MeV protons on W. The chapter starts with a description of the sample and subsequently the irradiation methodology. Results from post irradiation instrumented indentation testing are described and compared with heavy ion damage results. Finally, a discussion highlighting the difference created by combined damage as against pure displacement damage is described.

6.1 3 MeV damage

3 MeV protons have a range of 27 μm in W as shown in Figure 6.1. Initially the energy lost from the proton is due to electronic losses and as such produces low vacancies from collisions. As the energy decreases, the proton slows down and come in contact with nuclei which is seen by a sharp rise in the energy loss in the Bragg peak. This is also seen in the number of vacancies per ion which rises sharply as seen in Figure 6.2. Similar to the high energy protons, the range of investigation for 3 MeV protons in W is limited to the area preceding the Bragg peak, i.e. 15 μm as shown by the shaded region in 6.1. This corresponds to 2 - 3 grains of W. The limitation is placed till a linear increase in the cumulative vacancies per ion is seen as shown in Figure 6.2. Such a constant damage ensures that the post irradiation testing doesn't

¹This chapter has been submitted in part as an article to Nuclear Materials and Energy, (<https://doi.org/10.1016/j.nme.2020.100776>)

encounter any sudden variations in damage density, similar to neutron irradiation. The

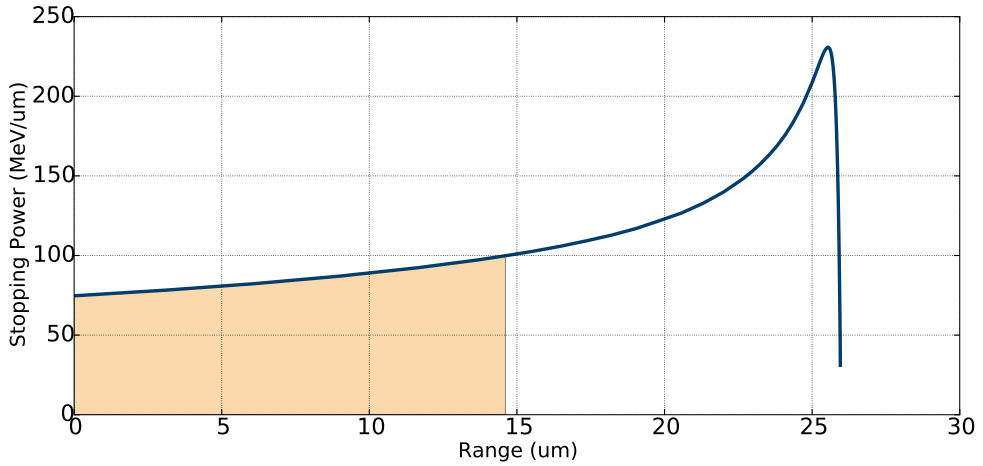


Figure 6.1: Range of 3 MeV protons in W, with the range of investigation being the plateau prior to the Bragg peak highlighted.

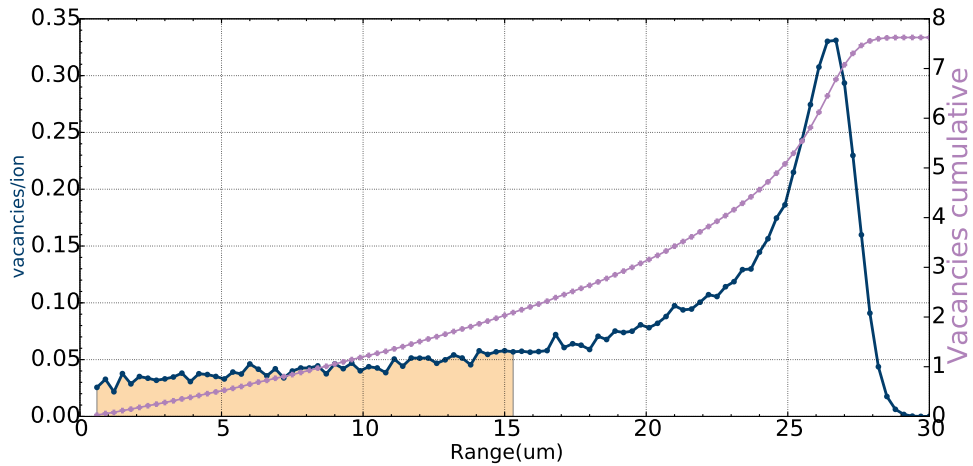


Figure 6.2: Vacancies created per ion per unit range and cumulative for 3 MeV protons on W calculated using the quick KP method in SRIM2008 [126].

displacement damage from 3 MeV protons as compared to a 20 MeV self ion W^+ damage can be visualised in 3d using SRIM2008 [126] as shown in Figure 6.3. A difference in the range can be immediately observed between self ion damage and 3 MeV proton damage. The self ions of 20 MeV W^+ penetrate upto 2 m while the proton has a Bragg peak at 25 m. Another important aspect which is observed is the peak damage slowly building up to the Bragg peak in the case of 3 MeV protons, i.e., the intensity of the 3 MeV proton damage is extremely strong in the Bragg peak as compared to the range of the ion leading to the Bragg peak. Self ions on the other hand have a bomb like effect, where intense damage is created within a small

volume or range. Thus, effectively limiting the range of investigation to 15 μm for 3 MeV proton damage ensures against influence from the Bragg peak.

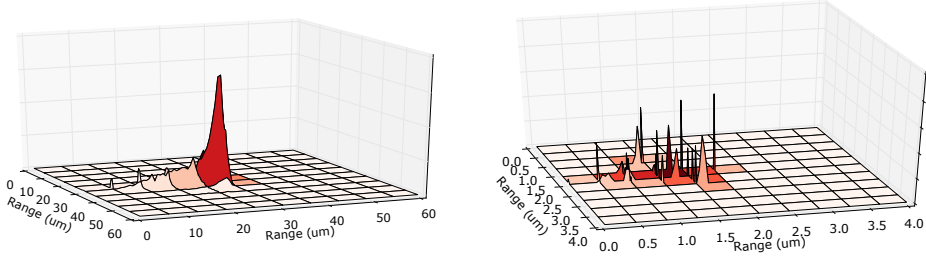


Figure 6.3: The 3 MeV proton damage in W on the left visualised in 3 dimensions and compared against a 20 MeV self ion damage on the right, plotted using the 3d displacement damage option in SRIM2008.

The damage calculation was performed according to the recommendations by Stoller et al. [219], using the quick Kinchin and Pease option and a displacement threshold energy of 90 eV for W [123] for a total of 99999 ions in SRIM2008 [126]. However, as the damage within the first 15 μm is considered, the vacancies per ion () upto that range using the vacancy file was used as an estimate. The damage was then calculated using the Equation 6.1, where N is total number of incident protons on the sample and $A d$ is the irradiation volume.

$$dpa = \frac{N}{6.32 \cdot 10^{22} A d} \quad (6.1)$$

As seen from the Equation, a concentrated damage volume would permit a higher damage rate and in turn larger damage doses on the sample. A new micro beam spot focus was recently installed on the beam line for ion beam analysis at the 1.7 MeV tandem accelerator. Three tunable quadrupole magnets focus the 5 mm diameter ion beam and have the ability to converge them to sizes between 2 \times 2 mm and 200 \times 200 μm , thus leading to higher damage rates. The beam spot size is adjusted using different magnetic configurations and a pico-ampere meter records the charge. A correction for backscattered electrons registers the exact current on the sample by secondary electron suppression. The sample is mounted on a sample holder which is loaded on a 3 linear and 1 rotational axis manipulator. The manipulator can travel in steps of 10 nm driven by piezo-electric motors. The entire sample assembly with the manipulator is fixed within a vacuum chamber operating at pressures lower than 10^{-7} mbar, brought about by a pre-pump and a turbo pump. The irradiation can be viewed using a telecentric observation camera which can also record the beam spots by positioning it on a scintillating material. The temperature during irradiation can be measured simultaneously using a K type thermocouple, attached to the back of the sample holder. The chamber is specifically designed for ion beam analysis and thus the detectors need to be dismantled prior to the irradiation itself.

The samples were cut, cleaned and polished as described in section 5.2. Two different types of sample geometries were irradiated as shown in Figure 6.4. The geometry shown on the left is a 5 mm thick pure W sample with sides of 10 \times 10 mm. The top side of the sample is polished to a mirror like finish to $Ra < 1 \mu\text{m}$ for exposures. These samples are regularly used in plasma exposures. The second sample is the same as that designed for high energy proton exposures, 500 μm thick and would also be mirror polished to 1 μm for irradiation.

The samples were loaded on the sample holder as shown in Figure 6.5 with a scintillator coated sample to obtain the beam spot size. The spot sizes were checked and registered a deviation of less than 5 pixels or 25 μm in either X or Y direction.

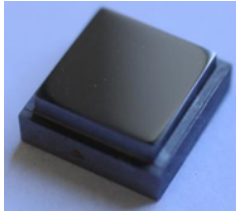


Figure 6.4: Two sample geometries were installed and irradiated with 3 MeV protons. The first is an established plasma exposure sample geometry while the geometry on the right is for comparison with high energy proton irradiations.

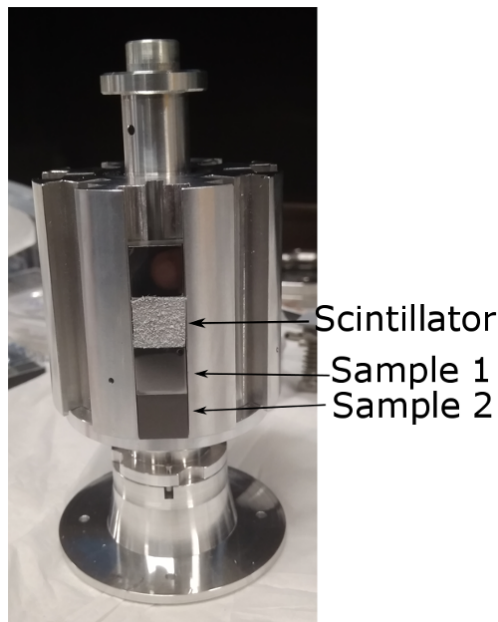


Figure 6.5: The samples were loaded on to the sample holder with a scintillation sample next to it in order to obtain the beam spot size.

By projecting the beam onto the scintillator and adjusting the magnetic configuration, the beam spot size can be viewed by the tele-centric camera and through the manipulator can be focussed onto the sample spot without any configuration changes. The sample holder is designed to hold multiple samples at the same time and can be rotated to irradiate multiple samples without breaking the vacuum. The thermocouple was attached to the base of the sample holder.

6.2 Bragg peak effects & heat loads

The samples were not connected to any external heating and as the manipulator can't exceed 60°C, the irradiation temperature is governed by beam heating, where the current was lowered in order to maintain 60°C. In order to quantify beam heating, Ansys calculations were performed using a constant heat load of 1.5 W (3 MeV 500 nA) on a beam spot size of 300 μm \times 300 μm . The beam spot is the heat source with an initial temperature of 22°C and the rear end of the sample is a sink which can reach a maximum temperature of 60°C. A three point linearly varying thermal conductivity was used for W as a material input and the results are shown in Figure 6.6. The image shows the beam impacting on the sample surface with a view into the perpendicular cut of the sample surface.

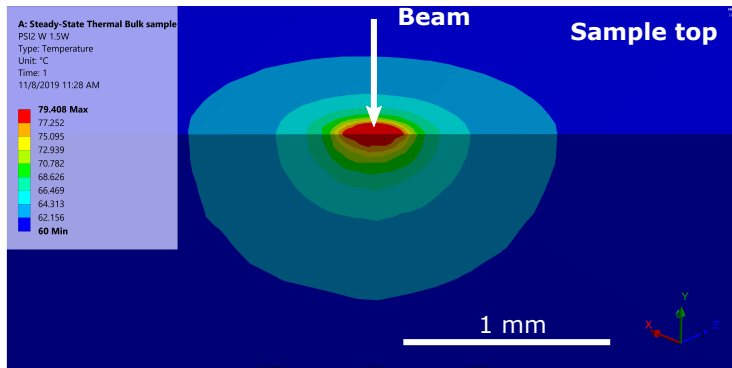


Figure 6.6: Temperature profile calculated by Ansys for a 3 MeV proton beam of 500 nA current on the W sample.

The temperature profile calculated by Ansys shows a rise in temperature to 79.4°C from beam heating at the irradiation spot. Just outside the beam spot, the temperature drops to 68.5°C. The temperature however, drops sharply to 60°C within a distance of 1 mm to the beam spot centre. This is due to the excellent thermal conductivity of W which keeps the sample at sink temperature. Initially, radiative cooling was included in the calculations, however no effect was seen from its inclusion. The irradiation dose and currents for the first sample W_nano1 are shown in Table 6.1. As the first sample was irradiated, formation of a blister was seen via the tele-centric camera. This blister was initially seen to grow and slowly stabilised with fluence. Post irradiation, these blisters were large enough to be seen with the naked eye and corresponded to the beam spot. They were examined under a scanning confocal microscope (Micromesure 2 from Stil SA) for closer observation. This technique uses the reflected white light from the sample to conduct contact-less measurement on the surface. The optical profilometry measured image is shown in Figure 6.7, where the blisters correspond to the irradiation beam spots.

The blisters show large cracks on their surface as a result of the blister formation. Altitude scans were performed on a linear path of spot 1, spot 2 and spot 3 which is shown in Figure 6.8. The altitude measurements on the Y axis are relative to the neighbouring measured flatness. Therefore the blister height measures between 10 - 25 μm . While a correlation might be noticed between the damage doses and the blister height for spots 1, 2 and 3, this pattern wasn't observed for all irradiation spots. A 3 dimensional representation of the blister also measured by optical profilometry shows an exact match to the irradiation spot. The very top

6.2. Bragg peak effects & heat loads

Spot	Net charge (C)	Beam spot size(m)	Avg. beam current(nA)	dpa
1	1070	200 220	280	0.2
2	4270	200 220	500	0.8
3	2135	200 220	600	0.4
4	1070	200 220	600	0.2
5	5451	440 440	600	0.2
6	9885	440 440	500	0.36
7	5950	400 310	550	0.35

Table 6.1: Irradiation characteristics for beam spots 1 - 7 on sample W_nano1. The beam spot areas are measured using the scintillator coated sample.

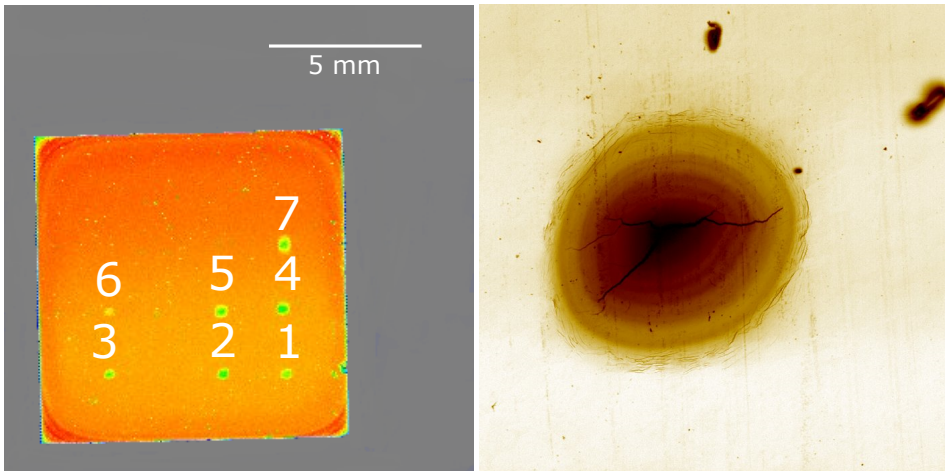


Figure 6.7: Optical profilometry measurements of the sample and a blister. The blisters correspond to the irradiation beam spots and large cracks are seen on the blister.

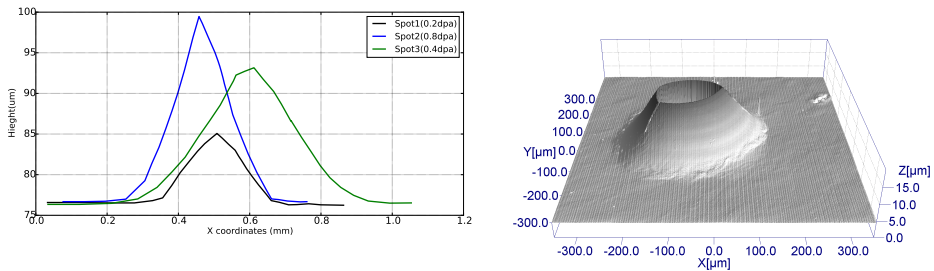


Figure 6.8: Altitude scans of sample irradiation spot 1, 2 and 3 with a 3 dimensional reconstruct of irradiation spot 1.

of the blister is cut as the sensitivity of the measurement decreased significantly in this area. This could be a result of the cracks which seem to originate from the top centre of the blister as shown in Figure 6.9.

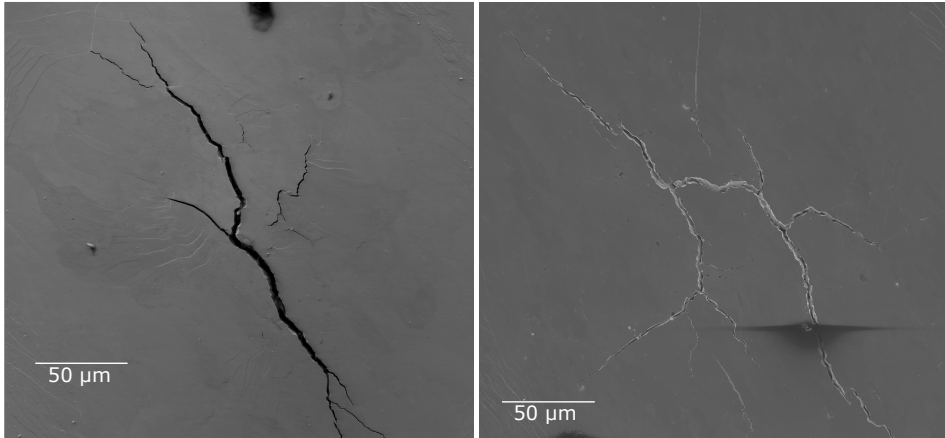


Figure 6.9: Cracks seen on the surface of the blister on the irradiated beam spots.

Similar results have been seen in a previous study [98] where they imply higher penetration depths from higher energies are responsible for the blistering. 3 MeV protons have a range of 25 μm and thus can't escape or diffuse out of the surface, in turn leading to the formation of blisters at low fluxes. With low energy plasma, protons often travel several μm , experiments with H plasma [220], [221], [222] have shown that the diffusion of protons in W is relatively high. The diffusion constant in W is $D_F = 4.1 \cdot 10^{-17} \text{ m}^2 \cdot \text{s}^{-1}$ [223] and grows exponentially with temperature. At low irradiation temperatures, the diffusion still enables protons to diffuse into nearby damage induced vacancies near the Bragg peak. The vacancies would combine and slowly grow to a large bubble which subsequently pushes material upwards and results in a blister. To observe the void bubble, a focussed ion beam was used to cut through the sample and is shown in Figure 6.10. The void corresponds to the area just past the Bragg peak, within the range of proton diffusion and measures between 1 - 1.4 μm in width. This pushes the material upwards which produces cracks and eventually the blister. Initially, the blisters were seen to rapidly grow on the tele-centric camera, which stabilises with progress through the irradiation. This could be thus, temperature dependent.

Segev et al. [224] also observed a threshold dose of $3 \cdot 10^{17} \text{ protons} \cdot \text{cm}^{-2}$ for polycrystalline W which was seen to be independent of irradiation temperature. The blistered samples were found unsuitable for indentation experiments. They displayed sudden drops in displacement and thus new irradiation beam spots were undertaken as described in Table 6.2. As understood from the initial growth and subsequent slowing down of the blister, the second experiment was conducted with high initial starting current density of upto $1290 \text{ A} \cdot \text{cm}^{-2}$. This leads to a rapid increase in the initial temperature and increases the diffusion of protons into the bulk substantially. Similar focussed ion beam cuts were carried out on the irradiated spots of the second sample. No big voids were noticed. However, indications of void motion about to combine was observed as a streak. This was just past the Bragg peak as seen for spot 5 in Figure 6.11. This technique was indeed able to suppress blister formation. A black coating was noticed post irradiation on the beam spot. This was confirmed to be ion assisted carbon deposition during irradiation by using nuclear reaction analysis. The extent of carbon

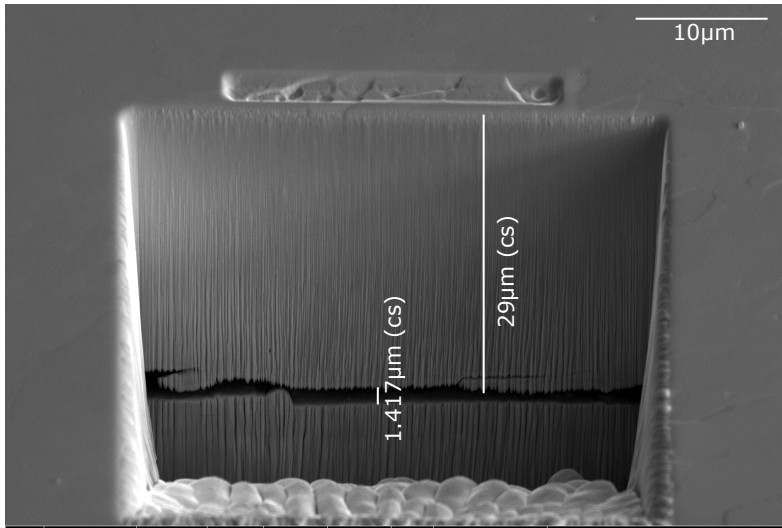


Figure 6.10: A focussed ion beam cut through a blister on the W sample showing a large void in the middle of the sample.

incorporation into the sample was found to be below 5 nm and it persisted even with vacuum conditions at $1 \cdot 10^{-7}$ mbar within the sample irradiation chamber. As the irradiation is over a range of 27 μ m, the 5 nm graphite layer is considered ineffective to create any significant change in the sample as compared to proton irradiation. A sample was further irradiated using the doses as shown in Table 6.3 The samples were further subjected to transmission electron microscopy (TEM) to comprehend the type and extent of damage created.

Spot	Net charge (C)	Beam spot size(μ m)	Avg. beam current(nA)	dpa
1	980	240 310	570	0.1
2	100	240 310	530	0.01
3	300	240 310	547	0.03
4	1970	240 310	573	0.2
5	2950	180 180	556	0.67
6	1539	180 180	444	0.35
7	5250	300 250	600	0.51

Table 6.2: Irradiation characteristics for beam spots 1 - 7 on sample W_nano2. The new sample was irradiated using high starting beam currents, which was gradually lowered to dispense off with the blisters.

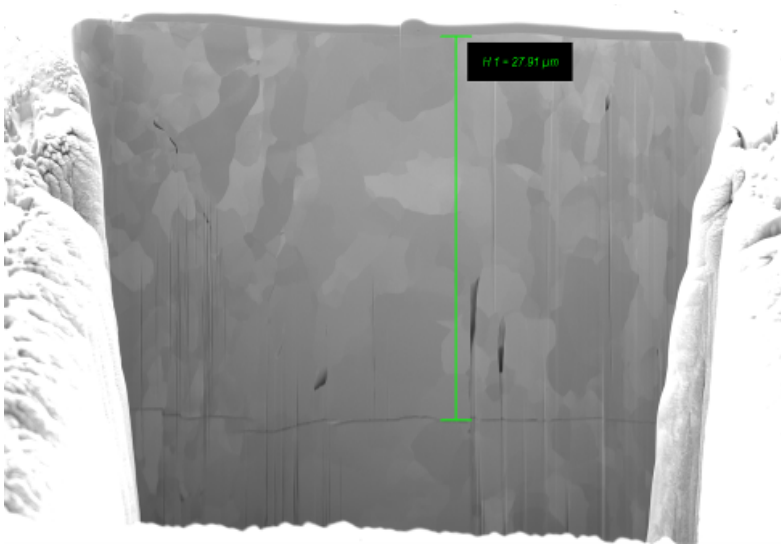


Figure 6.11: A focussed ion beam cut on the second irradiated sample with high starting currents to suppress blister formation.

Spot	Net charge (C)	Beam spot size(m)	Avg. beam current(nA)	dpa
1	7600	300 300	640	1.0
2	3800	300 300	470	0.5
3	760	300 300	500	0.1

Table 6.3: Irradiation characteristics on W samples for TEM characterisation. Three doses of 0.1, 0.5 and 1.0 dpa are undertaken to comprehend the changes in micro-structure. Similar to sample W_nano2, high starting currents were used to avoid any blister formation.

6.3 Post mortem analysis - TEM

Recrystallised W was additionally irradiated to understand the impact of 3 MeV protons on W. 300 300 m spots were carried out to damage doses of 0.1, 0.5 and 1.0 dpa. Post irradiations the samples were prepared for transmission electron microscopy (TEM) by cutting a 80 nm thin film of irradiated W. The focussed ion beam method of cutting was applied in stages to cut a thin slice (lift out) of irradiated material at the beam spot. Further, the liftouts were cleaned with 30 kV Ga⁺ ions till transparency was seen through shining a 10 kV electron beam. Finally, a soft polishing step using 5 kV Ga⁺ ion beam was used prior to TEM. An unirradiated spot on the sample was also cut and polished using the same technique to quantify the background cutting damage on the sample for comparison. The results from the TEM are shown in Figure 6.12

The microscopy was performed in bright field conditions. The image on the extreme left shows the unirradiated liftout with FIB cutting damage on it. Minuscule loops are seen to be formed from the FIB cutting which persist inspite of repeated polishing steps by Ga⁺ ions. A difference can be noticed on the 0.1 dpa damage dose image. A general cloudiness

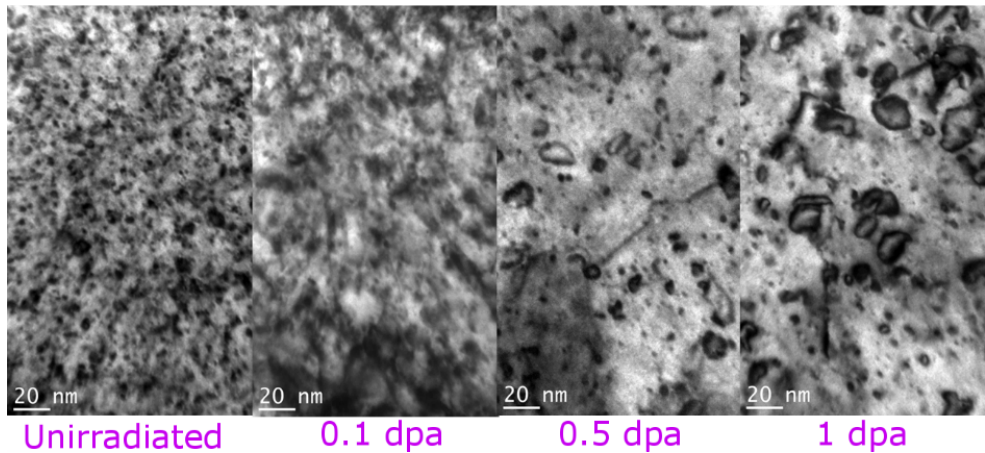


Figure 6.12: TEM images of damage induced from 3 MeV protons with increasing damage dose. The unirradiated picture is shown for comparison of proton damage with the cutting induced damage.

is seen for doses of 0.1 dpa levels where the dislocations loops are larger than the general black dots seen in the unirradiated image. With an increase in the damage dose, the loops are seen to grow larger. This can be clearly identified in the 0.5 dpa dose image. Further growth is seen in the 1.0 dpa damage dose image. The dislocation lines and loops are seen to be uniformly distributed with no presence of voids. Furthermore, no voids were detected using the under-over focus method within the irradiated sample.

A counting of the dislocation loops for 0.1, 0.5 and 1.0 dpa damage doses were undertaken using ImageJ software [225]. At least two bright field images of 500 500 nm were inverted and counted using the grey scale counting technique described in [226]. The counting principle is based on a noise tolerance level of the grey scale and its deviation within the image. Thus, any local maxima in the image is counted as a dislocation loop. By changing the grey scale value till all visible loops within that area, the loop density is estimated. As seen in the images of 0.5 and 1.0 dpa damage doses, the proton induced damage loops can be better judged against the background FIB cut loops, which is far more difficult to judge at 0.1 dpa damage dose level. Using a loop free area to check for the variation in grey scale, the uncertainty of this measurement is derived and added to the measurement. The dislocation loop density for the three doses is shown in Figure 6.13

Large errorbars seen in the loop densities due to the influence of FIB damage in the images. Also, the use of bright field imaging technique to count loops results in errors. However, in general a weak trend of decreasing loop density and saturation at doses below 1 dpa can be noticed. A similar trend was noticed using in-situ TEM with proton irradiations in [180], where a gradual decrease in the loop density and saturation was noticed post 0.3 dpa damage dose for pure W samples at 350°C. Self ion irradiations have shown an increase in the loop density with increasing damage dose [226].

The images were also converted into binary format and analysed for dislocation loop diameter sizes using the particle finder option of ImageJ software as described in [226]. The particle areas were obtained and under the assumption that the loops are circular, loop diameters were obtained using $d = \sqrt{4A/\pi}$. The loops with diameters below 1 nm were avoided due to the noisy background from FIB cuts. The remaining loops were binned in

groups between 1 - 10 nm and above 10 nm into a single group as shown in Figure 6.14.

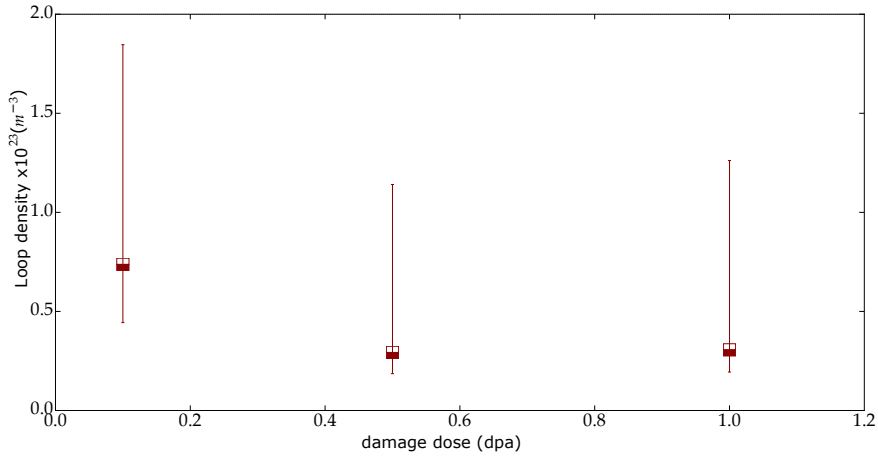


Figure 6.13: Loop density estimation for the three damage doses of 0.1, 0.5 and 1.0 dpa based on the grey scale reduction technique from [226].

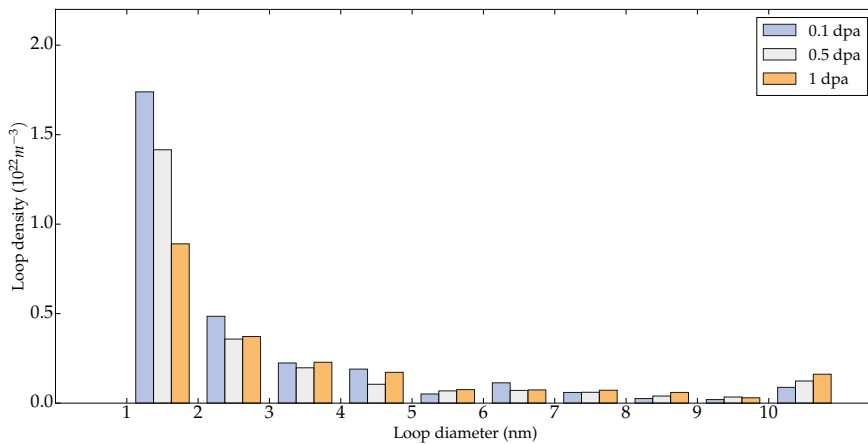


Figure 6.14: Loop diameter histograms for 0.1, 0.5 and 1 dpa damage doses on W from 3 MeV proton irradiation.

The histogram agrees well with Figure 6.12. As the damage dose increases, larger loop sizes are seen. 1 dpa damage dose is observed to have more number of larger sized (>10 nm) dislocation loops as compared to 0.1 dpa. This could be the result of smaller loops combining to form large loops. A steady decrease of 0.4×10^{22} is noticed for loop diameter of 1 - 2 nm between 0.1 and 0.5 dpa, and 0.5 - 1.0 dpa. Similar to the previous study [180], loops were observed at $a/2 \langle 111 \rangle$. This work being a pilot project, a burger vector analysis was not performed, however no large voids were observed.

6.4 Post mortem analysis - IIT

Post irradiation, hardness measurements were performed on the un-blistered W sample, W_{nano2}. As the micro-indentation measurements have a maximum depth of 2 μm , both micro and macro indentation (depth 15 μm) were performed on the same irradiated beam spot at room temperature. This allows for the direct comparison of the methods as well as a comparison between proton damage and self ion damage (based on nano indentation) indentation measurements. On average a 15 N force on instrumented indentation produces an impression of 100 \times 100 μm on the sample surface while traversing a depth of 15 μm . Thus, any irradiation spot size having dimensions of 150 \times 150 μm and above would qualify for testing.

Micro indentation was performed on an Agilent G200 Nanoindenter using a diamond Berkovich indenter tip. The continuous strain rate method of measurement as illustrated in [227] was applied at a strain rate of 0.05 s^{-1} . All measurements were parametrised to a maximum depth of 2 μm and arranged into arrays of 5 \times 5 (25) indents within the beam spot as shown in Figure 6.15. A distance of 20 μm was maintained between two indents which complies with the ISO norm for 10x distance between two successive indents. Pre-indentation calibration was carried out on a fused silica sample, from which the machine stiffness was calculated. The required inputs for micro-indentation are tabulated in Table 6.4. A force-displacement curve was obtained from each indent. Considering the influence of surface effects and polishing, the range between 500 - 1500 nm was considered for extracting data. The frame stiffness is adjusted for a constant indentation modulus and the average of 25 indents is reported as the indentation hardness with errors.

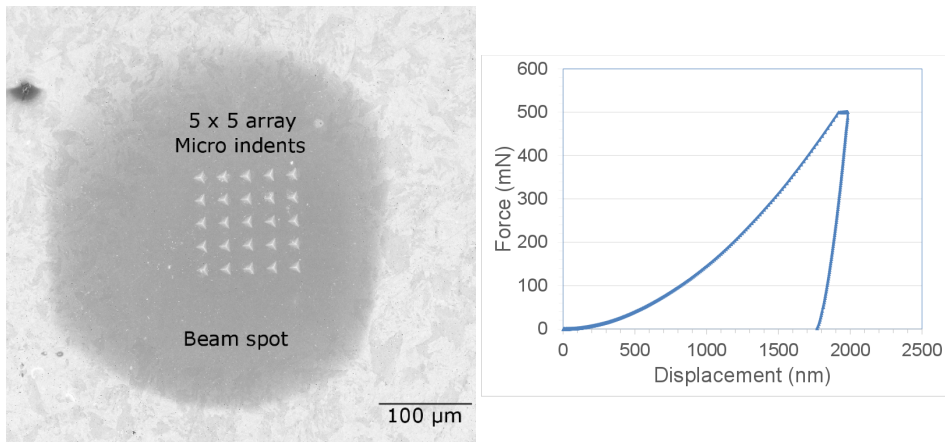


Figure 6.15: An array of 5 \times 5 indents of micro-indentation on the irradiated beam spot seen in dark grey and the force displacement diagram.

Macro-indentation was performed on the exact spots as micro indentation. The indentation was performed using a Zwiki ZHU2.5 machine at a maximum load of 15 N. A pyramidal diamond tip Vickers indenter was used for impression which resulted in an average indent size of 100 \times 100 μm . As the depth is 5x of micro-indentation, no influence of the previous indent was considered. The machine compliance was performed on a SS316L sample prior to the actual testing for loads upto 20 N indent force. Mono-cyclic loading with parameters at a load application rate of 0.133 N/s to a maximum of 15 N with a holding time of 10 s at maximum

S No.	Settings	Input
1.	Maximum depth	2000 μm
2.	Frequency target	45 Hz
3.	Strain rate	0.05 s^{-1}
4.	Harmonic displacement target	2 nm

Table 6.4: Necessary inputs for the micro-indentation measurements on irradiated W sample.

load was performed. The load-displacement curve was recorded for the mono-cyclic indent and is shown along with the scanning electron microscopy image of the indent in Figure 6.16. The load removal was performed at 2 N/s and according to the standard DIN EN ISO14577 [190], 95 - 50% of the unloading curve is fit using the Levenburg-Marquardt (least square) fit [228]. Using the same methodology, three indents are performed on the unirradiated portion of the sample. This is to determine a 0 damage dose unirradiated sample hardness comparison. Additionally, as only one indent per irradiated beam spot is possible, the error in the case of macro indentation is adopted from the unirradiated indent calculations of 20% error. Similarly, the beam spot is estimated using scintillation crystal pixels which results in an error of 5 pixels.

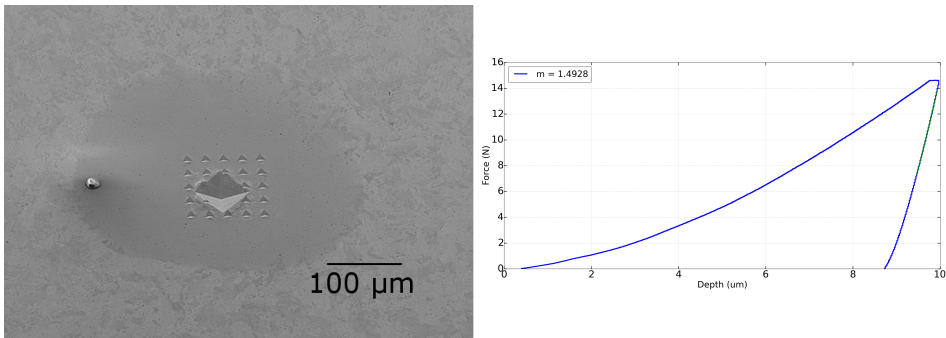


Figure 6.16: A macro-indent on the irradiation beam spot along with the micro indents and the force displacement diagram.

The results of both indentation methods are plotted and compared in Figure 6.17. Micro and macro indentation measurements show similar features of a rapid rise in hardness with initial damage dose and then a quick saturation. Within an initial damage dose of 0.01 dpa , the hardness is seen to increase by 0.8 GPa (15% increase). By increasing the damage dose to 0.03 dpa , the hardness again increases by 0.5 GPa for micro-indentation and 1 GPa for macro-indentation. Post 0.03 dpa damage dose, not further increase in hardness was observed within statistical reasoning and a saturation irradiation hardness of 7 GPa is observed. It is also noted that the macro-indentation has good agreement with micro-indentation method, which is highly sensitive and uses a continuous measurement. A higher unirradiated and irradiated hardness measurement for micro-indentation as compared to macro-indentation hardness measurements within error bars is observed. This is the result of a size effect with

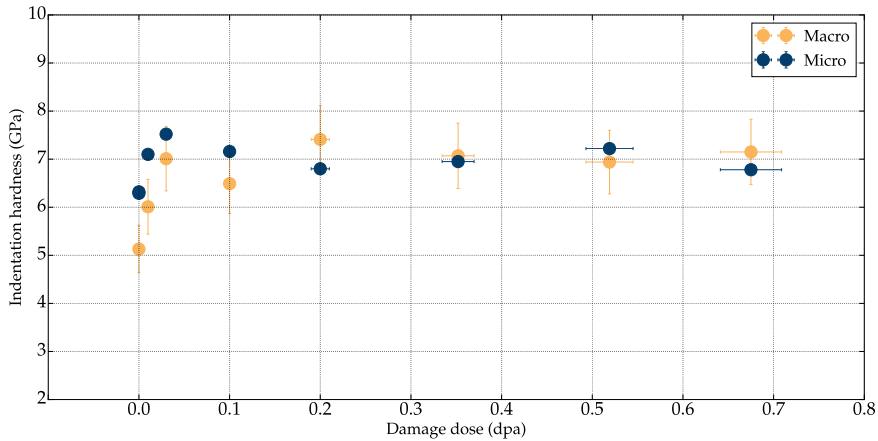


Figure 6.17: A comparison of the results of micro and macro indentation conducted on the same beam spots for 3 MeV irradiated W.

increasing depth as described by Nix and Gao in Equation 6.2 [229].

$$\frac{H}{H_0} = 1 + \frac{h}{h} \quad (6.2)$$

H is the hardness at the given depth of indentation ' h ', H_0 is the macroscopic hardness of the material at infinite depth and h is the characteristic length for the material. The size effect can be seen in the case of thin films and is seen to reduce to bulk properties after a few μm of range. Thus, the micro-indentation measurements would naturally result in a higher hardness as compared to the macro-indentation measurements. This difference seems to disappear at higher doses, it may be due to the radiation effect undermining the size effect. However, due to the large uncertainty, no conclusion could be presently drawn.

The TEM results indicate a saturation in loop density, however the loop sizes continue to grow even upto 1 dpa. In conjunction with the hardness results, it stands to show that the dislocation loop density plays a larger role as an obstacle as compared to the dislocation loop size. Hu et al. [159] has attempted to further show that dislocation loops are weak obstacles to dislocation plane motion, especially when compared with voids and precipitates and thereby could explain the saturation seen in irradiation hardening from 3 MeV protons.

Subsequent to large thicker sample irradiations, 3 MeV proton irradiations were also performed on 3 mm diameter 0.5 mm thickness, disk samples. This was done with the objective of having a direct comparison to the cyclotron irradiated disk samples. In order to obtain multiple indentation measurements, the beam spot size was increased to $2 \text{ mm} \times 2 \text{ mm}$. This is however at the cost of lower damage rates. The irradiation beam spot size was changed using the magnetic fields and thereby the focussing of the beam. It was measured using a scintillator as shown in Figure 6.18.

Four samples of 3 mm diameter disks each were irradiated to doses of 0.005 and 0.01 dpa damage doses at dose rates between $6 - 9 \times 10^7 \text{ dpa/s}$ against $1 \times 10^5 \text{ dpa/s}$ with micro-spots. The irradiation temperature was simulated to be 350 K . Similarly as before, post irradiation the samples were tested on the Zwick instrumented indentation machine to loads of 15 N and a waiting time of 12 s at maximum loading. As the depth of 3 MeV protons in

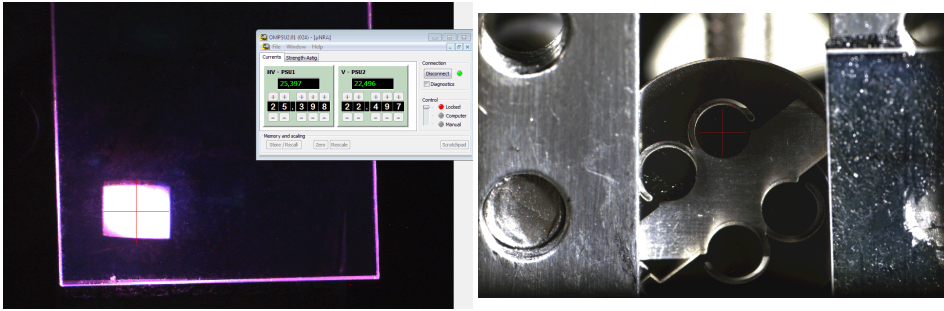


Figure 6.18: Beam spot as seen from the scintillator and placed on a 3 mm disk sample. Larger beam spots were attempted on the 3 mm disk samples to apportion multiple macro-indentations on the beam spot area.

W is 27 μm and the sample thickness is $> 300 \mu\text{m}$ (i.e. $> 10\times$ proton range), the rear side of the sample was considered to be unirradiated and unaffected by proton damage. Indentations performed on the rear side of the samples are presented as unirradiated estimates. These indentation results are given in Table 6.5. The errors shown correspond to standard error estimated from the mean of 8 indents.

Dose	indentation hardness(GPa)		HV1.5	
Unirradiated	5.56	0.24	4.37	0.07
0.005 dpa	6.13	0.23	4.44	0.05
0.01 dpa	6.23	0.20	4.92	0.02

Table 6.5: Estimated indentation hardness and measured Vickers hardness for a maximum load of 15 N on 3 mm disk samples irradiated to 0.005 and 0.01 dpa for comparison with cyclotron irradiations. The man of the tests along with the standard error of the mean is listed in the Table. An immediate jump in hardness is noticed even at low doses of 0.001 dpa damage.

An irradiation hardening is clearly noticed even at low doses of 0.005 dpa. This could be accounted by the immediate formation of dislocation loops which act as obstacles to dislocation motion. An increase of 0.57 \pm 0.33 GPa is seen between unirradiated and 0.005 dpa dose. The increase in hardening doesn't increase immediately between 0.005 and 0.01 dpa. The indentation results are in agreement with the 5 mm thick samples which also display an initial irradiation hardness jump of 0.8 GPa for 0.01 dpa. Subsequent irradiations are needed to investigate the propagation of irradiation hardness for 3 mm disk samples. However, as seen from the 5 mm thick samples, a saturation around 0.03 dpa is expected.

Summary of 3 MeV irradiation

In a pilot experiment, W samples were irradiated using 3 MeV protons at temperatures of 79°C and dose rates between $1 \cdot 10^5$ dpa/s (using micro spots) and $6 \cdot 10^7$ dpa/s (using larger spot size) to doses of 1 dpa. The high dose rate experiment is comparable to self ion

damage experiments. Initial observation of blisters are subdued using high (700 nA - 1 A) starting currents. TEM investigations performed on 0.1, 0.5 and 1 dpa dose show dislocation loop formation and growth in size with dose upto a dose of 1 dpa. The loop density shows indications of saturation with dose. This relates well with indentation measurements, which show irradiation hardening of 1.3 GPa and subsequent saturation at 0.03 dpa. Close agreement in hardness increase is seen between the high and low dose rate irradiations upto 0.01 dpa. Further experiments are scheduled.

Chapter 7

16 MeV proton irradiation

High energy protons can tunnel through the Coulomb barrier and induce nuclear reactions. Cross-sections for the neutron emission reaction (p,xn) on W are seen to get significant early on around 4 MeV. While (p,n+p) and (p,) reactions start to get significant for medium and heavy elements above 12 MeV. Through careful selection of the appropriate range of energies, the nuclear reactions can reproduce similar transmutational changes as neutrons as detailed in [61]. While 30 MeV proton irradiation is estimated to simulate a close approximation for the fusion neutron damage (see section 3.4), lower energies give faster damage accumulation. Thereby, as a prequel to 30 MeV irradiations, 16 MeV protons irradiations were carried out. This served multiple purposes:

- The cross-sections for (p,2p), (p,n+p) and (p,a) are low at 16 MeV (see Figure 3.8) and the irradiation would be devoid of H and He
- It serves as a comparison for Re production to damage ratio ($\frac{Re}{dpa}$), with 30 MeV proton irradiations
- It serves as a test bed for the sample, sample holder and cooling systems

The qualification and testing of the sample holder was performed on the baby cyclotron run by the Institute for Nuclear Chemistry (INM-5) within the institutes for neuroscience and medicine at Forschungszentrum Jülich. The cyclotron is normally used for regular ^{18}F and ^{11}C tracer production. However it also has a solid target, sample irradiation extension. This chapter details working of the cyclotron, followed by the solid target irradiation chamber. Subsequently, the sample holder design with the simulations are described with initial tests and the final working concept.

7.1 Baby cyclotron

Baby (BC1710) is a compact fixed energy cyclotron for medical purposes built by the Japan steel works Ltd and was installed in 1987. The low energy cyclotron was specifically built for nuclear medicine production and research. It deals with short lived isotopes such as ^{18}F , ^{11}C , ^{13}N and ^{15}O [230]. The BC1710 produces protons with 17 MeV beam energy and being a production machine has an internal maximum proton current of 50 A. A septum located at the edge of the magnetic Dee extracts the beam onto the target at a radius of 42 cm from the centre. Internal targets are usually irradiated at this location in the cyclotrons.

The baby cyclotron is attached to a 1.5 m long beam line with 6 target stations at the end as shown in Figure 7.1. An external beam line has a number of advantages; easy loading

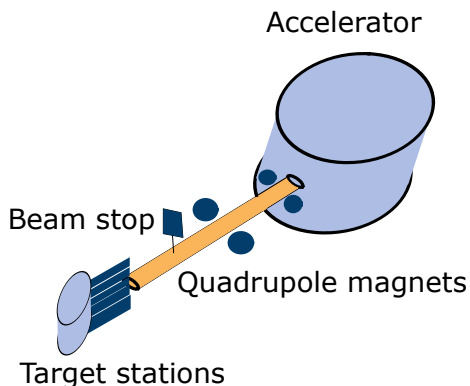


Figure 7.1: BC1710 aka Baby cyclotron located at the institute for nuclear chemistry and routinely used for the production of radio-isotopes such as ^{18}F and ^{11}C .

Collimator size(cm)	Target current(A)	Collimator current(A)
1.3	10	1.5
1.0	10	6.0
0.8	10	12
0.6	10	17
0.5	10	20

Table 7.1: Collimator current to target current ratio for various collimator diameters at Baby cyclotron taken from [232].

and unloading of the samples, more control on the beam focus/ defocus and shape along with collimation. Also, a variety of target stations can be mounted and irradiated [231]. Most low energy medical cyclotrons are operated with liquid and gas targets. Solid target systems require special beam lines with cooling for heat removal. The target station at the end of the baby cyclotron consists of 2 gas target stations, 2 water target stations, one beam test target and one solid target system [232]. The extracted beam at 42 cm from the centre is directed into the 1.5 m long external beam line using quadrupole magnets and steering magnets. The target stations are interchangeable using a remotely controlled spindle drive from the operators room.

A minimum vacuum pressure of $2 \cdot 10^{-2}$ mbar is required within the solid target system. This vacuum is separated from the beam line vacuum by a double window through which He gas is pumped. The solid target system has a water cooled Al collimator for shaping the beam onto the target. Smaller collimator diameters have a larger heat load for the same current on the target which is shown in Table 7.1 for various diameters from [232]. As the diameter is decreased, the beam strikes and dumps heat on the collimator. A 10 mm diameter collimator was used in our experiments as the ratio of current on collimator to the current on the sample is 60%.

7.2 Sample holder

Cu and Al are preferred materials for the sample holder which in itself is mounted on a sample rod as shown in Figure 7.2. The sample rod is inserted into the beam tube of the cyclotron

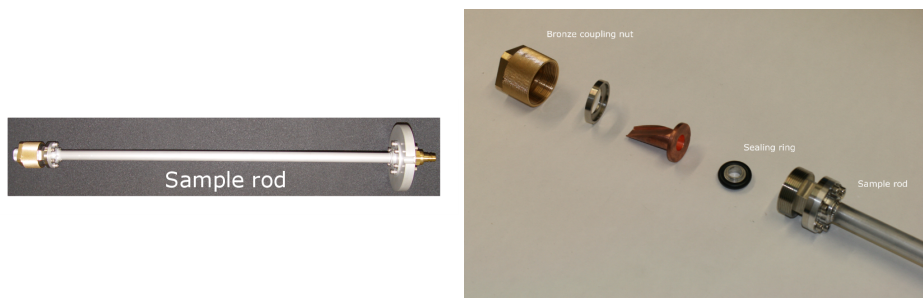


Figure 7.2: The sample rod which is inserted into the solid target system and encapsulates the solid target in it. It also has a cooling circuit for heat removal with the sample rod.

and fits in the solid target system. The sample rod has a bronze coupling nut which holds the sample in position. The sample itself sits on a sealing ring and attaches itself onto the sample rod. The rod also has an internal cooling circuit which directly cools the back side of the Cu sample holder. As the sample is in direct contact with the Cu sample holder, it is cooled through conduction. The cooling system is detached from the collimator cooling in order to avoid contamination and ensure proper heat removal. The cooling circuit actively cools the holder in a (180 degree) geometry [233].

Oxygen free Cu is used for the fabrication of a screw type sample holder as it is a good thermal conductor and has well known activation (reaction cross-sections). It can hold a sample of 13 mm diameter onto which the beam enters in a perpendicular manner. The sample holder as shown in Figure 7.3 has a cut-out on the back of the holder where the cooling water circulates and cools the sample holder. Through conduction the sample is cooled by the holder. Temperature measurements for a solid target on a production cyclotron are usually estimated using the beam current and cooling water temperature. In order to have a better approximation of the irradiation temperature, the design of the sample holder was adapted to include thermocouples. This addition to the sample holder uses vacuum sealed feed-throughs' for thermocouples, resulting in online temperature measurement. A thermocouple each of type K and type N having specifications as shown in Table 7.2, are used for in-situ measurements during the proton irradiation. The thermocouples have an outer diameter of 0.5 mm and are inserted into the Cu sample holder through the holes as shown in the Figure 7.3. The thermocouple is inserted far enough till it touches the back side of the sample and is kept in position by the feed back spring around the Cu sample holder. The insulated thermocouple is extended out of the solid target system using vacuum feed through and connected to a data logger system. The data logger is a temperature recorder which has a capacity of up to two years of on-line data measurements and is located in the basement, under the cyclotron. It also has an option for direct in-situ viewing of temperature build-up and change during the experiment via a Ethernet connection.

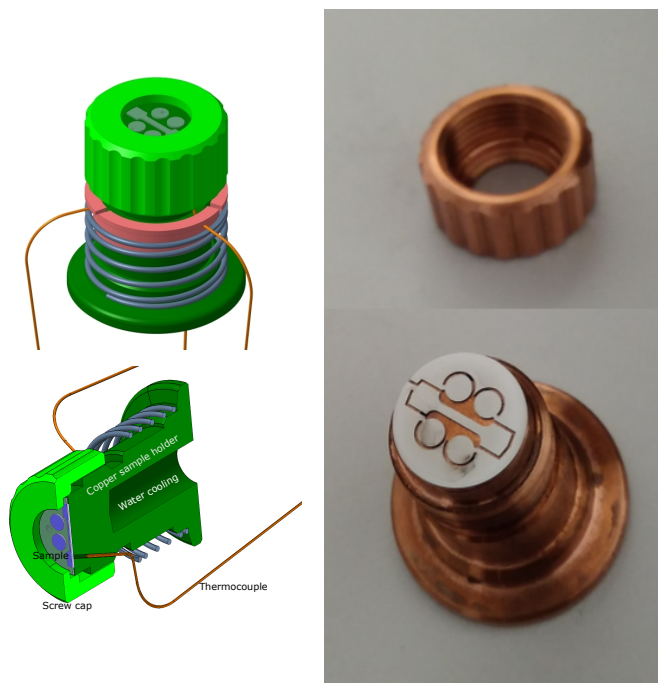


Figure 7.3: The sample holder made out of oxygen free Cu which is used to irradiate solid targets along with its design drawing.

Type	Base material	Sheath material	Temperature range	Diameter
N	Nickel-chrome-silicon/ nickel-silicon	VXS	-200°C to 1300°C	0.5 mm
K	Nickel-chrome/ nickel	Inconel600	-200°C to 1200°C	0.5mm

Table 7.2: Specifications of the thermocouples used for online irradiation temperature measurement fed into the sample holder.

7.3 Sample activity simulations

The entire sample holder assembly was simulated in MCNP6.1 [164] as shown in Figure 7.4. The monte-carlo method based MCNP6.1 allows multiple particle simulations and is run for protons, neutrons, alphas and electrons. The entire sample holder along with cooling water is simulated. This was done to determine the proton induced activation of the Cu sample holder, the Cu top screw and the Cu disk above the sample. Also, proton (p,xn) reactions generate neutrons which can additionally generate secondary reactions. The neutrons could potentially induce nuclear reactions in the cooling water and the sample holder. The MCNP6.1 simulation is based on actual dimensions, with the proton beam incident perpendicular onto the sample surface. The simulation is run for a minimum of 1440 minutes (24 hours) such that the statistical binned relative errors are below 5%. A 15 mm beam diameter is considered to include activation of the Cu sample holder head screw. The sample holder is simulated

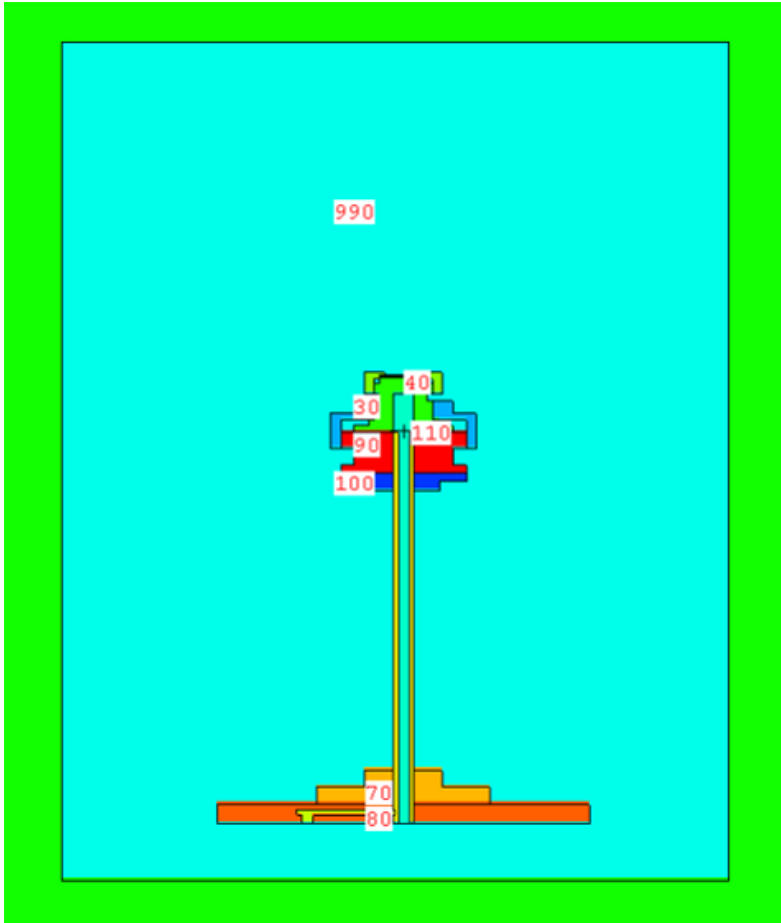


Figure 7.4: A MCNP6 representation of the sample holder. Each colour and number represents the cell numbering system used. As seen the Cu sample holder, the bronze cap and the entire sample holder assembly was simulated.

within a box of 20 cm × 20 cm × 50 cm, which formed the simulation universe and all particles which exited this are considered as lost and not followed. Each sub part of the sample holder is constructed using planes and surfaces and defined as a cell with material and volume. The proton flux and the neutron flux through the sample and other significant cells are estimated using the simulation.

The protons were grouped by energy into pre-defined CCFE-162 energy groups. The estimated flux per source proton for the W sample, Cu sample holder, Cu disk and the Cu screw head is shown in Figure 7.5. As intended, the W sample receives the high energy protons. As the Cu disk lies on top of the sample, it too registers the high energy protons. A much lower fraction of direct 16 MeV protons is seen to impact on the Cu screw head as expected as the centre of the beam is impacted on the sample and only the very edge of the sample head is impacted by the direct beam. The sample holder does not have any direct irradiation on it which is also noticed by the flux profile. The protons reaching the Cu sample holder are to

7.3. Sample activity simulations

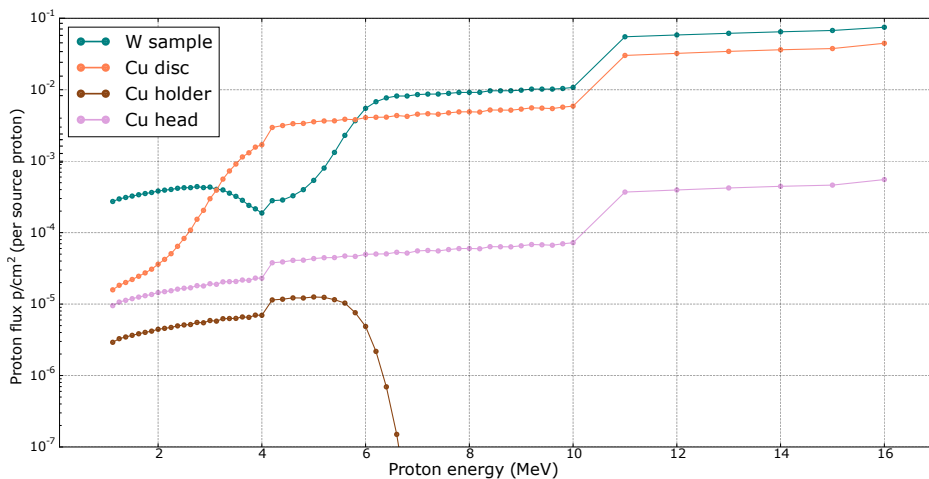


Figure 7.5: The proton flux per source proton estimated using MCNP6.1 for the W sample, the Cu sample holder, Cu disc and Cu screw top.

travel through the sample and thereby show energies ranging from 1 - 5.5 MeV. These fluxes were used as input in the inventory calculation software FISPACT II [90] along with different irradiation scenarios to comprehend the activity and dose rate. A example of the irradiation calculation is shown in Figure 7.6 where the dose rates are plotted against the irradiation scheme. Initially a 45 minute irradiation step was planned with a cooling time of 23 hours

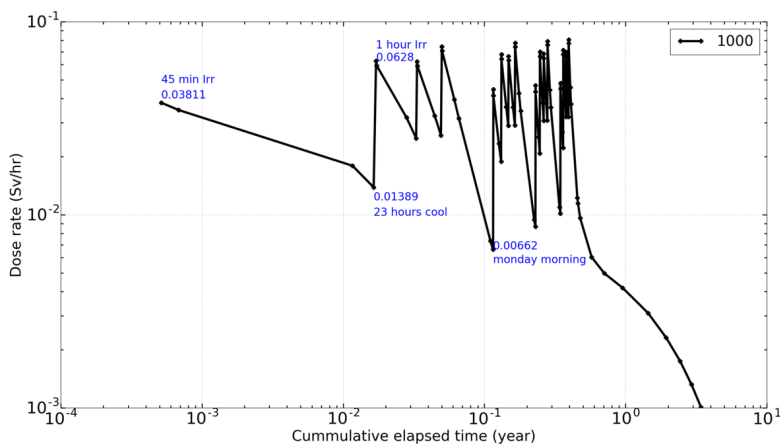


Figure 7.6: FISPACT II dose rate calculations for an irradiation scenario using the fluxes from MCNP6 to ascertain the induced activity and dose rates for the irradiated samples.

before the next irradiation step of 60 minutes is undertaken. Such a scenario was considered in case of any urgent need for sample removal and the dose rates are reported. A overnight drop from 38 mSv.hr⁻¹ to 13 mSv.hr⁻¹ is seen after the 45 minute irradiation. If the sample is left to cool over the weekend, a drop 65 mSv.hr⁻¹ to 6 mSv.hr⁻¹ can be seen as the short lived 181 Re decays.

As mentioned in section 3.4, the sample thickness is limited to ensure a near constant damage zone in the sample. This entails that most protons undergo electronic stopping in the sample and the large energy losses from nuclear stopping in the Bragg peak are deposited after the sample, within the sample holder. The sample holder is actively cooled and thereby functions effectively as the beam dump for protons. Seen in Figure 7.5, the proton with energies between 1 - 5.5 MeV induce (p,n) reactions on the Cu. The two major products formed from the (p,n) reaction on ^{63}Cu and ^{65}Cu are ^{63}Zn and ^{65}Zn , the latter which has a half life of 244 days. Thus the sample holder would bear significant radio activity post irradiation. The post irradiation activity for Cu disk, W sample and the Cu sample holder for the 3 part one hour irradiation scenario with 10 A, 10 mm diameter, proton beam irradiation scenario is shown in 7.7. The Cu screw head displays the highest activity post irradiation. As the half

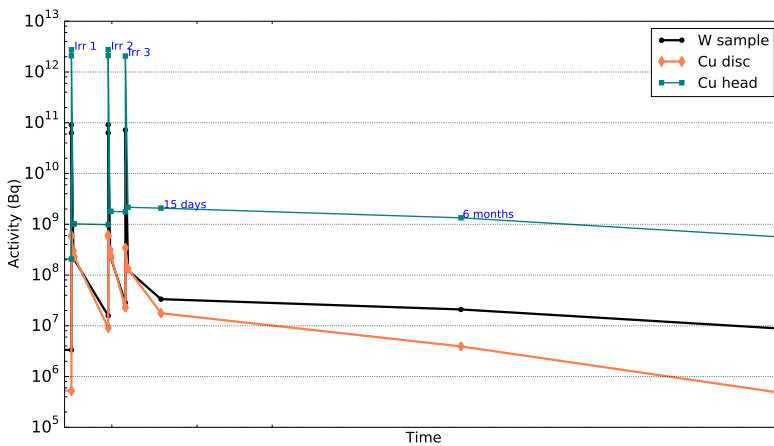


Figure 7.7: Post irradiation activity on W sample, Cu disk and Cu sample holder for a three one hour, 10 A, 16 MeV proton irradiation scenario calculated using proton fluxes from MCNP6.1 and inventory calculation software FISPACT-II.

life of the produced isotope ^{65}Zn is 244 days, the activity stays constant over a long period of time. The Cu disk above the sample is exposed to a higher proton energy range, is only 500 μm in thickness as against the holder with over 5 mm thickness and thereby doesn't show greater post irradiation activity levels as compared to the Cu head.

An estimate of the neutrons produced per source proton is shown in Figure 7.8. The neutrons are produced in the MeV range from a compound nucleus reactions which has a 4 π (360°) emission. As they are produced within the sample, the 3 mm disks and the tensile sample show the maximum flux. The maximum generation rate is seen to be 0.001x proton flux. The (p,xn) reaction generated neutrons have energies in the MeV range, i.e. large ranges with low interaction rates. Given the small thickness of the sample, no significant activation within the sample or holders is produced in comparison to the protons. The 3 mm disk and the tensile sample have a similar neutron generation as they are part of the exposed area. The sample holder below the sample registers a lower neutron flux. No cooling water activation was considered as the flux would be extremely low.

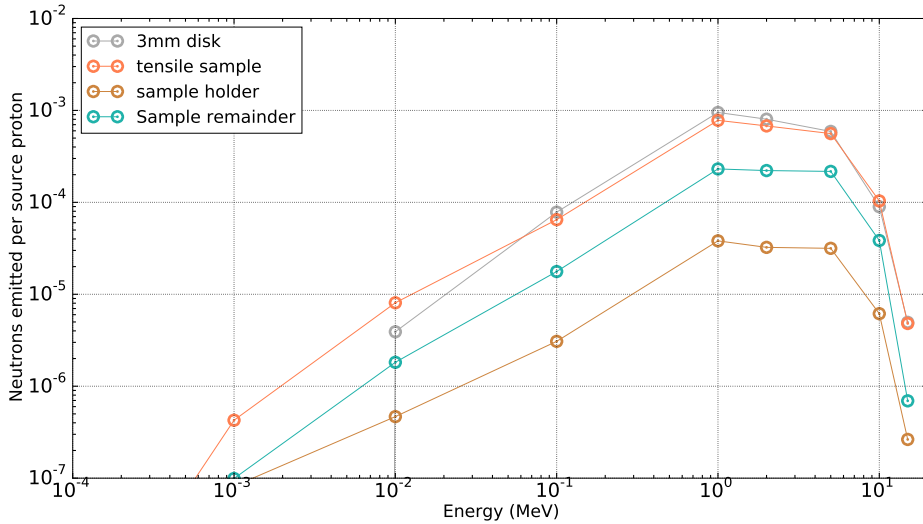


Figure 7.8: The neutrons produced per source proton from (p,xn) reactions of 16 MeV protons on W for different cells estimated using MCNP6.1. As seen the neutrons produced are mostly high energy and would leave the target area.

7.4 Irradiations & power loading

Three irradiations are performed at the baby cyclotron, each time with a technical upgrade of the sample holder. No radioactive dust or any contamination is seen in any of the irradiations conducted. Prior to each irradiation, a vacuum leak test, a beam current measurement check and cooling water leak test was carried out. While no issues with vacuum break or with the cooling water leakage are observed, often an electrical contact (short circuit) between the thermocouple extension and the external beam line is noticed. This is solved by using a non conductive, heat resistant polyimide sheath. The final design is then tested with an additional irradiation of 10 + 30 A.hours (10 A 4 hours) to qualify for long term irradiation exposure and post analysis.

Initially, a polished sample is placed on the Cu sample holder and considered for irradiation as shown in Figure 7.9. It is irradiated for 5 minutes at 5 A current and for 1 minute at 10 A current. A major drawback of this method is the large radioactivity induced in the Cu sample holder which makes it not reusable for further irradiations. Additionally, a good thermal contact between the sample and the sample holder is not achieved, which resulted in ineffective cooling and rapid heating of the sample. This is confirmed as it translated into a meagre 3.5°C rise on the temperature readout by the thermocouple. The sample being brittle also saw many fractures during installation onto the Cu sample holder.

A good thermal contact for the sample with the Cu sample holder is the foremost requirement for long term irradiations. This is achieved using a Cu plate of 0.5 mm on top of the sample which would push the sample down and ensure thermal contact. Cu is chosen as it doesn't react with W under high temperatures and shows no metallurgical bonding with W. The Cu plate is precisely cut matching at the irradiation areas as shown in Figure 7.10 The cuts ensure 16 MeV protons on the intended target areas of the sample such as the 5 mm gauge length of the tensile sample and 3 mm disks while the non-significant portion of the



Figure 7.9: 1st trial of the sample holder with the plain sample on the Cu sample holder.

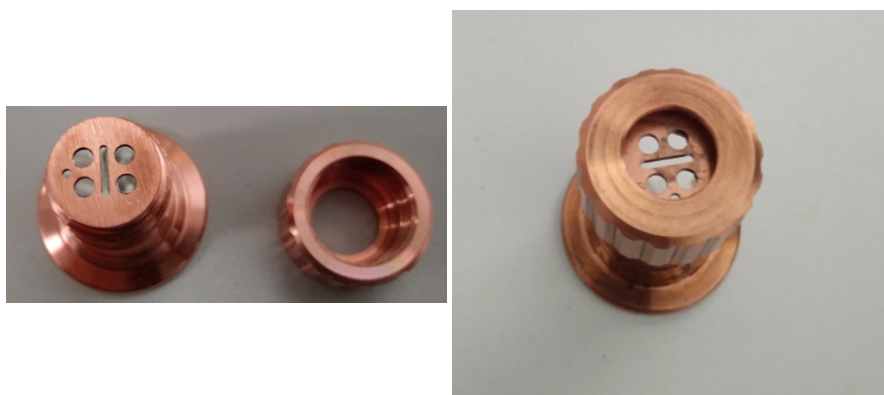


Figure 7.10: 2nd trial of the sample holder with a Cu plate above the sample for good thermal contact. Additionally, the Cu also protects the sample against the irradiation at non-significant areas.

sample is protected. As Cu activates less than W under proton irradiation, the inherent total radioactivity of the sample is reduced.

The Cu plate enclosed sample holder is subjected to one hour long test irradiation at 10 A proton current. The total heat load from the 16 MeV protons is approximated to (16 MeV 10 A) 160 W. The thermocouple recorded a temperature between 120°C and 130°C. However, post irradiation, it was noticed that the Cu plate is stuck to the sample holder top as shown

with the thermocouple readings in Figure 7.11. The Cu plate absorbed a large fraction of the proton flux and underwent local heating from the electronic stopping of protons. This resulted in the local bonding of the plate to the holder and defeated the objective of pressing the sample against the holder.

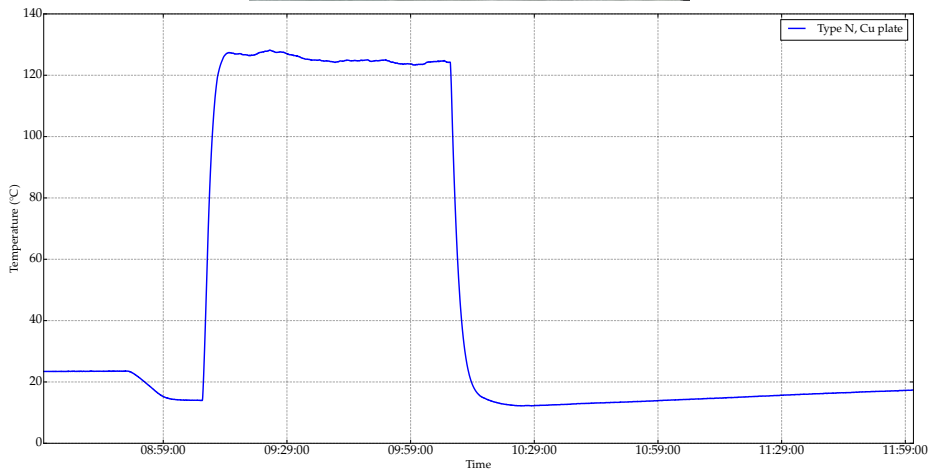
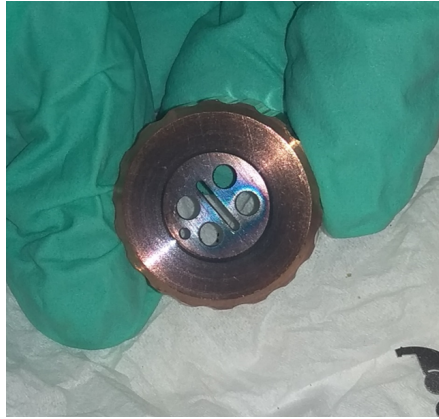


Figure 7.11: Post irradiation the Cu plate is stuck onto the Cu top due to improper thermal contact. Although the thermocouple reading indicate a good contact for the W sample.

Such a detachment might result in improper thermal contact for long term irradiations, hence a further technical improvement is sought. Graphite has good thermal conductivity and high stability even at temperatures of 1000°C and above. Another important consideration for graphite is the very quick decay of induced activity under 16 MeV proton irradiation. The ^{11}C formed from (p,n) reaction on ^{12}C has a rather short half life of 20.36 minutes and within 24 hours is completely decayed out. This makes handling of the sample post irradiation much easier. Considering the above advantages, graphite was used as a pressure plate for the sample as shown in Figure 7.12. Similar to the Cu sample, the graphite has holes cut into it to ensure 16 MeV irradiation on the W samples. However, the Cu plate still had to be additionally placed between the sample and the graphite in order to prevent the formation of tungsten-carbide. These three materials combine ideally due to good thermo-mechanical stability and the non reactivity of Cu with W and C with Cu.

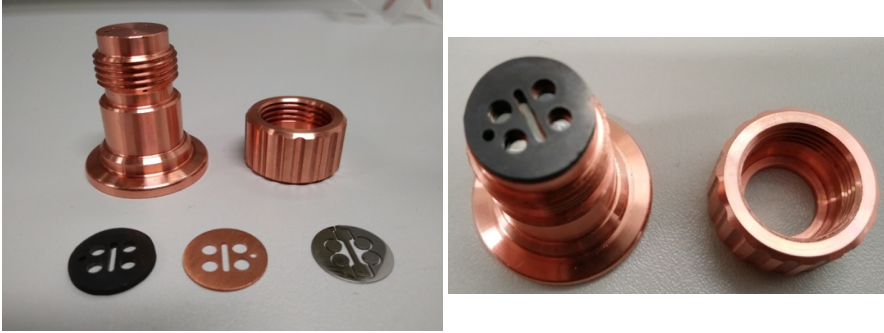


Figure 7.12: 3rd trial of the sample holder at the baby cyclotron with a graphite piece as the pressure plate for inducing thermal contact between the sample and the Cu sample holder.

Initially, 1.4 mm thick nuclear grade graphite is used which resulted in the melting of Cu disk due to the Bragg peak heat load. The Cu disk is only 0.5 mm thick and isn't actively cooled. When used, it melted and collapsed into the W sample as seen in Figure 7.13. The Bragg peak indicates a region of high damage but it is also the region where most of the beam energy is lost and thus effectively acts as a beam dump. Given the small volume of Bragg peak and the relatively low melting point of Cu in comparison to W and C (sublimation point), the Cu disk heated rapidly and melted. thereby, subsequently the thickness of the graphite was increased to 2 mm such that the beam dump is directed into the graphite.

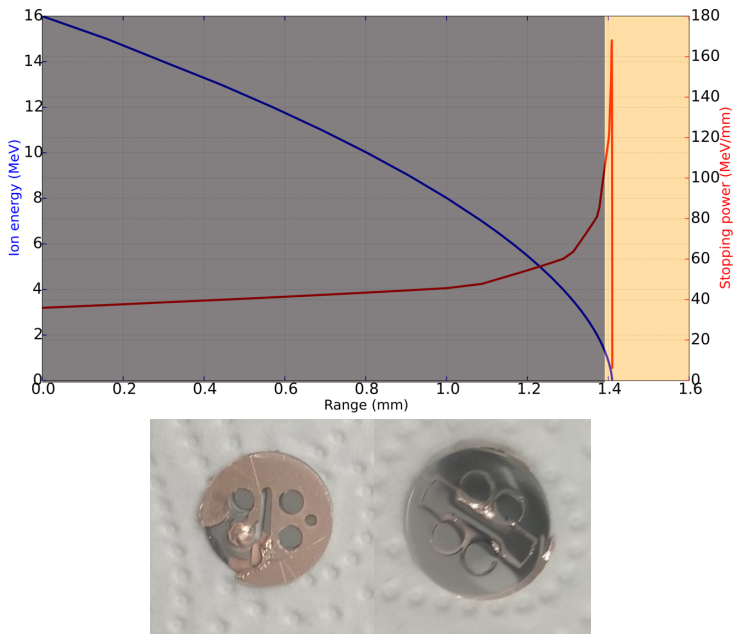


Figure 7.13: A diagram representing the Bragg peak in a mixture of C (grey) and Cu(gold). In the range diagram it is observed that the Bragg peak lies in the Cu which would act as the beam dump and melt the Cu during irradiation.

Upon use of the 2 mm thick graphite disk, no melting of the Cu disk is noticed. Also no further irradiation problems are encountered during an irradiation with 10 A, 16 MeV protons for 60 minutes. Successful thermocouple readings showed the temperature to be 100°C due to good thermal contact. Considering this, three more hours of 16 MeV proton irradiation at 10 A are carried out to a total of 40 A.hours. The long irradiation under a constant heat flux also qualifies the sample holder for large irradiation doses. A damage dose of 4.3×10^{-07} dpa/s to a total of 0.006 dpa. The irradiation times along with the cooling times are given in Table 7.3.

Date	Dose (A.hours)	Cooling time	Comments
27-07-2018	10 A.hours		test with 2 mm graphite
25-02-2020	20 A.hours	578 days	2 hour irradiation
03-03-2020	10 A.hours	7 days	1 hour irradiation

Table 7.3: The irradiation dates listed alongside cooling times relevant for decay and dose rate calculations.

The sample irradiation temperature is estimated using Ansys. The geometry of the sample including the casing was imported. The sample temperature at the rear end which is in contact with the actively cooled sample holder is measured by the thermocouple as 100°C and is stated as such. Considering 10 A beam current for 16 MeV protons projected onto a 10 mm diameter sample, the total heat load is 160 W or 2 MW/m^2 . Using an initial temperature of 18°C recorded from the thermocouple, a steady state thermal analysis calculation is used to estimate the irradiation temperature which is shown in Figure 7.14. As anticipated, the excellent thermal conductivity and the thin nature of the sample yield good cooling of the sample and an irradiation temperature variation of 4°C between the thermocouple readings and the top of the sample is noticed. It can be stated that the thermocouple correctly represents the irradiation temperature. Another aspect which can be observed is that the unirradiated section of the sample is also at irradiation temperature.

Although, it is known that the incoming proton energy is 16 MeV and the proton exit energy at the rear of the sample is estimated at 4 MeV from its range. Thus, a total of 12 MeV is lost to the W sample. This can be approximated as the internal heat generated within the sample and checked as a second alternative to irradiation temperature measurement. The simulation gave similar results and the two methods are compared in Figure 7.15. On the right side 3 mm disk, the internal heat generation is applied, while on the sample on the left, a heat flux is applied. Both the sources of heat show similar rise in temperature within 2°C . The difference is seen in the sample heat profile where the irradiation as internal heat generation shows a constant temperature. Thereby, the thermocouple temperature is considered as the irradiation temperature.

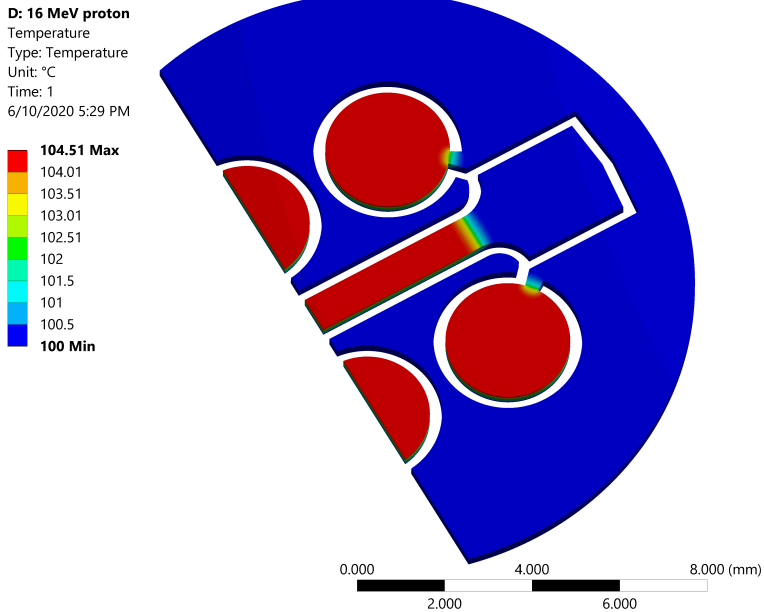


Figure 7.14: Estimation of the irradiation temperature profile through the sample using Ansys mechanical steady state heat solver. A change of 4°C is observed between the top and bottom side of the sample.

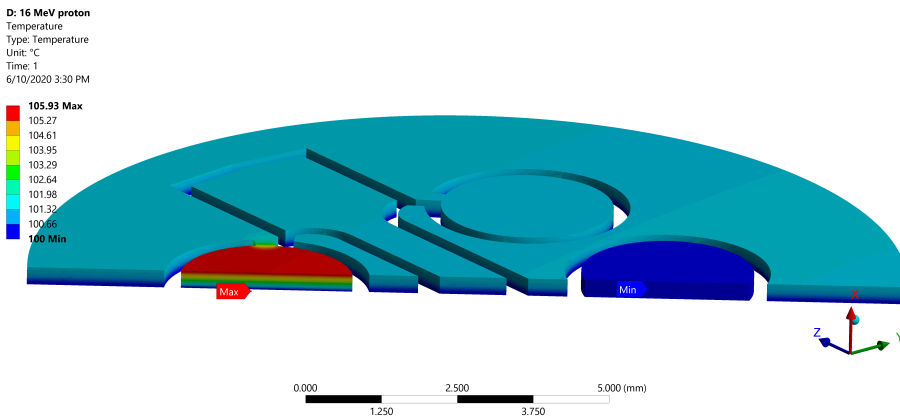


Figure 7.15: Comparison of two different methods of heat application. The 3 mm disk sample on the right has internal heat generation applied as the method of heating while the sample on the left shows heat flux applied as the source of heat.

7.5 Post irradiation sample analysis

Post irradiation, the dose rates are recorded for comparison with simulations. The irradiation and cooling times listed in Table 7.3 were fed to the FISPACT-II simulation to compare post irradiation sample dose rates. The need for this comparison is two fold; the concurrence of

the dose rates confirms the proper working of the simulation and by extension, the nuclides produced and their radio-activity. Secondly, the activity and dose rates are needed for radiation safety and handling. If the dose rates are extremely high, similar to fission reactors, a cooling time is considered prior to handling. Also, the transport of the samples for further testing is dependent on the dose rate for personnel safety.

All isotopes with radioactivity above 1 kBq estimated using FISPACT-II are considered and substituted into Nucleonica's dose rate measurement tool [234]. The major nuclides after 7 days of cooling time post last irradiation are listed in Table 7.4. Nucleonica dose rate

Nuclide	Estimated Activity (MBq)	Half lives
183Re	17.1	70 d
182Re	7.93	64.2 h
181W	6.81	121 d
184Re	3.52	38 d
186Re	2.81	3.76 d
181Re	1.06	19.9 h
184mRe	0.15	169 d
182mRe	0.03	12.7 h
183Ta	0.01	5.09 d

Table 7.4: The major nuclides as estimated using FISPACT-II simulation run for 16 MeV proton irradiation. As the short lived nuclides decay out, the long lived nuclides are dominant.

calculator estimates the gamma dose rates for a list of user defined nuclides and can be adapted for various source/detector distances. The source is considered as a point source with 4 π emission (360°) with the corresponding dose detection at a point. An additional option is to include a shielding material between the source and the detector with flexible options such as lead, water or concrete. However, the shielding is limited to a single material. Thereby, for contact dose rate calculations, the self shielding by W sample (0.3/2 = 0.15 mm) and the Cu disk (0.5 mm) are assumed as a combined W shield of 0.4 mm thickness. The results generated are compared to the measured dose as shown in Table 7.5. The dose rate is measured using an Automess dose rate meter 6150AD which has a dose rate range of 0.1 Sv.hr⁻¹ - 10 mSv.hr⁻¹. It is capable of measuring X rays and γ rays between 45 keV and 2.6 MeV. The contact dose rate while corrected in the simulation to a distance of 1.3 cm away

Description	Simulated(mSv.hr ⁻¹)	Measured(mSv.hr ⁻¹)
Contact dose	14.68	4.3
Lead shield (3.5 cm)	0.218	0.11

Table 7.5: Comparison of simulated and measured dose rates after 7 days of cooling post last irradiation. The beta dose rate is not recorded within the gamma dose analysis with nucleonica.

(to accommodate the graphite and the Cu sample top) from the sample still is over 3x the measured dose rate. However, the simulation shows closer conformity (2x) post lead shielding. A 3.5 cm lead shielding is considered as this is the thickness of the sample transport box. Although there is good agreement between the simulation and measurement, the deviation can be assigned to irradiation problem which is explained below.

The sample is unpacked post transport behind lead walls and once again a melting of the Cu disk is seen as shown in Figure 7.16. This is in contradiction to the starting one hour of irradiation, where no melting was observed and, thereby the sample is repacked. The sample melt is similar to the previous attempt. A non concentric beam tilted towards the bottom left of the sample is considered as the possible reasoning for this melting. It created a localised heat spot due to non-uniform beam spot focussing which melted the Cu disk. The contact dose rates measured varied widely for each of the 3 mm disks. The comparison alongside the simulated dose rate is shown in Table 7.6. The unfocussed beam spot would understandably create such a varied dose distribution and explain the differences in the contact dose rates observed. The lowest dose is noticed for sample SP3 which was shielded by the molten blob of Cu. In the future, this could be avoided by increasing the graphite size significantly to 5 mm thickness and measuring the temperature using all three thermocouples simultaneously.

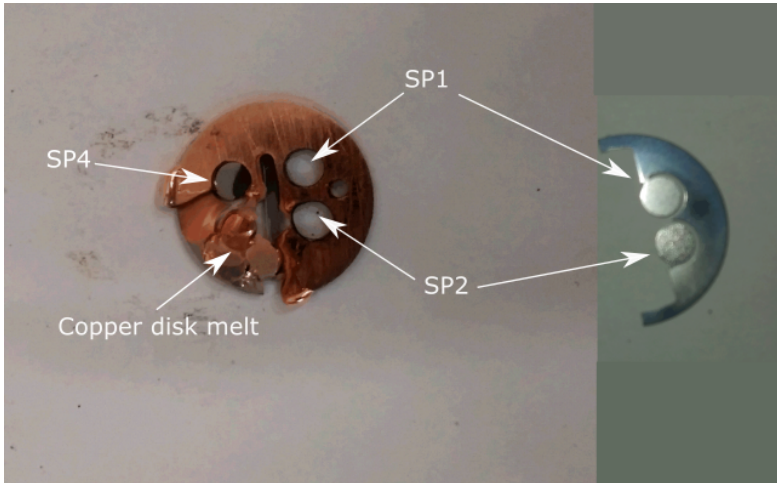


Figure 7.16: The samples with the Cu disk which melted during irradiation. A thicker graphite sample is sought for the next irradiation.

Optical microscopy of the sample suggested a direct roughening of the sample surface. Signs of damage are noticed on the the exposed surface of the sample which had the direct beam. In comparison, the rear side of the sample showed lesser signs of damage and cracking. Such a change is also noticed while comparing the unirradiated portion of the sample casing. The comparison is shown in Figure 7.17.

Here, the crack network is seen to follow the grain boundary structure, however, the cracks are much larger than the grain sizes and enclose the grains within itself. Such a crack network is also noticed post thermal shock however, these cracks are seen to originate on pure W sample between 160 - 200 MW/m² [235]. Also only surface modification is noticed above 100°C [235] from heat flux testing. In this work, the loading can be approximated as 2.04 MW/m² which is 100x below the threshold limit. Thereby, the combination of heat loading and irradiation is responsible for the production of crack impaled surface micro-structure.

Sample	measured dose (Sv.hr ⁻¹)	simulated (Sv.hr ⁻¹)
SP1	40 3	140
SP2	220 10	140
SP3	21 1	140
Tensile	160 3	381.5

Table 7.6: Contact dose rates measured for samples compared to simulation results and each other, 92 days post last irradiation. The uneven dose rates between the 3 mm disc samples implies a difference in the irradiation dose between the samples.

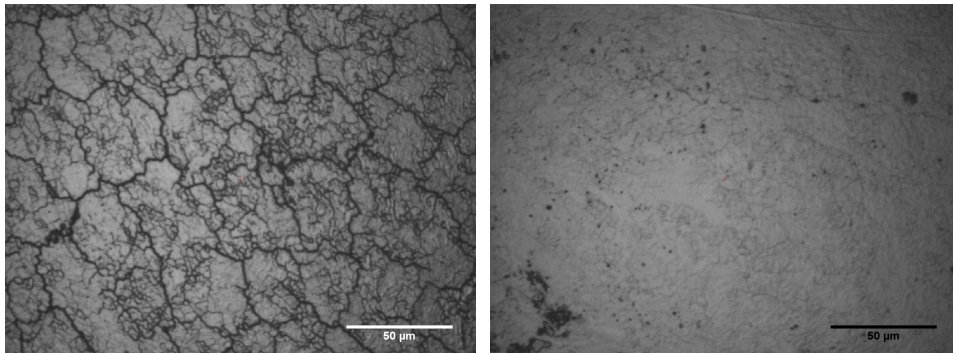


Figure 7.17: A comparison of the directly exposed sample surface(left) to the rear side of the sample(right). The rear side of the surface retains the original surface.

A comparison of the observed surface micro-structure by an optical microscope with 40x magnification is seen for samples Baby_SP2, Baby_SP3 and Baby_Ten in Figure 7.18. A distinction can be easily noticed for all three sample surfaces. The sample Baby_SP2 is impacted the most and shows a shiny melt like surface quality. The sample Baby_Ten, shows similar surface behaviour with crack network. However, the sample Baby_SP3, which is shielded by the Cu melt blob shows a developing crack network without any major surface change. In fact parts of sample Baby_SP3, do not show any surface change at all. This further adds understanding to the thought that, proton damage along with a high heat flux are responsible for the crack network seen on the sample.

Instrumented indentation testing carried out on the 3 mm disk samples and the tensile sample also displayed variation. This is a result of the inherent difference in damage dose. Additionally, the surface micro-structure is seen to play an effect on the measurements. The results are shown in Table 7.7. A maximum load of 15 N is applied for each indent with a waiting period of 12 s at the maximum load. The displacement and force are measured and evaluated to obtain the indentation hardness. The hardness order (Ten > SP1 > SP2 > SP3) shows no particular inclination to the measured dose (SP2 > Ten > SP1 > SP3). Thus, the variation is assumed to arise from the discrepancy in surface quality between the samples. Sample Baby_SP3 is mostly shielded by the molten blob of Cu but had the thermal flux through conduction. This could be a reason for the low indentation hardness seen on the sample. While this reasons well with the Vickers hardness measurements, large variation is also seen within the Vickers hardness. It is in fact surprising to note that all measurements are below the

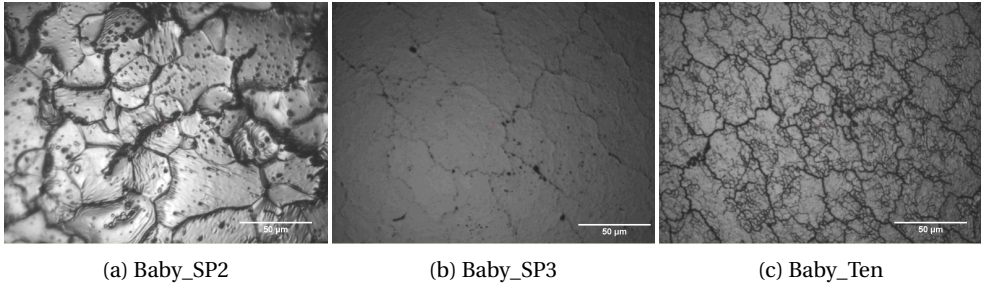


Figure 7.18: A comparison of the surface micro-structure of samples Baby_SP2, Baby_SP3 and Baby_Ten as seen under an optical microscope with 40x magnification and a scale bar reading of 50 μm .

unirradiated measurements. The order of decreasing Vickers hardness measurements (Ten > SP3 > SP1 > SP2) is again different from the dose rate measurements and the indentation measurements. Due to the irradiation related surface damage on the sample, large problems are encountered while identifying the diagonals for Vickers hardness measurements. This can be a reason for the disagreement in particular between the IIT results and the Vickers hardness results. Considering the disagreements, no particular conclusion is drawn from the indentation testing of Baby cyclotron irradiation sample. However, with reasonable thought, considering the dose rates measured at the tensile sample, the Vickers hardness results and the post irradiation observation that the tensile sample would be irradiated the same irrespective of the beam shift, the indentation hardness is assumed to be 6.35 GPa.

Sample	Indentation hardness(GPa)		HV1.5	
Unirradiated	5.48	0.2	4.38	0.02
Baby_SP1	5.88		4.05	0.02
Baby_SP2	5.21		3.68	0.03
Baby_SP3	4.38		4.08	0.03
Baby_Ten	6.35		5.0	0.05

Table 7.7: The indentation hardness and measured Vickers hardness for samples Baby_SP1, Baby_SP2, Baby_SP3 and Baby_Ten sample using a maximum force of 15 N and a waiting time of 12 s at maximum force. As only one indent was made for each sample, no error is reported for the irradiation hardening which is a derived quantity, however as Vickers hardness is a measured quantity the experimental uncertainty is shown.

This increase is similar to the increase registered by 3 MeV protons. At this stage of the irradiation damage dislocation loops originate and lead to the increase in hardening. Using FISPACT-II simulations, the transmutation content is estimated and tabulated in Table 7.8. Directly post irradiation, the sample registers the formation of 0.26 appm of Re. This decays to 0.15 appm, 92 days post irradiation, at the date of testing.

Element	0 days (appm)	92 days (appm)
Re	0.26	0.15
Os	0.004	0.01
Ta	0.021	0.05
He	1.76 $\cdot 10^4$	1.76 $\cdot 10^4$
H	2.51 $\cdot 10^4$	2.51 $\cdot 10^4$

Table 7.8: Transmutation based elemental precipitation from the 16 MeV proton irradiation of W to a dose of 0.006 dpa damage dose estimated using MCNP6.1 and FISPACT-II.

Summary of 16 MeV irradiation

The 16 MeV proton irradiations were carried out at the Baby cyclotron in Jülich. It served as a suitable test bed for sample and sample holder arrangement. A series of changes in the sample holder design were incorporated to avoid excessive radioactivity. The final design consists of a graphite disk, a Cu interlayer disk and the W sample, fixed in a Cu sample holder and, following irradiation testing, has been approved for high current targets. A novel in-situ temperature measurement system for solid target irradiation was designed and adapted for the final sample holder geometry. Trial runs show an irradiation temperature of 105°C for a steady state irradiation of 10 A 2 hour, fluence. The irradiation was carried out for a total of 40 A.hours with a dose rate of $4.3 \cdot 10^{-7}$ dpa/s to a total of 0.006 dpa. Following irradiation, the sample showed an irradiation hardening of 0.8 GPa similar to 3 MeV protons. Under a microscope the sample was observed to have an extensive surface crack network. This is possibly due to the thermal load of 16 W or 2 MW.m² on the samples. Similar crack networks have been observed under the thermal shock loading of W, but in these cases the thermal loads were 100x larger. As the W does not perform the function of a beam stop, the protons do not accumulate in the sample, except through transmutation. Thereby, the cracks observed are not a result of the hydrogen entrapment in the sample. A combination of irradiation and high thermal fluxes is a possible explanation for this observed behaviour. Planned focussed ion beam cuts and TEM analysis will help understand the micro-structure in detail.

Chapter 8

30 MeV proton irradiation

30 MeV protons produce combined displacement and transmutation damage, which culminates in radioactive samples. This work involved design and setting up of irradiation experiments with post irradiation measurements in a radioactive environment. Simulations using SPECTRA-PKA [59], MCN6.1 [164] and FISPACT-II [90] portray a close approximation of DEMO neutron damage using 30 MeV protons. The simulations also indicate that a constant damage for a sample range of 550 μm in W (refer section 3.4). This range allows for the use of macroscopic samples and extraction of macroscopic thermo-mechanical properties.

Initially, the experiments were planned on the newly built 30 MeV cyclotron from IBA (Cyclone 30). This is a high production machine which can deliver protons having energies between 15 - 30 MeV, having currents upto 350 μA and alpha particles of 30 MeV with currents of 50 μA . It has an internal beam split which can deliver two simultaneous beams of protons onto two different target systems [236]. As the commissioning of the cyclotron is severely delayed, only one experiment was possible using an old research cyclotron (JULIC). At the start of this chapter, the cyclotron JULIC is briefly described with the focus on the target station. Afterwards, the sample assembly and activation calculations using FISPACT-II are shown. Finally, post irradiation sample dose measurements and gamma spectra are analysed and compared with simulations.

8.1 Cyclotron

As the commissioning of the new 30 MeV cyclotron from IBA is delayed due to licensing issues, the injector cyclotron JULIC is used for the irradiation. JULIC (Jülich light ion cyclotron) is an injector cyclotron for the synchrotron (COSY) on the campus of Forschungszentrum Jülich. It has been operational since 1968 and can deliver polarised and non-polarised protons and deuterons [237]. The cyclotron, as shown in Figure 8.1 has three accelerating sectors with the RF generator on the upper magnetic yoke, while the ion source is located in the lower yoke [238]. JULIC produces 45 MeV H^+ and 76 MeV D^+ particles. It is operated by the institute for nuclear physics (IKP) at Forschungszentrum Jülich. Its main role is to support the FAIR accelerator development program and hadron physics experiments. Additionally JULIC has been used to simulate radiation damage in electronics for space applications [239] and medical radio-isotope production. A maximum current of 10 μA can be produced internally within the cyclotron. A moveable W septum is used to extract the beam using electrostatic forces into an external beam line. The beam is deflected in the gap between the septum and a high voltage electrode. However, a part of the beam is deposited onto the septum and the extraction efficiency decreases [233]. The beam is further aligned onto a sample with a

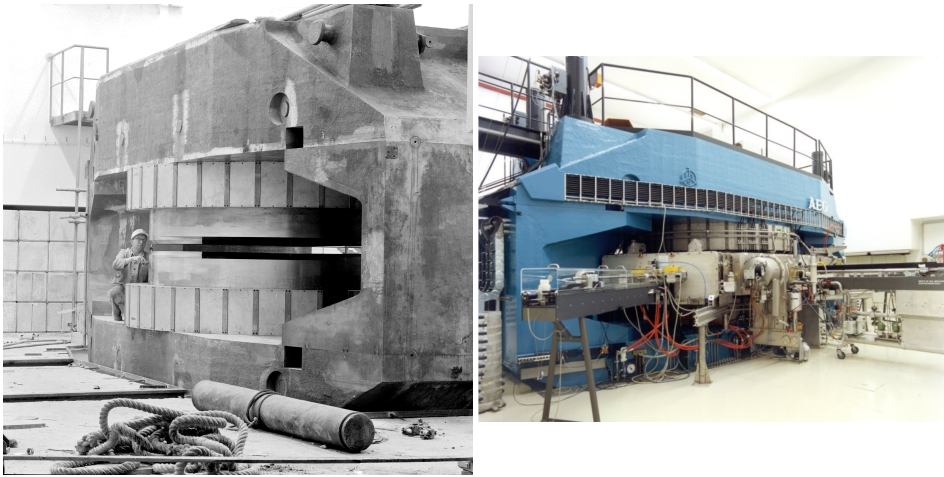


Figure 8.1: JULIC (Jülich light ion cyclotron) injector cyclotron.

beam diameter of about 10 mm. The maximum external current reached is 1.3 A under a vacuum pressure of $2 \cdot 10^{-02}$ mbar. The cyclotron isn't a production machine and thereby high currents aren't routinely extracted from the machine but it allows for a quantitative assessment of the technical design and radiological aspects. At the end an Aluminium plate seals the beam line and is additionally attached to a cooling circuit. The beam line is shown in Figure 8.2, where a focussing magnet directs the beam onto the sample at the very end of the line. The cooling circuit on the Al plate has a direct contact with the sample holder and is

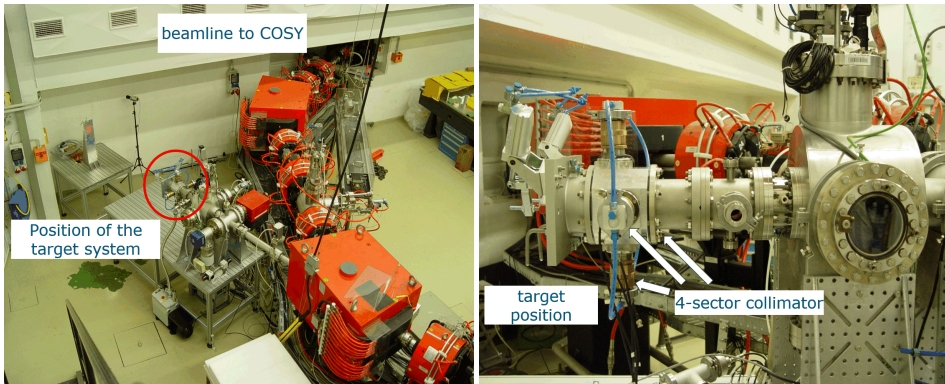


Figure 8.2: External beam line used for solid target irradiation at JULIC. A maximum beam current of 1.3 A under a vacuum pressure of $2 \cdot 10^{-02}$ mbar is achieved.

shown in Figure 8.3. The cooling water is drawn using a submersible pump and the cooling water temperature maintained at 18°C. The current measurements are conducted at the target station, however, the effects of secondary electrons are not eliminated. No temperature measurements of the sample are possible at this irradiation station.

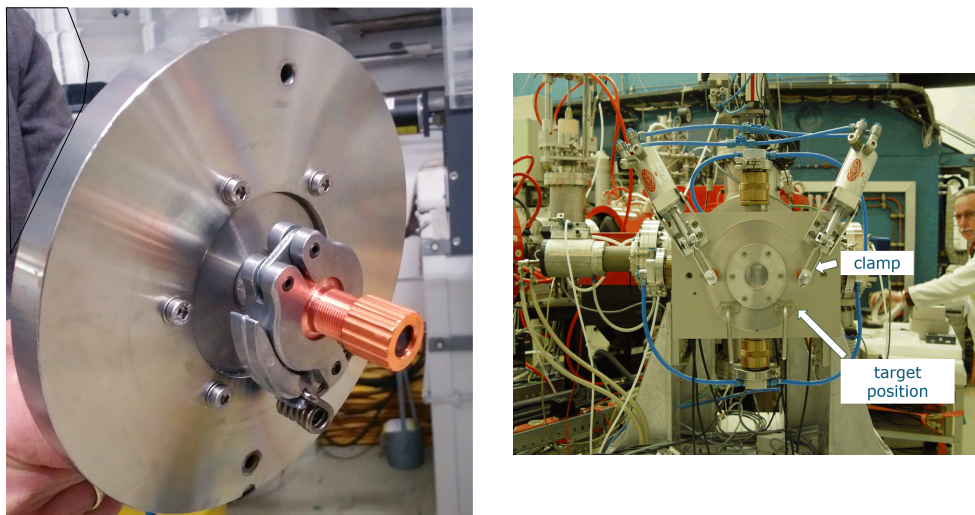


Figure 8.3: The Al sample holder with water connections for sample cooling is installed at the rear end of the beam line for solid target irradiations.

8.2 Irradiation & heat loading

The sample arrangement for JULIC was carefully planned to activate only significant sections of the sample while avoiding activation, oxidation and melting of other parts. Initially, as JULIC produces protons of 45 MeV energy, it needs degradation to 30 MeV for our experiment and thereby an energy degrader. Secondly, only the significant sections of the sample should be activated and thus a beam stop for the non active portions is required. Further loss of 15 MeV to electronic stopping takes place during the travel of the protons within the sample. Thus a second sample with exposure to 15 MeV protons can be placed directly trailing the 30 MeV sample. The exit energy from the 15 MeV sample is 4 MeV which would hit the copper holder and is safe not to induce significant activation of the holder.

The power loss in the 30 MeV sample from electronic stopping is $(15 \text{ MeV} \cdot 1.3 \text{ A}) \cdot 620 \text{ W.cm}^{-2}$ and for the 15 MeV sample is $(11 \text{ MeV} \cdot 1.3 \text{ A}) \cdot 455 \text{ W.cm}^{-2}$, which will lead to considerable heating of the sample. Thus the sample assembly should have sufficient thermal conductivity to avoid the oxidation of the samples under vacuum pressures of 10^{-2} mbar. The cooling on the sample holder acts as a heat sink and good thermal conductivity would help in rapid transfer of heat to the cooled holder. Another important aspect of sample assembly design is to avoid any metallurgical diffusion and alloying which could occur at high temperatures. Thus the materials chosen for the experiment remain the same as for 16 MeV; graphite disks of 4.95 mm and 5.18 mm, copper disk of 0.5 mm, W samples 550 μm and 300 μm and the copper sample holder.

The schematic diagram of the sample assembly is shown in Figure 8.4, where the "solid graphite" makes the first contact with the incoming 45 MeV beam. The solid graphite of 4.95 mm also is the beam degrader and by the end of the disk, the beam energy has a narrow distribution with the peak at 28 MeV. This 28 MeV proton beam passes through another graphite disk of 5.2 mm called the "holed graphite". The holed graphite bears dual purpose; the holes cut into it allow for high energy protons to impact the portion of the sample which is being tested (example only the gauge length of the tensile part), while the other portions ideally do

not undergo any proton damage. Secondly, as graphite is stable at high temperatures, it is also used as a beam stop or beam dump for the protons headed to the non active portion of the sample. The detailed sample holder assembly including energy degradation of energy is shown in Figure 8.5.

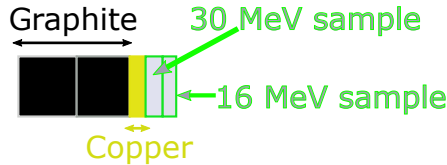


Figure 8.4: Sample assembly representation for JULIC cyclotron exposures.

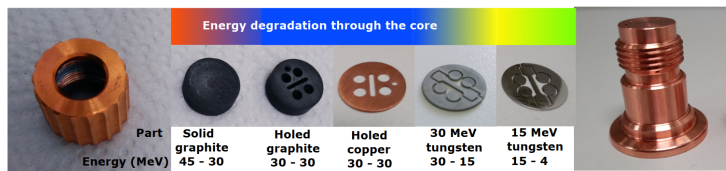


Figure 8.5: Detailed description of sample assembly for JULIC cyclotron irradiation. The colour variation at the top represents the energy degradation in the sample core from 45 to 4 MeV. The entire assembly is then stacked into the copper sample holder and placed in the Al plate for irradiation.

The holed copper essentially acts as an separator between the W sample and the holed graphite. This is essentially to avoid any tungsten carbide formation during the irradiation. The two W samples of 500 μm (COSY_30MeV) and 350 μm (COSY_15MeV) are placed simultaneously and are to be irradiated with 30 MeV and 15 MeV protons respectively. The exit energy of the protons into the copper sample holder is 4 MeV which acts a beam dump and is also actively cooled. The samples are attached onto the sample holder and irradiated for a total of 50 A.hours. This amounts to a displacement damage dose of 0.003 dpa under a displacement rate of 1.75×10^8 dpa/s for 30 MeV protons. The 15 MeV proton irradiated sample however has a displacement rate of 4.2×10^8 dpa/s and registers a damage dose of 0.0075 dpa. The irradiation times and the cooling period between the irradiations are shown in Table 8.1.

Temperature estimates are made using the finite element method based software Ansys14.1. As no physical temperature measurements are feasible in this set up, the cooling water at the copper sample holder is used as a boundary condition. This however undermines the electronic and nuclear stopping power losses from the irradiation greatly and can be used only as an estimate. The heat losses are introduced as an internal heat generation with the sample as discussed previously for the 16 MeV sample in section 7.4. The assembly including the graphite blocks, W samples and Cu sample holder are simulated. A steady state heat calculation is run with the initial temperature as 18°C and a heat input of 0.03 W.mm³, 0.99 W.mm³ and 1.18 W.mm³ in the graphite block, COSY_30MeV and COSY_16MeV sample respectively. The results of the analysis are shown in Figure 8.6. The sample temperature

Date	Dose (A.hours)	Cooling time	Comments
02-11-2019	1.9	41 days	1.03 A current
13-12-2019	9.1	15 hours	7 hours irradiation
14-12-2019	16	32 hours	16 hours irradiation
17-12-2019	13	14 hours	13 hours irradiation

Table 8.1: Irradiation schedule for 30 MeV proton irradiations at JULIC accelerator. Cooling time for gamma measurement and the activity calculations using FISPACT-II were accordingly considered.

is seen to be ranging between 45.2°C to 41.1°C. This isn't a true estimate as the contact between each part is assumed as bonded without any break and thereby is only used as a rough approximation.

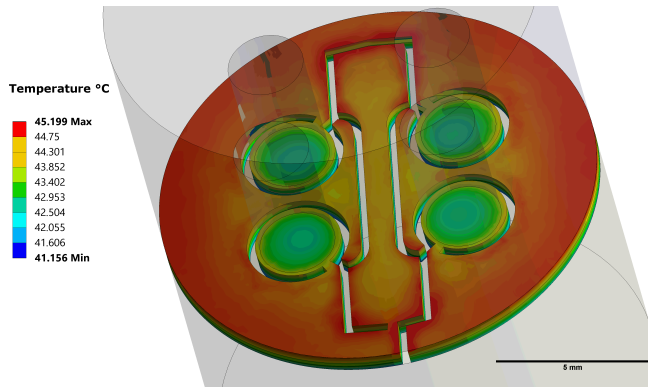


Figure 8.6: Temperature estimation using a steady state thermal calculation using Ansys14.1, a finite element method software. An internal heat generation method was used to account for the electronic and nuclear stopping power losses from the proton irradiation.

8.3 Post irradiation analysis

Post irradiation, the samples were removed and first optically inspected. The copper sample holder, the holed graphite and the holed copper showed no signs of damage. However, the sample had a blue-brown coating on it as shown in the Figure 8.7. This is likely due to formation of WO_x formed during irradiation. Under oxidation, W usually forms WO_3 which is yellow in colour and forms rapidly. However, between 300 - 400°C, a blue thin layer of oxide is formed [137]. As the layer noticed on the sample is blue-brown in colour, this is indicative of the formation of WO_2 during irradiation. The solid graphite sample and the holed graphite sample release oxygen from the beam heating and deposition. Under low partial pressures of oxygen and irradiation temperatures, $WO_{2,x}$ is thought to have been formed which is seen on the sample. The bluish tinge seen in the colour also shown later in Figure 8.12 is understood to be an interference [137]. However, as these oxides are known to be formed above 300°C,

the finite element method based calculations are inaccurate or there is a irradiation induced accelerated oxide formation.



Figure 8.7: Sample before irradiation (left) polished to 1 μm and post irradiation (right) with an oxide layer.

Gamma spectroscopy is performed on the solid graphite and W sample. A HPGe (high purity germanium) detector of 30% efficiency is used to measure the gamma emission spectrum from the sample. The detector is cooled through a liquid nitrogen tank and has a 1 cm protective shielding around it to minimize background radiation. The spectrum is recorded using Gammavision software. A polynomial fitting as shown in Equation 8.1 is used to correlate channel (Ch) and energy (E) using standard nuclides such as ^{60}Co and ^{137}Cs . The efficiency of the detector system is measured using a combination of isotopes, ^{60}Co , ^{88}Y , ^{133}Ba and ^{241}Am . These isotopes have a known activity and specific gamma emission lines to construct an efficiency calibration curve. The efficiency is described by Equation 8.2, where E is the energy and Ef is the efficiency of the detector system at 80 cm sample detector spacing. The detector and the efficiency calibration curve are shown in Figure 8.8. The W and the graphite sample are placed 80 cm away from the detector to reduce the dead time to 3% and 4% respectively. All measurements were conducted for a total live time of 86400 s (1 day). As the measurement was conducted after 56 days of cooling time, post the last irradiation, the cooling time was correctly considered in activity calculations. A background spectrum is also recorded after packing up the samples in lead containers for the same live time to correct for the natural radiation around the detector. The background spectrum had a dead time of 0.04%.

$$E = 8.107 \cdot 10^{-9} Ch^2 + 0.2862 Ch + 0.4604 \quad (8.1)$$

$$\ln(Ef) = 111.2 - 125.2(\ln(E)) + 49.5(\ln(E))^2 - 9.3(\ln(E))^3 + 0.8(\ln(E))^4 - 0.03(\ln(E))^5 \quad (8.2)$$

While a quick decay is estimated for the graphite sample under proton irradiation, an unusual peak at 477.6 keV is noticed as shown in Figure 8.9. This peak belongs to the decay

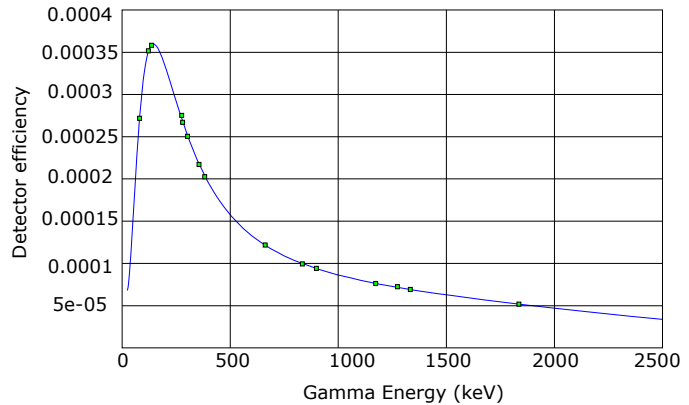


Figure 8.8: The gamma detector system and its calibrated efficiency curve using isotopes of known activity and specific high intensity gamma lines. The detector was calibrated for 80 cm.

of unstable ${}^7\text{Be}$ onto stable ${}^7\text{Li}$. The reaction results in an excited state of ${}^7\text{Li}$ which realises ground state by the release of 477.5 keV energy line. This is the result of the production of ${}^7\text{Be}$ from ${}^{12}\text{C}$ from protons of 25 MeV energies and above. Multiple production routes are possible and they along with their reaction threshold energies taken from [240] are listed in Table 8.2.

Reaction	Threshold energy
${}^{12}\text{C}(p, {}^6\text{Li}) {}^7\text{Be}$	24.5 MeV
${}^{12}\text{C}(p, \text{ } + \text{d}) {}^7\text{Be}$	26.1 MeV
${}^{12}\text{C}(p, \text{ } + \text{p} + \text{n}) {}^7\text{Be}$	28.5 MeV
${}^{12}\text{C}(p, \text{t} + \text{d} + \text{p}) {}^7\text{Be}$	47.6 MeV
${}^{12}\text{C}(p, \text{3d}) {}^7\text{Be}$	51.9 MeV

Table 8.2: The list of proton reactions on ${}^{12}\text{C}$ resulting in the production of ${}^7\text{Be}$ with their respective proton threshold energies taken from [240].

The activity of the sample is derived using net counts (C) under the 477.6 keV peak. The peak is fit using a Gaussian curve to the 477.6 keV gamma line. Considering a detector efficiency (ϵ) of 0.00015 estimated from Equation 8.2, a self absorption factor (f) of 0.95, in order to account for the self absorption within the graphite sample and a gamma emission intensity (I) amounting to 10.52%, the activity of the graphite sample is estimated as 24.6 MBq, using Equation 8.3.

$$\text{Activity} = \frac{C}{fI(1 - \exp^{-\lambda t_m})} \quad (8.3)$$

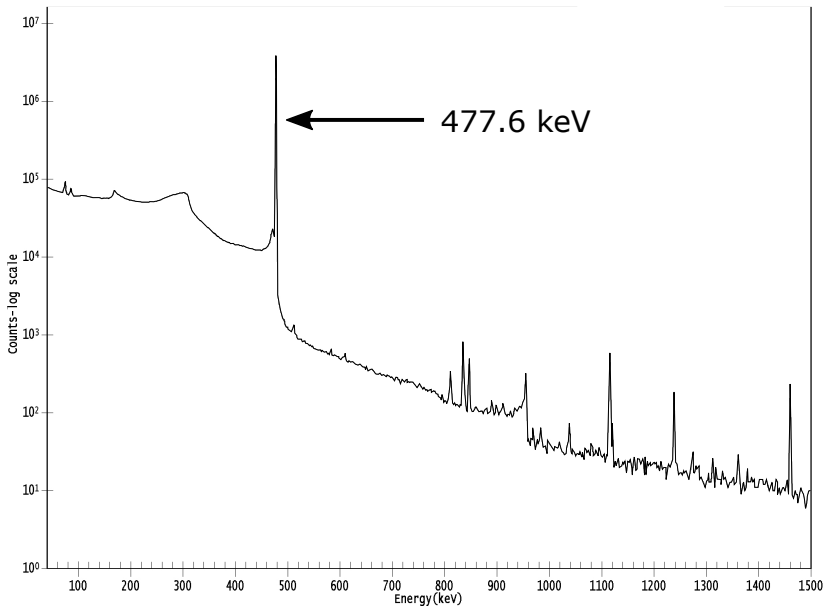


Figure 8.9: A clear 477.6 keV peak is seen on the gamma analysis of the graphite sample under proton irradiation. This peak is the result of decay of ⁷Be onto stable ⁷Li.

Here, the exponent \exp^{-t_m} accounts for the decay during measurement for time t_m which is 86400 s.

The production cross-section for ⁷Be from ¹²C is shown in Figure 8.10. Considering an approximate production cross-section (σ) of 10 mbarn for proton energies between 45 - 30 MeV, a beam current (I) of 1 A projected on a beam spot area (A) of 10 mm diameter, irradiation time (t_i) of 50 hours and an atomic density (N) of 4.43×10^{22} atoms.cm⁻³, the production activity can be approximated to 47.3 MBq using Equation 8.4. This is in agreement with the gamma analysis measured 24.6 MBq. Thus, the net irradiation of 50 A.hour coincides with the gamma activity of the graphite disk.

$$\text{Activity} = N \frac{I}{1.6 \times 10^{19} A} (1 - \exp^{-t_i}) \quad (8.4)$$

The production of ⁷Be or the 477.6 keV gamma line is a useful indicator and can be utilised to check for carbon contamination of the irradiated W samples. Also, to ensure that the blue-brown oxide coatings, are not traces of C deposition, gamma spectroscopy was also performed on a wipe from the sample's brown coating. It should be noted that vigorous scraping with pressure is performed in order to get a small portion of the oxide layer onto the wipe for testing. The characteristic peak of 477.6 keV is not seen on the wipe from the W surface which hints at the absence of any radioactive carbon on the W sample or the formation of tungsten carbide during irradiation. Even minute quantities of carbon irradiation would show up during the gamma analysis due to its high intensity gamma line. The gamma energy spectrum from the 16 MeV W sample (COSY_16M) is shown in Figure 8.11 which also doesn't show any gamma peak at 477.6 keV disproving any presence of carbide formation.

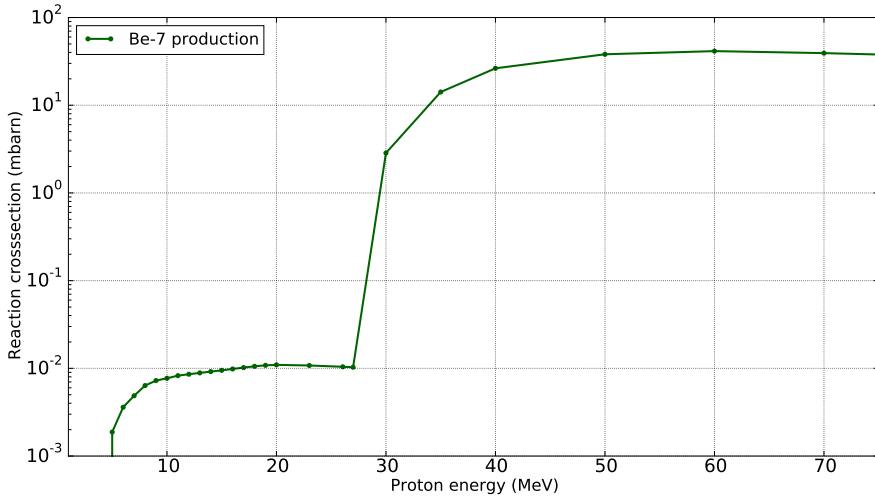


Figure 8.10: The production cross-section for ${}^7\text{Be}$ from ${}^{12}\text{C}$ plotted against incoming proton energy from [74]. The production sharply increases after 25 MeV for protons.

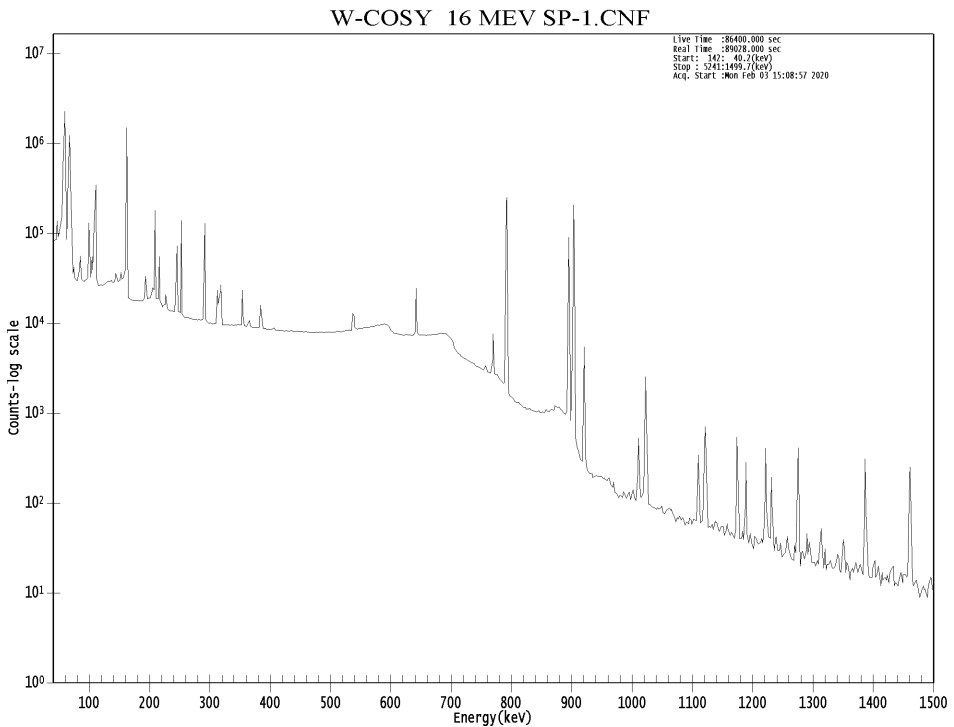


Figure 8.11: Gamma energy spectrum from the 16 MeV W sample post irradiation at JULIC. The spectrum was taken after a counting time of 86400 s.

The gamma analysis of COSY_16MeV W sample is entangled as most gamma lines (especially low energy) are a mixture of multiple nuclides. The gamma lines of ^{183}Re , ^{184}Re , ^{184m}Re and ^{182}Ta overlap as shown as an example in Table 8.3. To analyse the data the high energy gamma lines are analysed and fit using a Gaussian curve. Post detector system efficiency correction and self absorption corrections, the measured activity of the nuclides are shown in Table 8.4. The ^{183}Re is deduced from a low energy line of 162 keV energy and this could be

Energy (keV)	nuclide
1386.18	^{184}Re
1273.73	^{182}Ta & ^{182}Re
1257	^{182}Ta & ^{182}Re
1231	^{182}Ta & ^{182}Re
1221	^{182}Ta & ^{184m}Re
1189	^{182}Ta & ^{182}Re
1174	^{184m}Re
1010.3	^{184}Re
920.9	^{184m}Re
903	^{184m}Re & ^{184}Re

Table 8.3: List of high energy gamma lines which were used to estimate the production activity of the sample post irradiation.

Nuclide	Gamma analysis(Bq)				Simulated activity (Bq)	Ratio
^{184}Re	8.05	10^5	2.42	10^4	$1.42 \cdot 10^6$	0.57
^{184m}Re	8.79	10^4	2.61	10^3	$1.96 \cdot 10^5$	0.44
^{183}Re	9.22	10^5	2.76	10^4	$1.03 \cdot 10^7$	0.09
^{182}Ta	3.38	10^3	1.24	10^2	$9.91 \cdot 10^1$	50

Table 8.4: The activity of major nuclides measured by gamma analysis compared against simulated using FISPACT-II and TENDL-2015 cross-sections after a cooling period of 56 days post last irradiation. ^{182}Ta formation is 50x higher than that predicted. However, the Re isotopes show good conformity.

the reason for the deviation from predicted simulation result. Especially seen as the high energy line based measurement of ^{184}Re and ^{184m}Re isotopes show good agreement. However, a stark contrast is noticed between the ^{182}Ta measurement and simulation. A possible reason for this could be the lack of correct cross-sections. Production of ^{182}Ta is a result of (p,2p) and (p,2p+n) reactions on ^{183}W and ^{184}W respectively. While high energy proton measurements exist, only theoretical values are available below 50 MeV proton energies [241]. However, a peak in the production cross-section is noticed in TENDL-2015 at 20 MeV [241]. It is possible

that this peak extends below 20 MeV and is not calculated by TENDL-2015, due to which such a large discrepancy is noticed. In the measurement of ^7Be described earlier, the approximated activity is 2x of the measured, which differs from the W gamma measurements. However, all comparisons lie with a factor of 2 - 5x difference. Further detailing of the sample holder with precise flux calculations is considered to close this discrepancy.

Post irradiation the sample was transported in a 32 mm thick lead container into the HML for testing. The proton flux calculated using MCNP6.1 [164] is used along with TENDL-2015 [132] cross-sections as an input for FISPACT-II [90]. Using the appropriate irradiation schedule for the sample and the cooling times (listed in Table 8.1), the total sample activity is estimated by the software. Using them as an input in nucleonica dose rate calculator [234], dose rates are extracted and compared to the measured as shown in Table 8.5.

Description	Simulated mSv.hr ⁻¹	Measured mSv.hr ⁻¹
COSY_30MeV dose contact	28.25	18
COSY_30MeV dose beyond lead shielding	0.41	0.23

Table 8.5: Simulated and measured dose rate measurements for the radioactive sample for in contact with the sample holder (about 2 cm away from the sample which includes 0.5 cm of Copper disk) and in direct contact to the edge of a 3.5 cm lead shielding.

Optical microscopy of the samples revealed oxide formation on all of the samples however in varying proportions. An overview of the sample COSY_16MeV and COSY_30MeV taken post transport is shown in Figure 8.12. The blue-brown oxide coating can be seen on both samples. However, the coating isn't uniformly distributed. The 30 MeV proton irradiated sample COSY_30MeV is observed to have a higher deposit and surface darkening as compared to the 16 MeV sample, COSY_16MeV. This could be due to its proximity to the graphite samples, which are thought of being the source of oxygen. The arrow in Figure 8.12(a) points to a hole in the oxide layer formed. This corresponds to the hole in the Cu disk placed above the sample. Thus, there exists a link between the oxide layer generation and the Cu disk contact. Further investigation using EDX would be beneficial to understand this link, however is presently not possible on activated samples.

The difference in oxide formation is related to the immediate contact layer of the sample. The faces of both samples in contact with the Cu disk show a larger extent of darkening as against facing each other. This is seen in Figure 8.13 for COSY_16MeV and COSY_30MeV samples. Once again an irradiation based crack network is seen on the 16 MeV sample (COSY_16MeV). The oxide formation is seen to propagate along the crack boundary. On this occasion, the heat flux is 10x lower as the beam current was 1 A as against 10 A, which indicates that the crack network is a result of irradiation conditions. Surprisingly, the 30 MeV sample shows no crack network development.

Instrumented indentation measurements are performed on the samples COSY_30MeV and COSY_16MeV. A maximum load of 15 N is applied during each indent and held at maximum load for 12 s, as conducted previously. The loading rate is selected as 0.1 N.s⁻¹ while the load removal rate is set at 0.3 N.s⁻¹. At the final stage, just before contact, the speed of the contact is selected to be 0.5 mm.min⁻¹. Other important parameters for the indentation are tabulated in Table 8.6. 95 - 50% of the force-displacement curve is fit using a Levenberg-Marquardt (least square) fit [228]. The results of the indentation for each sub sample and the average are shown in Table 8.7.



(a) COSY_30MeV sample



(b) COSY_30MeV oxide layer



(c) COSY_16MeV sample



(d) COSY_16MeV sample oxide layer

Figure 8.12: An overview of the samples post transport to the hot material laboratory. The blue brown coating on W is clearly seen on the sample.

There is no difference seen in the indentation curves, such as sudden sharp rises or falls. Moreover, no cracking of the surface or any optical changes were noticed post indentation. Thereby, it is assumed that the oxide layers did not affect the indentation measurements. In general the 16 MeV sample show a larger hardening as compared to the 30 MeV samples. The unirradiated samples consistently tested at an average indentation hardness of 5.56 ± 0.24 GPa. An increase of 0.48 ± 0.26 GPa is seen for 30 MeV proton irradiation on to a dose of 0.003 dpa. While the increase for 16 MeV proton irradiation is measured at 0.71 ± 0.26 GPa for a

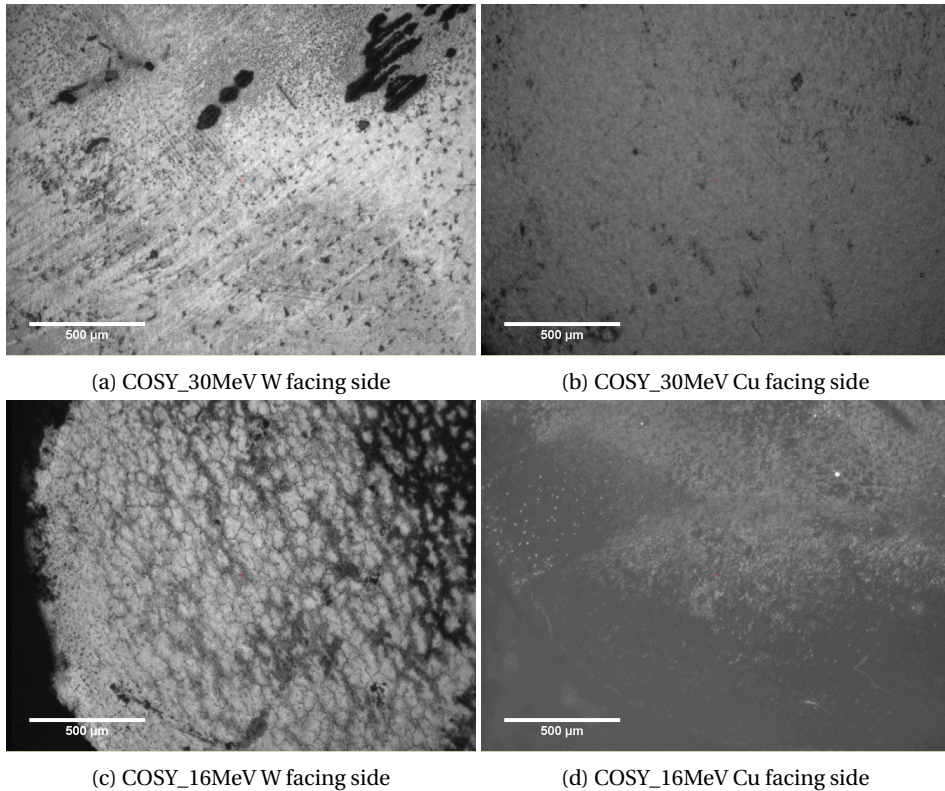


Figure 8.13: Comparison of the oxide formation on the sample faces. The oxide formation (darkening) seems to be higher on the side in contact with the Cu disk.

Description	Input
Approach speed	0.5 mm.min ⁻¹
Zero point determination	0.2 N
Loading rate	0.1 N.s ⁻¹
Unloading rate	0.3 N.s ⁻¹

Table 8.6: Inputs for macro-indentation of COSY_16MeV and COSY_30MeV samples.

damage dose of 0.007 dpa. Also, the indentation hardness of sample COSY_16MeV at 6.27 0.1 GPa compares well with the hardness 6.35 GPa reported using the tensile sample from the irradiation on the Baby cyclotron to a dose of 0.006 dpa.

The simulated transmutation build-up from FISPACT-II calculations of 30 MeV and 16 MeV proton irradiations post irradiation is shown in Table 8.8. Considering the good conformity to the gamma measurements, the Re concentration can be relied upon. A similar concentration of 0.37 appm (vs 0.26 appm) of Re is seen as compared to the previous irradiation at the Baby cyclotron using a different irradiation schedule. The 30 MeV protons irradiations produce a higher concentration of transmutation as compared to the 16 MeV proton irradiations. The

Sample	Indentation hardness (GPa)	
Unirradiated	5.56	0.24
COSY_16MeV_SP1	6.71	
COSY_16MeV_SP2	6.14	
COSY_16MeV_SP3	6.28	
COSY_16MeV_SP4	5.99	
COSY_16MeV_Ten	6.23	
COSY_16MeV	6.27	0.1
COSY_30MeV_SP1	6.07	
COSY_30MeV_SP2	6.35	
COSY_30MeV_SP3	6.56	
COSY_30MeV_SP4	5.56	
COSY_30MeV_Ten	5.73	
COSY_30MeV	6.04	0.1

Table 8.7: Measured indentation hardness for cyclotron irradiated samples COSY_16MeV & COSY_30MeV. Indents were made on each sub sample and the average is shown along with the standard error of the mean.

Re content from 30 MeV protons is estimated as 1.94 appm for 0.003 dpa dose while, the 16 MeV protons produce 0.37 appm of Re for 0.0075 dpa dose. In this damage range, the micro-structure starts to show damage based changes in terms of dislocations loops. For low quantities of Re, no large jumps in hardness are expected. This is seen in the hardness comparison between COSY_16MeV and COSY_30MeV. Even though the Re content is different, no major changes in hardness is noticed. Upon increasing the Re content, i.e. higher dosage with 16 MeV (low Re) and 30 MeV (high Re), we could get clarity and infer appropriate Re based combined damage formation and evolution in W.

Further tests are planned using the high current 30 MeV accelerator to higher doses. This would allow the build-up of Re and Ta to influential quantities. An important pre-step to the next irradiation would be the heat treatment under vacuum conditions to avoid the build-up of oxides. The present irradiation has also displayed the ability of simulation programs to optimistically predict the build-up of transmutation elements through proton irradiation. Additionally, further investigations into the micro-structural changes within W due to proton irradiation are planned to be undertaken.

Summary of 30 MeV proton irradiation

A 30 MeV proton irradiation of a 500 μ m thick W sample, COSY_30MeV was carried out at the JULIC cyclotron to a dose of 0.003 dpa, under a dose rate of 1.75×10^{-8} dpa/s. The energy of the protons exiting the sample COSY_30MeV was found to be 15 - 16 MeV. Thereby a

Element	16 MeV (appm)	30 MeV (appm)
Re	0.37	1.94
Os	0.003	0.005
Ta	0.003	0.04
He	0	0.03
H	0	0.09

Table 8.8: FISPACT-II simulated transmutation contribution for 16 & 30 MeV proton irradiated W.

second W sample of 350 μm thickness was placed directly underneath COSY_30MeV sample, within the same sample holder and was irradiated by 16 MeV protons. Thus, the irradiation of the two samples COSY_30MeV and COSY_16MeV were performed in tandem. Sample COSY_16MeV registered a damage dose of 0.0075 dpa under a dose rate of 4.2×10^{-8} dpa/s. The sample holder arrangement used was similar to that of the Baby cyclotron design, albeit without the in-situ thermocouple measurement. Post irradiation gamma measurements were conducted using a HPGe gamma detector. The measured gamma activity was compared to the MCNP6.1 and FISPACT-II simulations and showed good agreement (within 2x) for the Re isotopes. This result proves that it is possible to use the simulation conducted here to correctly estimate the transmutation behaviour.

Due to the higher energy of protons in JULIC to that generated by the Baby cyclotron, (30 MeV vs. 16 MeV), production of ^7Be from graphite is observed. As the gamma measurements of W show no presence of ^7Be , the formation of tungsten carbide can be effectively negated. Both, COSY_30MeV and COSY_16MeV samples showed irradiation hardening. An increase of 0.48–0.26 GPa was seen for 30 MeV proton irradiation for a dose of 0.003 dpa, while the increase for 16 MeV proton irradiation was measured to be 0.71–0.26 GPa for a damage dose of 0.007 dpa. Moreover, the indentation hardness of sample COSY_16MeV at 6.27–0.1 GPa compared well with the hardness of 6.35 GPa reported using the tensile sample from the irradiation in the Baby cyclotron to a dose of 0.006 dpa. The stability of the sample holder under long term irradiation (50 hours) has demonstrated the feasibility of conducting further irradiations. Combined with simulations and post irradiation analysis, this study has set the foundation for the analysis of fusion neutron damage using 30 MeV protons.

Chapter 9

Cold neutrons

Radiation induced precipitation and metallurgical changes of phases are associated commonly with neutron damage. Early examples of observations regarding Re precipitation in W are from the instability seen in W-Re thermocouples. They were used for high temperature fission neutron studies and underwent property changes which have been recorded [242],[243]. Post fission neutron irradiation, a high density of Re precipitates with acicular shape are found in pure W samples [244]. These precipitates contain between 12 - 25 atom% Re. This is far below the solubility limit of Re in W as shown in the phase diagram 9.1. The precipitates are accompanied with a sharp increase in hardness of the material. While displacement damage can be accessed through the use of low energy protons or heavy ions, the influence of pure transmutation of W isn't fully understood.

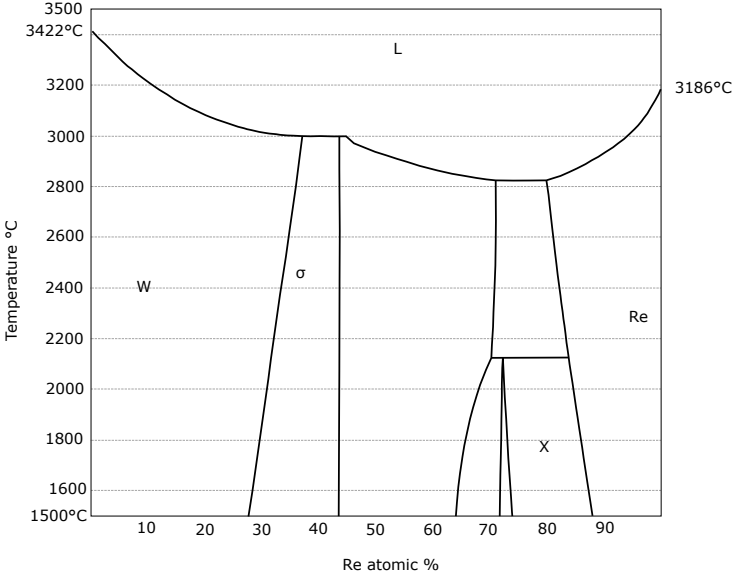


Figure 9.1: W-Re phase diagram adapted from [245]. Re is soluble to a high extent in W and forms of phases, however under neutron irradiation, precipitation far below solubility limits is known to occur.

Recent studies have attempted to associate vacancy concentrations and movement with the precipitation of Re into clusters [158]. Post irradiation has indeed observed the presence

of voids surrounded by Re precipitates. However, the ion experiments [179] have shown no excess vacancies in spite of Re precipitate formation. There is a notion that the self-interstitial atoms in BCC W form a highly mobile bond with the transmuted Re atoms and this is the start of Re clustering [246]. Understanding the formation of precipitation and its role in irradiation hardening is important. While a number of experiments in test reactors have been performed to understand the behaviour of Re in W, no concrete experimental proof or validity has been achieved. In order to understand this relation, an experiment involving cold neutrons was started in collaboration with Technical University of Munich and the Forschungs-Neutronenquelle Heinz Maier-Leibnitz (FRM II) reactor.

Cold neutrons have energies ranging from 10^{-9} MeV to 10^{-7} MeV. At such low energies, the neutrons travel slowly through the material and as such have an increased chance of material interaction. For most metals the displacement threshold is around 10^{-5} MeV and cold neutrons are 100 - 10000x lower energy in comparison. Thus, the cold neutrons can't introduce any displacements into the material. The cold neutrons on the other hand have large capture cross-sections and will introduce large transmutations. In order to reduce the resulting activity from the transmutation, the isotope ^{186}W was selected for experiments. The advantages are as follows:

- ^{186}W has one of the largest isotopic abundances among the natural W isotopes. This makes it easier to enrich.
- ^{186}W has the largest (n, γ) cross-sections amongst all the W isotopes.
- The capture reaction with ^{186}W would result in largely ^{187}W which has a half-life of 23.7 hours and thereby decays very quickly into stable Re, thus enabling post-mortem analysis in regular laboratories.

Using the no lattice damage from cold neutrons along with their increased transmutation behaviour, the association of W-Re atoms is likely. While no physical changes might be attributed, using TEM and atom probe tomography, a detailed observation under pure transmutation is attempted in this long-term study.

9.1 Sample preparation

The sample was prepared using green part pressing and pressureless sintering process under reducing atmospheric conditions. This method was selected for being the cleanest amongst other methods such as powder injection moulding (carbon binder contamination), hot isostatic press sintering (Ta-W solid solution) or spark plasma sintering (carbon deposition). Initially, centrifugally enriched isotopically pure W powder, ^{186}W was obtained from STB Isotopes GmbH, Germany. The average powder size ranged from 5 - 8 μm as seen in Figure 9.2. The powder has an isotopic purity of 99.9 \pm 0.1% and a chemical purity of 99.1 \pm 0.1%. The chemical purity was confirmed using ICP-MS and is shown against the manufacturer's specification in Table 9.1. The isotopic purity was also measured using ICP-MS and is shown against the natural composition and manufacturer's specification in Table 9.2.

The powder was initially pressed using a clean hardened steel punch and die into pellet form. Pressing was performed at room temperature in air. The applied pressure was increased in steps to a maximum of 7.5 tons/cm². At each pressure step, a holding time of 3 minutes was undertaken. Release of pressure was also conducted in steps. W being one of the strongest

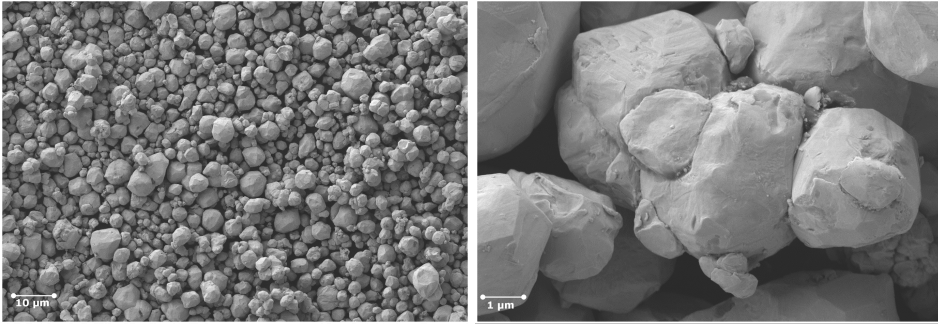


Figure 9.2: Scanning electron microscopy of isotopically pure ^{186}W powder which has an average powder size between 5 - 8 μm .

Element	Manufacturer's spec. ($\frac{\text{g}}{\text{g}}$)	ICP-MS ($\frac{\text{g}}{\text{g}}$)
Al	30	< 9
As	300	< 0.8
B	20	< 40
Ca	80	< 30
Co	100	< 2
Fe	240	5
Mg	30	2.6
Mo	80	1.4
Na	30	< 70
Ti	60	7
Zn	60	4
Zr	0	8

Table 9.1: The chemical purity was measured using ICP-MS. This was specifically done to confirm special isotopes which have large capture cross-sections for cold neutrons. Consider the upper limits of ICP-MS measurement, the sample is stated to have a chemical purity of 99.6%.

metals, couldn't be adequately pressed at the edges, although the center of the green sample was stable.

Subsequently to pressing, the sample was sintered. The sintering was performed in hydrogen atmosphere to prevent any formation of tungsten oxide (WO_2 or WO_3). The sintering time is a function of the sintering temperature as seen in Figure 9.3 adapted from [247]. In order to achieve high relative densities in short periods of time, a temperature higher than 2000°C is essential. Such high temperatures are normally achieved in graphite lined ovens. However with W, the formation of tungsten-carbide occurs, which needs to be avoided at all cost. At high temperatures, W also reacts aggressively with most materials. Pure metals which

Isotope	Natural comp.(%)	Manufacturer spec.(%)	Measured(%)
^{180}W	0.12	0.01	0.0002
^{182}W	26.5	0.01	0.029
^{183}W	14.3	0.01	0.016
^{184}W	30.64	0.15	0.17
^{186}W	28.44	99.82	99.78

Table 9.2: The isotopic composition measured using ICP-MS is compared against the natural isotopic composition and the manufacturer specifications. The isotopic purity of the ^{186}W is measured to be 99.78%.

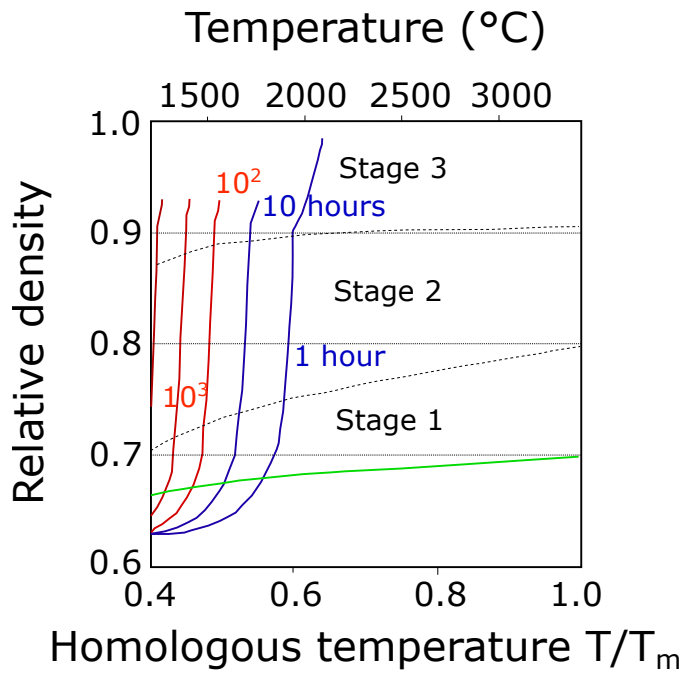


Figure 9.3: Sintering density diagram adapted from [247] for W spheres. With increasing density and temperature, the sintering time reduces drastically.

have higher melting points are soluble in W while commonly used ceramics such as Al_2O_3 or BN are reactive at high temperatures. The only stable ceramics which do not react with W at high temperatures are ThO_2 and UO_x in hydrogen atmospheres [248]. However most laboratories avoid them due to their natural radioactivity. The alternative of sintering within a W-lined oven was finally considered, however it shouldn't contaminate the isotopic purity of the

sample. The self diffusion in W is relatively small as shown in Equation 9.1 taken from [249].

$$D = 0.04 \exp\left(\frac{5.45}{kT}\right) - 46 \exp\left(\frac{6.9}{kT}\right) \quad (9.1)$$

Using, $k = 8.617 \times 10^{-5}$ and $T = 2273$ K, the diffusion amounts to 0.04 m^2 in 2 hours. Thereby the green part is sintered in a W oven and then checked for contamination. Sintering is performed in two stages; the first being a pre-sintering process at 1800°C for 2 hours and next the actual sintering at 2200°C also for two hours. Post sintering the sample measured 9.4 mm in diameter and 600 m thickness. The density was measured to be 91% using balances and the Archimedes's principle. Atom probe tomography (APT) was used to check on the sample post sintering. The surface showed no contamination prior to APT. Four samples were prepared and analysed using the laser mode at 250 kHz pulse frequency, 100 pJ pulse energy and a base temperature of 50 K . The results are shown in Figure 9.4. Ga^+ used for cutting the sample for analysis was found on the surface but neglected from the analysis. O, C and N atoms were found as impurities. The nitrogen was found to show tendencies of grain boundary segregation, while carbon was randomly distributed. Oxygen was also found to be homogeneously distributed in the sample. The evaluated composition is shown in Table 9.3.

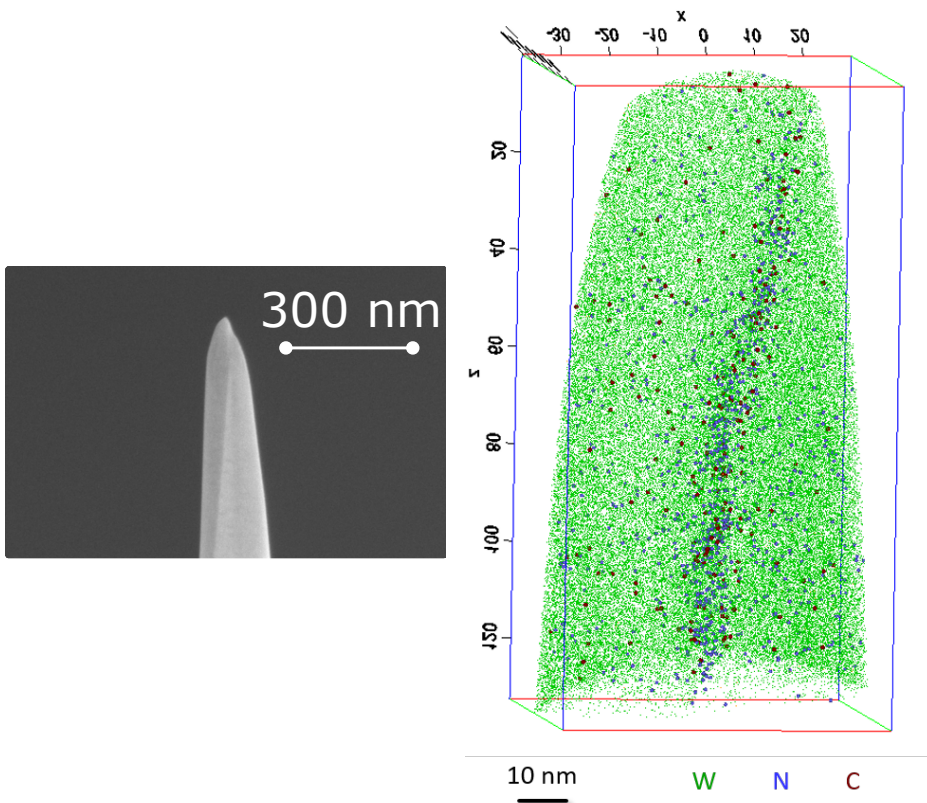


Figure 9.4: Atom probe tomography on the ^{186}W sample post sintering with a grain boundary within the sample. The carbon and nitrogen are seen to segregate near the grain boundary.

Entity	at%
186W	99.8
W (other isotopes)	0.2
O	0.03
N	0.01
C	< 0.01

Table 9.3: Composition of sample post sintering tested by APT using the laser mode. O, C and N atoms were found to be present within the sample.

9.2 Irradiation stations

FRM II is one of the most advanced neutron sources having multiple beam lines for advanced scientific experiments. The reactor is built on the concept of a single fuel element which surrounded by a pool of heavy water which significantly moderates the neutrons. The reactor also consists of a hot source (heated graphite block), a cold source (liquid deuterium) and a planned ultra cold source for scientific experiments. It also has a number of irradiation facilities for doping and industrial applications [250]. The schematic of the lines along with the sources is shown in Figure 9.5 taken from [251].

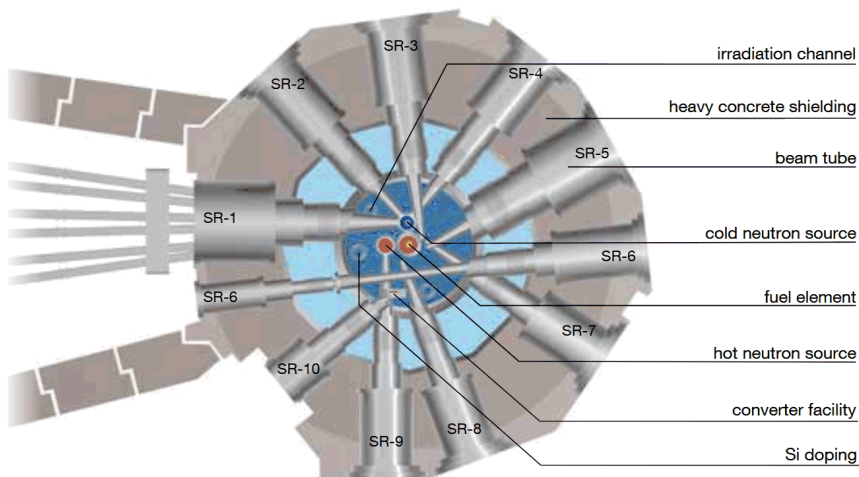


Figure 9.5: A schematic of the beam lines along with the sources taken from FRM2 experimental facilities brochure. The beam lines can be seen to originate along the hot source and the cold source based on experimental requirements.

The neutrons are immensely slowed down by the cold source. A number of beam lines in the immediate surrounding of the cold source extract these low energy neutrons to their scientific experiments. Two experimental stations are considered for the cold neutron W irradiation. SR4B is a high flux location at the end of guide tube SR-4. As seen in Figure 9.5, this guide tube looks directly into the cold neutron source and thereby has a high cold neutron

flux. However, as it is a straight view into the reactor, the neutron spectrum consists of thermal and fast neutrons from the fuel element near to the cold source. The other station NLC3 is part of a sub-beam line section of SR-1. This beam line gently curves at a radius of 460 m into the station NLC3. The cold neutrons are reflected alongside the polished specially designed beam lines during this curvature, while thermal and fast neutrons are lost. Thus a pure cold neutron spectrum however at a lower flux is found in station NLC3. The flux is computed using the McStas comparison for both stations is shown in Figure 9.6. As both stations are within the same reactor, a comparison between the two irradiations could additionally benefit post irradiation understanding of pure transmutation damage in W and the reasons behind the different behaviour of Re originating from alloying and transmutation.

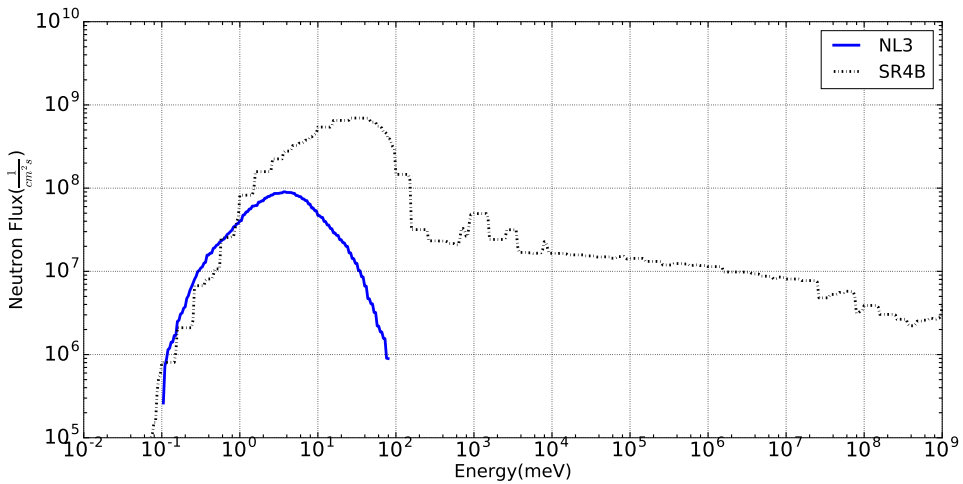


Figure 9.6: Flux comparison between the NL3 and SR4B stations at FRM II reactor in Munich. SR4B looks directly into the cold source, it has a higher flux albeit also thermal neutrons.

The use of SR4B station was authorised for two reactor cycles while the NLC3 for 6 cycles of 30 days each. SR4B integral flux is estimated as $4.82 \cdot 10^{10} \text{ n.cm}^{-2}\text{s}^{-1}$ while NLC3 is estimated to be $5.07 \cdot 10^9 \text{ n.cm}^{-2}\text{s}^{-1}$. Using the fluxes from SR4B and NL3 stations a FISPACT-II analysis is carried out for the ^{186}W with impurities. The dose rate calculations post irradiation for both stations are shown in Figure 9.7 with the background marked in red. The doses are seen to drop quickly and within 15 days are lower than 1 Sv.hr^{-1} . In 180 days they reach handling levels for post irradiation treatment. With every cycle the Re is built in from the transmutation reactions into the W sample. FISPACT-II calculations using TENDL-2015 cross-sections estimate a Re production between 30 - 40 appm. While these are far below the fission reactor produced compositions of 5% and higher or 30 MeV proton irradiation estimated 700 appm, a trend might already be observed within the sample. The atom probe tomography is able to measure Re at these levels.

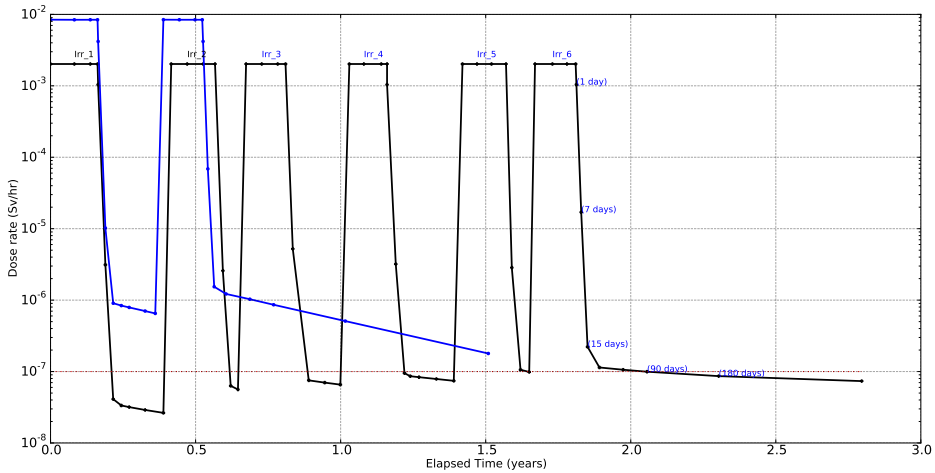


Figure 9.7: Dose rate calculations for SR4B station (blue) and NLC3 station (black) samples with the background environmental radiation indicated in red. The dose rates are calculated for a point source at a distance of 30 cm away. A pure cold neutron flux reaches near background radiation dose rate within a cooling period of 180 days.

9.3 Sample assembly

Sample assemblies for reactor irradiations require careful consideration in terms of material selection. The material selected as the sample holder should have low activation properties and short half lives for reaction products. The sample holder also should not significantly alter the neutron energy and spectrum of the incoming reactor neutrons. Reactor grade Aluminium having a low amount of Manganese as an additive is considered an ideal material for sample holders. The (n, γ) reaction with ^{27}Al creates ^{28}Al which has a half life of 2.24 minutes. Al foils of various thickness are used as the material for the sample holder and two different configurations are used for the sample irradiations at SR4B and NLC3.

The SR4B sample is installed at the removable beam stop plug at the reactor end inside the concrete shielding. The beam stop is covered by an Al plate of dimensions 213 mm \times 241 mm, which is replaced by the sample assembly. An image of the beam stop plug and the sample assembly construction is shown in Figure 9.8. The sample positioning revolves around replacing the Al window with an identical one, containing two horizontally laser cut slits. This slitted window is made out of 1 mm thick 99.8% Al sheet. The W sample being small and brittle, is first placed into a proportionally holed 1 mm thick Al sheet of 40 mm \times 40 mm. This is to hold the sample vertically in position during neutron irradiation. Subsequently, the sample containing Al sheet, is further wrapped in an Al pouch. A packaging wrapper (Al foil) of 100 μm forms a pouch around the sample and prevents it from falling out. This wrapper is further inserted into the slits of the Al window which makes up the window of the beam stop element. The entire assembly makes for a simple yet mechanically robust sample positioning which can be easily removed and replaced by the Al window post irradiation.

NLC3 station is located within an unused beam line which leads to the cold neutron source. The sample assembly is located on a shutter system which can slide into the beam location and is under vacuum conditions of 10^{-2} mbar pressure as shown in Figure 9.10. The shutter system has a Boron carbide plate on which the sample holder is hung. A sample

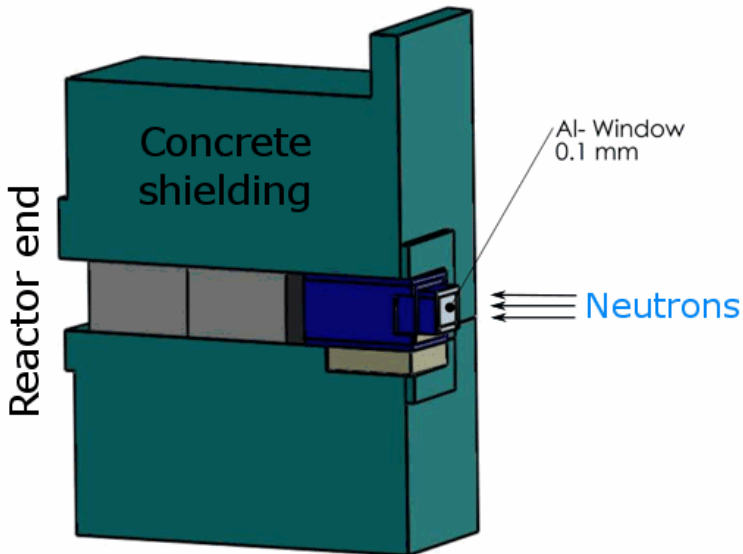


Figure 9.8: The SR4B station is located at the end of a beam line at the end of the reactor complex. The Al window is part of the shielding and is replaced with our sample setup.

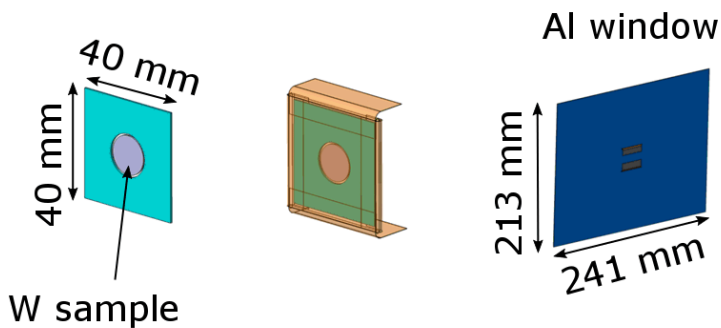


Figure 9.9: SR4B sample installation schematic. The Al windows shown in Figure 9.8 is replaced with an identical window shown in dark blue. The sample sits inside a pouch which is held and fit onto the Al window using slits for easy removal post irradiation.

pouch is constructed using 0.5 mm thick aluminium (Al) sheet. It is wrapped around with a 0.25 mm Al sheet where the sample is placed and held firmly within the pouch. A cut-out on the incoming neutron side of the pouch allows maximum flux to the sample centre and simultaneously binds the sample to avoid any displacement. This Al pouch is firmly bent around the top of the boron carbide plate and is held in place with the stopper from the shutter wagon. Figure 9.11 shows the sample assembly as in the reactor.

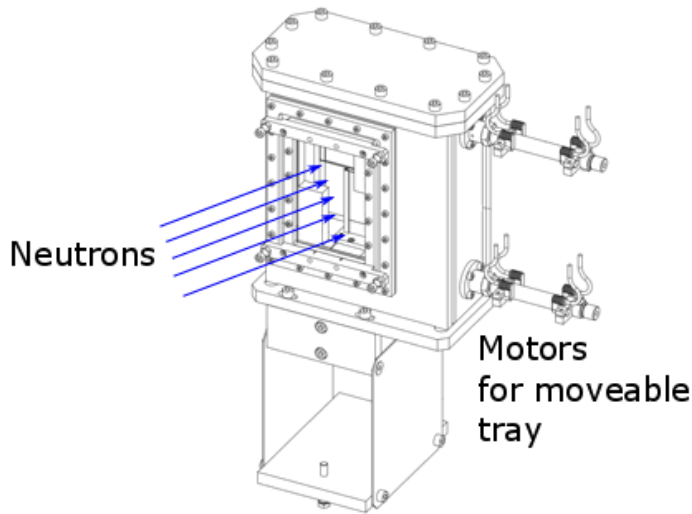


Figure 9.10: The NLC3 station with a sliding shutter system operated by motors.

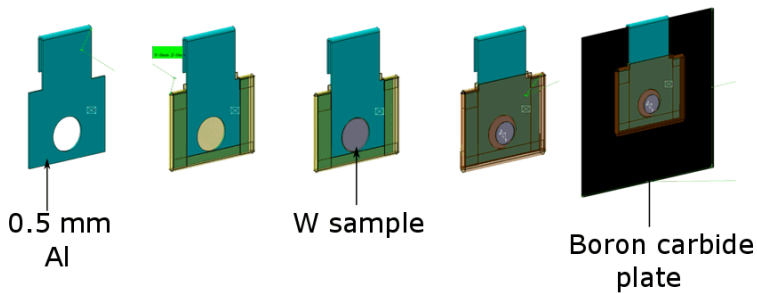


Figure 9.11: NLC3 station sample assembly schematic in the reactor for the pure transmutation damage study at FRM II. The sample sits inside a pouch covered by Al foil and loaded onto the boron carbide plate on the sliding shutter.

9.4 Proposal and discussion

Under neutron irradiation, W transmutes into Re, resulting in a change in the microstructural composition. Two years of DEMO neutron irradiation results in the formation of over 1% Re, as seen in Figure 2.8. TEM investigations have revealed a strong clustering and precipitation of the Re atoms, however, this precipitation of Re occurs far below the solubility limit of 27% [252] and has been observed in many reactor irradiations [84],[154], [85], [70] etc.. In fact, to date, a large discrepancy exists in identification of the Re phase formed during neutron irradiation of W [253]. The clustering and precipitation has been further linked to a steep increase in irradiation hardening [70] and is known to suppress void formation in W. Initially, the solute atom moving with the interstitial atom was thought to mix with the

vacancy-solute pair, accelerating the clustering of Re in W. However, Re is found to occupy grain boundaries [158], and a combination of APT and STEM-EDX confirmed these results, highlighting the fact that the formation of precipitation is still not understood [254]. A W-Re 3d dumbbell motion has been simulated and is considered to be the prime reason for precipitate formation in W [169].

There is a need to understand the interplay between Re and W under neutron irradiation. Many first principle studies are based on fission reactor irradiation experiment results. However, the aim of fission reactor studies is to assimilate and simulate DEMO relevant neutron damage for material property changes. The first principle studies are system dependent and can simulate upto a few hundred atoms and are unable to simulate fission neutron damage. Also, due to the multi damage nature of fission studies, they do not provide the necessary inputs for first principle studies. Using cold neutrons, Re is introduced without any displacement damage or creation of additional vacancies(point defects) within the sample. To date, no study has been undertaken on pure transmutation damage in W and in this endeavour, both W(interstitial)-Re motion and vacancy-Re bonding will be investigated. Additionally, without displacement damage, the interstitial to Re ratio is largely reduced, which alters the experiment with respect to fission irradiations. Under such a change, inputs for the 3d dumbbell motion of W-Re atoms are expected. However, certain open questions remain regarding the experiment, such as, if the 30-40 appm of Re produced is significant enough to observe a difference in micro-structure.

In this study, two parallel experiments are setup at two different stations; SR4B and NLC3, within the FRM2 reactor. The experiment SR4B, records the influence of combined displacement and transmutation damage while the NLC3 records pure transmutation damage at the same reactor. The use of ^{186}W registers a quick fall in dose rate post irradiation and the sample can be safely tested without any radiation control after a short cooling period of 3 months. However, the experiment is set to undergo 6 cycles of 30 irradiation days at its minimum. The reactor registers 2 - 3 cycles a year. Accounting for certain delays, the irradiation of the samples is scheduled to run until 2022, and consequently, the post irradiation analysis lies outside the scope of the present work.

Chapter 10

Concluding discussion

Neutron irradiation is known to induce drastic changes in material behaviour over time (dose). These changes lead to deviation from the correct functionality of the material and eventually result in the early onset of failure. To avoid such a scenario, it is essential to identify and quantify the changes in material property over neutron dose. Currently, no high flux fusion neutron source exists to test and qualify materials under fusion relevant neutron damage. Consequently, fission reactor studies and ion damage simulations are carried out to understand the changes in micro-structure upon irradiation.

Ion damage is experimentally versatile and can be used to study specific damages, such as high energy cascades, or the influence of voids etc. The selection of the ion and its energy determines the type of damage and its range of investigation. For instance, self ions create pure displacement damage in the sample, with large cascade development within a shallow range of damage and are mostly limited to under 2 μm range in W. Protons on the other hand have a larger range of penetration and thereby investigation. With increasing energy, the range of investigation also increases. For example, 3, 16 & 30 MeV protons have a homogeneous investigation range of 15, 300 & 500 μm , respectively in W. Thus, macroscopic damage can be realised using protons. The damage is dispersed over a larger area with lower scattering density as compared to self ion damage. Additionally, with increasing energy, protons can induce transmutation reactions similar to those of neutrons, leading to a combination of displacement and transmutation damage. The threshold for W is seen to be at 3 MeV proton energy. Selection of the appropriate proton energy above the threshold would enable closer approximation to fusion relevant compositions. In this study, the best suiting energy was noted to be around 30 MeV for W. However, similar to neutron irradiated W, the samples are radioactive and require special radioactive permits and handling.

The active nature of the samples within this work required engineering and redesign of samples, holders, sample handling equipment and testing methods. Such challenges were overcome with a complete pre-irradiation, irradiation and post irradiation comprehension. Conformity to radiation safety principle ALARA (as low as reasonably achievable) was always followed to reduce exposure to personnel and machines. The use of nuclear codes MCNP6.1, FISPACT-II was undertaken to pre-estimate the activity and dose rate of the samples. The entire sample assembly was designed to include the secondary neutron activation effects. Close conformity of Re isotope production was measured and confirmed within 2x of simulation estimates using gamma measurements, a reasonable agreement considering uncertainties of input cross-sections. Consequently, the Re content estimated for 30 MeV protons matches fusion estimates within a factor of 5x. Additionally, using SPECTRA-PKA and TENDL-2015 cross-sections, the recoil PKA spectrum from 30 MeV protons was compared against the

DEMO neutrons. As the recoil cross-sections have a lower cut off at 5 keV, a high energy biased average PKA energy range between 20 - 145 keV was seen for 30 MeV protons on W. This compares well with the average PKA energy range of 2 - 85 keV estimated for fusion energy neutrons and enforces the ability of 30 MeV protons to replicate high energy PKA and cascade formation similar to fusion neutrons.

A sample holder was designed using 3 mm disks to reduce overall activity, while supporting power loads of at least 160 W for high damage rates. The samples are complementary to fission reactor irradiations. Their thickness is macroscopic ranging from 300 μ m to 550 μ m for 16 MeV and 30 MeV respectively. This is comparable to fission reactor irradiations which have sample thickness between 250 μ m to 4 mm. In order to have redundancy towards irradiated material property measurements, four individual 3 mm disks were placed in each experiment along with a tensile sample. This leads to multiple samples irradiated under the same irradiation conditions, which can be subjected to testing. Additionally, Cu and graphite disks were added to absorb the radiation at the outer casing for easier handling. A thermocouple based in-situ temperature measurement was installed with the sample. This is the first time a solid state in-situ temperature measurement has been attempted in a medium energy cyclotron. It was also shown to represent the correct irradiation temperature using Ansys calculations.

Irradiated sample testing was also set up within the scope of this work. Instrumented indentation was set up for hot cell implementation, while a new design for shear punch testing was constructed. Instrumented indentation and Vickers hardness testing are standard methods of testing used for self ion irradiation testing and fission irradiation testing. Punch testing has gained acceptance over the last 2 decades and is linked with tensile testing for irradiated material studies. The data acquisition for both methods was modified in order to be hot cell compliant. Methods for remote calibration using standardised samples of given hardness were tested. Moreover, in the course of this work numerous operational modifications such as the offset based shear punch sample holder die or a pneumatic sample handling pen towards easier remote handling operation, were undertaken. This practical aspect is crucial for enabling the testing capabilities of active samples in a hot cell, remote handling environment. This study has focussed on the proton irradiations and post irradiation work as outlined above. In parallel, nuclear engineering of solutions for radiation exposed work with proton activated samples is accomplished.

Eight samples were irradiated at a tandem accelerator using 3 MeV protons and at two different cyclotrons using 16, and 30 MeV protons. The 3 MeV irradiated samples are subject to pure displacement damage, similar to self ion irradiation. As no transmutation is induced within the sample, they are inactive and can be readily analysed. TEM observations on the 3 MeV irradiated sample in comparison to self ion irradiation and fission neutron irradiation (HFIR) is shown in Figure 10.1. The difference in temperatures should be noted as this is an important factor for irradiated micro-structure development. The 3 MeV proton irradiations are at an irradiation temperature of 87°C, while the self ion irradiation is reported at 500°C and the HFIR irradiations are at 700 - 800°C. The damage comparison is shown at an approximately consistent dose of 0.5 vs 1 dpa damage.

Similar to self ion irradiations, 3 MeV proton irradiation shows a build-up of dislocation loops. These loops are seen to combine steadily and grow in size, with increasing irradiation dose. As the 3 MeV proton irradiations are carried out at low temperatures, no voids are seen in the sample. Recent investigations have shown the production of voids under 40 keV proton irradiation conducted at temperatures of 800°C and 1000°C [181]. This is also expected for 3 MeV protons at higher temperatures. However, no voids have been noticed under self ion

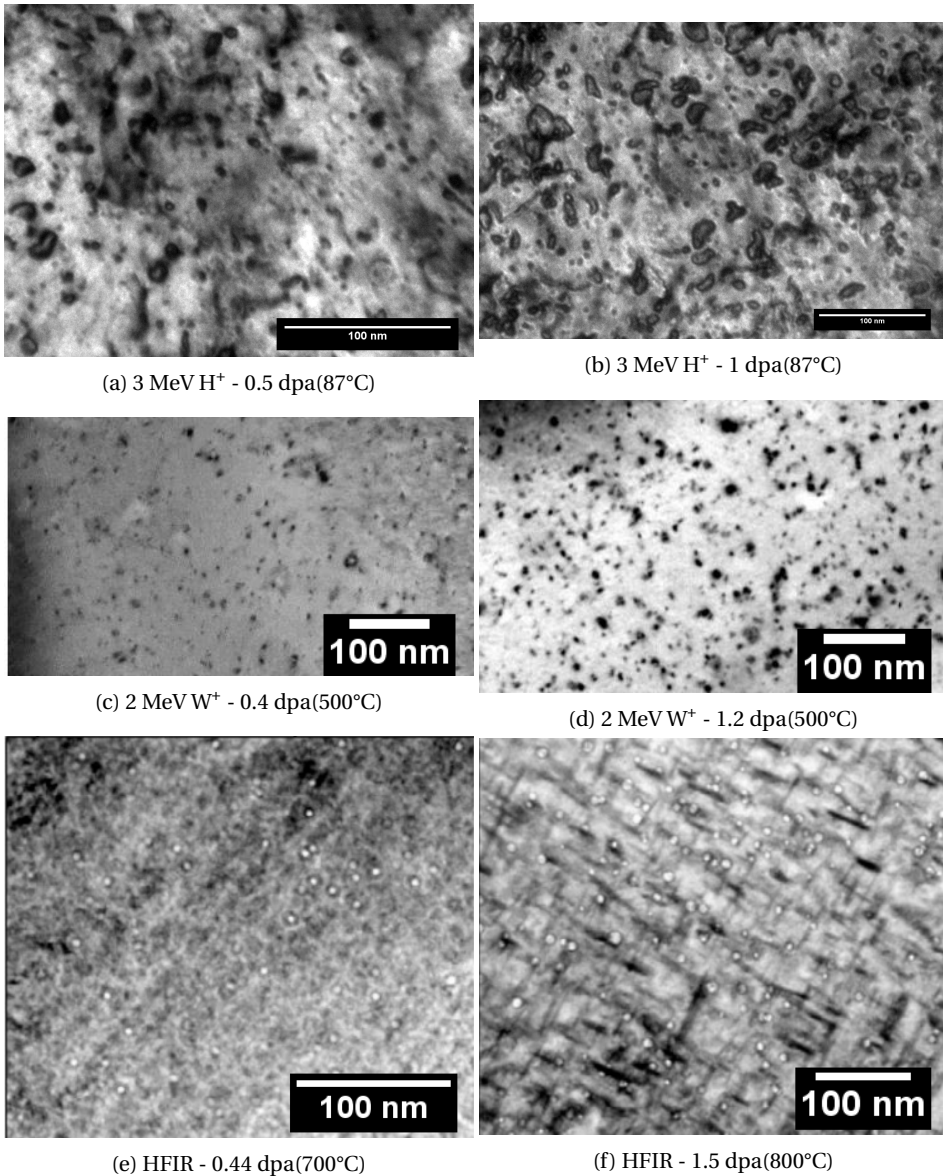


Figure 10.1: Micro-structure comparison between 3 MeV proton irradiation, 2 MeV self ion irradiation [226] and HFIR neutron irradiation [70] under TEM. The irradiation temperatures are different, however the doses are approximately compared at 0.5 and 1.0 dpa damage. A clear distinction is observed within the damage produced between neutrons and ions. Voids and precipitates are seen in neutron irradiated samples, while no voids are observed under self ion irradiations. Dislocation loops can be noticed in both self ion irradiations and 3 MeV proton irradiations. For damages near and above 1 dpa, fission reactor studies estimate the Re content to be 5% and the transmutation can be clearly seen as needle like precipitates.

irradiations upto temperatures of 500°C. This could be due to the excess amount of interstitials from the irradiation, representing a potential difference between protons and heavy ions. With increasing temperature, the loop density is observed to decrease in self ion irradiation [226] and a similar effect is anticipated for 3 MeV proton irradiations. This is due to the stage II recovery in W, which is applicable between -170 to 350°C. Within this stage, the smaller clusters combine resulting in larger visible clusters [226]. At even higher temperatures of stage III recovery between 350-640°C, vacancies are mobile and recombine with interstitials leading to a drop in loop density [226]. Additionally, a saturation in loop density is seen for 3 MeV proton irradiation. This is also noticed in the case of self ion irradiation [87]. At the start of irradiation, point defects are produced and their annihilation is negligible. However, as the dose builds up and defect density increases, the recombination starts to play a major role and is thought to be the reason for the saturation in loop density [226].

The TEM observations from neutron irradiations at HFIR portray a different micro-structure evolution. As seen in Figure 10.1, the dislocation loops are seen in combination with voids. These are observed to form early on during the irradiation at dose levels of 0.1 dpa or lower [70], similar to the ion irradiations. While voids are anticipated at higher temperatures using 3 MeV protons, with further increase in dose, precipitates are seen in the micro-structure. This is a feature of fission irradiations and might not represent the true picture for fusion neutron damage. At doses above 1 dpa, the fission irradiation strongly deviates from the fusion irradiation damage scenario and undergoes 100x higher transmutation. The Re concentration in fission irradiations exceeds 10% [70] and has a biased effect on the damage. Re precipitates seen in fission irradiations are known to constrict cavities and eventually undermine swelling. Thus, the correct evolution of damage above 0.1 dpa dose for W under fusion neutron irradiation conditions is urgently sought. In line with this, 30 MeV protons are capable of better approximating the correct transmutation behaviour of fusion neutron irradiated W and might provide clues to the realistic development of W micro-structure under irradiation. As the samples are radioactive, immediate TEM observations of the 30 MeV irradiated W sample are not yet feasible. However, the path towards such experiments was set in this work.

It is well established that the behaviour and properties of materials are directly dependent on their micro-structure. As irradiation influences the micro-structure of materials, post irradiation material behaviour needs to be quantified. In this work, instrumented indentation tests were performed on all irradiated samples under identical loading and unloading conditions, to a maximum force of 15 N. After a holding time of 12 s, the irradiation hardening was estimated using the unloading curve. While studies on fission irradiations have reported the lack of any strong co-relation between irradiation hardening and irradiation temperature [70], it is dependent on the evolution of micro-structure. As the proton irradiations were performed at temperatures below 100°C, fission reactor irradiations performed at 90°C are compared with W⁺ self ion irradiations conducted at 300°C and hardness results obtained from this work. It is important to note that the fission irradiation results represent Vickers hardness, while the self ion irradiations use a Berkovich indenter and the continuous stiffness method for estimating the instrumented indentation, resulting in hardness offsets.

Figure 10.2 clearly shows the effect of the irradiation conditions on material properties. W is irradiated by fission neutrons in HFIR. Neutrons create combined, displacement and transmutation damage, which leads to the development of dislocation loops and voids. With increasing dose, a void lattice develops and precipitates are formed within the sample. The continuous change and development of micro-structure results in a constant increase in obstacles to dislocation motion. This is reflected in the constant increase in hardening.

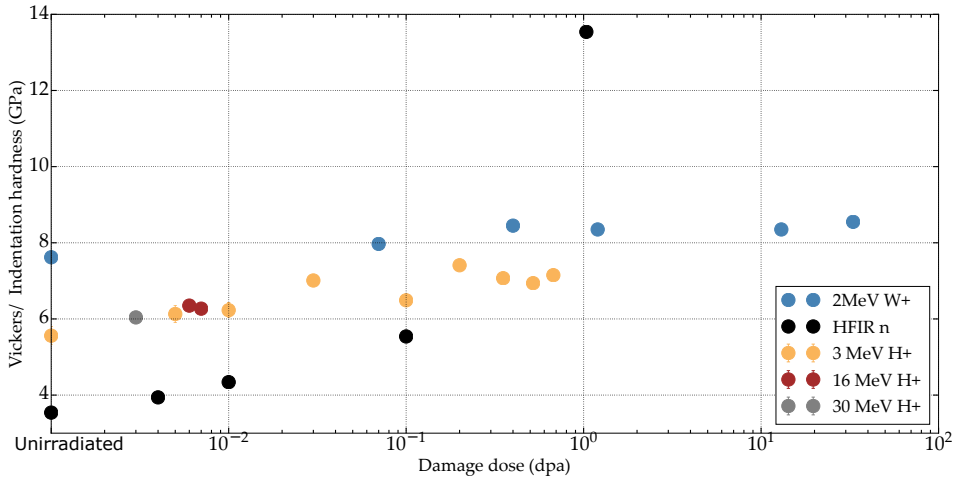


Figure 10.2: Visualisation of irradiation hardness increase with respect to increasing dose for proton irradiation (this study), self ion irradiation [178] and HFIR neutron irradiation [70] [159]. This study has used macro indentation to obtain indentation hardness for proton irradiations shown in orange, red and grey. Neutron irradiation results in black represent Vickers hardness, while self ion and proton irradiation represent instrumented hardness. The use of different techniques results in hardness offsets, but the trend is clearly visible.

However, beyond 1 dpa damage in HFIR, precipitates are observed. This is seen to promote accelerated increase in irradiation hardening of W and is reflected as an extreme jump of 8 GPa between 0.1 and 1 dpa dose for neutron irradiations (black). They are strong obstacles to dislocation motion as compared to dislocation loops [159]. Thus, under fission neutron irradiation Re and Os precipitates are the principle cause of irradiation hardening at high damage doses. This might be different under the fusion environment, where the Re and Os content is under 1% for 1 dpa damage.

Similar to self ion irradiation (blue), 3 MeV protons (orange) induce pure displacement damage in the sample. The micro-structure shows the formation of dislocation loops which are responsible for the increase in hardness of 0.6 GPa, seen early on at levels of 0.005 and 0.01 dpa dose. This further increases to a maximum difference of 1.85 GPa irradiation hardening and then saturates. Similar observations were noted for self ion irradiations by Armstrong et al. [87]. Simulation work performed by Hu et al. [159] designates dislocation loops as weak obstacles and thereby can only register a certain maximum hardening in the samples. As no further void development occurs under 3 MeV proton irradiation at 87°C and self ion irradiation at 300°C, the hardness is seen to saturate. This also directly relates to dislocation loop density saturation. However, an Orwan based hardening model would suggest that the increase in dislocation size should register an increase in irradiation hardening. Further work at higher temperatures with a detailed TEM investigation and Burgers vector analysis is needed to understand the influence of dislocation loop size and density.

The 16 MeV and 30 MeV proton irradiated samples which were limited to a single dose point in this work, also displayed irradiation hardening. An increase of 0.48–0.26 GPa is registered for a 30 MeV proton irradiation dose of 0.003 dpa, against an increase of 0.4 GPa in Vickers hardness measured for a neutron irradiation dose of 0.004 dpa. 16 MeV protons

measured a change of 0.71 ± 0.26 GPa against a damage dose of 0.007 dpa. The different ion irradiation energies and also neutron irradiations show similar hardening in this DPA range, as would be expected due to the low amount of Re produced at these low doses. While TEM investigation of the radioactive samples is pending, optical investigations have shown a change in the surface quality post irradiation. The 16 MeV samples registered a surface cracking with the crack network following the grain boundaries. This is observed to be similar to a thermal shock treated sample subjected to heat loads of $160 - 200 \text{ MW.m}^{-2}$ [51]. As the heat loading is limited to 6.5 MW.m^{-2} (160 W), the crack network might be the result of a combined irradiation and heat loading. The range of protons extends beyond the sample thickness, hence excessive hydrogen implantation cannot be drawn responsible here. In order to ascertain the depth of the cracks in the sample, further investigation is required using perpendicular cuts. In conclusion, the low dose region (<0.1 dpa) shows agreement between all irradiation types through the understanding of defect physics. However, the literature and simulations conducted here suggest large differences above 0.5 dpa.

Gamma analysis confirmed the presence of Re isotopes in 16 and 30 MeV proton irradiated W. The analysis showed a slightly higher presence of Re isotopes than simulated (1.5 - 4.5x). This substantiates the ability to reasonably predict the transmutation component produced by 30 MeV protons. At 1 dpa damage dose, the Re composition under fission neutron irradiation exceeds 5 atomic % as against 700 appm expected in a fusion reactor. Simulations suggest that 30 MeV protons are expected to produce 195 appm of Re. This represents a better approximation to fusion irradiation conditions as compared to fission reactors. Moreover, 30 MeV protons would also generate H and He, which can't be simulated using fission reactors, due to energy thresholds. Additionally, high energy recoils are generated by 30 MeV protons, as calculated using recoil cross-sections. Based on these factors, in the absence of a fusion neutron source, the fusion neutron damage can be reasonably described by 30 MeV protons.

Summary

Nuclear fusion is seen as a promise of long term, environment friendly energy source. While many engineering challenges still exist in the realisation of a commercial, sustainable and profitable fusion driven power plant, materials are often the deciding factor for the design, operation capability and lifetime of the plant. The core of the fusion reactor confines the high temperature ($\sim 10^6$ K) plasma where the nuclear fusion reaction occurs. The plasma facing materials encounter the triple threat of high heat loads, plasma loads and high energy neutrons, upto 14.1 MeV. W is a prime plasma facing material candidate for fusion reactors. Its high thermal conductivity, melting point, sputtering resistance and low tritium retention are favourable properties. However these properties undergo degradation under the fusion operating environment. While high heat loads and plasma loads can be readily tested in laboratories around the world under real fusion conditions, such as PSI-2, JUDITH 2, MAGNUM-PSI, GLADIS, PISCES-B etc., high energy fusion neutrons presently lack suitable reproduction. It is essential to conduct realistic testing under fusion neutron irradiation conditions as material degradation is known to occur with time and dose. Presently the materials are irradiated in fission reactors and tested post irradiation to understand the change in properties. However, the neutron spectrum is different to fusion reactors and consequently the resulting damage is not correctly represented.

The high flux ($\sim 10^{14}$ n.cm⁻²s⁻¹) test reactors (fission) HFIR, JOYO, HFR etc. have a divergent neutron spectrum and cannot reproduce the neutrons over 2 MeV energy. This implies that the large cascades generated from high energy neutrons cannot be replicated by fission reactor irradiations. In W, the high energy fusion neutrons produce PKAs of up to 300 keV. Simulations have shown large cascade development and lower recombination above 100 keV energies influencing the effective DPA per incident neutron. The remaining point defects evolve and create obstructions to dislocation movement. This leads to increase in hardness and resistivity over irradiation dose. In addition, H and/or He generated in significant quantities (\sim ppm levels) under fusion neutron irradiations cannot be sufficiently simulated in a fission environment as their production reactions have a higher threshold. Threshold transmutation reactions such as (n,p) and (n, α) create voids in W, which leads to swelling. Additionally, fission reactors have a large, low energy (< eV energies) neutron tail, which is absent from the fusion neutron spectrum. This low energy neutron tail induces large (n, α) transmutations and overestimates them in comparison to the fusion environment upto 100x for 1 dpa. Transmutation reactions in W register a change in the chemical composition. Over time, pure W changes into a mixture of W-xRe (0.5 x 10) and other elements. Large Re precipitates are seen post neutron irradiation which also induce large hardness changes and increase brittleness. While literature study suggests a similar evolution of hardening in the low dose range (<0.1 dpa) due to displacement dominated hardening, Re precipitates seem to dominate the hardening in the high dose regime (>0.5 dpa) at least under fission irradiation.

Ion irradiation has been explored to simulate aspects of fusion neutron irradiation. With the growth in small scale testing methods, ion irradiation has gained high acceptance. This connects the success of ion irradiations directly to the development of small scale testing methods. Small scale testing methods are specially focussed on extracting material properties from activated samples. The smaller sample size reduces overall radioactivity and dose for the personnel and equipment. It also ensures a uniformity in the sample irradiation conditions. Additionally, small quantities of newly developed alloys or fibre composites produced with latest technologies, which are not fully scaled to production, can be analysed. Using comparatively lower quantities of the sample, macroscopic material properties such as hardness, modulus and ductility are assessed. These lay the basis for material selection and relevant dpa ranges for fusion devices. Combined with the advancement in small scale testing methods, ion irradiation has led to increased understanding of damage methodology. Heavy ions and self ions of selected energies (20 MeV to several GeV) are used to simulate displacement cascades similar to that produced by high energy neutrons. The heavy ion and self ion irradiation experiments have shown large scale recombination as the primary cascade collapses. These experiments have been successfully compared and reproduced with first principle simulations. Similarly, experiments have been performed using heavy ions and self ions to induce clustering in alloys. This simulates the radiation induced precipitation observed under neutron irradiation. Low energy proton irradiations have been used to induce corrosion behaviour in samples. Post irradiation studies are combined with tests such as transmission electron microscopy and atom probe tomography to investigate the micro-structure of irradiation damage. A practical advantage of low energy protons and self ion damage is the lack of transmutation reactions. This renders the sample inactive post irradiation and eases post irradiation investigations. However, the damage is purely based on displacement (scattering) reactions and does not represent the correct nature of neutron damage.

Protons with energies > 3 MeV (16 - 100 MeV) have the ability to tunnel through the Coulomb barrier and induce transmutation reactions. These reactions produce similar elements as observed by neutron irradiations, although with different isotopes. Thus a similar chemical behaviour as neutron irradiation can be induced. A particular good match was found for 30 MeV protons in W. Moreover, high energy protons have the ability to create high energy recoils, which leads to similar cascade formation as neutron damage. Thereby, the use of high energy protons would combine the displacement and transmutation damage into combined damage, similar to neutron induced damage in materials. The damage is produced uniformly over a range of ~ 300 nm rendering macroscopic tests feasible. The large range of damage also favours direct comparison with fission irradiations. Positively, the use of high current accelerators and the higher scattering cross-section of protons allows considerable acceleration of damage compared to fission reactors. Irradiations in the high dpa regime (> 0.5 dpa) which have cycle times ranging from 6 months to years can be achieved in days to weeks on accelerators. However, similar to neutron irradiation, the experiments induce high levels of radioactivity in the samples. This requires special adaptation of test equipment for post irradiation handling.

This work lays the foundation for high energy (16 & 30 MeV) proton irradiation of W samples, enabling answering the open questions e.g. of high dpa fusion material behaviour. It comprises designing the sample, sample manufacturing, polishing, irradiation and post irradiation investigation of first samples, under the complex boundary conditions of a nuclear environment. Extensive effort to reduce cycle time and ease of handling was undertaken during the course of this work to avoid radiation exposure to workers and machines. Additionally,

redundancy was sought in case of technical problems.

Electro-discharge machined W samples were cut from a bar of 99.9% pure sintered W and polished to 1 μ m finish. A suitable combination of cutting and polishing methods were developed and applied for obtaining well defined samples. They were subjected to proton irradiation in order to simulate fusion neutron damage. Three different proton energies (3, 16 & 30 MeV) were explored to induce damage in W samples of 5 mm, 300 μ m and 500 μ m thickness. The irradiation characteristics are noted in the table below. A range of damage doses were investigated using 3 MeV proton irradiations. Micro-spot, 3 MeV proton irradiation studies for fast damage accumulation with dose rates of 5 - 8 $\times 10^5$ dpa/s, comparable to self ion irradiation were performed alongside larger beam spot irradiations. Moreover, irradiation on W samples for doses upto 0.007 and 0.003 dpa were undertaken by 16 & 30 MeV respectively. Compatible sample holders with thermocouple slots were designed and the in-situ temperature measurement was attempted for the first time on solid target irradiations for 16 MeV protons. Thermal design and manufacturing were conducted in order to allow for relevant heat loads of 100 W onto the samples. This target system is submitted for license approval towards its use in the new cyclotron beam line. However, the lack of device beam time limited this work to single irradiations for 16 & 30 MeV proton energies.

Energy (MeV)	Temp. (K)	Dose rate (dpa/s)	Total dose	Remarks
3	352	$10^5 - 10^7$	0.01 - 0.67	In active sample
3	352	10^5	0.1, 0.5 & 1.0	TEM investigations
16	381	4.3×10^7	0.006	Cu disk melt
16	316	4.2×10^8	0.0075	WO _x formation
30	308	1.75×10^8	0.003	WO _x formation

Table 10.1: Summary of the irradiation conditions for proton irradiation undertaken in this work. As 3 MeV proton irradiations lead to inactive samples, a range of irradiation doses were obtained. The high radioactivity and limited beam time resulted in only two high energy proton irradiation experiments.

Simultaneously, simulations were performed to realistically estimate the damage created in the samples. Alongside, post irradiation tests, instrumented indentation and shear punch testing was set up for active samples and hot cell operation. The installation of instrumented indentation in a hot cell is completed, based on new designs of wiring and support structures and a commercial indenter. A new shear punch machine design has been tested in prototype phase. This new design for shear punch testing is developed in order to reduce mismatch of clamping force on the sample and has a central clamp. All machines are adapted to hot cell environment and suitable sample holders and manipulator (remote handling) compatible modifications were carried out. Post irradiation, the inactive 3 MeV samples were subjected to transmission electron microscopy and instrumented indentation. The radioactive 16 & 30 MeV samples were tested on the instrumented indentation machine, finding an agreement of hardening between all irradiation conditions as also suggested by literature findings. Shear punch and TEM investigations are scheduled.

In summary, during the course of this work, a complete engineering cycle from sample design, irradiation technology and planning and post irradiation technology and experimental investigation has been carried out. The use of 30 MeV protons as a viable method for

simulating fusion neutron irradiation damage has been demonstrated, with a close match of Re content to fusion conditions and under consideration of technical and safety feasibility. The demonstration of the working of this method implies that the method isn't limited to testing of tungsten but can be adapted to other materials as well. The rapid irradiation of weeks which can be achieved as compared to fission reactors implies that newly developed materials and mixtures such as tungsten fibre reinforced tungsten or HiperFer materials can be fast tracked using this method. The choice of ideal proton energy to replicate the damage would need to be recalculated for each material based on the methodology applied here.

Outlook

Irradiation pre-treatment

An important lesson learnt from the 30 MeV irradiation of tungsten sample is the necessity of pre-treatment prior to irradiation. The formation of WO_x was noticed on the sample surface which is connected to the copper and graphite disks. Graphite releases absorbed oxygen under irradiation beam heating which results in the formation of WO_x . This would be avoided by preheating and annealing of the sample holder and all sub parts to remove oxygen in a high temperature vacuum oven. Annealing of the sample would also create a standard starting point for all microstructural investigations in the future. This combined with higher vacuum conditions within the beam line would avoid any oxidation during irradiation.

Systematic study of dose

The understanding of material behaviour under neutron irradiation can be only gained through systematic step wise damage dose studies. This work has laid the path for the irradiation and post irradiation investigations of materials using cyclotron irradiated samples for simulating combined fusion neutron damage. An initial dose of 0.003 dpa has been tested using 30 MeV proton irradiations. The next step would be to further the dose steps upto a damage level of 1 dpa dose. Accompanied with instrumented indentation, tensile testing and shear punch testing, the effect of irradiation damage with a closer to fusion transmutation component is essential for W.

Fission irradiations have shown that room temperature hardening is noticed already at dose levels of 10 mdpa. In the 0.01-0.1 dpa range, hardness increases of a few GPa are observed which is presumably due to dislocation loops and vacancy clusters. Effects of precipitates formed under fission irradiation might already deviate the results from a fusion neutron damage regime. Further damage to 1 dpa shows large increases in hardness and major loss of ductility. It is assumed that the precipitates play a major role at this stage. Thereby, a correct representation of the transmutation damage is essential and can be illustrated using 30 MeV proton irradiations. Logarithmic dose steps starting from 0.003 dpa to 1 dpa will indicate any saturation of hardness or an increase similar to fission irradiations. Tensile testing of the samples would allow ductility and work hardening measurements from the irradiated samples.

The irradiations performed in the scope of this work are pilot experiments at low temperature. In order to correctly measure the fusion neutron damage, the Mansur temperature shift would need to be calculated and the irradiation carried out at the relevant temperatures. This would ensure a correct generation, diffusion and annihilation of the point defects, voids and precipitates.

TEM & APT

Microscopy is an essential component of the post irradiation analysis. Modern techniques of transmission electron microscopy and atom probe tomography afford a better understanding and detailing of the induced irradiation changes. A TEM study should accompany the irradiation step to understand and evaluate microscopic changes created in the sample through irradiation. This has a direct link to the macroscopic behaviour displayed by the sample.

However, as the samples are radioactive a polishing method remains to be established in order to produce TEM and APT probes. The TEM sample volume is extremely small and the radioactivity is generally insignificant. Thereby, the samples can be analysed in regular laboratories. However, the production of such samples generates radioactive dust and can be performed only in hot laboratories. Different methods of polishing small TEM and APT probes are to be considered and standard methods in other active laboratories such as twin jet polishing are being considered to be installed.

Adaptation to high temperature testing

The irradiation temperature plays an important role in understanding the damage of W created at high operating temperatures. This is a mixture of defect generation, combination, diffusion and annihilation, all at different rates which leads to the correct damage microstructure. However, in order to qualify the material for its operation in a fusion power plant, the testing of the damage must also be performed at the operating temperature. The change in engineering properties such as tensile strength, hardness, ductility are significant to the selection of plasma facing materials.

The active samples are to be tested in a hot cell environment. Tensile, shear punch and instrumented indentation testing are selected to extract the macroscopic engineering properties. Initially, the tensile testing and shear punch testing is anticipated to be modified for high temperature testing. Pencil heaters or cartridge heaters are able to locally heat samples upto 600°C. Such solutions are being considered for adaptation. A challenge to adapt high temperature testing is the high oxidation rate of W above 400°C. Thereby, suitable inert gas environment would also be required. The installation of such a chamber within the hot cells which are kept at a slight under-pressure compared to its surroundings for radiation protection reasons needs forethought.

Another challenge for the adaptation of instrumented indentation to high temperatures is the extreme sensitivity of the travel transducer. The travel transducer can measure steps of 20 nm in order to allow the precise measurement of displacement. Modifications will be installed in collaboration with the company and after a study of the available high temperature indentation devices.

Be irradiation

Proton irradiation isn't limited to study of tungsten and can be expanded into the study of ⁹Be, Eurofer-97 or Tungsten fibre reinforced tungsten. The proton energy however would need to be correctly identified and simulated for the correct fusion neutron condition.

Bibliography

- [1] C. Rochlin, "Is electricity a right?" *The Electricity Journal*, vol. 15, no. 2, pp. 31–36, 2002. DOI: 10.1016/s1040-6190(02)00264-6.
- [2] S. Tully, "The human right to access electricity," *The Electricity Journal*, vol. 19, no. 3, pp. 30–39, 2006. DOI: 10.1016/j.tej.2006.02.003.
- [3] P. J. Burke, D. I. Stern, and S. B. Bruns, "The impact of electricity on economic development: A macroeconomic perspective," *International Review of Environmental and Resource Economics*, vol. 12, no. 1, pp. 85–127, 2018, ISSN: 1932-1465. DOI: 10.1561/101.00000101. [Online]. Available: <http://dx.doi.org/10.1561/101.00000101>.
- [4] R. Best and P. J. Burke, "Electricity availability: A precondition for faster economic growth?" *Energy Economics*, vol. 74, pp. 321–329, 2018.
- [5] *World Energy Outlook*. International Energy Agency, 2018, ISBN: 978-92-64-30677-6.
- [6] *International Energy Outlook 2016: With Projections to 2040*. Energy Information Administration (US) and Government Publications Office, 2016.
- [7] P. Alstone, D. Gershenson, and D. M. Kammen, "Decentralized energy systems for clean electricity access," *Nature Climate Change*, vol. 5, no. 4, pp. 305–314, 2015. DOI: 10.1038/nclimate2512.
- [8] R. S. Dimitrov, "The paris agreement on climate change: Behind closed doors," *Global Environmental Politics*, vol. 16, no. 3, pp. 1–11, 2016. DOI: 10.1162/glep_a_00361.
- [9] J. Tollefson, "Is the 2°C world a fantasy?" *Nature*, vol. 527, no. 7579, pp. 436–438, 2015. DOI: 10.1038/527436a.
- [10] M. Wahlström, M. D. V. Piotr Kocyba, and J. D. Moor, "Protest for a future: Composition, mobilization and motives of the participants in Fridays For Future climate protests on 15 March, 2019 in 13 European cities," Tech. Rep., 2019. [Online]. Available: [http://eprints. keele. ac. uk/ id/ eprint/ 6571](http://eprints. Keele.ac.uk/id/eprint/6571).
- [11] T. Goh, B. Ang, B. Su, and H. Wang, "Drivers of stagnating global carbon intensity of electricity and the way forward," *Energy Policy*, vol. 113, pp. 149–156, 2018. DOI: 10.1016/j.enpol.2017.10.058.
- [12] B. Ang and B. Su, "Carbon emission intensity in electricity production: A global analysis," *Energy Policy*, vol. 94, pp. 56–63, 2016. DOI: 10.1016/j.enpol.2016.03.038.
- [13] R. Adib, H. Murdock, F. Appavou, A. Brown, B. Epp, A. Leidreiter, C. Lins, H. Murdock, E. Musolino, K. Petrichenko, *et al.*, "Renewables 2015 global status report," *Paris: REN21 Secretariat*, vol. 83, p. 84, 2015.

- [14] H. Liu, X. Xie, and W. Liu, "An oscillatory stability criterion based on the unified -frame impedance network model for power systems with high-penetration renewables," *IEEE Transactions on Power Systems*, vol. 33, no. 3, pp. 3472–3485, 2018. DOI: 10.1109/tpwrs.2018.2794067.
- [15] L. Reichenberg, F. Hedenus, M. Odenberger, and F. Johnsson, "Tailoring large-scale electricity production from variable renewable energy sources to accommodate baseload generation in europe," *Renewable Energy*, vol. 129, pp. 334–346, 2018. DOI: 10.1016/j.renene.2018.05.014.
- [16] M. D. Leonard, E. E. Michaelides, and D. N. Michaelides, "Substitution of coal power plants with renewable energy sources – shift of the power demand and energy storage," *Energy Conversion and Management*, vol. 164, pp. 27–35, 2018. DOI: 10.1016/j.enconman.2018.02.083.
- [17] D. G. Victor, "Strategies for cutting carbon," *Nature*, vol. 395, no. 6705, pp. 837–838, 1998. DOI: 10.1038/27532.
- [18] M. I. Hoffert, K. Caldeira, G. Benford, D. R. Criswell, C. Green, H. Herzog, A. K. Jain, H. S. Khesghi, K. S. Lackner, J. S. Lewis, H. D. Lightfoot, W. Manheimer, J. C. Mankins, M. E. Mauel, L. J. Perkins, M. E. Schlesinger, T. Volk, and T. M. L. Wigley, "Advanced technology paths to global climate stability: Energy for a greenhouse planet," *Science*, vol. 298, no. 5595, pp. 981–987, 2002. DOI: 10.1126/science.1072357.
- [19] J. B. Greenblatt, N. R. Brown, R. Slaybaugh, T. Wilks, E. Stewart, and S. T. McCoy, "The future of low-carbon electricity," *Annual Review of Environment and Resources*, vol. 42, no. 1, pp. 289–316, 2017. DOI: 10.1146/annurev-environ-102016-061138.
- [20] D. Houssin, T. Dujardin, R. Cameron, C. Tam, H. Paillere, M. Baroni, A. Bromhead, M. Baritaud, M. Cometto, R. Gaghen, *et al.*, "Technology road-map-nuclear energy," Organisation for Economic Co-Operation and Development, Tech. Rep., 2015.
- [21] Y. Wu, Z. Chen, L. Hu, M. Jin, Y. Li, J. Jiang, J. Yu, C. Alejaldre, E. Stevens, K. Kim, D. Maisonnier, A. Kalashnikov, K. Tobita, D. Jackson, and D. Perrault, "Identification of safety gaps for fusion demonstration reactors," *Nature Energy*, vol. 1, no. 12, 2016. DOI: 10.1038/nenergy.2016.154.
- [22] L. Wood and J. Nuckolls, "Fusion power," *Environment: Science and Policy for Sustainable Development*, vol. 14, no. 4, pp. 29–33, 1972. DOI: 10.1080/00139157.1972.9933015.
- [23] M. S. Dresselhaus and I. L. Thomas, "Alternative energy technologies," *Nature*, vol. 414, no. 6861, pp. 332–337, 2001. DOI: 10.1038/35104599.
- [24] R. Rhodes, "God's big fix," Tech. Rep., 1974.
- [25] S. C. Cowley, "The quest for fusion power," *Nature Physics*, vol. 12, no. 5, pp. 384–386, 2016. DOI: 10.1038/nphys3719.
- [26] C. de Camargo Barros and I. E. da Cunha, "Nuclear matter in the early universe," AIP, 2015. DOI: 10.1063/1.4937199.
- [27] H.-G. Attendorn and R. N. C. Bowen, "Nucleosynthesis: Fons et origo of the chemical elements in the universe and on earth," in *Radioactive and Stable Isotope Geology*, Springer Netherlands, 1997, pp. 30–55. DOI: 10.1007/978-94-011-5840-4_2.
- [28] J. Lilley, *Nuclear Physics*. John Wiley and Sons Ltd, Apr. 26, 2001, 412 pp., ISBN: 0471979368.

- [29] T. Tanabe, "Tritium issues to be solved for establishment of a fusion reactor," *Fusion Engineering and Design*, vol. 87, no. 5-6, pp. 722–727, 2012. DOI: 10.1016/j.fusengdes.2012.02.009.
- [30] J. McNally Jr., K. Rothe, and R. Sharp, "Fusion reactivity graphs and tables for charged particle reactions (Oak Ridge National Laboratory) report ORNL," *TM-6914*, 1979.
- [31] J. Adams, "Can we master the thermonuclear plasma?" *New Scientist*, vol. 17, 1963.
- [32] O. Neubauer, G. Czymek, B. Giesen, P. W. Hüttemann, M. Sauer, W. Schalt, and J. Schruoff, "Design features of the tokamak TEXTOR," *Fusion Science and Technology*, vol. 47, no. 2, pp. 76–86, 2005. DOI: 10.13182/fst05-a689.
- [33] S. Mirnov, "Tokamak evolution and view to future," *Nuclear Fusion*, vol. 59, no. 1, p. 015001, 2018. DOI: 10.1088/1741-4326/aaee92.
- [34] R. Pitts, R. Buttery, and S. Pinches, "Fusion: The way ahead," *Physics World*, vol. 19, no. 3, pp. 20–26, 2006. DOI: 10.1088/2058-7058/19/3/35.
- [35] J. Team *et al.*, "Physics of high performance JET plasmas in DT," *Nuclear Fusion*, vol. 39, no. 9Y, p. 1227, 1999.
- [36] M. Keilhacker, A. Gibson, C. Gormezano, P. Lomas, P. Thomas, M. Watkins, P. Andrew, B. Balet, D. Borba, C. Challis, *et al.*, "High fusion performance from deuterium-tritium plasmas in JET," *Nuclear Fusion*, vol. 39, no. 2, p. 209, 1999.
- [37] D. Meade, "50 years of fusion research," *Nuclear Fusion*, vol. 50, no. 1, p. 014004, 2009. DOI: 10.1088/0029-5515/50/1/014004.
- [38] M. Abdou, N. B. Morley, S. Smolentsev, A. Ying, S. Malang, A. Rowcliffe, and M. Ulrickson, "Blanket/first wall challenges and required R&D on the pathway to DEMO," *Fusion Engineering and Design*, vol. 100, pp. 2–43, 2015, ISSN: 0920-3796. DOI: <https://doi.org/10.1016/j.fusengdes.2015.07.021>.
- [39] M. Gilbert, T. Eade, C. Bachmann, U. Fischer, and N. Taylor, "Activation, decay heat, and waste classification studies of the european DEMO concept," *Nuclear Fusion*, vol. 57, no. 4, p. 046015, 2017. DOI: 10.1088/1741-4326/aa5bd7.
- [40] "ITER Organization," Tech. Rep.
- [41] R. Pitts, X. Bonnin, F. Escourbiac, H. Frerichs, J. Gunn, T. Hirai, A. Kukushkin, E. Kaveeva, M. Miller, D. Moulton, V. Rozhansky, I. Senichenkov, E. Sytova, O. Schmitz, P. Stangeby, G. D. Temmerman, I. Veselova, and S. Wiesen, "Physics basis for the first ITER tungsten divertor," *Nuclear Materials and Energy*, vol. 20, p. 100696, 2019, ISSN: 2352-1791. DOI: <https://doi.org/10.1016/j.nme.2019.100696>.
- [42] Y. Ueda, K. Schmid, M. Balden, J. Coenen, T. Loewenhoff, A. Ito, A. Hasegawa, C. Hardie, M. Porton, and M. Gilbert, "Baseline high heat flux and plasma facing materials for fusion," *Nuclear Fusion*, vol. 57, no. 9, p. 092006, 2017. DOI: 10.1088/1741-4326/aa6b60.
- [43] D. Stork and S. Zinkle, "Introduction to the special issue on the technical status of materials for a fusion reactor," *Nuclear Fusion*, vol. 57, no. 9, p. 092001, 2017. DOI: 10.1088/1741-4326/aa69e4.
- [44] G. McCracken and P. Stott, "Plasma-surface interactions in tokamaks," *Nuclear Fusion*, vol. 19, no. 7, pp. 889–981, 1979. DOI: 10.1088/0029-5515/19/7/004.

- [45] J. P. Gunn, A. Azéroual, M. Bécoulet, J. Bucalossi, C. Bush, Y. Corre, L. Costanzo, P. Devynck, P. Ghendrih, R. Gianella, C. Grisolia, R. Guirlet, A. Grosman, F. Laugier, T. Loarer, G. Martin, B. Meslin, P. Monier-Garbet, D. Moulin, J.-Y. Pascal, B. Pégourié, R. Reichle, F. Saint-Laurent, B. Schunke, and J.-C. Vallet, “Particle recirculation in the ergodic divertor of Tore Supra,” *Plasma Physics and Controlled Fusion*, vol. 41, no. 12B, B243–B257, 1999. DOI: 10.1088/0741-3335/41/12b/318.
- [46] G. Federici and C. Skinner, “Tritium inventory in the materials of the ITER plasma-facing components,” in *Nuclear Fusion Research*, Springer, 2005, pp. 287–317.
- [47] F. Cismondi, L. Boccaccini, G. Aiello, J. Aubert, C. Bachmann, T. Barrett, L. Barucca, E. Bubelis, S. Ciattaglia, A. D. Nevo, E. Diegele, M. Gasparotto, G. D. Gironimo, P. D. Maio, F. Hernandez, G. Federici, I. Fernández-Berceruelo, T. Franke, A. Froio, C. Gliss, J. Keep, A. Loving, E. Martelli, F. Maviglia, I. Moscato, R. Mozzillo, Y. Poitevin, D. Rapisarda, L. Savoldi, A. Tarallo, M. Utili, L. Vala, G. Veres, and R. Zanino, “Progress in EU breeding blanket design and integration,” *Fusion Engineering and Design*, vol. 136, pp. 782–792, 2018. DOI: 10.1016/j.fusengdes.2018.04.009.
- [48] B. van der Schaaf, F. Tavassoli, C. Fazio, E. Rigal, E. Diegele, R. Lindau, and G. LeMarois, “The development of EUROFER reduced activation steel,” *Fusion Engineering and Design*, vol. 69, no. 1-4, pp. 197–203, 2003. DOI: 10.1016/s0920-3796(03)00337-5.
- [49] C. Linsmeier, M. Rieth, J. Aktaa, T. Chikada, A. Hoffmann, J. Hoffmann, A. Houben, H. Kurishita, X. Jin, M. Li, A. Litnovsky, S. Matsuo, A. von Müller, V. Nikolic, T. Palacios, R. Pippin, D. Qu, J. Reiser, J. Riesch, T. Shikama, R. Stieglitz, T. Weber, S. Wurster, J.-H. You, and Z. Zhou, “Development of advanced high heat flux and plasma-facing materials,” *Nuclear Fusion*, vol. 57, no. 9, p. 092007, 2017. DOI: 10.1088/1741-4326/aa6f71.
- [50] G. Federici, W. Biel, M. Gilbert, R. Kemp, N. Taylor, and R. Wenninger, “European DEMO design strategy and consequences for materials,” *Nuclear Fusion*, vol. 57, no. 9, p. 092002, 2017. DOI: 10.1088/1741-4326/57/9/092002.
- [51] M. Wirtz, J. Linke, T. Loewenhoff, G. Pintsuk, and I. Uytendhouwen, “Thermal shock tests to qualify different tungsten grades as plasma facing material,” *Physica Scripta*, vol. T167, p. 014015, 2016. DOI: 10.1088/0031-8949/t167/1/014015.
- [52] M. Rieth, R. Doerner, A. Hasegawa, Y. Ueda, and M. Wirtz, “Behavior of tungsten under irradiation and plasma interaction,” *Journal of Nuclear Materials*, vol. 519, pp. 334–368, 2019. DOI: 10.1016/j.jnucmat.2019.03.035.
- [53] M. Zucchetti, L. Candido, V. Khripunov, B. Kolbasov, and R. Testoni, “Fusion power plants, fission and conventional power plants. radioactivity, radiotoxicity, radioactive waste,” *Fusion Engineering and Design*, vol. 136, pp. 1529–1533, 2018. DOI: 10.1016/j.fusengdes.2018.05.049.
- [54] M. Gorley, E. Diegele, S. Dudarev, and G. Pintsuk, “Materials engineering and design for fusion—towards DEMO design criteria,” *Fusion Engineering and Design*, vol. 136, pp. 298–303, 2018. DOI: 10.1016/j.fusengdes.2018.02.012.
- [55] F. Wagner, “Fusion energy,” *MRS Energy & Sustainability*, vol. 5, 2018. DOI: 10.1557/mre.2018.8.
- [56] J. Knaster, A. Moeslang, and T. Muroga, “Materials research for fusion,” *Nature Physics*, pp. 424–434, 2016. DOI: 10.1038/nphys3735.

- [57] M. Gilbert, S. Dudarev, D. Nguyen-Manh, S. Zheng, L. Packer, and J.-C. Sublet, “Neutron-induced dpa, transmutations, gas production, and helium embrittlement of fusion materials,” *Journal of Nuclear Materials*, vol. 442, no. 1-3, S755–S760, 2013. DOI: 10.1016/j.jnucmat.2013.03.085.
- [58] W. Setyawan, G. Nandipati, K. J. Roche, H. L. Heinisch, B. D. Wirth, and R. J. Kurtz, “Displacement cascades and defects annealing in tungsten, part I: Defect database from molecular dynamics simulations,” *Journal of Nuclear Materials*, vol. 462, pp. 329–337, 2015. DOI: 10.1016/j.jnucmat.2014.12.056.
- [59] J.-C. S. Mark R. Gilbert, *Handbook of activation, transmutation, and radiation damage properties of the elements simulated using FISPACT-II & TENDL-2015; Magnetic Fusion Plants*. CCFE, 2016. [Online]. Available: [http://www.ccfef.ac.uk/assets/Documents/easy/CCFE-R\(16\)36.pdf](http://www.ccfef.ac.uk/assets/Documents/easy/CCFE-R(16)36.pdf).
- [60] R. Harrison, “On the use of ion beams to emulate the neutron irradiation behaviour of tungsten,” *Vacuum*, vol. 160, pp. 355–370, 2019. DOI: 10.1016/j.vacuum.2018.11.050.
- [61] R. Rayaprolu, S. Möller, C. Linsmeier, and S. Spellerberg, “Simulation of neutron irradiation damage in tungsten using higher energy protons,” *Nuclear Materials and Energy*, vol. 9, pp. 29–35, 2016. DOI: 10.1016/j.nme.2016.09.008.
- [62] G. Lucas, G. Odette, H. Matsui, A. Möslang, P. Spätig, J. Rensman, and T. Yamamoto, “The role of small specimen test technology in fusion materials development,” *Journal of Nuclear Materials*, vol. 367-370, pp. 1549–1556, 2007. DOI: 10.1016/j.jnucmat.2007.04.034.
- [63] N. Taylor and P. Cortes, “Lessons learnt from ITER safety & licensing for DEMO and future nuclear fusion facilities,” *Fusion Engineering and Design*, vol. 89, no. 9-10, pp. 1995–2000, 2014. DOI: 10.1016/j.fusengdes.2013.12.030.
- [64] M. T. Robinson, “Basic physics of radiation damage production,” *Journal of Nuclear Materials*, vol. 216, pp. 1–28, 1994. DOI: 10.1016/0022-3115(94)90003-5.
- [65] S. J. Zinkle and G. Was, “Materials challenges in nuclear energy,” *Acta Materialia*, vol. 61, no. 3, pp. 735–758, 2013.
- [66] D. Iracane, P. Chaix, and A. Alamo, “Jules Horowitz Reactor: A high performance material testing reactor,” *Comptes Rendus Physique*, vol. 9, no. 3-4, pp. 445–456, 2008. DOI: 10.1016/j.crhy.2007.11.003.
- [67] J. Ahlf, R. Conrad, G. Tartaglia, and G. Tsotridis, “The HFR petten as a test bed for fusion materials and components,” *Journal of Nuclear Materials*, vol. 212-215, pp. 1635–1639, 1994. DOI: 10.1016/0022-3115(94)91104-5.
- [68] P. Vladimirov and A. Möslang, “Comparison of material irradiation conditions for fusion, spallation, stripping and fission neutron sources,” *Journal of Nuclear Materials*, vol. 329-333, pp. 233–237, 2004. DOI: 10.1016/j.jnucmat.2004.04.030.
- [69] N. Luzginova, J.-W. Rensman, M. Jong, P. ten Pierick, T. Bakker, and H. Nolles, “Overview of 10 years of irradiation projects on EUROFER97 steel at high flux reactor in petten,” *Journal of Nuclear Materials*, vol. 455, no. 1-3, pp. 21–25, 2014. DOI: 10.1016/j.jnucmat.2014.03.028.

- [70] Y. Katoh, D. Clark, Y. Ueda, Y. Hatano, M. Yoda, A. S. Sabau, T. Yokomine, L. M. Garrison, J. W. Geringer, A. Hasegawa, T. Hinoki, M. Shimada, D. Buchenauer, Y. Oya, and T. Muroga, "Progress in the U.S./Japan PHENIX Project for the Technological Assessment of Plasma Facing Components for DEMO Reactors," *Fusion Science and Technology*, pp. 1–11, 2017. DOI: 10.1080/15361055.2017.1333868.
- [71] E. Gaganidze and J. Aktaa, "Assessment of neutron irradiation effects on RAFM steels," *Fusion Engineering and Design*, vol. 88, no. 3, pp. 118–128, 2013. DOI: 10.1016/j.fusengdes.2012.11.020.
- [72] E. Lang, N. Reid, L. Garrison, C. Parish, and J. P. Allain, "Pre-irradiation comparison of W-Based alloys for the PHENIX campaign: Microstructure, composition, and mechanical properties," *Fusion Science and Technology*, vol. 75, no. 6, pp. 533–541, 2019. DOI: 10.1080/15361055.2019.1602400.
- [73] M. Chadwick, M. Herman, P. Obložinský, M. Dunn, Y. Danon, A. Kahler, D. Smith, B. Pritychenko, G. Arbanas, R. Arcilla, R. Brewer, D. Brown, R. Capote, A. Carlson, Y. Cho, H. Derrien, K. Guber, G. Hale, S. Hoblit, S. Holloway, T. Johnson, T. Kawano, B. Kiedrowski, H. Kim, S. Kunieda, N. Larson, L. Leal, J. Lestone, R. Little, E. McCutchan, R. MacFarlane, M. MacInnes, C. Mattoon, R. McKnight, S. Mughabghab, G. Nobre, G. Palmiotti, A. Palumbo, M. Pigni, V. Pronyaev, R. Sayer, A. Sonzogni, N. Summers, P. Talou, I. Thompson, A. Trkov, R. Vogt, S. van der Marck, A. Wallner, M. White, D. Wiarda, and P. Young, "ENDF/B-VII.1 Nuclear Data for Science and Technology: Cross sections, Covariances, Fission product yields and Decay data," *Nuclear Data Sheets*, vol. 112, no. 12, pp. 2887–2996, 2011. DOI: 10.1016/j.nds.2011.11.002.
- [74] N. Soppera, M. Bossant, and E. Dupont, "JANIS 4: An improved version of the NEA java-based nuclear data information system," *Nuclear Data Sheets*, vol. 120, pp. 294–296, 2014.
- [75] R. Stoller, "Primary radiation damage formation," in *Comprehensive Nuclear Materials*, Elsevier, 2012, pp. 293–332. DOI: 10.1016/b978-0-08-056033-5.00027-6.
- [76] J. A. Brinkman, "On the nature of radiation damage in metals," *Journal of Applied Physics*, vol. 25, no. 8, pp. 961–970, 1954. DOI: 10.1063/1.1721810.
- [77] G. H. Kinchin and R. S. Pease, "The displacement of atoms in solids by radiation," *Reports on Progress in Physics*, vol. 18, no. 1, p. 1, 1955.
- [78] G. S. Was, *Fundamentals of Radiation Material Science*. Springer-Verlag Berlin Heidelberg, 2010, ISBN: 978-3-540-49472-0. DOI: 10.1007/978-1-4939-3438-6.
- [79] J. Sanders, "On recoil numbers in crystalline structures," *Physica*, vol. 32, no. 11-12, pp. 2197–2200, 1966. DOI: 10.1016/0031-8914(66)90181-9.
- [80] J. Lindhard, M. Scharff, and H. Schiott, "K. Dan. Vidensk. Selsk. Mat.-Fys. Medd.," 1963.
- [81] K. Nordlund, S. J. Zinkle, A. E. Sand, F. Granberg, R. S. Averback, R. E. Stoller, T. Suzudo, L. Malerba, F. Banhart, W. J. Weber, F. Willaime, S. L. Dudarev, and D. Simeone, "Primary radiation damage: A review of current understanding and models," *Journal of Nuclear Materials*, 2018. DOI: 10.1016/j.jnucmat.2018.10.027.
- [82] T. Troev, N. Nankov, and T. Yoshiie, "Simulation of displacement cascades in tungsten irradiated by fusion neutrons," *Nuclear Instruments and Methods in Physics Research Section B: Beam Interactions with Materials and Atoms*, vol. 269, no. 6, pp. 566–571, 2011. DOI: 10.1016/j.nimb.2011.01.010.

- [83] M. Gilbert, J. Marian, and J.-C. Sublet, “Energy spectra of primary knock-on atoms under neutron irradiation,” *Journal of Nuclear Materials*, vol. 467, pp. 121–134, 2015. DOI: <https://doi.org/10.1016/j.jnucmat.2015.09.023>.
- [84] T. Tanno, A. Hasegawa, M. Fujiwara, J.-C. He, S. Nogami, M. Satou, T. Shishido, and K. Abe, “Precipitation of solid transmutation elements in irradiated tungsten alloys,” *Materials Transactions*, vol. 49, no. 10, pp. 2259–2264, 2008, ISSN: 1345-9678. DOI: [10.2320/matertrans.MAW200821](https://doi.org/10.2320/matertrans.MAW200821).
- [85] T. Koyanagi, N. K. Kumar, T. Hwang, L. M. Garrison, X. Hu, L. L. Snead, and Y. Katoh, “Microstructural evolution of pure tungsten neutron irradiated with a mixed energy spectrum,” *Journal of Nuclear Materials*, vol. 490, pp. 66–74, 2017, ISSN: 0022-3115. DOI: <http://doi.org/10.1016/j.jnucmat.2017.04.010>.
- [86] G. Cottrell, “Sigma phase formation in irradiated tungsten, tantalum and molybdenum in a fusion power plant,” *Journal of Nuclear Materials*, vol. 334, no. 2-3, pp. 166–168, 2004. DOI: [10.1016/j.jnucmat.2004.07.001](https://doi.org/10.1016/j.jnucmat.2004.07.001).
- [87] D. E. J. Armstrong, P. D. Edmondson, and S. G. Roberts, “Effects of sequential tungsten and helium ion implantation on nano-indentation hardness of tungsten,” *Applied Physics Letters*, vol. 102, no. 25, p. 251901, 2013. DOI: [10.1063/1.4811825](https://doi.org/10.1063/1.4811825).
- [88] X.-C. Li, Y.-N. Liu, Y. Yu, G.-N. Luo, X. Shu, and G.-H. Lu, “Helium defects interactions and mechanism of helium bubble growth in tungsten: A molecular dynamics simulation,” *Journal of Nuclear Materials*, vol. 451, no. 1-3, pp. 356–360, 2014. DOI: [10.1016/j.jnucmat.2014.04.022](https://doi.org/10.1016/j.jnucmat.2014.04.022).
- [89] M. Victoria, N. Baluc, and P. Spätig, “Structural materials for fusion reactors,” *Nuclear Fusion*, vol. 41, no. 8, pp. 1047–1053, 2001. DOI: [10.1088/0029-5515/41/8/308](https://doi.org/10.1088/0029-5515/41/8/308).
- [90] J.-C. Sublet, J. Eastwood, J. Morgan, M. Gilbert, M. Fleming, and W. Arter, “FISPACT-II: An advanced simulation system for activation, transmutation and material modelling,” *Nuclear Data Sheets*, vol. 139, pp. 77–137, 2017.
- [91] T. Suzudo and A. Hasegawa, “Suppression of radiation-induced point defects by rhenium and osmium interstitials in tungsten,” *Scientific Reports*, vol. 6, no. 1, 2016. DOI: [10.1038/srep36738](https://doi.org/10.1038/srep36738).
- [92] J. McCarthy, “Phase evolution during neutron irradiation of commercial Fe-Cr-Mn alloys,” *Journal of Nuclear Materials*, vol. 179-181, pp. 626–628, 1991. DOI: [10.1016/0022-3115\(91\)90166-5](https://doi.org/10.1016/0022-3115(91)90166-5).
- [93] F. Soisson and T. Jourdan, “Radiation-accelerated precipitation in Fe–Cr alloys,” *Acta Materialia*, vol. 103, pp. 870–881, 2016. DOI: [10.1016/j.actamat.2015.11.001](https://doi.org/10.1016/j.actamat.2015.11.001).
- [94] K. Ehrlich, E. Bloom, and T. Kondo, “International strategy for fusion materials development,” *Journal of Nuclear Materials*, vol. 283-287, pp. 79–88, 2000. DOI: [10.1016/S0022-3115\(00\)00102-1](https://doi.org/10.1016/S0022-3115(00)00102-1).
- [95] M. Fukuda, N. K. Kumar, T. Koyanagi, L. M. Garrison, L. L. Snead, Y. Katoh, and A. Hasegawa, “Neutron energy spectrum influence on irradiation hardening and microstructural development of tungsten,” *Journal of Nuclear Materials*, vol. 479, pp. 249–254, 2016. DOI: [10.1016/j.jnucmat.2016.06.051](https://doi.org/10.1016/j.jnucmat.2016.06.051).
- [96] Y. Lizunov, A. Möslang, A. Ryazanov, and P. Vladimirov, “New evaluation of displacement damage and gas production for breeder ceramics under IFMIF, fusion and fission neutron irradiation,” *Journal of Nuclear Materials*, vol. 307-311, pp. 1680–1685, 2002. DOI: [10.1016/S0022-3115\(02\)01275-8](https://doi.org/10.1016/S0022-3115(02)01275-8).

- [97] L. Mansur, A. Rowcliffe, R. Nanstad, S. Zinkle, W. Corwin, and R. Stoller, "Materials needs for fusion, generation IV fission reactors and spallation neutron sources – similarities and differences," *Journal of Nuclear Materials*, vol. 329-333, pp. 166–172, 2004. DOI: 10.1016/j.jnucmat.2004.04.016.
- [98] I. G. Segev, E. Yahel, I. Silverman, and G. Makov, "Blister formation at subcritical doses in tungsten irradiated by MeV protons," *Journal of Nuclear Materials*, vol. 496, pp. 77–84, 2017. DOI: 10.1016/j.jnucmat.2017.09.024.
- [99] A. Longest, J. Corum, D. Heatherly, and K. Thoms, "Design of spectrally tailored fusion reactor materials experiments in the HFIR RB capsule irradiation facility," *Journal of Nuclear Materials*, vol. 155-157, pp. 1346–1349, 1988. DOI: 10.1016/0022-3115(88)90524-7.
- [100] P. Raymond, G. Bignan, and J. Guidez, "Research reactor status for future nuclear research in Europe," *Revue Générale Nucléaire*, no. 6, pp. 77–81, 2010. DOI: 10.1051/rgn/20106077.
- [101] Y. Inaba, M. Ishihara, M. Niimi, and H. Kawamura, "Present status of refurbishment and irradiation technologies in JMTR," *Journal of Nuclear Materials*, vol. 417, no. 1-3, pp. 1348–1351, 2011. DOI: 10.1016/j.jnucmat.2011.01.094.
- [102] A. P. Grinberg, "History of the invention and development of accelerators (1922-1932)," *Soviet Physics Uspekhi*, vol. 18, no. 10, pp. 815–831, 1975.
- [103] B. J. Holzer, "Introduction to particle accelerators and their limitations," *CERN Yellow Report CERN*, vol. CERN-2016-001, pp. 29–50, 2016.
- [104] D. J. Clark, "Accelerators for nuclear physics," *Reports on Progress in Physics*, vol. 35, no. 3, pp. 1007–1075, 1972. DOI: 10.1088/0034-4885/35/3/302.
- [105] R. Nelson, D. Mazey, and J. Hudson, "The use of ion accelerators to simulate fast neutron-induced voidage in metals," *Journal of Nuclear Materials*, vol. 37, no. 1, pp. 1–12, 1970. DOI: 10.1016/0022-3115(70)90176-5.
- [106] C. Logan, J. Anderson, and A. Mukherjee, "Proton simulation of displacement effects induced in metals by 14 MeV neutrons," *Journal of Nuclear Materials*, vol. 48, no. 3, pp. 223–232, 1973. DOI: 10.1016/0022-3115(73)90017-2.
- [107] C. Cawthorne and E. J. Fulton, "Voids in irradiated stainless steel," *Nature*, vol. 216, no. 5115, pp. 575–576, 1967. DOI: 10.1038/216575a0.
- [108] G. Kulcinski, A. Wittkower, and G. Ryding, "Use of heavy ions from a tandem accelerator to simulate high fluence, fast neutron damage in metals," *Nuclear Instruments and Methods*, vol. 94, no. 2, pp. 365–375, 1971. DOI: 10.1016/0029-554x(71)90592-1.
- [109] R. Cauvin and G. Martin, "Solid solutions under irradiation. I. a model for radiation-induced metastability," *Physical Review B*, vol. 23, no. 7, pp. 3322–3332, 1981. DOI: 10.1103/physrevb.23.3322.
- [110] N. Q. Lam, P. Okamoto, and R. Johnson, "Solute segregation and precipitation under heavy-ion bombardment," *Journal of Nuclear Materials*, vol. 78, no. 2, pp. 408–418, 1978. DOI: 10.1016/0022-3115(78)90462-2.
- [111] K.-i. Fukumoto, H. Matsui, Y. Candra, K. Takahashi, H. Sasanuma, S. Nagata, and K. Takahiro, "Radiation-induced precipitation in V-(Cr,Fe)-Ti alloys irradiated at low temperature with low dose during neutron or ion irradiation," *Journal of Nuclear Materials*, vol. 283-287, pp. 535–539, 2000. DOI: 10.1016/s0022-3115(00)00373-1.

- [112] D. Thompson, A. Omar, and J. Robinson, "10–16 MeV proton irradiation damage in iron and copper," *Journal of Nuclear Materials*, vol. 85-86, pp. 509–513, 1979. DOI: 10.1016/0022-3115(79)90539-7.
- [113] R. Averback, "Atomic displacement processes in irradiated metals," *Journal of Nuclear Materials*, vol. 216, pp. 49–62, 1994. DOI: [https://doi.org/10.1016/0022-3115\(94\)90006-X](https://doi.org/10.1016/0022-3115(94)90006-X).
- [114] B. Singh, "Impacts of damage production and accumulation on materials performance in irradiation environment," *Journal of Nuclear Materials*, vol. 258-263, pp. 18–29, 1998. DOI: 10.1016/S0022-3115(98)00264-5.
- [115] A. Kohyama, Y. Katoh, M. Ando, and K. Jimbo, "A new multiple beams–material interaction research facility for radiation damage studies in fusion materials," *Fusion Engineering and Design*, vol. 51-52, pp. 789–795, 2000. DOI: 10.1016/S0920-3796(00)00181-2.
- [116] S. J. Zinkle and A. Möslang, "Evaluation of irradiation facility options for fusion materials research and development," *Fusion Engineering and Design*, vol. 88, no. 6-8, pp. 472–482, 2013. DOI: 10.1016/j.fusengdes.2013.02.081.
- [117] X. Yi, M. Jenkins, M. Briceno, S. Roberts, Z. Zhou, and M. Kirk, "In-situ study of self-ion irradiation damage in W and W-5Re at 500°C," *Philosophical Magazine*, vol. 93, no. 14, pp. 1715–1738, 2013. DOI: 10.1080/14786435.2012.754110.
- [118] M. Li, M. Kirk, P. Baldo, D. Xu, and B. Wirth, "Study of defect evolution by TEM within situ irradiation and coordinated modeling," *Philosophical Magazine*, vol. 92, no. 16, pp. 2048–2078, 2012. DOI: 10.1080/14786435.2012.662601.
- [119] D. Kiener, P. Hosemann, S. A. Maloy, and A. M. Minor, "In situ nanocompression testing of irradiated copper," *Nature Materials*, vol. 10, no. 8, pp. 608–613, 2011. DOI: 10.1038/nmat3055.
- [120] A. Reichardt, M. Ionescu, J. Davis, L. Edwards, R. Harrison, P. Hosemann, and D. Bhattacharyya, "In situ micro tensile testing of He+2 ion irradiated and implanted single crystal nickel film," *Acta Materialia*, vol. 100, pp. 147–154, 2015. DOI: 10.1016/j.actamat.2015.08.028.
- [121] B. Unterberg, R. Jaspers, R. Koch, V. Massaut, J. Rapp, D. Reiter, S. Kraus, A. Kreter, V. Philipps, H. Reimer, U. Samm, L. Scheibl, B. Schweer, J. Schuurmans, I. Uytendhouwen, R. Al, M. van den Berg, S. Brons, H. van Eck, W. Goedheer, M. Graswinckel, T. van der Grift, A. Kleyn, W. Koppers, O. Kruyt, A. Lof, H. van der Meiden, W. Melissen, M. van de Pol, G. van Rooij, P. Smeets, J. Scholten, D. Schram, G. D. Temmerman, W. Vijvers, P. Z. van Emmichoven, and J. Zielinski, "New linear plasma devices in the trilateral euregio cluster for an integrated approach to plasma surface interactions in fusion reactors," *Fusion Engineering and Design*, vol. 86, no. 9-11, pp. 1797–1800, 2011. DOI: 10.1016/j.fusengdes.2011.03.082.
- [122] G. Was and T. Allen, "Radiation-induced segregation in multicomponent alloys: Effect of particle type," *Materials Characterization*, vol. 32, no. 4, pp. 239–255, 1994. DOI: 10.1016/1044-5803(94)90101-5.
- [123] "Standard practice for neutron radiation damage simulation by charged-particle irradiation," West Conshohocken, PA, Tech. Rep., 1996, Reapproved 2009. [Online]. Available: <http://cds.cern.ch/record/1483021>.

- [124] G. F. Knoll, *Radiation Detection and Measurement*. John Wiley & Sons Inc, Aug. 4, 2010, 864 pp., ISBN: 0470131489.
- [125] J. F. Ziegler, “Stopping of energetic light ions in elemental matter,” *Journal of Applied Physics*, vol. 85, no. 3, pp. 1249–1272, 1999. DOI: 10.1063/1.369844.
- [126] J. F. Ziegler, M. Ziegler, and J. Biersack, “SRIM – the stopping and range of ions in matter (2010),” *Nuclear Instruments and Methods in Physics Research Section B: Beam Interactions with Materials and Atoms*, vol. 268, no. 11-12, pp. 1818–1823, 2010. DOI: 10.1016/j.nimb.2010.02.091.
- [127] J. L. Brimhall and G. L. Kulcinski, “Void formation in ion bombarded niobium,” *Radiation Effects*, vol. 20, no. 1-2, pp. 25–31, 1973. DOI: 10.1080/00337577308232262.
- [128] G. Gupta, Z. Jiao, A. Ham, J. Busby, and G. Was, “Microstructural evolution of proton irradiated T91,” *Journal of Nuclear Materials*, vol. 351, no. 1-3, pp. 162–173, 2006. DOI: 10.1016/j.jnucmat.2006.02.028.
- [129] G. Was, J. Busby, T. Allen, E. Kenik, A. Jensson, S. Bruemmer, J. Gan, A. Edwards, P. Scott, and P. Andreson, “Emulation of neutron irradiation effects with protons: Validation of principle,” *Journal of Nuclear Materials*, vol. 300, no. 2-3, pp. 198–216, 2002. DOI: 10.1016/s0022-3115(01)00751-6.
- [130] M. Izerroukenn, O. Menchi, A. Sari, W. Djerourou, and H. Medjkoun, “Radiation damage induced in Zircaloy-4 by 2.6 MeV proton irradiation,” *Journal of Radioanalytical and Nuclear Chemistry*, vol. 311, no. 3, pp. 1917–1921, 2017. DOI: 10.1007/s10967-017-5170-9.
- [131] M. R. Gilbert, J.-C. Sublet, and R. A. Forrest, “Handbook of activation, transmutation, and radiation damage properties of the elements simulated using FISPACT-II & TENDL-2014; nuclear fission plants (HFR focus),” *Tech. Rep. CCFE-R*, vol. 15, p. 32, 2015.
- [132] A. Koning, D. Rochman, J. Kopecky, J. C. Sublet, E. Bauge, S. Hilaire, P. Romain, B. Morillon, H. Duarte, S. van der Marck, S. Pomp, H. Sjostrand, R. Forrest, H. Henriksson, O. Cabellos, S. G. J. Leppanen, H. Leeb, A. Plompen, and R. Mills, “TENDL-2015: TALYS-based evaluated nuclear data library,” *Tech. Rep.* [Online]. Available: https://tendl.web.psi.ch/tendl_2015/tendl2015.html.
- [133] A. Cezairliyan *et al.*, “Measurement of melting point and electrical resistivity (above 3600 K) of tungsten by a pulse heating method,” *NATIONAL BUREAU OF STANDARDS REPORT*, p. 109, 1972.
- [134] S. Yih and C. Wang, “Tungsten: Sources, metallurgy, properties, and applications,” *New York, Plenum Press, 1979. 512 p*, 1979.
- [135] E. Gaganidze, D. Rupp, and J. Aktaa, “Fracture behaviour of polycrystalline tungsten,” *Journal of Nuclear Materials*, vol. 446, no. 1-3, pp. 240–245, 2014. DOI: 10.1016/j.jnucmat.2013.11.001.
- [136] S. Zinkle and N. Ghoniem, “Operating temperature windows for fusion reactor structural materials,” *Fusion Engineering and Design*, vol. 51-52, pp. 55–71, 2000. DOI: 10.1016/s0920-3796(00)00320-3.
- [137] E. Lassner and W.-D. Schubert, *Tungsten: properties, chemistry, technology of the element, alloys, and chemical compounds*. Springer Science & Business Media, 2012.

- [138] A. Manhard, K. Schmid, M. Balden, and W. Jacob, "Influence of the microstructure on the deuterium retention in tungsten," *Journal of Nuclear Materials*, vol. 415, no. 1, S632–S635, 2011. DOI: 10.1016/j.jnucmat.2010.10.045.
- [139] A. Manhard, M. Balden, and S. Elgeti, "Quantitative microstructure and defect density analysis of polycrystalline tungsten reference samples after different heat treatments," *Practical Metallography*, vol. 52, no. 8, pp. 437–466, 2015. DOI: 10.3139/147.110354.
- [140] J. W. Pugh, "On the short time creep rupture," *Metallurgical Transactions*, vol. 4, no. 2, pp. 533–538, 1973. DOI: 10.1007/bf02648706.
- [141] C. E. Beck, S. G. Roberts, P. D. Edmondson, and D. E. J. Armstrong, "Effect of alloy composition & helium ion-irradiation on the mechanical properties of tungsten, tungsten-tantalum & tungsten-rhenium for fusion power applications," *MRS Proceedings*, vol. 1514, pp. 99–104, 2013. DOI: 10.1557/op1.2013.356.
- [142] M. W. Thompson, "The damage and recovery of neutron irradiated tungsten," *Philosophical Magazine*, vol. 5, no. 51, pp. 278–296, 1960. DOI: 10.1080/14786436008235842.
- [143] L. Keys and J. Moteff, "Neutron irradiation and defect recovery of tungsten," *Journal of Nuclear Materials*, vol. 34, no. 3, pp. 260–280, 1970. DOI: 10.1016/0022-3115(70)90193-5.
- [144] R. Herschitz and D. Seidman, "An atomic resolution study of homogeneous radiation-induced precipitation in a neutron irradiated W-10at.% Re alloy," *Acta Metallurgica*, vol. 32, no. 8, pp. 1141–1154, 1984. DOI: 10.1016/0001-6160(84)90121-4.
- [145] J. L. Rempe and S. C. Wilkins, "High temperature thermocouples for in-pile applications," 2005.
- [146] J. Matolich, H. Nahm, and J. Moteff, "Swelling in neutron irradiated tungsten and tungsten-25% rhenium," *Scripta Metallurgica*, vol. 8, no. 7, pp. 837–841, 1974. DOI: 10.1016/0036-9748(74)90304-4.
- [147] K. Lacefield, J. Moteff, and J. P. Smith, "Neutron radiation damage in tungsten single crystals," *Philosophical Magazine*, vol. 13, no. 125, pp. 1079–1081, 1966. DOI: 10.1080/14786436608213157.
- [148] P. Krautwasser, H. Derz, and E. Kny, "Influence of fast neutron fluence on the ductile-brittle transition temperature of tungsten, W-10Re, and W-3.4Ni-1.6Fe," *High Temperatures-High Pressures*, vol. 22, no. 1, pp. 25–32, 1990.
- [149] J. Herring, K. A. McCarthy, and T. J. Dolan, "Safety analyses of the ARIES tokamak reactor designs," *Fusion Engineering and Design*, vol. 25, no. 1-3, pp. 193–204, 1994. DOI: 10.1016/0920-3796(94)90064-7.
- [150] I. Smid, M. Akiba, G. Vieider, and L. Plöchl, "Development of tungsten armor and bonding to copper for plasma-interactive components," *Journal of Nuclear Materials*, vol. 258-263, pp. 160–172, 1998. DOI: 10.1016/s0022-3115(98)00358-4.
- [151] Y. Nemoto, A. Hasegawa, M. Satou, and K. Abe, "Microstructural development of neutron irradiated W-Re alloys," *Journal of Nuclear Materials*, vol. 283-287, pp. 1144–1147, 2000. DOI: 10.1016/s0022-3115(00)00290-7.
- [152] T. Tanno, A. Hasegawa, J.-C. He, M. Fujiwara, S. Nogami, M. Satou, T. Shishido, and K. Abe, "Effects of transmutation elements on neutron irradiation hardening of tungsten," *Materials Transactions*, vol. 48, no. 9, pp. 2399–2402, 2007. DOI: 10.2320/matertrans.maw200722.

- [153] M. Fukuda, T. Tanno, S. Nogami, and A. Hasegawa, "Effects of Re content and fabrication process on microstructural changes and hardening in neutron irradiated tungsten," *Materials Transactions*, vol. 53, no. 12, pp. 2145–2150, 2012. DOI: 10.2320/matertrans.mbw201110.
- [154] A. Hasegawa, M. Fukuda, T. Tanno, and S. Nogami, "Neutron irradiation behavior of tungsten," *Materials Transactions*, vol. 54, no. 4, pp. 466–471, 2013. DOI: 10.2320/matertrans.mg201208.
- [155] M. Fukuda, K. Yabuuchi, S. Nogami, A. Hasegawa, and T. Tanaka, "Microstructural development of tungsten and tungsten–rhenium alloys due to neutron irradiation in HFIR," *Journal of Nuclear Materials*, vol. 455, no. 1-3, pp. 460–463, 2014. DOI: 10.1016/j.jnucmat.2014.08.002.
- [156] A. Hasegawa, M. Fukuda, K. Yabuuchi, and S. Nogami, "Neutron irradiation effects on the microstructural development of tungsten and tungsten alloys," *Journal of Nuclear Materials*, vol. 471, pp. 175–183, 2016. DOI: 10.1016/j.jnucmat.2015.10.047.
- [157] A. Hasegawa, M. Fukuda, S. Nogami, and K. Yabuuchi, "Neutron irradiation effects on tungsten materials," *Fusion Engineering and Design*, vol. 89, no. 7-8, pp. 1568–1572, 2014. DOI: 10.1016/j.fusengdes.2014.04.035.
- [158] M. Klimenkov, U. Jäntschi, M. Rieth, H. Schneider, D. Armstrong, J. Gibson, and S. Roberts, "Effect of neutron irradiation on the microstructure of tungsten," *Nuclear Materials and Energy*, vol. 9, pp. 480–483, 2016. DOI: 10.1016/j.nme.2016.09.010.
- [159] X. Hu, T. Koyanagi, M. Fukuda, N. K. Kumar, L. L. Snead, B. D. Wirth, and Y. Katoh, "Irradiation hardening of pure tungsten exposed to neutron irradiation," *Journal of Nuclear Materials*, vol. 480, pp. 235–243, 2016. DOI: 10.1016/j.jnucmat.2016.08.024.
- [160] L. Garrison, Y. Katoh, and N. K. Kumar, "Mechanical properties of single-crystal tungsten irradiated in a mixed spectrum fission reactor," *Journal of Nuclear Materials*, vol. 518, pp. 208–225, 2019. DOI: 10.1016/j.jnucmat.2019.02.050.
- [161] G. Cottrell, "Void migration in fusion materials," *Journal of Nuclear Materials*, vol. 302, no. 2-3, pp. 220–223, 2002. DOI: 10.1016/S0022-3115(02)00803-6.
- [162] J. Marian, C. S. Becquart, C. Domain, S. L. Dudarev, M. R. Gilbert, R. J. Kurtz, D. R. Mason, K. Nordlund, A. E. Sand, L. L. Snead, T. Suzudo, and B. D. Wirth, "Recent advances in modeling and simulation of the exposure and response of tungsten to fusion energy conditions," *Nuclear Fusion*, vol. 57, no. 9, p. 092008, 2017. DOI: 10.1088/1741-4326/aa5e8d.
- [163] M. Gilbert, S. Dudarev, S. Zheng, L. Packer, and J.-C. Sublet, "An integrated model for materials in a fusion power plant: Transmutation, gas production, and helium embrittlement under neutron irradiation," *Nuclear Fusion*, vol. 52, no. 8, p. 083019, 2012. DOI: 10.1088/0029-5515/52/8/083019.
- [164] T. Goorley, M. James, T. Booth, F. Brown, J. Bull, L. J. Cox, J. Durkee, J. Elson, M. Fensin, R. A. Forster, J. Hendricks, H. G. Hughes, R. Johns, B. Kiedrowski, R. Martz, S. Mashnik, G. McKinney, D. Pelowitz, R. Prael, J. Sweezy, L. Waters, T. Wilcox, and T. Zukaitis, "Initial MCNP6 release overview," *Nuclear Technology*, vol. 180, no. 3, pp. 298–315, 2012. DOI: 10.13182/nt11-135.

- [165] C. Becquart and C. Domain, “Ab initio calculations about intrinsic point defects and He in W,” *Nuclear Instruments and Methods in Physics Research Section B: Beam Interactions with Materials and Atoms*, vol. 255, no. 1, pp. 23–26, 2007. DOI: 10.1016/j.nimb.2006.11.006.
- [166] M. Muzyk, D. Nguyen-Manh, K. J. Kurzydłowski, N. L. Baluc, and S. L. Dudarev, “Phase stability, point defects, and elastic properties of W-V and W-Ta alloys,” *Physical Review B*, vol. 84, no. 10, 2011. DOI: 10.1103/physrevb.84.104115.
- [167] A. D. Backer, P. Lhuillier, C. Becquart, and M. Barthe, “Modelling of the implantation and the annealing stages of 800 keV 3He implanted tungsten: Formation of nanovoids in the near surface region,” *Journal of Nuclear Materials*, vol. 429, no. 1-3, pp. 78–91, 2012. DOI: 10.1016/j.jnucmat.2012.05.024.
- [168] T. Suzudo, M. Yamaguchi, and A. Hasegawa, “Stability and mobility of rhenium and osmium in tungsten: First principles study,” *Modelling and Simulation in Materials Science and Engineering*, vol. 22, no. 7, p. 075006, 2014.
- [169] T. Suzudo, T. Tsuru, and A. Hasegawa, “First-principles study of solvent-solute mixed dumbbells in body-centered-cubic tungsten crystals,” *Journal of Nuclear Materials*, 2018. DOI: 10.1016/j.jnucmat.2018.03.052.
- [170] A. E. Sand, S. L. Dudarev, and K. Nordlund, “High-energy collision cascades in tungsten: Dislocation loops structure and clustering scaling laws,” *EPL (Europhysics Letters)*, vol. 103, no. 4, p. 46003, 2013. DOI: 10.1209/0295-5075/103/46003.
- [171] J. Fu, Y. Chen, J. Fang, N. Gao, W. Hu, C. Jiang, H.-B. Zhou, G.-H. Lu, F. Gao, and H. Deng, “Molecular dynamics simulations of high-energy radiation damage in W and W-Re alloys,” *Journal of Nuclear Materials*, vol. 524, pp. 9–20, 2019. DOI: 10.1016/j.jnucmat.2019.06.027.
- [172] C.-H. Huang, M. R. Gilbert, and J. Marian, “Simulating irradiation hardening in tungsten under fast neutron irradiation including Re production by transmutation,” *Journal of Nuclear Materials*, vol. 499, pp. 204–215, 2018. DOI: 10.1016/j.jnucmat.2017.11.026.
- [173] A. Sand, K. Nordlund, and S. Dudarev, “Radiation damage production in massive cascades initiated by fusion neutrons in tungsten,” *Journal of Nuclear Materials*, vol. 455, no. 1-3, pp. 207–211, 2014. DOI: 10.1016/j.jnucmat.2014.06.007.
- [174] S. Zinkle and L. Snead, “Opportunities and limitations for ion beams in radiation effects studies: Bridging critical gaps between charged particle and neutron irradiations,” *Scripta Materialia*, vol. 143, pp. 154–160, 2018. DOI: 10.1016/j.scriptamat.2017.06.041.
- [175] X. Yi, M. L. Jenkins, M. A. Kirk, Z. Zhou, and S. G. Roberts, “In-situ TEM studies of 150 keV W+ ion irradiated W and W-alloys: Damage production and microstructural evolution,” *Acta Materialia*, vol. 112, pp. 105–120, 2016. DOI: 10.1016/j.actamat.2016.03.051.
- [176] F. Ferroni, X. Yi, K. Arakawa, S. P. Fitzgerald, P. D. Edmondson, and S. G. Roberts, “High temperature annealing of ion irradiated tungsten,” *Acta Materialia*, vol. 90, pp. 380–393, 2015. DOI: 10.1016/j.actamat.2015.01.067.

- [177] T. Hwang, M. Fukuda, S. Nogami, A. Hasegawa, H. Usami, K. Yabuuchi, K. Ozawa, and H. Tanigawa, "Effect of self-ion irradiation on hardening and microstructure of tungsten," *Nuclear Materials and Energy*, vol. 9, pp. 430–435, 2016. DOI: 10.1016/j.nme.2016.06.005.
- [178] D. Armstrong, X. Yi, E. Marquis, and S. Roberts, "Hardening of self ion implanted tungsten and tungsten 5-wt% rhenium," *Journal of Nuclear Materials*, vol. 432, no. 1-3, pp. 428–436, 2013. DOI: 10.1016/j.jnucmat.2012.07.044.
- [179] A. Xu, C. Beck, D. E. Armstrong, K. Rajan, G. D. Smith, P. A. Bagot, and S. G. Roberts, "Ion-irradiation-induced clustering in W–Re and W–Re–Os alloys: A comparative study using atom probe tomography and nanoindentation measurements," *Acta Materialia*, vol. 87, pp. 121–127, 2015. DOI: 10.1016/j.actamat.2014.12.049.
- [180] I. Ipatova, R. Harrison, P. Wady, S. Shubeita, D. Terentyev, S. Donnelly, and E. Jimenez-Melero, "Structural defect accumulation in tungsten and tungsten-5wt.% tantalum under incremental proton damage," *Journal of Nuclear Materials*, vol. 501, pp. 329–335, 2018. DOI: 10.1016/j.jnucmat.2017.11.030.
- [181] I. Ipatova, R. Harrison, S. Donnelly, M. Rushton, S. Middleburgh, and E. Jimenez-Melero, "Void evolution in tungsten and tungsten-5wt.% tantalum under in-situ proton irradiation at 800 and 1000°C," *Journal of Nuclear Materials*, vol. 526, p. 151 730, 2019. DOI: 10.1016/j.jnucmat.2019.07.030.
- [182] R. Abernethy, "Predicting the performance of tungsten in a fusion environment: A literature review," *Materials Science and Technology*, vol. 33, no. 4, pp. 388–399, 2016. DOI: <http://dx.doi.org/10.1080/02670836.2016.1185260>.
- [183] G. E. Lucas, "Review of small specimen test techniques for irradiation testing," *Metalurgical Transactions A*, vol. 21, no. 5, pp. 1105–1119, 1990. DOI: 10.1007/bf02698242.
- [184] P. Jung, A. Hishinuma, G. Lucas, and H. Ullmaier, "Recommendation of miniaturized techniques for mechanical testing of fusion materials in an intense neutron source," *Journal of Nuclear Materials*, vol. 232, no. 2-3, pp. 186–205, 1996. DOI: 10.1016/s0022-3115(96)00394-7.
- [185] "ASTM E8 / E8M-16ae1, Standard test methods for tension testing of metallic materials," ASTM International, West Conshohocken, PA, Tech. Rep., 2016.
- [186] A. Manhard, G. Matern, and M. Balden, "A step-by-step analysis of the polishing process for tungsten specimens," *Practical Metallography*, vol. 50, no. 1, pp. 5–16, 2013.
- [187] L. Garrison, F. Meyer, M. Bannister, and K. Unocic, "Effects of machining and polishing on the near surface region of tungsten for use as a plasma-facing component," in *16th International Conference on Plasma Facing Materials and Components for Fusion Applications Neuss/Düsseldorf, Germany*, 2017.
- [188] A. Manhard, U. von Toussaint, M. Balden, S. Elgeti, T. Schwarz-Selinger, L. Gao, S. Kapser, T. Płociński, J. Grzonka, M. Gloc, *et al.*, "Microstructure and defect analysis in the vicinity of blisters in polycrystalline tungsten," *Nuclear Materials and Energy*, 2016.
- [189] J. Hay, "Introduction to instrumented indentation testing," *Experimental Techniques*, vol. 33, no. 6, pp. 66–72, 2009. DOI: 10.1111/j.1747-1567.2009.00541.x.

- [190] ISO/TC 164/SC 3 Hardness testing, “Metallic materials — Instrumented indentation test for hardness and materials parameters ISO 14577-1:2015,” English, Tech. Rep.
- [191] W. Oliver and G. Pharr, “An improved technique for determining hardness and elastic modulus using load and displacement sensing indentation experiments,” *Journal of Materials Research*, vol. 7, no. 06, pp. 1564–1583, 1992. DOI: 10.1557/jmr.1992.1564.
- [192] I. Sacksteder, “Instrumented indentation for characterization of irradiated materials at room and high temperature,” Ph.D. dissertation, Karlsruher Institut für Technologie, 2011.
- [193] Zwick/Roell, “ZHU/zwickiline universal hardness tester for instrumented indentation tests,” Tech. Rep. [Online]. Available: <https://www.zwick.com/en/hardness-testers-for-instrumented-indentation-tests/zhu-zwickiline>.
- [194] C. Ullner, E. Reimann, H. Kohlhoff, and A. Subaric-Leitis, “Effect and measurement of the machine compliance in the macro range of instrumented indentation test,” *Measurement*, vol. 43, no. 2, pp. 216–222, 2010. DOI: 10.1016/j.measurement.2009.09.009.
- [195] M. Newville, T. Stensitzki, D. B. Allen, and A. Ingargiola, “LMFIT: Non-linear least-square minimization and curve-fitting for Python,” Tech. Rep., 2014. DOI: 10.5281/ZENODO.11813.
- [196] S. Soltysiak, M. Abendroth, M. Kuna, Y. Klemm, and H. Biermann, “Strength of fine grained carbon-bonded alumina (Al₂O₃-C) materials obtained by means of the small punch test,” *Ceramics International*, vol. 40, no. 7, pp. 9555–9561, 2014. DOI: 10.1016/j.ceramint.2014.02.030.
- [197] B. Merle, X. Kraus, M. Tallawi, B. Scharfe, M. E. Fray, K. Aifantis, A. Boccaccini, and M. Göken, “Dynamic mechanical characterization of poly(glycerol sebacate)/poly(butylene succinate-butylene dilinoleate) blends for cardiac tissue engineering by flat punch nanoindentation,” *Materials Letters*, vol. 221, pp. 115–118, 2018. DOI: 10.1016/j.matlet.2018.03.051.
- [198] E. Gennesseaux, T. Sedran, J. M. Torrenti, and M. Hardy, “Formulation of optimized excavatable cement treated materials using a new punching test apparatus,” *Materials and Structures*, vol. 51, no. 3, 2018. DOI: 10.1617/s11527-018-1184-1.
- [199] A. M. Mohaghegh, J. Silfwerbrand, and V. Årskog, “Shear behavior of high-performance basalt fiber concrete-part II: Laboratory punching shear tests on small slabs with macrofibers without bars,” *Structural Concrete*, vol. 19, no. 2, pp. 331–339, 2018. DOI: 10.1002/suco.201700207.
- [200] R. C. Hurst, R. J. Lancaster, S. P. Jeffs, and M. R. Bache, “The contribution of small punch testing towards the development of materials for aero-engine applications,” *Theoretical and Applied Fracture Mechanics*, vol. 86, pp. 69–77, 2016. DOI: 10.1016/j.tafmec.2016.07.013.
- [201] CWA, CEN, “15627, 2006,” in *Workshop Agreement: Small Punch Test Method for Metallic Materials (Part A)*, European Committee for Standardisation.
- [202] V. Karthik, K. Laha, P. Parameswaran, K. Chandravathi, K. Kasiviswanathan, T. Jayakumar, and B. Raj, “Tensile properties of modified 9Cr-1Mo steel by shear punch testing and correlation with microstructures,” *International Journal of Pressure Vessels and Piping*, vol. 88, no. 10, pp. 375–383, 2011. DOI: 10.1016/j.ijpvp.2011.07.001.

- [203] V. Rajagopal, "Simulation studies of shear punch testing in the regime up to ultimate tensile strength," M.S. thesis, Ernst-Abbe-Hochschule Jena, Forschungszentrum Juelich GmbH, 2019.
- [204] M. Hamilton, M. Toloczko, and G. Lucas, "Recent progress in shear punch testing," in *International symposium on miniaturized specimens for testing of irradiated materials; Juelich (Germany); 22-23 Sep 1994*, 1995. [Online]. Available: <https://www.osti.gov/scitech/servlets/purl/10110747>.
- [205] M. Manahan, A. Argon, and O. Harling, "The development of a miniaturized disk bend test for the determination of postirradiation mechanical properties," *Journal of Nuclear Materials*, vol. 104, pp. 1545–1550, 1981. DOI: 10.1016/0022-3115(82)90820-0.
- [206] X. Mao and H. Takahashi, "Development of a further-miniaturized specimen of 3 mm diameter for TEM disk (\varnothing 3 mm) small punch tests," *Journal of Nuclear Materials*, vol. 150, no. 1, pp. 42–52, 1987. DOI: 10.1016/0022-3115(87)90092-4.
- [207] G. Hankin, M. Toloczko, M. Hamilton, and R. Faulkner, "Validation of the shear punch–tensile correlation technique using irradiated materials," *Journal of Nuclear Materials*, vol. 258-263, pp. 1651–1656, 1998. DOI: 10.1016/s0022-3115(98)00203-7.
- [208] M. Toloczko, M. Hamilton, and G. Lucas, "Ductility correlations between shear punch and uniaxial tensile test data," *Journal of Nuclear Materials*, vol. 283-287, pp. 987–991, 2000. DOI: 10.1016/s0022-3115(00)00198-7.
- [209] M. Toloczko, Y. Yokokura, K. Abe, M. Hamilton, F. Garner, and R. Kurtz, "The effect of specimen thickness and grain size on mechanical properties obtained from the shear punch test," in *Small Specimen Test Techniques: Fourth Volume*, vol. 1418, ASTM International, 2002, pp. 371–379. DOI: 10.1520/stp10833s.
- [210] M. Toloczko, K. Abe, M. Hamilton, F. Garner, and R. Kurtz, "The effect of test machine compliance on the measured shear punch yield stress as predicted using finite element analysis," in *Small Specimen Test Techniques: Fourth Volume*, vol. 1418, ASTM International, 2002, pp. 339–349. DOI: 10.1520/stp10831s.
- [211] R. Guduru, K. Darling, R. Kishore, R. Scattergood, C. Koch, and K. Murty, "Evaluation of mechanical properties using shear–punch testing," *Materials Science and Engineering: A*, vol. 395, no. 1, pp. 307–314, 2005, ISSN: 0921-5093.
- [212] V. Karthik, P. Visweswaran, A. Vijayaraghavan, K. Kasiviswanathan, and B. Raj, "Tensile–shear correlations obtained from shear punch test technique using a modified experimental approach," *Journal of Nuclear Materials*, vol. 393, no. 3, pp. 425–432, 2009. DOI: 10.1016/j.jnucmat.2009.06.027.
- [213] S. Maloy, T. Romero, P. Hosemann, M. Toloczko, and Y. Dai, "Shear punch testing of candidate reactor materials after irradiation in fast reactors and spallation environments," *Journal of Nuclear Materials*, vol. 417, no. 1-3, pp. 1005–1008, 2011. DOI: 10.1016/j.jnucmat.2011.02.003.
- [214] V. Karthik, R. Kumar, A. Vijayaraghavan, C. Venkiteswaran, V. Anandaraj, P. Parameswaran, S. Saroja, N. Muralidharan, J. Joseph, K. Kasiviswanathan, T. Jayakumar, and B. Raj, "Characterization of mechanical properties and microstructure of highly irradiated SS 316," *Journal of Nuclear Materials*, vol. 439, no. 1-3, pp. 224–231, 2013. DOI: 10.1016/j.jnucmat.2012.06.006.

- [215] P. Sellamuthu, P. Collins, P. Hodgson, and N. Stanford, "Correlation of tensile test properties with those predicted by the shear punch test," *Materials & Design*, vol. 47, pp. 258–266, 2013. DOI: 10.1016/j.matdes.2012.11.057.
- [216] G. Hankin, M. Toloczko, K. Johnson, M. Khaleel, M. Hamilton, F. Garner, R. Davies, and R. Faulkner, "An investigation into the origin and nature of the slope and x-axis intercept of the shear punch-tensile yield strength correlation using finite element analysis," in *Effects of Radiation on Materials: 19th International Symposium*, vol. 1366, ASTM International, 2000, pp. 1018–1018–11. DOI: 10.1520/stp12448s.
- [217] M. Toloczko, R. Kurtz, K. Abe, and A. Hasegawa, "Tensile property estimates obtained using a low compliance shear punch test fixture," in *Effects of Radiation on Materials: 21st International Symposium*, ASTM International, 2004, pp. 612–612–11. DOI: 10.1520/stp11261s.
- [218] S. Möller, R. Krug, R. Rayaprolu, B. Kuhn, E. Joußen, and A. Kreter, "Deuterium retention in tungsten and reduced activation steels after 3 MeV proton irradiation," *Nuclear Materials and Energy*, vol. 23, p. 100742, 2020. DOI: 10.1016/j.nme.2020.100742.
- [219] R. Stoller, M. Toloczko, G. Was, A. Certain, S. Dwaraknath, and F. Garner, "On the use of SRIM for computing radiation damage exposure," *Nuclear Instruments and Methods in Physics Research Section B: Beam Interactions with Materials and Atoms*, vol. 310, pp. 75–80, 2013. DOI: 10.1016/j.nimb.2013.05.008.
- [220] R. A. Causet and T. J. Venhaus, "The use of tungsten in fusion reactors: A review of the hydrogen retention and migration properties," *Physica Scripta*, vol. T94, no. 1, p. 9, 2001. DOI: 10.1238/physica.topical.094a00009.
- [221] J. Roth and K. Schmid, "Hydrogen in tungsten as plasma-facing material," *Physica Scripta*, vol. T145, p. 014031, 2011. DOI: 10.1088/0031-8949/2011/t145/014031.
- [222] T. Tanabe, "Review of hydrogen retention in tungsten," *Physica Scripta*, vol. T159, p. 014044, 2014. DOI: 10.1088/0031-8949/2014/t159/014044.
- [223] R. Frauenfelder, "Permeation of hydrogen through tungsten and molybdenum," *The Journal of Chemical Physics*, vol. 48, no. 9, pp. 3955–3965, 1968.
- [224] I. G. Segev, E. Yahel, I. Silverman, A. Perry, L. Weismann, and G. Makov, "Hydrogen blister formation in single crystal and polycrystalline tungsten irradiated by MeV protons," *Journal of Nuclear Materials*, 2018. DOI: 10.1016/j.jnucmat.2018.11.005.
- [225] C. A. Schneider, W. S. Rasband, and K. W. Eliceiri, "NIH image to ImageJ: 25 years of image analysis," *Nature Methods*, vol. 9, no. 7, pp. 671–675, 2012. DOI: 10.1038/nmeth.2089.
- [226] X. Yi, M. L. Jenkins, K. Hattar, P. D. Edmondson, and S. G. Roberts, "Characterisation of radiation damage in W and W-based alloys from 2 MeV self-ion near-bulk implantations," *Acta Materialia*, vol. 92, pp. 163–177, 2015. DOI: 10.1016/j.actamat.2015.04.015.
- [227] W. Oliver and G. Pharr, "Measurement of hardness and elastic modulus by instrumented indentation: Advances in understanding and refinements to methodology," *Journal of Materials Research*, vol. 19, no. 01, pp. 3–20, 2004. DOI: 10.1557/jmr.2004.19.1.3.

- [228] M. Newville, R. Otten, A. Nelson, A. Ingargiola, T. Stensitzki, D. Allan, A. Fox, F. Carter, Michał, D. Pustakhod, Y. Ram, , Glenn, C. Deil, Stuermer, A. Beelen, O. Frost, N. Zobrist, G. Pasquevich, A. L. R. Hansen, A. Stark, T. Spillane, S. Caldwell, A. Polloreno, Andrewhannum, J. Borreguero, J. Fraine, Deep-42-Thought, B. F. Maier, B. Gamari, and A. Almarza, “Lmfit/lmfit-py 0.9.14,” Tech. Rep., 2019. DOI: 10.5281/zenodo.3381550.
- [229] W. D. Nix and H. Gao, “Indentation size effects in crystalline materials: A law for strain gradient plasticity,” *Journal of the Mechanics and Physics of Solids*, vol. 46, no. 3, pp. 411–425, 1998. DOI: 10.1016/s0022-5096(97)00086-0.
- [230] Y. Toda, Y. Satoh, Y. Kaneda, I. Suzukawa, and T. Yamada, “JSW’s baby cyclotron,” Tech. Rep. Vol NS-30m No. 2, 1983. [Online]. Available: <http://ieeexplore.ieee.org/document/4332544/>.
- [231] S. Qaim, “Target development for medical radioisotope production at a cyclotron,” *Nuclear Instruments and Methods in Physics Research Section A: Accelerators, Spectrometers, Detectors and Associated Equipment*, vol. 282, no. 1, pp. 289–295, 1989. DOI: 10.1016/0168-9002(89)90155-1.
- [232] S. Spellerberg, B. Scholten, I. Spahn, W. Bolten, M. Holzgreve, H. Coenen, and S. Qaim, “Target development for diversified irradiations at a medical cyclotron,” *Applied Radiation and Isotopes*, vol. 104, pp. 106–112, 2015. DOI: 10.1016/j.apradiso.2015.06.010.
- [233] G. Blessing, W. Brautigam, H. Boge, N. Gad, B. Scholten, and S. Qaim, “Internal irradiation system for excitation function measurement via the stacked-foil technique,” *Applied Radiation and Isotopes*, vol. 46, no. 9, pp. 955–960, 1995. DOI: 10.1016/0969-8043(95)00179-h.
- [234] Nucleonica Nuclear Science Portal, “Dosimetry & shielding (h*10),” Nucleonica GmbH (www.nucleonica.com), Tech. Rep., 2017.
- [235] O. M. Wirtz, “Thermal shock behaviour of different tungsten grades under varying conditions,” Ph.D. dissertation, 2012, ISBN: 978-3-89336-842-6.
- [236] J.-M. Geets and B. Nactergal, “The cyclone 30XP multiparticles cyclotron and At-211, Cu-67 production,” *Journal of Nuclear Medicine*, vol. 52, no. supplement 1, pp. 1514–1514, 2011.
- [237] R. Gebel, R. Brings, O. Felden, R. Maier, S. Mey, and D. Prasuhn, “20 years of JULIC operation as COSY’s injector cyclotron,” 2013.
- [238] U. Schmidt-Rohr, “The AEG isochronous cyclotron at Jülich; progress and status January 1966,” *IEEE Transactions on Nuclear Science*, vol. 13, no. 4, pp. 438–440, 1966. DOI: 10.1109/tns.1966.4324269.
- [239] S. Hoeffgen, S. Metzger, R. Brings, O. Felden, R. Gebel, R. Maier, D. Prasuhn, M. Brugger, and R. G. Alia, “Past, present and future activities for radiation effects testing at JULIC/COSY,” in *presented at Cyclotrons 2013*, 2013.
- [240] I. R. Williams and C. B. Fulmer, “Cross section for formation of Be7 by 20-155-MeV proton-induced reactions in carbon,” *Physical Review*, vol. 154, no. 4, pp. 1005–1007, 1967. DOI: 10.1103/physrev.154.1005.

- [241] F. Tárkányi, F. Ditrói, S. Takács, and A. Hermanne, “New measurements of excitation functions of $^{186}\text{W}(p,x)$ nuclear reactions up to 65MeV. production of a $^{178}\text{W}/^{178}\text{mTa}$ generator,” *Nuclear Instruments and Methods in Physics Research Section B: Beam Interactions with Materials and Atoms*, vol. 391, pp. 27–37, 2017. DOI: 10.1016/j.nimb.2016.11.027.
- [242] A. R. Driesner, C. P. Kempter, C. E. Landahl, C. A. Linder, and T. E. Springer, “High temperature thermocouples in the rover program,” *IRE Transactions on Nuclear Science*, vol. 9, no. 1, pp. 247–252, 1962. DOI: 10.1109/tns2.1962.4315916.
- [243] R. K. Williams, F. W. Wiffen, J. Bentley, and J. O. Stiegler, “Irradiation induced precipitation in tungsten based, W-Re alloys,” *Metallurgical Transactions A*, vol. 14, no. 3, pp. 655–666, 1983. DOI: 10.1007/bf02643781.
- [244] A. Hasegawa, T. Tanno, S. Nogami, and M. Satou, “Property change mechanism in tungsten under neutron irradiation in various reactors,” *Journal of Nuclear Materials*, vol. 417, no. 1-3, pp. 491–494, 2011. DOI: 10.1016/j.jnucmat.2010.12.114.
- [245] “Re-W reference phase diagrams,” MSI Eureka, Effenberg, G. (Ed.) by MSI, Materials Science International Services GmbH, Stuttgart, Tech. Rep., 2012.
- [246] C.-H. Huang, L. Gharaee, Y. Zhao, P. Erhart, and J. Marian, “Mechanism of nucleation and incipient growth of Re clusters in irradiated W-Re alloys from kinetic monte carlo simulations,” *Physical Review B*, vol. 96, no. 9, 2017. DOI: 10.1103/physrevb.96.094108.
- [247] F. Swinkels and M. Ashby, “A second report on sintering diagrams,” *Acta Metallurgica*, vol. 29, no. 2, pp. 259–281, 1981. DOI: 10.1016/0001-6160(81)90154-1.
- [248] E. Best, *Gmelin handbook of inorganic chemistry. W: Metal, chemical reactions with inorganic and organic compounds*. Heidelberg: Springer, 1986, ISBN: 9783662086872.
- [249] J. N. Mundy, S. J. Rothman, N. Q. Lam, H. A. Hoff, and L. J. Nowicki, “Self-diffusion in tungsten,” *Physical Review B*, vol. 18, no. 12, pp. 6566–6575, 1978. DOI: 10.1103/physrevb.18.6566.
- [250] H. Gerstenberg and I. Neuhaus, “A brief overview of the research reactor FRM II,” *International Journal of Nuclear Energy Science and Technology*, vol. 4, no. 4, p. 265, 2009. DOI: 10.1504/ijnest.2009.028587.
- [251] “Experimental facilities,” Heinz Maier-Leibnitz Zentrum (MLZ), Tech. Rep.
- [252] B. Ralph and D. G. Brandon, “A field ion microscope study of some tungsten-rhenium alloys,” *Philosophical Magazine*, vol. 8, no. 90, pp. 919–934, 1963. DOI: 10.1080/14786436308214452.
- [253] X. Hu, C. M. Parish, K. Wang, T. Koyanagi, B. P. Eftink, and Y. Katoh, “Transmutation-induced precipitation in tungsten irradiated with a mixed energy neutron spectrum,” *Acta Materialia*, vol. 165, pp. 51–61, 2019. DOI: 10.1016/j.actamat.2018.11.032.
- [254] M. J. Lloyd, R. G. Abernethy, D. E. J. Armstrong, P. A. J. Bagot, M. P. Moody, E. Martinez, and D. Nguyen-Manh, “Radiation-induced segregation in W-Re: From kinetic monte carlo simulations to atom probe tomography experiments,” *The European Physical Journal B*, vol. 92, no. 10, 2019. DOI: 10.1140/epjb/e2019-100244-y.

List of Figures

1.1	Comparison of fusion reaction rates for light ions [30]. Deuterium tritium reactions have the highest cross-section for lower ion temperatures. This is due to the release of a stable alpha particle (helium nucleus) as a reaction product.	3
1.2	A general sketch of Tokamak facility highlighting the toroidal coils and the central solenoid adapted from [32]. The magnetic flux representation are also shown for particle motion.	4
1.3	The progress in fusion is often measured by the scale up of the fusion triple product over the years. The graph adapted from [34] accounts that the product should be higher than $5 \cdot 10^{21}$ keVm ³ s for a deuterium tritium plasma to ignite and shortly displays the steps/ machines used to reach them.	5
1.4	Poloidal cuts of the plasma chamber.	6
1.5	Divertor design and cassette.	7
2.1	Cross-section comparison for (n,p) reaction on Cu65, Au197, Fe56 and Ni58. The cross-sections are material and neutron energy dependent which in turn determines the reaction rates for the material. Cross-sections taken from ENDF/B-VII.1 [73] and JANIS [74].	12
2.2	Neutron displacement damage flowchart.	13
2.3	Depiction of the interstitials created along the path followed by a PKA post neutron scattering interaction. Adapted from [76].	13
2.4	Kinchin Pease model for secondary displacements resulting from a PKA of energy T in a lattice with displacement threshold energy E_d and an upper cut off energy E_c .	15
2.5	Dependence of material properties as a function of increasing displacement damage(dpa) in the lattice due created by neutron irradiation. Adapted from [78].	18
2.6	(n,), (n,p), (n,2n) and (n,) reaction cross-section for ¹⁸⁶ W from ENDFVII.I [73] and JANIS4.0 [74]. The particle emissions are threshold reactions requiring energies greater than 7 MeV.	19
2.7	Neutron reaction and decay routes for ¹⁸⁶ W. The blue lines depict the end products from the various neutron transmutation reactions and the yellow dotted lines indicate further decay routes onto stable products.	20
2.8	Elemental composition change in W under neutron irradiation for DEMO reactor from [59]. Pure W changes into an alloy of 1 atomic % (10 ⁴ ppm) Re in under two years.	20
2.9	Contact doses post two years of irradiation in a 1.6 GW DEMO reactor for candidate elements. Data taken from [59].	22

2.10 Neutron damage is the combination of the two types of neutron interactions; scattering induced displacement damage and neutron absorption induced transmutation damage.	23
2.11 Sub-division of fission and fusion neutron spectrum based on neutron energy with the effective displacement cutoff superimposed. Binned neutron-energy flux spectrum for fission (HFR) and fusion (DEMO) and cold neutron (FRM-II) reactors taken from [83]. A clear distinction in the neutron energies between the spectra, especially with the 14 MeV peak for a fusion reactor is observed. . .	24
2.12 Superimposed captures of the extent of peak damage from a 5 keV PKA (maroon), 10 keV PKA (pink) and 100 keV PKA (blue) MD simulations in iron at 100 K adapted from [75]. The high energy 100 keV cascade splits itself into mini sub cascades, resulting in greater number of surviving defects.	24
2.13 Elemental build up from transmutation reactions in W within a fission (bold) and fusion (dotted) reactors. Thermal neutrons are responsible for the rapid rise of Re and Os in W for fission reactors while this is much slower in fusion reactors.	25
3.1 Construction of a tandem accelerator where two stages of acceleration exist in tandem within a single machine. The source is a negative ion and a stripper converts it halfway into a positive ion which adds further to the acceleration. . .	28
3.2 Schematic representation of a Sloan-Lawrance, drift tube linear accelerator. Here a series of drift tubes connected to an alternating rf supply conducts the ions through it.	28
3.3 Sketch of a cyclotron with the two semi-circular dees, adapted from [28].	29
3.4 Representation of the path and damage by various ions having 1 MeV energy on a sample of pure Ni adapted from [122]. Neutrons and protons have widely spaced interactions while heavy ions induce cascades of similar intensities to that of neutrons.	31
3.5 Range comparison for 20 MeV self ion (W+) on the left and 5 MeV & 30 MeV protons in tungsten on the right. The self ion deposits its energy in the first 2 m while, 5 MeV & 30 MeV have a range of 60 m & 1 mm respectively. The highlighted areas indicate the area of interest for damage investigation.	34
3.6 Damage vs range for different ions and neutrons in Nickel sample taken from [127] and adapted from [127]. The range of ions in materials depends on the interaction between ion and the sample material which also determines the damage registered in the material.	35
3.7 Reaction pathways undertaken by protons and neutrons which lead to similar chemical changes within the material over time.	37
3.8 Cross-sections vs energy for common proton induced reactions on 186W. Data taken from [74]. A minimum cross-section of 1 mbarn was considered for noticeable reaction rates. As seen a threshold energy is required to activate reactions. The shaded area represents a region where all major reactions occur simultaneously.	38
3.9 Modelling of 30 MeV proton flux spectra in a 550 m sample of W compared with the DEMO neutron spectrum, computed using MCNP6.1. The protons have a narrow energy width and degrade from 30 MeV at entry to 15 MeV at exit of the sample. This is the first step in the feasibility study of proton irradiation for fusion neutron damage simulation.	39

3.10	Modelling the change in transmutation elements in appm post 1 dpa of 30 MeV proton irradiation over a sample depth of 550 μ m. The production of Re is stable and within 2x over the entire range of 550 μ m. This reinforces the validity of macroscopic sample testing using protons.	40
3.11	Activity calculations for 30 MeV protons on W calculated using FISPACT-II for a total dose of 1 dpa. The dots represent the dose rate which the bars represent the induced activity in Bq. The blue representing ^{187}W activity is seen to be the largest source of activity.	40
3.12	High energy PKA recoil spectra for proton entry at 30 MeV(blue) per second per W atom per proton compared with the DEMO and HFR recoil spectrum.	42
3.13	Modelling of the complete PKA recoil spectra obtained from SPECTRA-PKA [59] in comparison with recoil spectra from 30 MeV protons. Using recoil cross-sections, this novel approach allows a correct displacement damage scenario is estimated.	42
3.14	The cumulative PKA-energy distribution for W isotopes shows the difference in recoil energies from 30 MeV protons on W. The naturally occurring W isotopes consist of low energy recoils while the transmutation produced show higher recoil energies from the Q value.	43
4.1	The development of irradiation defects from fission neutron irradiation on W, adapted from [156].	51
4.2	Compilation of defects observed from neutron damage on pure W adapted from [157]. At high temperatures and high dpa, only voids can be observed.	51
4.3	Increase in hardness with dose, based on post irradiation measurements at HFIR and JMTR adapted from [159].	52
4.4	The 2 dimensional interpretation of a MD simulation result for a collision cascade in W from a 200 keV PKA adapted from [162]. Recoils having energy > 10 eV are shown in the Figure. The Figure on the left shows the starting impact of the PKA while the grab on the right shows the same cascade post 40 ps simulation time.	53
4.5	Simulated PKA energy dependent, number of surviving Frenkel pairs post a displacement cascade. The red line indicates recent results from [58]. The Figure adapted from [171] shows two different zones of PKA energy dependence at 40 keV. The Frenkel pairs are seen to scale upwards with increasing PKA energy for high energy cascades.	54
5.1	Recommended tensile sample dimensions from [184].	61
5.2	Sample geometry with dimensions. The sample itself consists of one miniaturised tensile sample and four shear punch samples. The cut sub samples are shown on the right.	62
5.3	Scanning electron microscopy images of EDM cut tensile sample on the left and laser cut sample on the right under same magnification. Notice the heat affected band around the laser cut sample. While for EDM cut samples oxide layers are seen on the surface.	63
5.4	2 dimensional mapping of the elements recognised from EDX measurements on the interface between the oxide layer and the buld sample for the EDM cut W.	63
5.5	A line scan of the interface using EDX showing the atomic concentration in % for W, O, Cu and Zn in the EDM cut W sample.	64

5.6	The electro-polishing set-up with a DC voltage power supply, an electric stirrer and the cathode wire mesh.	65
5.7	Comparison between mechanical grinding on the sample upto P4000 and electro-polishing. Clear scratches are seen on the mechanically ground sample while large grains can be recognised on the surface of the electro-polished sample. 66	66
5.8	A comparison of the bulk sample below the surface post P 4000 grinding and EP. The perpendicular cross-section reveals a thin layer of damage just below the surface from mechanical grinding. This layer is removed by electro-polishing the sample.	66
5.9	Cracks seen after polishing on an EDM cut sample. The cracks are of 1 μ m thickness and penetrate more than 10 μ m deep.	66
5.10	A basic force displacement curve for instrumented indentation showing the maximum indentation depth h_{max} at the maximum force F , permanent indentation depth h_p post load removal and the point of intersection from the tangent to the curve at maximum force taken from [190].	67
5.11	The head of Zwick Z2.5 consisting of the force and displacement transducers as adapted from [194]. The head consists of a ring which measures surface contact and enables the measurement for miniature samples like the 3 mm disks. . . .	69
5.12	The loading and unloading curves for a W, SS316L, Aluminium(Al), Copper (Cu), and ASTM P-92. The maximum force for materials except Cu (10 N) is 15 N. As expected, a deeper indent is inscribed in Al while W shows a rather high resistance to indentation.	69
5.13	The compliance measured on a W sample using the linear regression between total compliance and $F^{-0.5}$	70
5.14	The loading-unloading curve from a Martens hardness test using a macroscopic instrumented indentation which measures the Vickers hardness at the end of the test. The unloading curve is fit using the least square method [195] according to [190].	71
5.15	Instrumented indentation results on an unirradiated 316L sample showing 10 indents on the same sample. The variation between each indent can be observed in the Vickers hardness and indentation modulus.	71
5.16	A cross-sectional view of the set-up and a size comparison of the sample with the punched out disks.	72
5.17	A typical force vs displacement curve for a shear punch test adapted from [202]. Similar to tensile testing, the punch curve has an elastic and plastic region. . .	73
5.18	A sequential punching process with numbers corresponding to the various stages of the process taken from [203].	74
5.19	The concept and prototype of the Shear punch test design for 3 mm disks. . . .	75
5.20	2 dimensional finite element model of the shear punch prototype in Ansys. A wire mesh using 4 node and 3 node plane-182 elements are used with a finer allocation in the clearance region and the sample-die interaction areas. Adapted from [203].	76
5.21	Results from the punch simulation performed in Ansys on a 3 mm W disk. The stages (a),(b),(c) and (d) represent elastic regime, yield point, sample yielding and plastic zone in the sample. The values listed show shear stress in the sample. 76	76
5.22	The sample has a compressive and tensile stress component which leads to a compound state of stress rather than pure shear adapted from [203].	77

5.23	Hot cells in Forschungszentrum Jülich with the steel box in orange and enclosed with lead and concrete walls. The activities inside can be seen through a lead glass (blue) which is used to stop gamma rays and operations including handling of radioactive materials is performed using robotic arm manipulators (yellow).	79
5.24	The cable diagram along with the placement inside the hot cells designed as part of this work. Cables lengths often longer than 5 m are needed for routing.	80
5.25	Manipulator finger masks which are welded on work tools and parts requiring movement for easier manipulator operation.	80
5.26	A vacuum operated pincer set for sample loading and unloading which can be suitably adapted onto the manipulator arms.	81
5.27	Sample holder with an offset cavity for the complete sample with 3 mm disks. The 3 mm disks are in the centre for the punch.	81
5.28	A moveable table designed for the instrumented indentation machine within the hot cell. Using the table, the machine can be conveniently moved into proper view for sample installation and suitable repair work if required.	82
6.1	Range of 3 MeV protons in W, with the range of investigation being the plateau prior to the Bragg peak highlighted.	84
6.2	Vacancies created per ion per unit range and cumulative for 3 MeV protons on W calculated using the quick KP method in SRIM2008 [126].	84
6.3	The 3 MeV proton damage in W on the left visualised in 3 dimensions and compared against a 20 MeV self ion damage on the right, plotted using the 3d displacement damage option in SRIM2008.	85
6.4	Two sample geometries were installed and irradiated with 3 MeV protons. The first is an established plasma exposure sample geometry while the geometry on the right is for comparison with high energy proton irradiations.	86
6.5	The samples were loaded on to the sample holder with a scintillation sample next to it in order to obtain the beam spot size.	86
6.6	Temperature profile calculated by Ansys for a 3 MeV proton beam of 500 nA current on the W sample.	87
6.7	Optical profilometry measurements of the sample and a blister. The blisters correspond to the irradiation beam spots and large cracks are seen on the blister.	88
6.8	Altitude scans of sample irradiation spot 1, 2 and 3 with a 3 dimensional reconstruct of irradiation spot 1.	88
6.9	Cracks seen on the surface of the blister on the irradiated beam spots.	89
6.10	A focussed ion beam cut through a blister on the W sample showing a large void in the middle of the sample.	90
6.11	A focussed ion beam cut on the second irradiated sample with high starting currents to suppress blister formation.	91
6.12	TEM images of damage induced from 3 MeV protons with increasing damage dose. The unirradiated picture is shown for comparison of proton damage with the cutting induced damage.	92
6.13	Loop density estimation for the three damage doses of 0.1, 0.5 and 1.0 dpa based on the grey scale rediction technique from [226].	93
6.14	Loop diameter histograms for 0.1, 0.5 and 1 dpa damage doses on W from 3 MeV proton irradiation.	93
6.15	An array of 5 5 indents of micro-indentation on the irradiated beam spot seen in dark grey and the force displacement diagram.	94

6.16	A macro-indent on the irradiation beam spot along with the micro indents and the force displacement diagram.	95
6.17	A comparison of the results of micro and macro indentation conducted on the same beam spots for 3 MeV irradiated W.	96
6.18	Beam spot as seen from the scintillator and placed on a 3 mm disk sample. Larger beam spots were attempted on the 3 mm disk samples to apportion multiple macro-indentations on the beam spot area.	97
7.1	BC1710 aka Baby cyclotron located at the institute for nuclear chemistry and routinely used for the production of radio-isotopes such as such as ¹⁸ F and ¹¹ C.	100
7.2	The sample rod which is inserted into the solid target system and encapsulates the solid target in it. It also has a cooling circuit for heat removal with the sample rod.	101
7.3	The sample holder made out of oxygen free Cu which is used to irradiate solid targets along with its design drawing.	102
7.4	A MCNP6 representation of the sample holder. Each colour and number represents the cell numbering system used. As seen the Cu sample holder, the bronze cap and the entire sample holder assembly was simulated.	103
7.5	The proton flux per source proton estimated using MCNP6.1 for the W sample, the Cu sample holder, Cu disk and Cu screw top.	104
7.6	FISPACT II dose rate calculations for an irradiation scenario using the fluxes from MCNP6 to ascertain the induced activity and dose rates for the irradiated samples.	104
7.7	Post irradiation activity on W sample, Cu disk and Cu sample holder for a three one hour, 10 A, 16 MeV proton irradiation scenario calculated using proton fluxes from MCNP6.1 and inventory calculation software FISPACT-II.	105
7.8	The neutrons produced per source proton from (p,xn) reactions of 16 MeV protons on W for different cells estimated using MCNP6.1. As seen the neutrons produced are mostly high energy and would leave the target area.	106
7.9	1 st trial of the sample holder with the plain sample on the Cu sample holder.	107
7.10	2 nd trial of the sample holder with a Cu plate above the sample for good thermal contact. Additionally, the Cu also protects the sample against the irradiation at non-significant areas.	107
7.11	Post irradiation the Cu plate is stuck onto the Cu top due to improper thermal contact. Although the thermocouple reading indicate a good contact for the W sample.	108
7.12	3 rd trial of the sample holder at the baby cyclotron with a graphite piece as the pressure plate for inducing thermal contact between the sample and the Cu sample holder.	109
7.13	A diagram representing the Bragg peak in a mixture of C (grey) and Cu(gold). In the range diagram it is observed that the Bragg peak lies in the Cu which would act as the beam dump and melt the Cu during irradiation.	109
7.14	Estimation of the irradiation temperature profile through the sample using Ansys mechanical steady state heat solver. A change of 4°C is observed between the top and bottom side of the sample.	111
7.15	Comparison of two different methods of heat application. The 3 mm disk sample on the right has internal heat generation applied as the method of heating while the sample on the left shows heat flux applied as the source of heat.	111

7.16	The samples with the Cu disk which melted during irradiation. A thicker graphite sample is sought for the next irradiation.	113
7.17	A comparison of the directly exposed sample surface(left) to the rear side of the sample(right). The rear side of the surface retains the original surface.	114
7.18	A comparison of the surface micro-structure of samples Baby_SP2, Baby_SP3 and Baby_Ten as seen under an optical microscope with 40x magnification and a scale bar reading of 50 μm	115
8.1	JULIC (Jülich light ion cyclotron) injector cyclotron.	118
8.2	External beam line used for solid target irradiation at JULIC. A maximum beam current of 1.3 A under a vacuum pressure of $2 \cdot 10^{-02}$ mbar is achieved.	118
8.3	The Al sample holder with water connections for sample cooling is installed at the rear end of the beam line for solid target irradiations.	119
8.4	Sample assembly representation for JULIC cyclotron exposures.	120
8.5	Detailed description of sample assembly for JULIC cyclotron irradiation. The colour variation at the top represents the energy degradation in the sample core from 45 to 4 MeV. The entire assembly is then stacked into the copper sample holder and placed in the Al plate for irradiation.	120
8.6	Temperature estimation using a steady state thermal calculation using Ansys14.1, a finite element method software. An internal heat generation method was used to account for the electronic and nuclear stopping power losses from the proton irradiation.	121
8.7	Sample before irradiation (left) polished to 1 μm and post irradiation (right) with an oxide layer.	122
8.8	The gamma detector system and its calibrated efficiency curve using isotopes of known activity and specific high intensity gamma lines. The detector was calibrated for 80 cm.	123
8.9	A clear 477.6 keV peak is seen on the gamma analysis of the graphite sample under proton irradiation. This peak is the result of decay of ^7Be onto stable ^7Li	124
8.10	The production cross-section for ^7Be from ^{12}C plotted against incoming proton energy from [74]. The production sharply increases after 25 MeV for protons.	125
8.11	Gamma energy spectrum from the 16 MeV W sample post irradiation at JULIC. The spectrum was taken after a counting time of 86400 s.	125
8.12	An overview of the samples post transport to the hot material laboratory. The blue brown coating on W is clearly seen on the sample.	128
8.13	Comparison of the oxide formation on the sample faces. The oxide formation (darkening) seems to be higher on the side in contact with the Cu disk.	129
9.1	W-Re phase diagram adapted from [245]. Re is soluble to a high extent in W and forms ϵ phases, however under neutron irradiation, precipitation far below solubility limits is known to occur.	133
9.2	Scanning electron microscopy of isotopically pure ^{186}W powder which has an average powder size between 5 - 8 μm	135
9.3	Sintering density diagram adapted from [247] for W spheres. With increasing density and temperature, the sintering time reduces drastically.	136
9.4	Atom probe tomography on the ^{186}W sample post sintering with a grain boundary within the sample. The carbon and nitrogen are seen to segregate near the grain boundary.	137

9.5	A schematic of the beam lines along with the sources taken from FRM2 experimental facilities brochure. The beam lines can be seen to originate along the hot source and the cold source based on experimental requirements.	138
9.6	Flux comparison between the NL3 and SR4B stations at FRM II reactor in Munich. SR4B looks directly into the cold source, it has a higher flux albeit also thermal neutrons.	139
9.7	Dose rate calculations for SR4B station (blue) and NLC3 station (black) samples with the background environmental radiation indicated in red. The dose rates are calculated for a point source at a distance of 30 cm away. A pure cold neutron flux reaches near background radiation dose rate within a cooling period of 180 days.	140
9.8	The SR4B station is located at the end of a beam line at the end of the reactor complex. The Al window is part of the shielding and is replaced with our sample setup.	141
9.9	SR4B sample installation schematic. The Al windows shown in Figure 9.8 is replaced with an identical window shown in dark blue. The sample sits inside a pouch which is held and fit onto the Al window using slits for easy removal post irradiation.	141
9.10	The NLC3 station with a sliding shutter system operated by motors.	142
9.11	NLC3 station sample assembly schematic in the reactor for the pure transmutation damage study at FRM II. The sample sits inside a pouch covered by Al foil and loaded onto the boron carbide plate on the sliding shutter.	142
10.1	Micro-structure comparison between 3 MeV proton irradiation, 2 MeV self ion irradiation [226] and HFIR neutron irradiation [70] under TEM. The irradiation temperatures are different, however the doses are approximately compared at 0.5 and 1.0 dpa damage. A clear distinction is observed within the damage produced between neutrons and ions. Voids and precipitates are seen in neutron irradiated samples, while no voids are observed under self ion irradiations. Dislocation loops can be noticed in both self ion irradiations and 3 MeV proton irradiations. For damages near and above 1 dpa, fission reactor studies estimate the Re content to be 5% and the transmutation can be clearly seen as needle like precipitates.	147
10.2	Visualisation of irradiation hardness increase with respect to increasing dose for proton irradiation (this study), self ion irradiation [178] and HFIR neutron irradiation [70] [159]. This study has used macro indentation to obtain indentation hardness for proton irradiations shown in orange, red and grey. Neutron irradiation results in black represent Vickers hardness, while self ion and proton irradiation represent instrumented hardness. The use of different techniques results in hardness offsets, but the trend is clearly visible.	149

List of Tables

- 2.1 W recoil and displacement cascade size as predicted by the NRT model using Lindhard’s screened electronic loss partitioning. Adapted from similar calculations described for iron (Fe) in [75]. 16
- 3.1 Upper, lower and average recoil energies in Tungsten using $E_d = 90$ eV [123] for high energy protons and self ions calculated using the Coulomb potential and Rutherford scattering against the DEMO average PKA recoil energy of 3.2 keV [83]. 33
- 3.2 The 3 main radionuclides along with their half lives resulting from the 30 MeV proton irradiation on W over a cooling time of 1 year. The produced amount and half life result in the corresponding change of nuclides over time. Such an estimate is provided for nuclear safety and dose rate calculations. 41
- 3.3 The average PKA energy for W isotopes and net W element, calculated by SPECTRA-PKA for 30 MeV protons, compared against DEMO neutron irradiation. The PKA energy for 30 MeV protons on W has a lower limit of 5 keV due to the recoil cross-section availability in TENDL-2015. The average differs from 3.1 due to the lower limit of 5 keV placed, additionally, these calculations are based on recoil cross-sections as against approximations. 43
- 3.4 Comparison of ion damage with neutron damage on W. The initial modelling of protons performed in this work and listed within this section as the early development stage of proton damage shows promising results and proof-of-concept for the current work. 44
- 4.1 A comparison of the impurities measured using ICP-MS and ICP-OES with the manufacturer’s specification leading to a chemical purity of 99.98%. The impurities are listed in $\frac{g}{g}$ or ppm of W. Most impurities are below the manufacturers limits except Al. 49
- 4.2 The isotopic composition of W measured using ICP-MS and TOF-SIMS against its natural isotopic composition. 49
- 5.1 Reactor based tensile test specimen geometry for miniaturised samples considered for irradiation campaigns taken from [183]. 61
- 5.2 An approximation of the mechanical polishing steps used prior to electro-polishing. 64
- 5.3 Maximum permitted licensed activity in HML for some expected nuclides based on the area and source type in Bq. 78
- 6.1 Irradiation characteristics for beam spots 1 - 7 on sample W_nano1. The beam spot areas are measured using the scintillator coated sample. 88

6.2	Irradiation characteristics for beam spots 1 - 7 on sample W_nano2. The new sample was irradiated using high starting beam currents, which was gradually lowered to dispense off with the blisters.	90
6.3	Irradiation characteristics on W samples for TEM characterisation. Three doses of 0.1, 0.5 and 1.0 dpa are undertaken to comprehend the changes in micro-structure. Similar to sample W_nano2, high starting currents were used to avoid any blister formation.	91
6.4	Necessary inputs for the micro-indentation measurements on irradiated W sample.	95
6.5	Estimated indentation hardness and measured Vickers hardness for a maximum load of 15 N on 3 mm disk samples irradiated to 0.005 and 0.01 dpa for comparison with cyclotron irradiations. The man of the tests along with the standard error of the mean is listed in the Table. An immediate jump in hardness is noticed even at low doses of 0.001 dpa damage.	97
7.1	Collimator current to target current ratio for various collimator diameters at Baby cyclotron taken from [232].	100
7.2	Specifications of the thermocouples used for online irradiation temperature measurement fed into the sample holder.	102
7.3	The irradiation dates listed alongside cooling times relevant for decay and dose rate calculations.	110
7.4	The major nuclides as estimated using FISPACT-II simulation run for 16 MeV proton irradiation. As the short lived nuclides decay out, the long lived nuclides are dominant.	112
7.5	Comparison of simulated and measured dose rates after 7 days of cooling post last irradiation. The beta dose rate is not recorded within the gamma dose analysis with nucleonica.	112
7.6	Contact dose rates measured for samples compared to simulation results and each other, 92 days post last irradiation. The uneven dose rates between the 3 mm disc samples implies a difference in the irradiation dose between the samples.	114
7.7	The indentation hardness and measured Vickers hardness for samples Baby_SP1, Baby_SP2, Baby_SP3 and Baby_Ten sample using a maximum force of 15 N and a waiting time of 12 s at maximum force. As only one indent was made for each sample, no error is reported for the irradiation hardening which is a derived quantity, however as Vickers hardness is a measured quantity the experimental uncertainty is shown.	115
7.8	Transmutation based elemental precipitation from the 16 MeV proton irradiation of W to a dose of 0.006 dpa damage dose estimated using MCNP6.1 and FISPACT-II.	116
8.1	Irradiation schedule for 30 MeV proton irradiations at JULIC accelerator. Cooling time for gamma measurement and the activity calculations using FISPACT-II were accordingly considered.	121
8.2	The list of proton reactions on ^{12}C resulting in the production of ^7Be with their respective proton threshold energies taken from [240].	123
8.3	List of high energy gamma lines which were used to estimate the production activity of the sample post irradiation.	126

8.4	The activity of major nuclides measured by gamma analysis compared against simulated using FISPACT-II and TENDL-2015 cross-sections after a cooling period of 56 days post last irradiation. ¹⁸² Ta formation is 50x higher than that predicted. However, the Re isotopes show good conformity.	126
8.5	Simulated and measured dose rate measurements for the radioactive sample for in contact with the sample holder (about 2 cm away from the sample which includes 0.5 cm of Copper disk) and in direct contact to the edge of a 3.5 cm lead shielding.	127
8.6	Inputs for macro-indentation of COSY_16MeV and COSY_30MeV samples.	129
8.7	Measured indentation hardness for cyclotron irradiated samples COSY_16MeV & COSY_30MeV. Indents were made on each sub sample and the average is shown along with the standard error of the mean.	130
8.8	FISPACT-II simulated transmutation contribution for 16 & 30 MeV proton irradiated W.	131
9.1	The chemical purity was measured using ICP-MS. This was specifically done to confirm special isotopes which have large capture cross-sections for cold neutrons. Consider the upper limits of ICP-MS measurement, the sample is stated to have a chemical purity of 99.6%.	135
9.2	The isotopic composition measured using ICP-MS is compared against the natural isotopic composition and the manufacturer specifications. The isotopic purity of the ¹⁸⁶ W is measured to be 99.78%.	136
9.3	Composition of sample post sintering tested by APT using the laser mode. O, C and N atoms were found to be present within the sample.	138
10.1	Summary of the irradiation conditions for proton irradiation undertaken in this work. As 3 MeV proton irradiations lead to inactive samples, a range of irradiation doses were obtained. The high radioactivity and limited beam time resulted in only two high energy proton irradiation experiments.	153
2	Elemental wt% composition for SS316L(N)-IG steel used in the vacuum vessel from [39]	190
3	Elemental wt% composition for reduced activation EUROFER steel used as the general purpose steel for the components within the vacuum vessel [39]	191

Elemental composition

Element	wt(%) composition
C	0.03
Mn	2
Si	0.5
P	0.025
S	0.01
Cr	18
Ni	12.5
Mo	2.7
N	0.08
B	0.001
Cu	0.3
Co	0.05
Nb	0.01
Ti	0.1
Ta	0.01
Fe	63.68

Table 2: Elemental wt% composition for SS316L(N)-IG steel used in the vacuum vessel from [39]

Element	wt(%) composition
C	0.12
Mn	0.6
P	0.005
S	0.005
Cr	9.5
Si	0.05
Ni	0.01
Mo	0.005
V	0.24
W	1.2
Cu	0.01
Nb	0.005
Al	0.01
N	0.045
B	0.002
Co	0.01
As	0.01
Sn	0.01
Sb	0.01
Zr	0.01
Ti	0.02
Ta	0.14
Fe	87.98

Table 3: Elemental wt% composition for reduced activation EUROFER steel used as the general purpose steel for the components within the vacuum vessel [39]

Cold neutrons



Stable isotopes for medicine, science and industry

STB Isotope Germany GmbH

www.stb-isotope.com

Address / Adresse: Stb. BRB, Friesenweg 2C, Hamburg 22763, Deutschland / Germany

In English: Tel.: +49 (0)3834 84 80 177 Fax: +49 (0)3834 84 85 166 E-mail: info@stb-isotope.com

In Deutsch: Tel.: +49 (0)174 336 88 86 Fax: +49 (0)3834 84 85 166 E-mail: dagan@stb-isotope.com

667.

Certificate of Analysis (CoA)

Gilt als Lieferschein

Page 1/2

Invoice address:
Forschungszentrum Jülich GmbH
F-BK
52425 Jülich
Germany

Delivery address:
Forschungszentrum Jülich GmbH
Warenannahme (M-ME) Gebäude 20.05
Rayaprolu 10.14 S037
Leo-Brandt-Straße
52428 Jülich
Germany

Seite 1-2
Bitte überprüfen!
Lieferung i.O.

Contact Person:
Mrs. Elisabeth Bauer/W50
Tel.: 02461 613037
Email: e.bauer@fz-juelich.de

Contact Person:
Mr. Rahul Rayaprolu
Tel.: 02461/61-5126
Email: r.rayaprolu@fz-juelich.de

19.06.18
Datum/Unterschrift
Lieferschein bitte an IEK-4KV
zurück. Vielen Dank!

Table with 2 columns: Field (Order No., Date of order), Value (42183375, 21.03.2018)

Table with 2 columns: Field (Certificate No., Date), Value (7610, 13.06.2018)

The description, isotopic distribution and chemical admixtures relating to the above referenced order number are certified to be as follows:

Description

Table with 2 columns: ISOTOPE, ENRICHMENT, ELEMENT WEIGHT, FORM; Values: W-186, 99,9(±0,1)%, 2000 mg, Metal Powder

Wareneingang M-ME
Heimig, Tel. 5040
Lieferschein zurück an M-ME
15. Juni 2018
Name in Klerschrift: Unterschrift:

Isotopic Distribution

Table with 6 columns: ISOTOPE, W-180, W-182, W-183, W-184, W-186; Values: <0,01, <0,01, <0,01, 0,1 (±0,05), 99,9(±0,1)

Chemical Admixtures

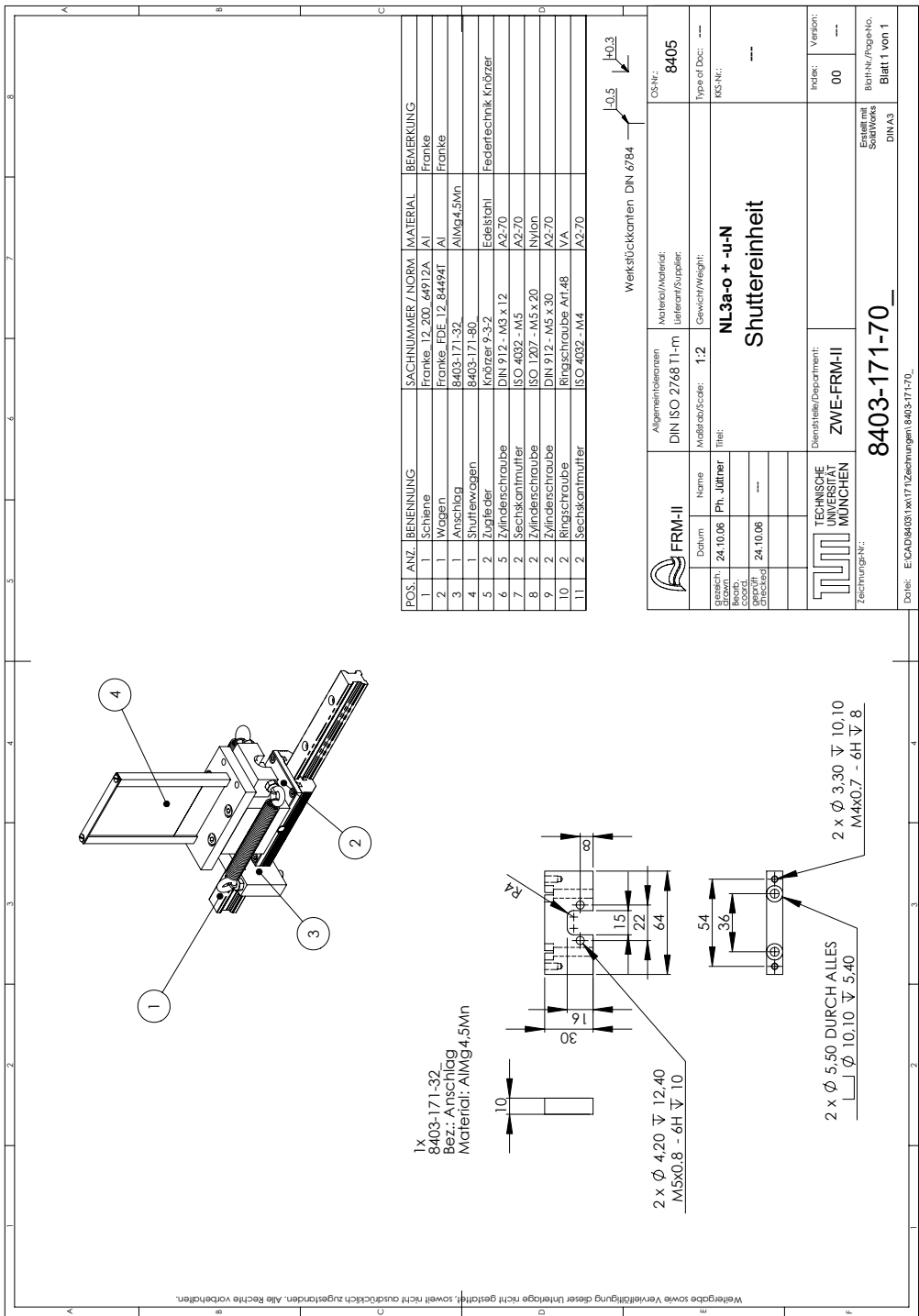
Table with 11 columns: ELEMENT, Al, As, B, Be, Ca, Co, Cr, Cu, Fe, Ge; Values: <30, <300, <20, <2, <80, <100, <80, <2, 240, <40

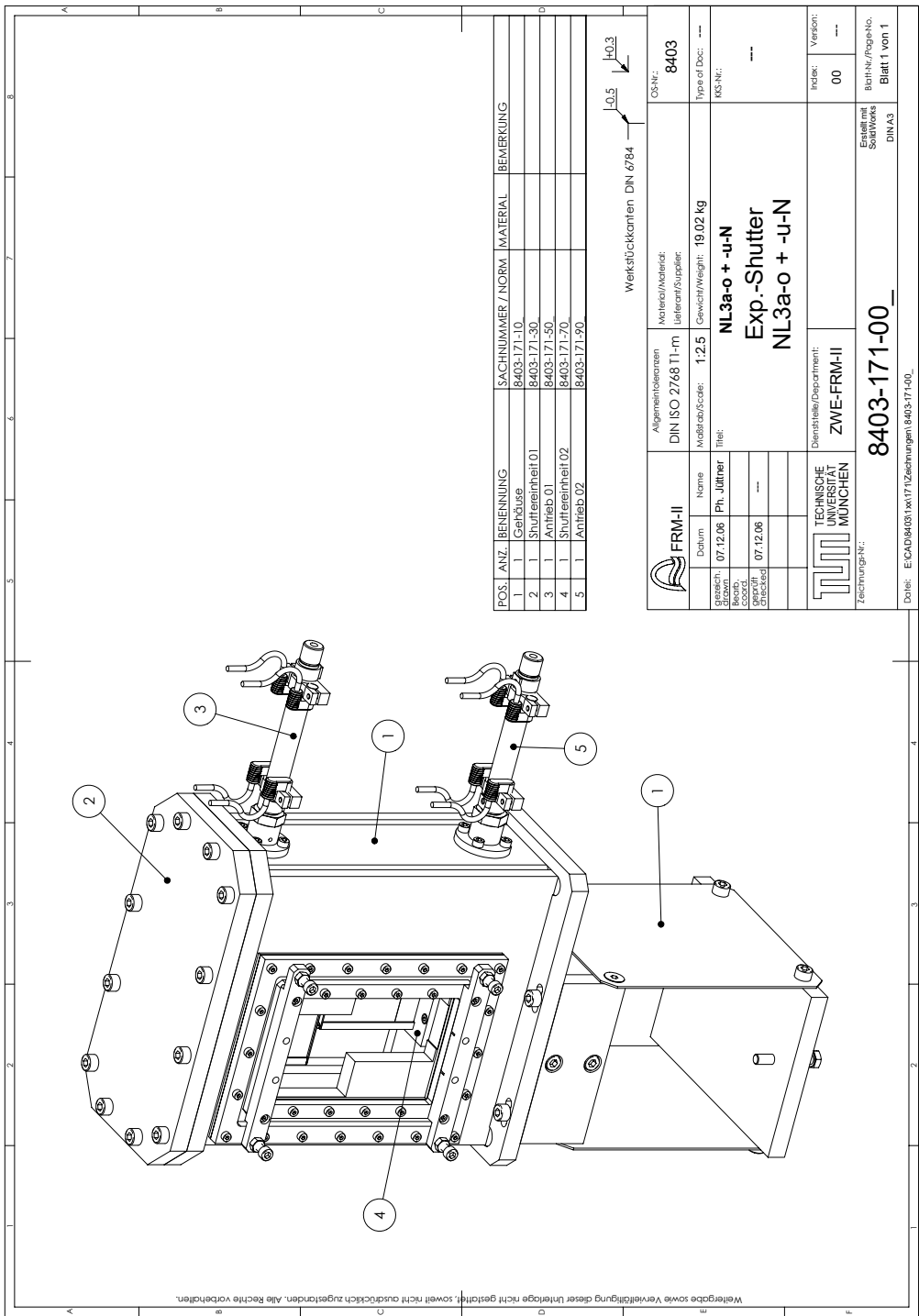
Table with 10 columns: ELEMENT, Mg, Mn, Mo, Na, Ni, Sc, Si, Ti, Zn; Values: 30, 20, <80, 30, <20, <10, <20, <60, <60

826 777

Erfüllungsort und Gerichtsstand ist Hamburg
Amtsgericht Hamburg HRB 73139
Geschäftsführer: Allan Pashitovsky
Ust-IdNr. (VAT): DE 204141705

Bankverbindung - Bank Information: Hypovereinsbank AG, Alter Wall 22, Hamburg
Euro Konto (Account) 421826, IBAN: DE46 2003 0000 0000 421826, BLZ 20030000
USD Account (Konto) 910053545, IBAN: DE87 700 202 700 910053545 BLZ 70020270
SWIFT: HYVEDE33





Weißgabe sowie Verfertigung dieser Unterteile nicht gestattet, soweit nicht ausdrücklich zugestanden. Alle Rechte vorbehalten.

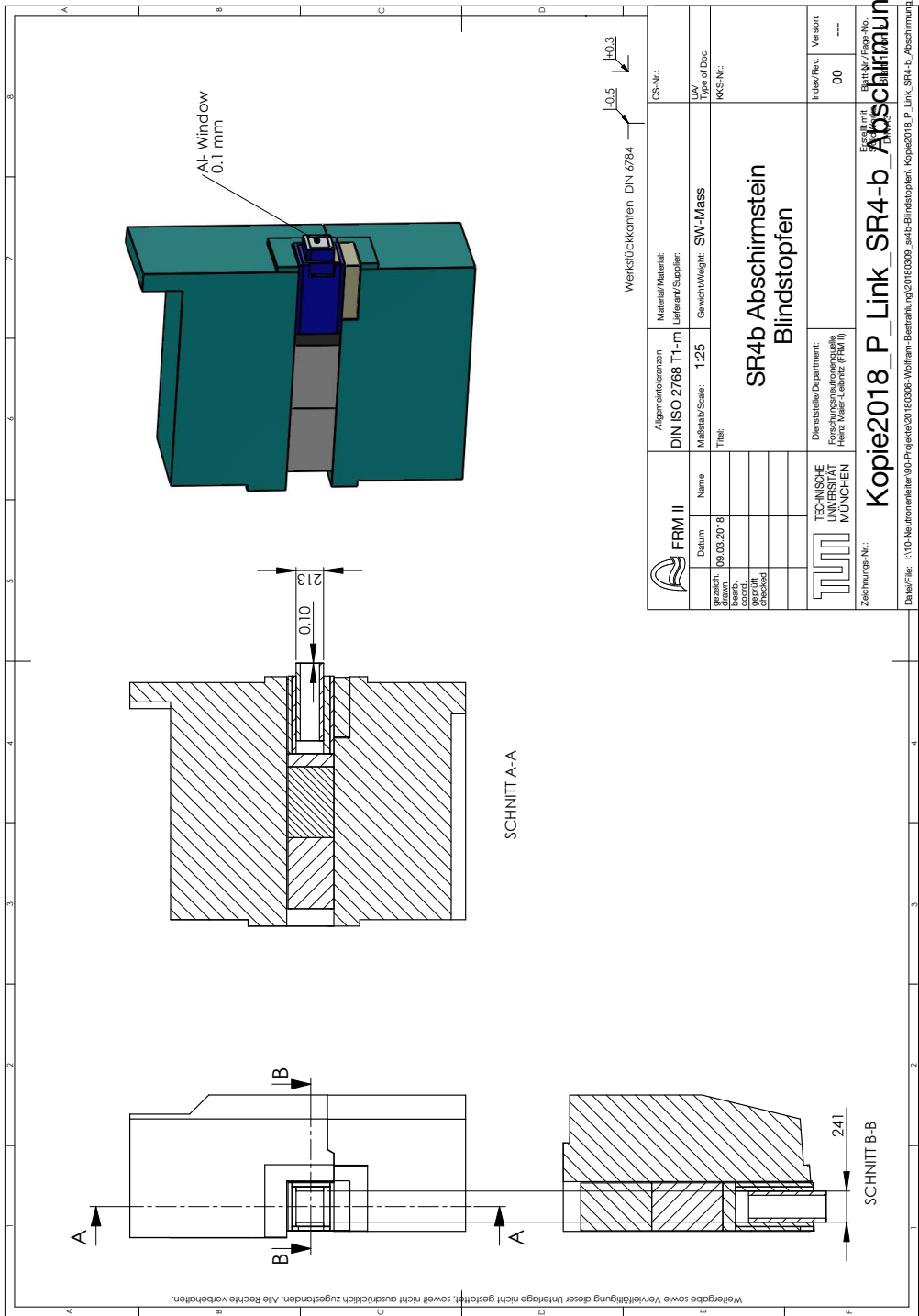
POS.	ANZ.	BENENNUNG	SACHNUMMER / NORM	MATERIAL	BEMERKUNG
1	1	Gehäuse	8403-171-10		
2	1	Shuttermittel 01	8403-171-30		
3	1	Antistieb 01	8403-171-50		
4	1	Shuttermittel 02	8403-171-70		
5	1	Antistieb 02	8403-171-90		

Weikstückkonten DIN 6784

±0,5

	FRM-II		Allgemeinbezeichnung DIN ISO 2768 T1-m	Material/Material: 8403
	Datum 07.12.06	Name Ph. Jüdtner	Maßstab/Scale: 1:2,5	Lieferant/Supplier: ---
Grözüch. Beschränkt 07.12.06	Gezeichnet 07.12.06	Titel: NL3a-o + -u-N Exp.-Shutter NL3a-o + -u-N	Gewicht/Weight: 19,02 kg	Type of Doc.: ---
		Dienststelle/Department: ZWE-FRM-II	Index: 00	Version: ---
Zeichnungs-Nr.: 8403-171-00		Blatt-Nr./Page-No. Blatt 1 von 1		

Datfile: E:\CAD\8403\1x171\Zeichnungen\8403-171-00

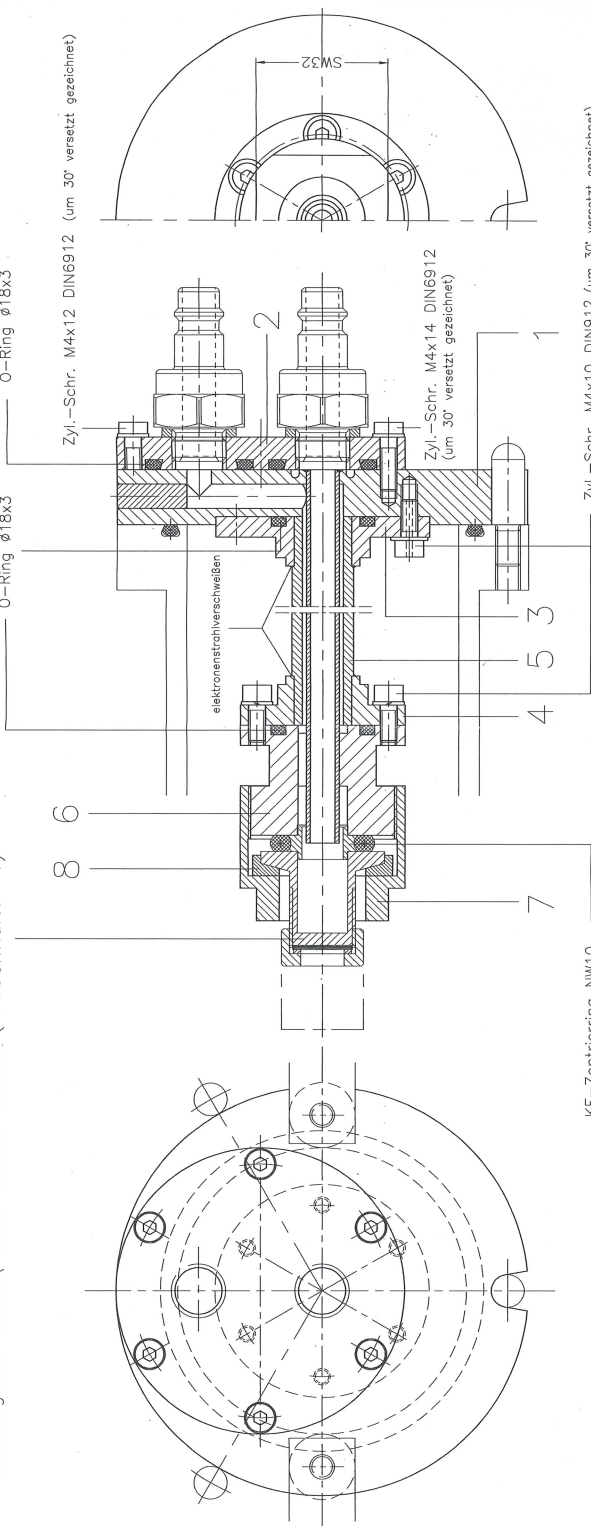


Weißgabe sowie Verfertigung dieser Unterlage nicht gestattet, soweit nicht ausdrücklich zugestanden. Alle Rechte vorbehalten.

		FRM II Name: _____ Datum: 09.03.2018 gezeichnet: _____ bearbeitet: _____ checked: _____ checked: _____	Allgemeintoleranzen DIN ISO 2768 T1-m Maßstab/Scale: 1:25 Titel: SR4b Abschirmstein Blindstopfen	OS-Nr.: _____ Material/Material: Lieferant/Supplier: Gewicht/Weight: SW-Mass UZ/ Type of Doc: KKS-Nr.: _____	Werkstückkonten DIN 6784 H0.5 H0.3
		Dienststelle/Department: Forschungsneutronenquelle Heinz Heine (FRM II)	Holz/Rev.: 00 Version: ----	Zeichnungs-Nr.: Kopie2018_P_Link_SR4-b_Abschirmung	Blatt-Nr./Page-No.: 00
Date/Date: I:\10-Neutronenleiter\9b-Projekte\20180309-Wolfram-Bestrahlung\20180309_sr4b-Blindstopfen_Kopie2018_P_Link_SR4-b_Abschirmung.dwg					

Accelerator target

Zeichng.Nr.: CV28\Folien-Stack-Halter (Probenhalter 1)

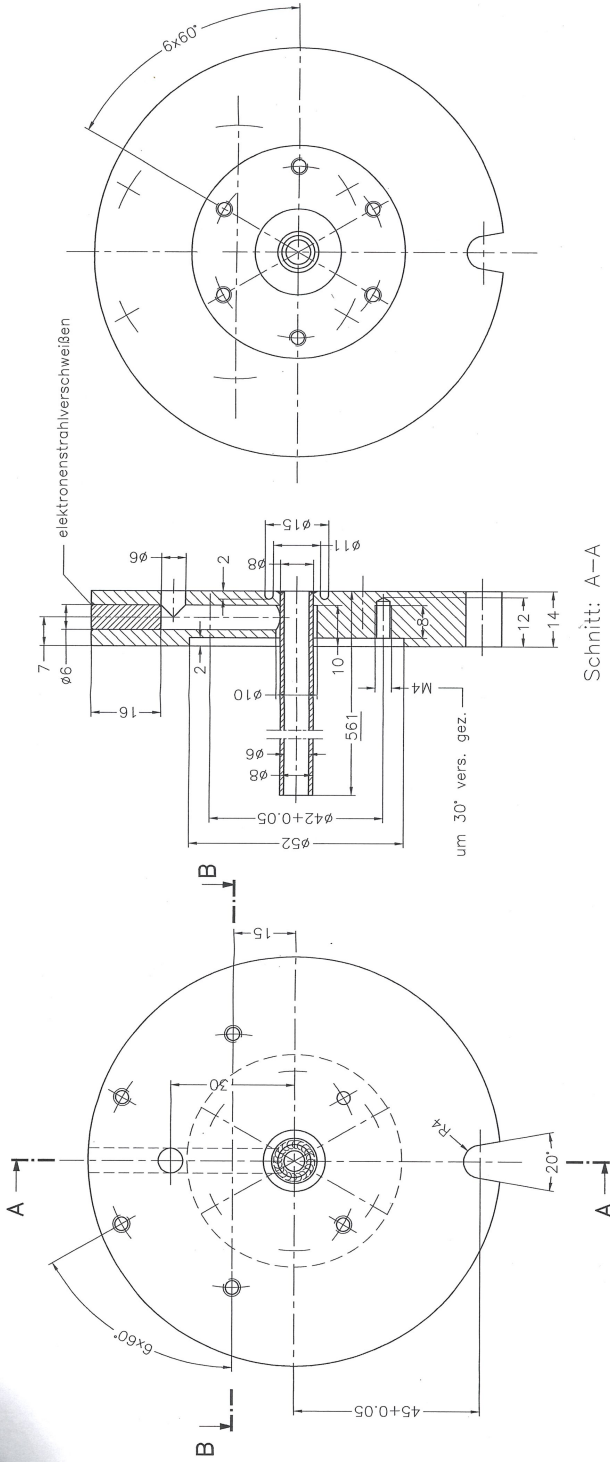


KF-Zentrierring NW10

Zyl.-Schr. M4x10 DIN912 (um 30° versetzt gezeichnet)
6 Stck. Zyl.-Schr. M4x10 mit Ø1,5mm längs durchbohren

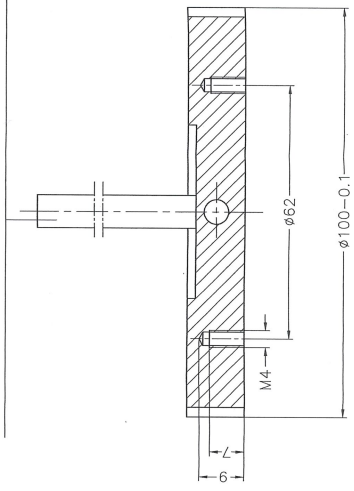
Schweißerarbeiten im Elektronenschweißverfahren durchführen
Achtung: auf Planheit und genaue Bohrungsflucht von Flansch 3 mit 4 beim Verschweißen und Rechtwinklichkeit mit Rohr (5) achten!

Verwendungsbereich		Zul.Abw.	Oberfläche	Maßstab:	Gewicht:
				Werkstoff: AlMg3, 1.4571, G-CuSn12Pb	
				Polzeigung:	
				Rohrzeichn.	
				Benennung:	
				Dummy-Target für Probenhalter 1	
				Zeichnungsnummer:	
				bobyklotr. Adapter für Folien-Stack-Halter	
				Blatt:	
				Ers. d.:	
Zust. Änderung	Datum	Name	Kostenstelle	FZJ	



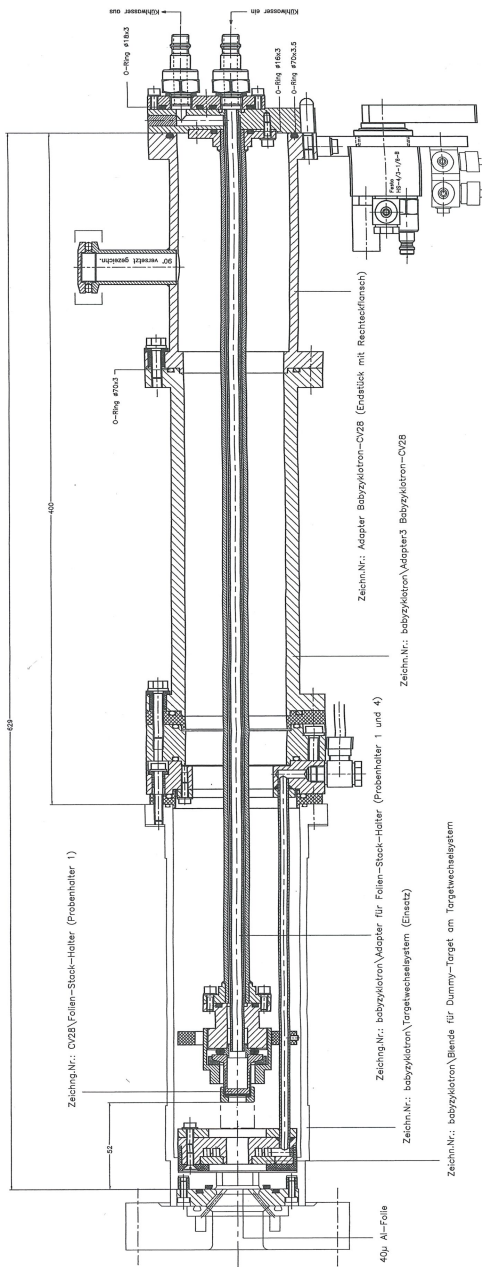
Schnitt: A-A

eingeschweißtes Rohr (elektronenstrahlverschweißen)
(eventuell als Verschweiß-Hilfsmittel einen Zentrierflansch drehen)



Schnitt: B-B

Verwendungsbereich	Zul.Abw.	Oberfläche	Maßstab:	1:1	Gewicht:
			Werkstoff:	AlMg3	
			Halbzug:		
			Rohstell-Nr.:		
			Benennung: Dummy-Target für Probenhalter 1		
			Datei: Teil.5264		
			(Flansch für Kühlwasserschluß)		
			Zeichnungsnummer:		
			babyklotz\Adapter für Folien-Stack-Halter		
			Blatt:		
			Bl.		
Zust./Änderung	Datum	Name	Ers. d.:		
			Ers. d.:		



Zeichn.Nr.: CV28\Folien-Stack-Halter (Probenthaler 1)

40µ Al-Folie

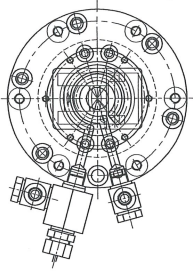
Zeich.Nr.: babyzyklon\Adapter für Folien-Stack-Halter (Probenthaler 1 und 4)

Zeichn.Nr.: babyzyklon\Targetwechselsystem (Einsatz)

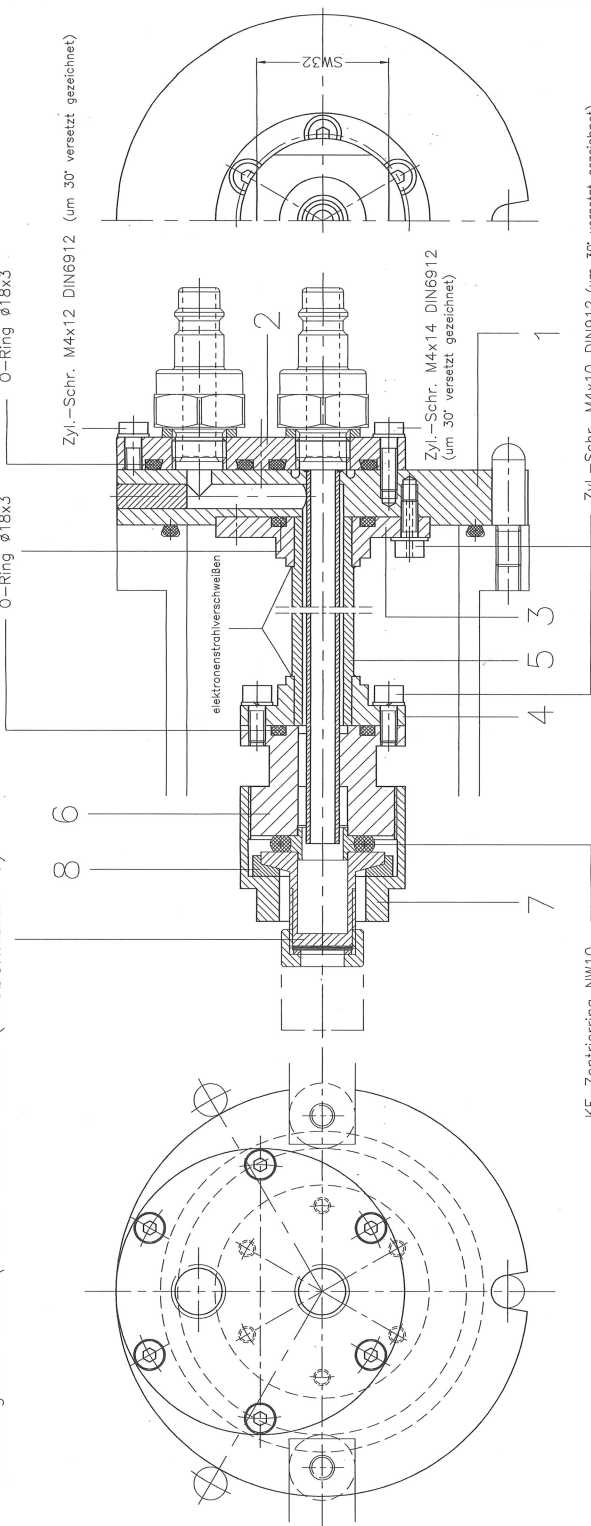
Zeichn.Nr.: Adapter Babyzyklon-CV28 (Ersatzstück mit Rechteckfenst.)

Zeichn.Nr.: babyzyklon\Adapter3 Babyzyklon-CV28

Zeichn.Nr.: babyzyklon\Bende für Dummy-Target am Targetwechselsystem



Zeichng.Nr.: CV28\Folien-Stack-Halter (Probenhalter 1)



Kf-Zentrierring NW10

Zyl.-Schr. M4x10 DIN912 (um 30° versetzt gezeichnet)
6 Stck. Zyl.-Schr. M4x10 mit ø1.5mm längs durchbohren

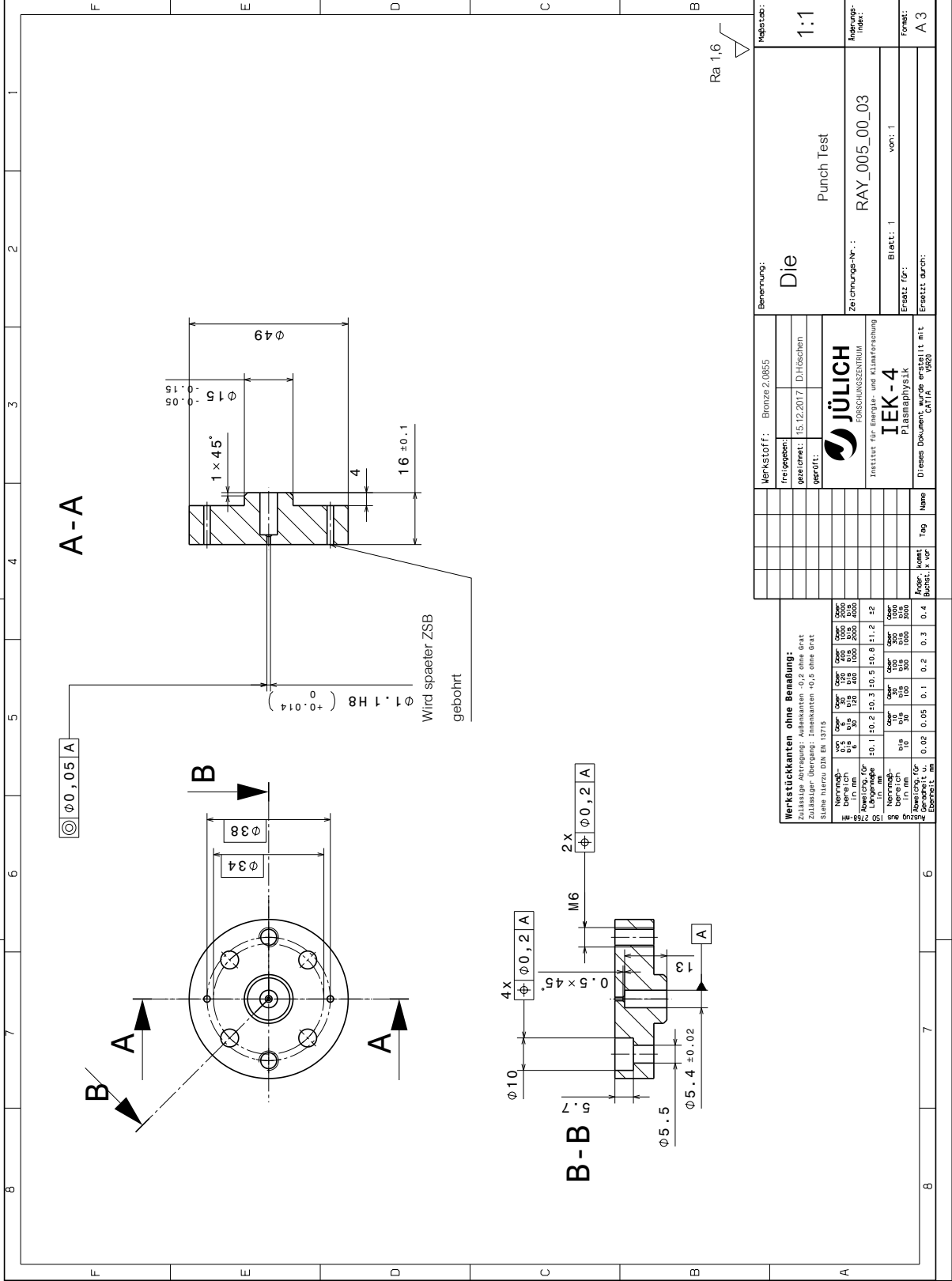
Schweißen im Elektronenschweißverfahren durchführen
Achtung: auf Planheit und genaue Bohrungsflucht von Flansch 3 mit 4 beim Verschweißen und Rechtwinklichkeit mit Rohr (5) achten!

Verwendungsbereich	Zul.Abw.	Oberfläche	Massstab:	Gewicht:
			Werkstoff: AlMg3, 1.4571, G-CuSn12Pb	
			Werkzeug:	
			Rohrteil-Nr.:	
			Benennung: Dummy-Target für Probenhalter 1	
		Datum:	Zeichnungsnummer:	
		Bearb. 20.09.07 W.Bolten	bobyz/oktr\Adapter für Folien-Stack-Halter	
		Gepr. Teil.5284	Blatt:	
		Norm	B1	
Zust., Änderung	Datum	Name	Ers. f.:	
		FZJ		

Shear punch

Schutzvermerk DIN 34 beachten

Tolerierung ISO 8015
 Allgemeintoleranz ISO 2768-MH
 Angabe zur Oberflächenbeschaffenheit nach DIN-ISO 1302
 Dieses Dokument unterliegt - nicht - dem Änderungsdienst
 BGR 901



Werkstückkanten ohne Bemalung:		
1	0,05	0,1
2	0,1	0,2
3	0,2	0,3
4	0,3	0,4
5	0,4	0,5
6	0,5	0,6
7	0,6	0,7
8	0,7	0,8
9	0,8	0,9
10	0,9	1,0
11	1,0	1,1
12	1,1	1,2
13	1,2	1,3
14	1,3	1,4
15	1,4	1,5
16	1,5	1,6
17	1,6	1,7
18	1,7	1,8
19	1,8	1,9
20	1,9	2,0
21	2,0	2,1
22	2,1	2,2
23	2,2	2,3
24	2,3	2,4
25	2,4	2,5
26	2,5	2,6
27	2,6	2,7
28	2,7	2,8
29	2,8	2,9
30	2,9	3,0

Freigegeben:	Werkstoff:	Bemerkung:	Maßstab:
gezeichnet:	Bronze 2,0855	Die	1:1
geprüft:	15.12.2017	Punch Test	
		Zeichnungs-Nr.: RAY_005_00_03	
			Angabefeld:
			Blatt: 1 von: 1
			Format:
			A3

JÜLICH
 FORSCHUNGSZENTRUM
 Institut für Energie- und Klimaforschung
IEK-4
 Plasmaphysik

Dieses Dokument wurde erstellt mit CATIA V5R20

Name	Tag	Anr.-Num.	Kommt.	Formst.	Stanz.	Fr.

Werkstückkanten ohne Bemalung:
 Zählstapfel Abtragung: Außenkanten +0,2 ohne Grat
 Innenkanten: Außenkanten +0,1 ohne Grat
 siehe hierzu DIN EN 13715

Nennmaß	0-1	1-3	3-6	6-10	10-15	15-30	30-50	50-100	100-200	200-300	300-400	400-500	500-600	600-700	700-800	800-1000	1000-1500	1500-2000	2000-3000	3000-4000	
beibeh.	0,05	0,06	0,07	0,08	0,09	0,10	0,11	0,12	0,13	0,14	0,15	0,16	0,17	0,18	0,19	0,20	0,22	0,25	0,30	0,35	0,40
in mm																					
in mm																					
in mm																					
in mm																					

Schutzwinkel DIN 34 beachten

Dieses Dokument unterliegt - nicht - dem Änderungsdienst

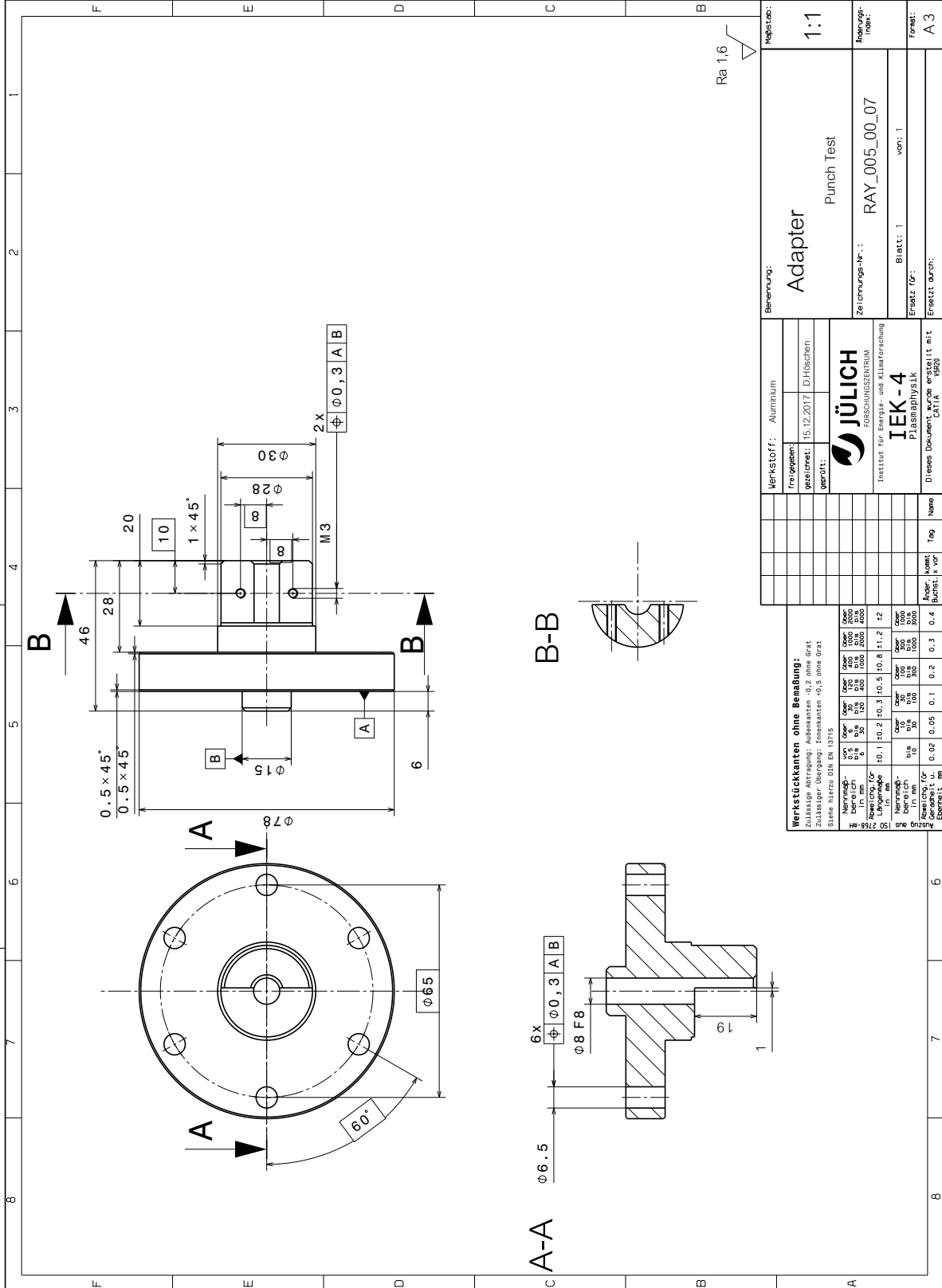
Werkstücknamen nach DIN EN 13715

Angaben zur Oberflächenbeschaffenheit nach DIN-ISO 1302

Allgemeinanz 150 2760-01
 Allgemeinanz 150 2760-01
 Allgemeinanz 150 2760-01

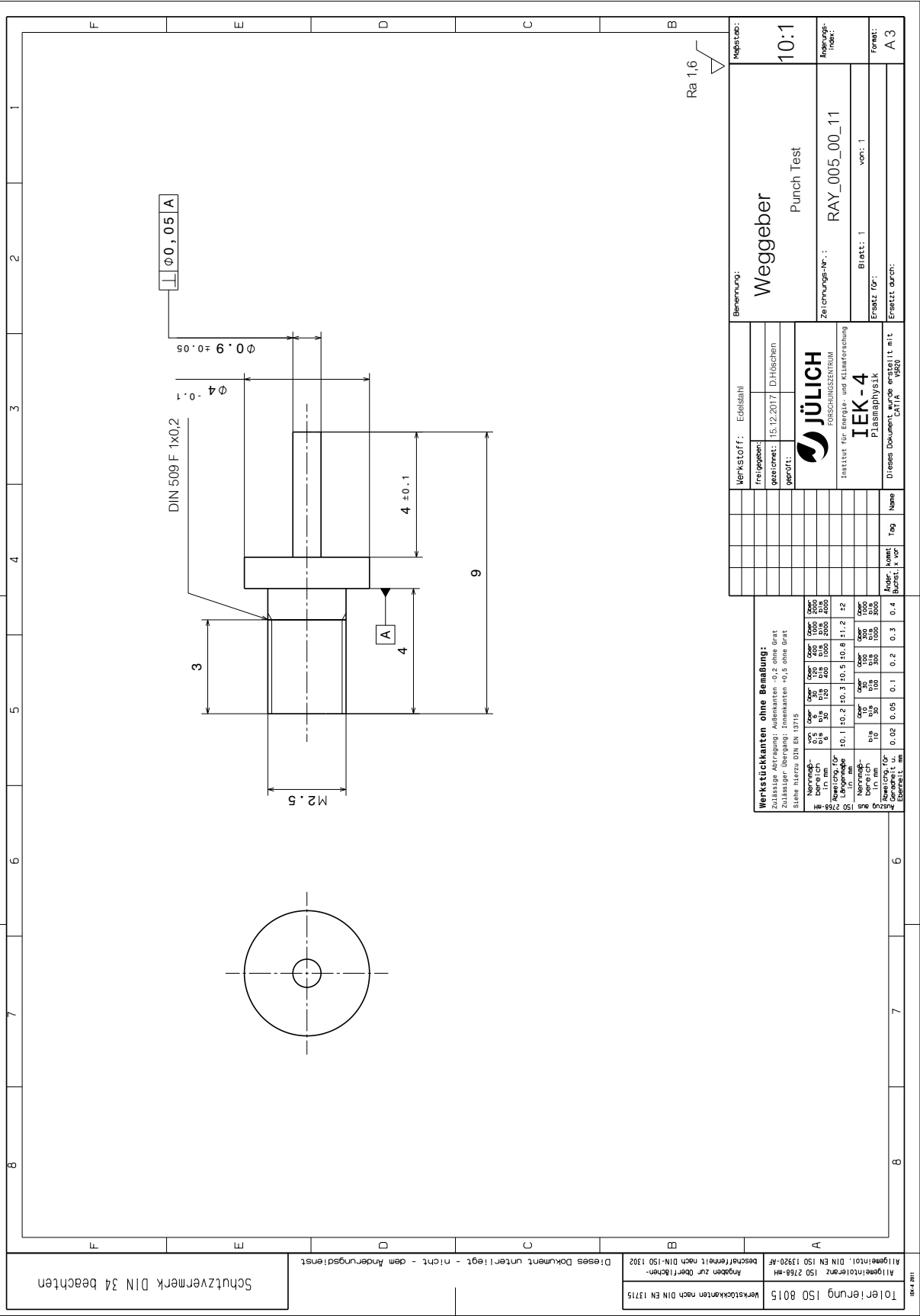
10er-Toleranz 150 8015

REV: 001



Werkstoff: Aluminium		Benennung: Adapter		Maßstab: 1:1	
freigegeben:		gezeichnet: 15.12.2017 D.Höschchen		Punch Test	
geprüft:		JÜLICH FORSCHUNGSZENTRUM Institut für Energie- und Klimaforschung		Zeichnungs-Nr.: RAY_005_00_07	
		IEK-4 Plasmaphysik		Blatt: 1 von: 1	
		Dieses Dokument wurde erstellt mit CATIA V5R20		Erstellt durch:	
		Name		Format: A 3	
		Tag			
		Anz. Blatt / v. v.		Anzahl Blätter	
		Komm.		Anzahl	

Werkstückkanten ohne Bemalung:					
Zulässiger Abtragung: Außenkanten ±0,2 ohne Grat					
Zulässiger Abtragung: Innenkanten ±0,1 ohne Grat					
Siehe hierzu DIN EN 13715					
Werkstückkanten	Größe	Größe	Größe	Größe	Größe
Werkstückkanten	0,5	0,5	0,5	0,5	0,5
Werkstückkanten	1,0	1,0	1,0	1,0	1,0
Werkstückkanten	1,5	1,5	1,5	1,5	1,5
Werkstückkanten	2,0	2,0	2,0	2,0	2,0
Werkstückkanten	3,0	3,0	3,0	3,0	3,0
Werkstückkanten	4,0	4,0	4,0	4,0	4,0
Werkstückkanten	5,0	5,0	5,0	5,0	5,0
Werkstückkanten	6,0	6,0	6,0	6,0	6,0
Werkstückkanten	8,0	8,0	8,0	8,0	8,0
Werkstückkanten	10,0	10,0	10,0	10,0	10,0
Werkstückkanten	15,0	15,0	15,0	15,0	15,0
Werkstückkanten	20,0	20,0	20,0	20,0	20,0
Werkstückkanten	30,0	30,0	30,0	30,0	30,0
Werkstückkanten	40,0	40,0	40,0	40,0	40,0
Werkstückkanten	50,0	50,0	50,0	50,0	50,0
Werkstückkanten	60,0	60,0	60,0	60,0	60,0
Werkstückkanten	80,0	80,0	80,0	80,0	80,0
Werkstückkanten	100,0	100,0	100,0	100,0	100,0
Werkstückkanten	150,0	150,0	150,0	150,0	150,0
Werkstückkanten	200,0	200,0	200,0	200,0	200,0
Werkstückkanten	300,0	300,0	300,0	300,0	300,0
Werkstückkanten	400,0	400,0	400,0	400,0	400,0
Werkstückkanten	500,0	500,0	500,0	500,0	500,0
Werkstückkanten	600,0	600,0	600,0	600,0	600,0
Werkstückkanten	800,0	800,0	800,0	800,0	800,0
Werkstückkanten	1000,0	1000,0	1000,0	1000,0	1000,0
Werkstückkanten	1500,0	1500,0	1500,0	1500,0	1500,0
Werkstückkanten	2000,0	2000,0	2000,0	2000,0	2000,0
Werkstückkanten	3000,0	3000,0	3000,0	3000,0	3000,0
Werkstückkanten	4000,0	4000,0	4000,0	4000,0	4000,0
Werkstückkanten	5000,0	5000,0	5000,0	5000,0	5000,0
Werkstückkanten	6000,0	6000,0	6000,0	6000,0	6000,0
Werkstückkanten	8000,0	8000,0	8000,0	8000,0	8000,0
Werkstückkanten	10000,0	10000,0	10000,0	10000,0	10000,0
Werkstückkanten	15000,0	15000,0	15000,0	15000,0	15000,0
Werkstückkanten	20000,0	20000,0	20000,0	20000,0	20000,0
Werkstückkanten	30000,0	30000,0	30000,0	30000,0	30000,0
Werkstückkanten	40000,0	40000,0	40000,0	40000,0	40000,0
Werkstückkanten	50000,0	50000,0	50000,0	50000,0	50000,0
Werkstückkanten	60000,0	60000,0	60000,0	60000,0	60000,0
Werkstückkanten	80000,0	80000,0	80000,0	80000,0	80000,0
Werkstückkanten	100000,0	100000,0	100000,0	100000,0	100000,0
Werkstückkanten	150000,0	150000,0	150000,0	150000,0	150000,0
Werkstückkanten	200000,0	200000,0	200000,0	200000,0	200000,0
Werkstückkanten	300000,0	300000,0	300000,0	300000,0	300000,0
Werkstückkanten	400000,0	400000,0	400000,0	400000,0	400000,0
Werkstückkanten	500000,0	500000,0	500000,0	500000,0	500000,0
Werkstückkanten	600000,0	600000,0	600000,0	600000,0	600000,0
Werkstückkanten	800000,0	800000,0	800000,0	800000,0	800000,0
Werkstückkanten	1000000,0	1000000,0	1000000,0	1000000,0	1000000,0
Werkstückkanten	1500000,0	1500000,0	1500000,0	1500000,0	1500000,0
Werkstückkanten	2000000,0	2000000,0	2000000,0	2000000,0	2000000,0
Werkstückkanten	3000000,0	3000000,0	3000000,0	3000000,0	3000000,0
Werkstückkanten	4000000,0	4000000,0	4000000,0	4000000,0	4000000,0
Werkstückkanten	5000000,0	5000000,0	5000000,0	5000000,0	5000000,0
Werkstückkanten	6000000,0	6000000,0	6000000,0	6000000,0	6000000,0
Werkstückkanten	8000000,0	8000000,0	8000000,0	8000000,0	8000000,0
Werkstückkanten	10000000,0	10000000,0	10000000,0	10000000,0	10000000,0
Werkstückkanten	15000000,0	15000000,0	15000000,0	15000000,0	15000000,0
Werkstückkanten	20000000,0	20000000,0	20000000,0	20000000,0	20000000,0
Werkstückkanten	30000000,0	30000000,0	30000000,0	30000000,0	30000000,0
Werkstückkanten	40000000,0	40000000,0	40000000,0	40000000,0	40000000,0
Werkstückkanten	50000000,0	50000000,0	50000000,0	50000000,0	50000000,0
Werkstückkanten	60000000,0	60000000,0	60000000,0	60000000,0	60000000,0
Werkstückkanten	80000000,0	80000000,0	80000000,0	80000000,0	80000000,0
Werkstückkanten	100000000,0	100000000,0	100000000,0	100000000,0	100000000,0



Schutzvermerk DIN 34 beachten

Dieses Dokument unterliegt - nicht - dem Änderungsdienst

Tolerierung ISO 8015 Werkstücknenn nach DIN EN 13715

Allgemeintoleranz ISO 2768-HM Angaben zur Oberflächenbeschaffenheit nach DIN-ISO 1302

Werkstückkanten ohne Bemalung:
 zulässiger Abtragung: Außenkanten -0,2 ohne Grat
 Innenkanten -0,2 ohne Grat
 Zylinderkanten -0,1 ohne Grat
 Siehe hierzu DIN EN 13715

Nennmaß	R0,4		R0,8		R1,6		R3,2		R6,3		R12,5	
	in mm	in µm	in mm	in µm	in mm	in µm	in mm	in µm	in mm	in µm	in mm	in µm
0,1	±0,1	±0,2	±0,3	±0,5	±0,8	±1,2	±2					
0,2	±0,2	±0,4	±0,6	±1,0	±1,6	±2,5	±4					
0,5	±0,5	±1,0	±1,6	±2,5	±4	±6,3	±10					
1	±1	±2	±3	±5	±8	±12,5	±20					
2	±2	±4	±6	±10	±16	±25	±40					
5	±5	±10	±16	±25	±40	±63	±100					
10	±10	±20	±30	±50	±80	±125	±200					
20	±20	±40	±60	±100	±160	±250	±400					
50	±50	±100	±150	±250	±400	±630	±1000					
100	±100	±200	±300	±500	±800	±1250	±2000					
200	±200	±400	±600	±1000	±1600	±2500	±4000					
500	±500	±1000	±1500	±2500	±4000	±6300	±10000					
1000	±1000	±2000	±3000	±5000	±8000	±12500	±20000					

Werkstoff: Edelstahl	Freigegeben:	gezeichnet: 15.12.2017	D.Höschken
	geprüft:		
 Institut für Energie- und Klimaforschung IEK-4 Plasmaphysik CITA 1920			
Name	Tag	Anr.-Num.	Kompl. / vor
Dieses Dokument wurde erstellt mit Ersatz durch: CATIA V5R20			

Bemernung:	Weggeber	Maßstab:	10:1
	Punch Test		
Zerchungs-Nr.:	RAY_005_00_11	Abg.-Nr.:	
		Blatt: 1	von: 1
Ersatz durch:			
Format: A 3			

	10ⁿ-fach der Freigrenze gemäß StrSchV Anl. III Tab. 1 unter Anwendung der Summenformel			
	HML-1	HML-2	HML-3	chem. und phys. Beschaffenheit
<i>H-3</i>	$2,5 \times 10^1$	$2,5 \times 10^1$	$2,5 \times 10^1$	gasförmig
	$2,5 \times 10^4$	$2,5 \times 10^4$	$2,5 \times 10^4$	umschlossen, beliebig
sonstige radioaktive Stoffe	5×10^7	1×10^{11}	1×10^9	fest, nicht staubförmig
	5×10^6	5×10^9	1×10^8	beliebig, staub- und gasförmig in fester Umhüllung
	5×10^5	1×10^8	1×10^6	beliebig, nicht gasförmig
	$2,5 \times 10^4$	5×10^6	5×10^6	gasförmig, offen
<i>Hauptnuklide</i>				
<i>Be-7</i>	<i>Fe-59</i>	<i>Sr-90</i>	<i>Ta-182</i>	siehe „sonstige radioaktive Stoffe“
<i>Be-10</i>	<i>Co-58</i>	<i>Zr-95</i>	<i>W-181</i>	
<i>Be-11</i>	<i>Co-60</i>	<i>Nb-93m</i>	<i>W-185</i>	
<i>Cr-51</i>	<i>Ni-63</i>	<i>Nb-95</i>	<i>W-187</i>	
<i>Mn-54</i>	<i>Zn-65</i>	<i>Ag-110</i>	<i>W-188</i>	
<i>Fe-55</i>	<i>Sr-89</i>	<i>Ag-110m</i>	<i>Re-188</i>	

Acknowledgement

At the very start I would like to thank my supervisors, Prof. Christian Linsmeier and Dr. Sören Möller, for their support and belief in this project. Their guidance has been invaluable. I would also like to thank Prof. Dirk Bosbach, who welcomed the idea and made it easy for me to graduate. The IEK-4 department has been a great place for ideas and discussions. I would like to thank the institute leaders and group leaders for creating such an atmosphere. Dr. Jan Coenen and Prof. Bernhard Unterberg, for the discussions and support, I would like to thank you. Angelika Hallmanns, Judith Schönbrener, Marlene Hoffmann, Ruth Hanke and Martina Mangels, thank you for taking care of us in the institute.

This project has been directly supported by many colleagues, to whom I remain extremely grateful. Daniel Höschen, who designed everything with me and made my designs better, in fact he made them workable. Beatrix Göths who helped me setup the polishing method inspite of repeated failures and made great ion beam cuts for me while sipping coffee. Dr. Timo Dittmar, who stayed in late (or as usual) while I was having late nights at the accelerator. Dr. Marcin Rasinski for the TEM, SEM images and FIB cuts.

I am also thankful to Prof. Bernd Neumaier, who gave me beam time at the Baby accelerator. I remain grateful to Dr. Ingo Spahn, who supported me in every way, even though I am not from his institute. Stefan Spellerberg and the Baby accelerator team for multiple visits wherein I caused multiple grievances. Dr. Olaf Felden, I would like to thank you for taking the time out and saving my work from collapsing. Thank you for giving me beam time, even though it was Christmas time already. I am forever grateful.

Many thanks to Dr. Mark Gilbert who welcomed me at CCFE and Oxford, gave me neutron data, helped me with my simulations and taught me fusion neutronics. Dr. Robert Abernethy, thanks for the many conversations ranging from neutron damage to cricket, I enjoyed them all. Dr. Peter Link, Christian Breunig from FRM-II and Stefan Antusch from KIT, thank you for the excellent support towards the cold neutron irradiation project.

Dr. Gerald Pintsuk, Friedel Gormann, Achim Gülpen, Alois Kafka and the HML team, thank you for trying to get things working and expediting everything for my work. I am truly thankful.

My friends who made my time here fun and enjoyable. My colleagues Michael Hubeny, Fleix Klein, Simon Heuer, Philipp Drews, Dieter Boeyaert, Tobias Wegner, Miroslaw Zlobinski, Juri Romazanov, thank you for the good times. The S.C.L.P.DO.HFamily, you guys rock. Ralf, man all the good discussions. Claire, to all the times you stayed up and waited patiently when the accelerator came calling, thank you, Can't stop!. Mum, Dad and Unnu, thanks for everything, always being there, the never ending love and support.

Bill Watterson for Calvin and Hobbes and letting us know that its okay to have ridiculous expectations and ideas.

Band / Volume 526

**Atmospheric Trace Gas Measurements Using Chemical Ionisation
Time-of-Flight Mass Spectrometry**

Y. Li (2020), xi, 110 pp

ISBN: 978-3-95806-520-8

Band / Volume 527

**Uranium accumulation in agricultural soils as derived from long-term
phosphorus fertilizer applications**

Y. Sun (2020), XII, 136 pp

ISBN: 978-3-95806-521-5

Band / Volume 528

**Entwicklung von Schutzschichten für nicht-oxidische
Faserverbundwerkstoffe**

M. Wolf (2021), VI, 150, 2 pp

ISBN: 978-3-95806-524-6

Band / Volume 529

**Mechanical reliability and oxygen permeation of $\text{Ce}_{0.8}\text{Gd}_{0.2}\text{O}_{2-\delta}$ - FeCo_2O_4
dual phase membranes**

F. Zeng (2021), IV, VI, 222 pp

ISBN: 978-3-95806-527-7

Band / Volume 530

**Capacitance-Based Methods to Study Charge Transport and
Recombination in Organic Solar Cells**

I. Zonno (2021), vi, 153 pp

ISBN: 978-3-95806-528-4

Band / Volume 531

**Einflüsse von Klimavariabilität und -wandel auf Ausbau
und Erzeugung im Europäischen Stromsystem**

F. P. Gotzens (2021), XXIII, 231 pp

ISBN: 978-3-95806-530-7

Band / Volume 532

**Weltweite Infrastruktur zur Wasserstoffbereitstellung
auf Basis erneuerbarer Energien**

P.-M. Heuser (2021), VII, 231 pp

ISBN: 978-3-95806-531-4

Band / Volume 533

**Mechanische Eigenschaften von katalysatorbeschichteten Membranen
für die Polymer-Elektrolyt-Membran Elektrolyse**

E. Borgardt (2021), viii, 181 pp

ISBN: 978-3-95806-533-8

Band / Volume 534

Techno-economic Assessment of Hybrid Post-combustion Carbon Capture Systems in Coal-fired Power Plants and Steel Plants

Y. Wang (2021), IV, xx, 230 pp

ISBN: 978-3-95806-545-1

Band / Volume 535

Wissenschaftliche Begleitstudie der Wasserstoff Roadmap Nordrhein-Westfalen

S. Cerniauskas, P. Markewitz, J. Linßen, F. Kullmann, T. Groß, P. Lopion, P-M. Heuser, T. Grube, M. Robinius und D. Stolten (2021), IV, 89 pp

ISBN: 978-3-95806-547-5

Band / Volume 536

High-Resolution Photocurrent Mapping of Thin-Film Silicon Solar Cells Using Scanning Near-Field Optical Microscopy

Z. Cao (2021), xiii, 148 pp

ISBN: 978-3-95806-548-2

Band / Volume 537

Kompressionseigenschaften der Gasdiffusionslage einer Hochtemperatur-Polymerelektrolyt-Brennstoffzelle

E. Hoppe (2021), viii, 153 pp

ISBN: 978-3-95806-549-9

Band / Volume 538

Transparent Passivating Contact for Crystalline Silicon Solar Cells

M. Köhler (2021), 186 pp

ISBN: 978-3-95806-550-5

Band / Volume 539

Distribution of trace gases with adverse effects on fuel cells

D. Klemp, R. Wegener, R. Dubus, L. Karadurmus, N. Kille, Z. Tan (2021), 160 pp

ISBN: 978-3-95806-551-2

Band / Volume 540

Cyclotron Irradiation on Tungsten & Co-relation of Thermo-Mechanical Properties to Displacement and Transmutation Damage

R. Rayaprolu (2021), xiv, 211 pp

ISBN: 978-3-95806-552-9

Energie & Umwelt / Energy & Environment
Band / Volume 540
ISBN 978-3-95806-552-9